Neutron Energy Tuning Assemblies for Nuclear Weapon Environment Applications at the National Ignition Facility

DISSERTATION

Nicholas J. Quartemont, Captain, USAF

AFIT-ENP-DS-21-S-033

DEPARTMENT OF THE AIR FORCE
AIR UNIVERSITY

AIR FORCE INSTITUTE OF TECHNOLOGY

Wright-Patterson Air Force Base, Ohio

AFIT-ENP-DS-21-S-033

NEUTRON ENERGY TUNING ASSEMBLIES FOR NUCLEAR WEAPON ENVIRONMENT APPLICATIONS AT THE NATIONAL IGNITION FACILITY

DISSERTATION

Presented to the Faculty

Graduate School of Engineering and Management

Air Force Institute of Technology

Air University

Air Education and Training Command

in Partial Fulfillment of the Requirements for the

Degree of Degree of Doctor of Philosophy in Nuclear Engineering

Nicholas J. Quartemont, B.S., M.S.

Captain, USAF

September 2021

AFIT-ENP-DS-21-S-033

NEUTRON ENERGY TUNING ASSEMBLIES FOR NUCLEAR WEAPON ENVIRONMENT APPLICATIONS AT THE NATIONAL IGNITION FACILITY

DISSERTATION

Nicholas J. Quartemont, B.S., M.S.
Captain, USAF

Committee Membership:

Maj James E. Bevins (Chairman)

Dr. Abigail A. Bickley (Member)

Dr. Clark N. Taylor (Member)

Dr. Narek Gharibyan (Member)

Abstract

An energy tuning assembly was developed to spectrally shape the National Ignition Facility deuterium-tritium fusion neutron source to a notional thermonuclear and prompt fission neutron spectrum to fulfill capability gaps in available neutron source environments. In this work, a nuclear data covariance framework was developed utilizing stochastic sampling of the radiation transport cross sections to predict the energy tuning assembly performance to create the objective spectrum and assess anticipated experimental outcomes. The experimental neutron environment was characterized with activation foil dosimetry measurements coupled with a neutronics model and unfolded with the neutron transport covariance information. The unfold resulted in broad agreement with the modeled environment with a reduced chi-square statistic of 1.6, which validated the framework for the neutronics modeling techniques. Additionally, the neutron spectrum was unfolded with a heuristic-based regularized technique, which was shown to extend to characterize less well-quantified neutron activation dosimetry experiments. The first energy tuning assembly was experimentally demonstrated to create a synthetic spectrally-accurate post-detonation fission product distribution, enhancing U.S. technical nuclear forensic capabilities for nuclear weapon attribution and device reconstruction.

ATHENA, a second-generation energy tuning assembly, was also optimized to meet similar objectives, but the new platform neutron fluence efficiency was increased by a factor of 2.7. The ATHENA platform was experimentally fielded to benchmark and validate the new models looking forward to an active measurement of electronic devices as the energy tuning assembly capability was extended to an

experimental short-pulse neutron source with a neutron pulse length of ∼50 ns in the spectrally-shaped test chamber. The radiation environment was unfolded with a reduced chi-square metric of 1.4, again indicating strong agreement with the model; however, additional experimentation was required to diagnose the ionizing radiation environment at higher fidelity. The analysis performed in this research enabled the successful fielding of two energy tuning assembly experiments at the National Ignition Facility. The novel ATHENA platform provides a capability to perform integral nuclear data measurements and active experimentation on electronics component in a unique radiation environment, beneficial to the technical nuclear forensics components and radiation effects on electronics communities.

Acknowledgements

First, I would like to thank my research advisor and dissertation committee chair, Maj James Bevins, whose support and thought provoking guidance was invaluable to this work. I would like to thank my dissertation research committee members, Dr. Abigail Bickley, Dr. Clark Taylor, and Dr. Narek Gharibyan for your contributions and support. I owe many thanks to the SCALE group at Oak Ridge National Laboratory who contributed much to the success of this work. Finally, I want to thank the great group of engineers and scientists at Lawrence Livermore National Laboratory and the National Ignition Facility who without, much of this work would not have been possible.

Nicholas J. Quartemont

This dissertation is dedicated to my family, whose love and support I will always be grateful for.

Table of Contents

Page

Page

Page

List of Figures

List of Tables

NEUTRON ENERGY TUNING ASSEMBLIES FOR NUCLEAR WEAPON ENVIRONMENT APPLICATIONS AT THE NATIONAL IGNITION FACILITY

I. Introduction

1.1 Motivation

Nuclear deterrence is the cornerstone of U.S. nuclear policy and strategy [1]. A key component of deterrence theory that enables U.S. strategic objectives is the credibility of the U.S. nuclear capability. Two key aspects related to the Department of Defense (DOD) nuclear deterrence credibility are attribution capabilities to hold potential threats accountable and the surety of nuclear weapon systems to function if needed.

The final full-scale U.S. nuclear weapon test was performed on 23 September, 1992. The non-proliferation of nuclear weapons, and general health and environmental concerns from the radioactive emissions were key drivers for eliminating testing of any kind. The Comprehensive Test-Ban Treaty (CTBT) was designed to ban nuclear explosions for all signatories or supporting nations for an indefinite duration since 1996. A handful of tests have been conducted after the CTBT was opened for signature; none have been by the U.S.

However, the 2018 U.S. National Defense Strategy identified the modernization of the nuclear triad as a key requirement for deterrence credibility [2]. Therefore, there is still a need for the capabilities previously provided through nuclear testing for the study of nuclear environments to support the credibility of the nuclear deterrent. Previous work has shown that the decision to cease nuclear testing has

created a capability gap to reproduce radiation environments relevant to national security applications such as nuclear weapons effects (NWE) and technical nuclear forensics (TNF) [3, 4].

1.1.1 Nuclear Weapon Certification Capability Gap.

Each U.S. administration has supported the requirement and maintenance of a nuclear force structure after the elimination of nuclear tests. Recently, former President Donald Trump stated at the 2018 State of the Union Address, "As part of our defense, we must modernize and rebuild our nuclear arsenal, hopefully never having to use it, but making it so strong and powerful that it will deter any acts of aggression [5]." To this end, the National Nuclear Security Administration (NNSA) is tasked with the mission of maintaining the nuclear stockpile's safety, security, and effectiveness under the Stockpile Stewardship Program (SSP). Full-scale system testing in relevant environments is generally recognized as a critical requirement for nuclear weapon certification, just as it is for any DOD weapon system. Since actual system level tests cannot be performed, demonstration of components or subsystems in a relevant environment is an important part of assessing the technology readiness level as part of the DOD acquisition strategy, as laid out in Instruction 5000.02 series [6], and the DOD nuclear certification process, as specified in DOD Directive 3150.02 [7].

Representative nuclear weapons system and effects testing supporting the SSP is carried out by the Department of Energy (DOE), DOD, and supporting organizations. The scope of the testing sites is wide, ranging from radio frequency communications to the prompt γ-ray and neutron emissions following a nuclear event. Some testing is conducted on components of the nuclear weapons themselves, such as the near-system-level hydrodynamic tests performed with inert pits [8]. However, many aspects of

nuclear weapons are only testable via computational methods or experiments which may not truly represent the physics involved in a nuclear weapon. Not employing full-scale nuclear testing accentuates uncertainty in nuclear force credibility, so alternative testing methods are of extreme importance to the nuclear enterprise.

One important gap identified is the availability of neutron environments for testing at current U.S. facilities in comparison with the environment that a nuclear weapon would experience or produce [3]. Current U.S. neutron sources do not have an accurate energy or temporal distribution for the nuclear environment that nuclear systems are required to survive in certification testing. This problem is complicated further as the transmitted neutron flux through the physical environment and to the target varies significantly in energy and temporal distribution depending on the scenario and system being considered. Furthermore, the neutron fluence and energy spectrum internal to the weapon cannot be directly measured but must be inferred from sources such as activation products. The lack of a relevant facility has led to a reliance on simulations and large engineering safety factors [9]. To address this capability gap, it would be beneficial to have a neutron environment testing capability with an accurate neutron energy and temporal profile.

1.1.2 Technical Nuclear Forensic Capability Gap.

A key strategy for countering nuclear terrorism identified in the 2018 Nuclear Posture Review is the importance of "deterring state support for nuclear terrorism through advanced forensics and attribution capabilities [1]." To this end, the technical nuclear forensic (TNF) community requires the ability to generate representative post-detonation debris samples for training and development of attribution techniques as fission debris is paramount to the nuclear device reconstruction capabilities [10]. However, the generation of accurate fission product

inventories in the representative debris is both extremely important for the attribution and very difficult to do with existing U.S. facilities due to a diminishing pool of subject matter experts and outdated facilities [11].

According to the Joint Nuclear Forensics Working Group report from 2013,

> Current post-detonation debris analysis techniques derive largely from the nuclear weapons test programs of the Cold War. Leveraging the Cold War infrastructure enabled a baseline forensics capability to be established quickly, but has resulted in a capability that relies largely on science and technology developed in the nuclear-testing era, with timelines and priorities sometimes distinct from those of nuclear forensics. In addition, current analysis methods are often labor-intensive, and rely on education and training that are no longer prominent in the U.S. university system [12].

Advances in attribution capabilities for TNF require facilities that produce nuclear weapon relevant environments that drive the distribution of observed fission products. Of course, the attribution problem is more complex than just getting the correct starting population in that chemical and physical processes can drastically impact the post-detonation debris. Nonetheless, the generation of realistic synthetic weapons debris would be of enormous benefit to the TNF community for training and research to improve the nation's forensic-based attribution capabilities, and accurately reproducing the initial fission product population is a strong first step in that direction.

A primary component of the debris critical for these capabilities is the fission product inventory in the debris. Post-detonation fission product analysis provides a means of determining many characteristics of a nuclear device. In particular, according to a U.S. National Research Council report from 2009, the fission debris can provide the most accurate measurement of weapon yield when combined with device information [13]. Additionally, the CTBTO utilizes fission products to verify

compliance with the nuclear test ban [10].

1.1.3 Neutron Environment Capability Gap.

The capability gaps outlined for nuclear weapons certification and TNF motivate the need to generate spectrally accurate nuclear weapon relevant neutron environments. In particular, the present U.S. testing capability does not have the ability to produce neutron spectra that combine a thermonuclear (TN) and prompt fission neutron spectrum (PFNS). The vast majority of U.S. testing facilities are focused on the Watt-fission spectrum, while a few are capable of producing the 14.1 MeV TN component from the deuterium-tritium (DT) fusion process [14, 15]. Several examples of U.S. testing facilities for prompt neutrons are the Sandia Pulsed Reactor III (SPR-III), Sandia Annual Core Research Reactor (ACRR), White Sands Missile Range (WSMR) Fast Burst Reactor (FBR), the Los Alamos National Laboratory (LANL) Rotating Target Neutron Source (RTNS), and the LANL Weapons Neutron Research facility (WNR). The neutron spectral profile of these facilities compared to a notional objective TN+PFNS is shown in Figure 1.1.

Each of the available neutron sources has an important purpose for national security applications; however, they cannot meet the energy spectrum for every nuclear testing requirement. In comparison with the TN+PFNS, nearly all of the neutron sources are heavily weighted to lower energies and do not contain enough high-energy neutrons to represent the TN component of a nuclear weapon. The RTNS has a high-energy component, but the magnitude of the flux is substantially lower than required for nuclear hardness applications where the timing profile and integral fluence is important. Additionally, these large facilities are often at risk of shutdown, such as the RTNS source in 1987 and the SPR-III decommissioning for storage at the Nevada Test Site in late 2006 [16, 17]. Others, such as WSMR FBR,

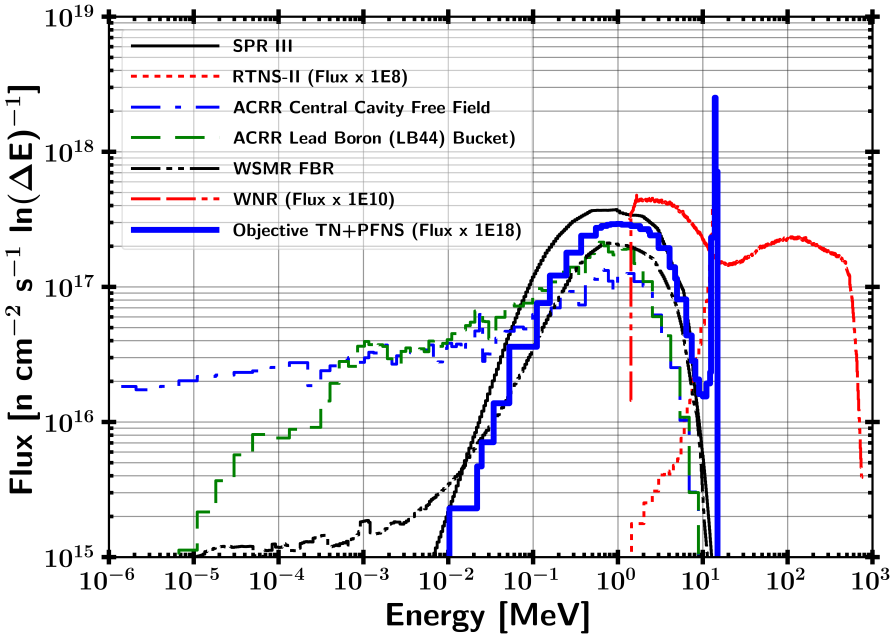

Figure 1.1. Comparison of selected neutron sources to notional TN+PFNS [4].

are discussed for shutdown with growing regulatory demands and security requirements for storing highly enriched uranium (HEU) [18].

Neutron environment timing and intensity are also important characteristic metrics for neutron testing and play a large role in device response. Different neutron environments can be broadly compared on the basis of displacement damage, where the spectrum is represented as a collapsed 1-MeV fluence of neutrons in a material, (1-MeV (Si) for example), based on the equivalency of displacement damage at a reference energy, outlined in ASTM 19−722 and discussed further in Section 2 [19]. Fast burst reactors such as the dismantled SPR-III or WSMR FBR, the gold standard for prompt fission spectrum neutron irradiation, can produce a neutron fluence of 5×10^{14} 1-MeV(Si) $\frac{n}{cm^2}$ with a approximately 100 μs full width at half max (FWHM) [20, 21]. Facilities such as the National Ignition Facility (NIF) can provide a prompt (<1 ns) source of 14.1 MeV neutrons from deuterium-tritium (D-T) fusion reactions above 10^{13} 1-MeV(Si) $\frac{n}{cm^2}$ [22]. Nuclear reactors, such as the

ACRR, can produce in excess of 10^{15} 1-MeV(Si) $\frac{n}{cm^2}$ over a longer 6 ms timescale in pulsed mode; however, they include a larger ionizing dose with a thermal neutron component to the overall spectrum [23].

Accurate experimental results requires a neutron flux spectrum equivalent to that of a true nuclear event, which creates a need for a neutron source capable of emulating the environment. Therefore, development of a TN+PFNS source would enable production of the correct fission product inventory in surrogate debris and thereby enhance the ability of the TNF community to perform the attribution mission. Furthermore, the need for an accurate source term and timing environments increases as newer technology moves farther away from trusted and validated data sets. A TN+PFNS source capable of NWE testing would also greatly benefit the nuclear weapon certification process.

1.2 Background

Many approaches can be used to create nuclear weapon-relevant neutron spectra in the absence of full-scale nuclear weapons testing. Some mechanisms are only applicable within different communities in the nuclear sciences. Four main ways that neutron environments can be approximated for synthetic fission product debris production are sample doping, direct production using fission converters, surrogate methods, and spectral modification of existing sources [4]. In the context of neutron effects on electronics, the key approaches utilize existing sources, computational models, and surrogate charged particle reactions [4, 24]. Each of these methods are limited in representing the neutron environment experienced in a nuclear weapon. For example, neutron effects testing on electronics requires knowledge of the neutron energy spectrum, timing, and integral neutron fluence. Additionally, simultaneous γ-ray environments also play a role causing ionization effects which

can be formulated as a combined effects experiment or introduce noise into a primarily neutron effects experiment.

The sample doping technique is accomplished by selectively correcting mass chains to modeled equivalent ratios. The resultant sample is built so as to look like it was produced with a desired energy-dependent fluence. This has been done for the production of glass surrogate fallout debris for use in exercises or training [25]. The glassy matrix is created to emulate the solidified fission debris and entrained environment that is swept up in the stem of a nuclear explosion. The glass is doped with uranium and irradiated under various neutron environments depending on the requirements; however, the irradiation is often done with a thermal neutron reactor.

A key deficiency with utilizing a thermal reactor is that the neutron energy spectrum is not a close approximation to a weapon spectrum, and the resultant fission product ratios that follow will therefore not be accurate either. Utilizing a harder, or higher energy, neutron reactor spectrum is a better approximation; however, it is still not an accurate representation of the fission product distribution. The valley fission products will be significantly lower than for a higher energy weapon spectrum.

Alternatively, the sample doping technique can be approached by irradiating different samples at different facilities. A final sample which has the "correct" fission product ratios can be created by selectively pulling mass chains from the irradiated samples. This sample doping technique creates a useful fission product debris sample; however, the spectral and temporal nature of the sample is not equivalent to what would be produced in a real nuclear explosion, and the overall matrix is incorrect as it is often generated in a thermal nuclear reactor.

Direct production using fission converters utilizes nuclear reactions to create a shaped neutron flux, which can be done via charged particle interactions or through

fusion sources with a fission converter [26]. It has been shown that direct production is "impractical, complex, and unlikely to be implemented for safety or technological limitations [4]."

Surrogate methods rely on the formation of an equivalent compound nucleus through an alternative reaction mechanism [27, 28]. Surrogate methods are popular in studies where forming the product nucleus through the desired reaction is difficult or the energy cannot be fine-tuned. An example of this is neutron-induced fission on ^{235}U where a possible surrogate for the ^{235}U neutron-induced fission reaction, (n,f), is ^{232}Th (α,f), both of which form the ^{236}U compound nucleus. The surrogate approach has seen success; however, the nuclear data supporting the reactions is not as well understood [29, 30]. Additionally, there are some assumptions on the compound nuclear equilibration and spin-parity state which can impact the decay channels of the studied reactions [27].

Another commonly used alternative reaction surrogate method is to utilize charged particles for neutron damage in radiation effects on electronics. Ion beams can be used as a surrogate for neutrons by comparing the relative displacements per atom caused by the charged particle compared to a neutron [31]. A major benefit of using ion beams is that the energy can be finely tuned both in energy and deposition location, whereas neutrons are not as easily controlled. While this allows for precisely exploring device damage, it is not generally or broadly representative of neutron damage that creates a distribution of recoil ion energies relatively uniformly throughout the entire device due to the neutron mean free path being much greater than device dimensions. Another disadvantage of using charged particles is that a large portion of the energy deposition as it travels through materials is based on electronic stopping power, while the neutral neutrons have negligible electronic interactions.

The Qualification Alternatives to the Sandia Pulsed Reactor (QASPR) program

is the most significant venture into the use of surrogate ions to perform neutron effects component level testing as a replacement alternative for the SPR [3]. QASPR combines operational irradiation facilities with modeling to predict neutron effects on electronic performance. While there have been substantial improvements to increasing the verification and validation of simulated charged particles to experimental outcomes, the validation for the experimental data benchmarked to neutron experimental data is lacking in many cases [24].

The last main approach to create accurate energy distribution neutron environments that could be used is spectral modification, which is a method of altering a neutron spectrum through nuclear interactions to generate an energy spectrum of interest. Fundamentally, spectral modification is the goal of moderated nuclear reactors to increase efficiency and allow the use of low-enriched uranium fuel.

Spectral modification is also performed in beam shaping assemblies used for boron neutron capture therapy (BNCT), where neutrons are used to treat tumors through neutron capture reactions in boron. BNCT has been explored with a wide variety of sources including accelerators and deuterium-deuterium (DD) fusion. A beam shaping assembly can be designed to moderate a source neutron flux to appropriate thermal, epithermal, and fast spectra for BNCT [32], and an optimized objective neutron spectrum focused on the epithermal region is published by the International Atomic Energy Agency (IAEA) [33]. The build up of a design is produced primarily through moderation, reflection, and collimation of neutrons to the patient [34].

However, the approach to designing a beam shaping assembly lends itself to inefficiencies from an energy and population perspective. The collimation process blocks out a portion of potentially usable particles. Additionally, the beam shaping assembly resultant spectrum is often under-optimized as the result is often

determined from a limited parametric study. The development process could be enhanced to increase efficiency and spectral profile agreement with the objectives.

A novel spectral modification approach was developed by the University of California-Berkeley and Lawrence Livermore National Laboratory (LLNL) for the development of an energy tuning assembly (ETA) to modify the NIF source to produce a TN+PFNS [4]. To perform the spectral modification, the Coeus metaheuristic optimization software package was developed to avoid manpower-intensive parametric studies and enable the rapid design of ETAs to convert a facility's characteristic source spectrum to any arbitrary objective spectrum, within the constraints imposed by physics [35]. Gnowee, the Coeus optimization engine, was developed for "rapid convergence to nearly globally optimum solutions" of this class of engineering problems [36]. It is important to note that the Gnowee and Coeus codes have applicability over a wide range of engineering problems, not just for the production of a TN+PFNS source.

The first ETA design was built and preliminary validation tests were conducted at the Lawrence Berkeley National Laboratory's 88-Inch Cyclotron [4, 37, 38]. The preliminary validation utilized 33 MeV deuterium breakup on tantalum as a neutron source and investigated the ability to model the ETA performance [38]. Integral validation of the ETA at NIF was performed in fiscal year (FY) 2019 [39] followed by the construction and validation of an enhanced ETA design in FY2020.

1.3 Research Objectives

There are several key problems that require investigation for the use of ETAs to fulfill the requirements to spectrally shape neutron sources into a targeted TN+PFNS [4]. The overarching research problem for this endeavor is "*What capability can an ETA provide to existing sources such as the NIF, and how can*

ETAs be utilized to provide a spectrally- and temporally-relevant neutron source term for nuclear environments?"

This research effort aims to address the characterization and analysis of the 2019 ETA experiment with a primary goal of demonstrating the platform to produce spectrally accurate fission product debris. Second, an updated ETA platform, ATHENA, was designed and validated with the ultimate objective for an experimental platform as a short pulse TN+PFNS for neutron effects testing on electronics. The integral ATHENA-I environment is used as a baseline for the modified ATHENA-II platform where active electronics can be fielded for radiation environment testing under the unique TN+PFNS at short pulse time-scales. Finally, activation foil experimental measurements were used to validate the modeled neutron environments through neutron spectrum unfolding, and an unfolding technique was developed to improve upon current solution methods. The generalized research areas are detailed below in Table 1.1, organized by the problem and capability that they support as summarized by Chapters 3-7.

Table 1.1. Research Objectives

Objective	Chapters
ETA Experiment	3 - Nuclear Data Covariance Analysis 4 - ETA Analysis Methods 5 - ETA Fission Product Experiment
ATHENA Experiment	6
Neutron Spectrum Unfolding	7

The research objectives are provided below and include information to answer the overarching research problem. The main experiments conducted include the fielding of ETA at NIF in 2019 and ATHENA in 2020. Where, a general aim is to create and modify tools that are capable of measuring the created environments to aid in the development of an experimentally-validated modeling capability. A strongly supported model with realistic uncertainties helps to determine

environments at locations other than the direct measurement positions. The ATHENA platform was able to heavily leverage the analysis techniques developed for the original ETA platform, so the framework created for ETA also served for ATHENA.

1. 2019 ETA Fission Product NIF Experiment

    - **Quantify the impact of nuclear data covariance on the simulated results for the ETA sample region:** For accurate characterization of the neutron environment using spectrum unfolding methods, the systematic uncertainty, driven mostly by nuclear data uncertainty, must be characterized as the modeled statistical uncertainty for well-converged models can be removed by increasing the number of histories performed in a simulation.
    - **Design an improved foil activation diagnostic pack to be more robust over a broader energy range:** Fielded diagnostic activation foils and their energy dependent reaction products were also of importance for neutron spectrum unfolding, where the neutron spectrum is deconvolved from measured activation products and reaction cross sections. Ideally, activation reactions would be chosen to cover the entire experimental energy range. The primary challenge here was to provide more data to the epithermal neutron energy region, which suffers from a low number of independent reaction channels.
    - **Model ETA fission products production:** An understanding of the neutron environment convolved with energy-dependent fission product production channels required the use of theoretical fission models coupled with semi-empirical relationships for first and second-chance fission on U

isotopes. The most current nuclear data libraries did not contain energy-dependent fission yield correlation, which can under-predict the modeled uncertainties, as needed for matching experimental results.

- **Validate the ETA models at NIF:** The 2019 ETA platform functioned as an option for producing spectrally accurate fission products with a prompt source of TN+PFNS neutrons, preventing decay during the irradiation conditions. This required the collective models for fission product distribution and the neutron spectrum to be characterized.

2. 2020 ATHENA Platform NIF shot

- **Develop an improved ETA design that better conforms to the optimal ETA placement at NIF**: The development and optimization of an ETA at NIF required pushing the limits of the NIF facility to reduce standoff ranges and compress the design of an ETA to minimize spherical divergence losses. The primary challenge was to maintain spectral agreement with a TN+PFNS, and improve upon the efficiency and desired neutron spectrum.
- **Develop an enlarged sample irradiation area subject to the TN+PFNS:** Irradiation of actively monitored and powered equipment inside of the ATHENA platform required a modular internal design for the ATHENA platform. Although ATHENA was not optimized for this purpose, the internal portion of ATHENA was modified to allow for an expanded 7 cm diameter, 8 cm high cylindrical irradiation configuration with an external primarily D-T irradiation position to allow for multiple, larger experiments to be conducted on one platform.
- **Characterize the ATHENA platform as a short pulse neutron**

source: The analysis of ATHENA required an in-depth radiation environment characterization, similar to ETA. However, the ATHENA platform must also be assessed for ionizing radiation environments, which can effect devices, along with the temporal aspects of the radiation.

3. Neutron Flux Unfolding Techniques

- **Develop a heuristic-based neutron flux unfolding algorithm to address gaps in available codes:** Neutron environment unfolding techniques on ETA and ATHENA required a strong understanding of the achieved TN+PFNS distribution. However, current neutron flux unfolding techniques generally require an *a priori* estimate of the neutron environment. Many techniques fail if a relevant starting guess is not available for part of the environment. A heuristic based unfolding technique that does not require a full initial guess was leveraged with a regularization parameter to unfold neutron spectra that are missing partial characterization.
- **Perform neutron flux unfolding on several cases of neutron trial spectra:** Demonstration of an unfolding technique required testing the framework on multiple activation environments. The primary issue to address was the strength of the regularization term, which is often a subjective parameter. Additionally, the physics-based similar dependence of reaction cross sections coupled with a low amount of possible reaction mechanisms in the epithermal neutron energy range presented challenges for this technique.

1.4 Assumptions and Limitations

An omnipresent limitation in many studies of science and engineering is the quality and quantity of available data for applications. Nuclear engineering commonly draws from published works containing the relevant nuclear data and the uncertainties behind them. There is also uncertainty in the published uncertainties as much of the available data are derived from models and never directly tested. The results presented in this document are limited by the currently accepted understanding of nuclear physics phenomena and by the limitations of published data that are consistently being improved upon by the nuclear science community.

The second assumption of this work is that the nuclear covariance follows a multivariate normal distribution. Further analysis of this assumption is outlined in Section 3. Additionally, the uncertainty was assumed to be relatively insensitive to group structure.

One delimitation, which is done for convenience and publishing ability, is that the nuclear weapon environments are presented at an unclassified level. All information used to develop the neutron flux and profile is available in open literature or derived from unclassified information and references. The scope of this work aims to provide a capability where, if desired, one could go from the unclassified spectrum to one that meets a requirement.

An assumption for this work is that the NIF is the most effective choice of the neutron source. Other sources may exist that would also perform the role, but the NIF has unique benefits such as the prompt nature of the neutron yield and the fast neutrons arising from DT fusion. Although the NIF has been in operation since approximately 2010, there is a potential insertion of systematic error based on the source characterization and variability in the source output. However, any changes to the magnitude of the NIF source output will produce linear responses to the results

shown here, so uncertainty in determining the source strength is not a high risk item. Additionally, the NIF geometric uncertainty is considered negligible due to rigid tolerances for the positioning systems and material construction.

The TN+PFNS as an objective spectrum was assumed for this work. Nuclear weapons can be categorized into three general classes: fission, boosted, and TN [40, 41]. Currently, the majority of the present capability to produce synthetic debris is focused on fission devices [4]. The TN+PFNS was chosen because it is an area that lacks substantial source development [4], but it is important to note that there is not just one spectrum that can classify the TN+PFNS. The TN portion of the weapon spectrum is assumed to be pure DT fusion [41]. The impact of weapon design, which can vary substantially and play a large role in the resultant neutron energy spectrum, is not evaluated in this work.

Some physical phenomena present in a full-scale nuclear event are not taken into consideration for this analysis. First, the temperatures achieved in nuclear weapons are on the order of 10^7 K, which is not experimentally feasible at NIF [42]. Second, the time dependency of the internal neutron flux distribution is not taken into account. Additionally, there will be large changes to the flux from initiation to burnout; this work only considers a time- and volume-average result. Third, the synthetic weapon debris is created without induced fractionation. In a real nuclear detonation chemical fractionation occurs when the nuclear debris formed solidifies based on the condensation point of the constituent materials [43]. Finally, the neutron spectrum considered is the internal weapon relevant spectrum which would be attenuated in magnitude and energy through material and the atmosphere. For fission product generation, the internal weapon spectrum is the key item of interest; however, nuclear certification testing would require an environment-modified objective spectrum.

1.5 Approach

The broad spectral shaping problem to create a TN+PFNS for surrogate weapon debris and a source for radiation effects on electronics has accompanying objectives and constraints. For this research, the objectives for ETA and ATHENA were a formulation of the TN+PFNS to generate a relevant nuclear weapon radiation environment based on neutron transport through critical assemblies of uranium. The objective neutron spectrum is also appropriate for neutron effects for high altitude burst or space environments. The constraints for the problem were governed by the NIF polar direct drive exploding pusher (PDXP) source, stay-out angle defined by the incident lasers to drive the fusion, and the weight and mounting constraints of the NIF Target and Diagnostic Manipulator (TANDM). The input objectives and constraints were utilized in Coeus to produce a nearly-globally optimum solution for an ETA [4], which lead to the enhanced ATHENA platform.

The work performed previously completed a baseline design for the original ETA [4]. The point design for ETA was modeled with two software packages, MCNP5 and SCALE version 6.2, to perform neutron radiation transport with ENDF-B/VII.0 [44–46]. ATHENA was primarily modeled with MCNP6 and SCALE version 6.3 beta 14 to utilize the most recent nuclear data libraries and group structures made available after the publishing of the ETA work [47]. MCNP was used for the continuous energy solution, while SCALE was used for group-wise nuclear data covariance analysis. Utilizing two different radiation transport models also increased the degree of confidence in the results. The International Reactor Dosimetry and Fusion File (IRDFF) library was used for activation nuclear data and covariance cross section information (Versions 1.05 and II were utilized for code compatibility; however, little change occurred between the two for the work performed in this application) [48]. The radiation transport simulations provided

results for the reaction rates for foil activation, neutron energy spectra, and temporal aspect of the radiation environments.

The General Description of Fission Observables (GEF) code was utilized for developing the expected fission product yields [49]. GEF is a Monte Carlo- and theory-based approach that incorporates experimental data to determine fission observables, such as fission product yields [50]. Empirical methods for determining fission product distributions also exist as alternative approaches to GEF. A formulation of this fit by S. Nagy was also used and is beneficial for comparison to GEF in addition to providing isotope yields [51]. These empirical methods often include simplifications, such as ignoring neutron multiplicity, to create a simpler equation and more direct tie to existing data —both a benefit and limitation of this approach.

The radiation environment was primarily measured with activation foil diagnostics and thermoluminescent dosimeters (TLDs) on ATHENA for a total ionizing dose measurement. Separate foil packs were designed for ETA and ATHENA to leverage new nuclear reactions available in natural abundance form. The foil pack designed was created to successfully unfold the incident neutron spectra from the activation foils, and the foils were selected with many important factors including the confidence in the nuclear data and energy range covered. The modeled foil activities were used with the underlying nuclear data to unfold the neutron spectrum using Pacific Northwest National Laboratory (PNNL) STAYSL code. STAYSL relies on least-squares spectral adjustment based on the chi-squared of the measured activities to determine the incident neutron flux [52].

1.6 Contributions to the Field

This research advanced the field of nuclear science and engineering in a few key areas and applications:

1. **Demonstrated ETA as a novel platform for the production of spectrally and temporally nuclear weapon relevant fission product inventories:** This work improved upon the methodology to predict uranium fission product distributions. The ETA experiment was also the first instantaneous production of a TN+PFNS to generate fission products to current knowledge, paving the way for more robust integral experiments in unique environments.

2. **Formulated capabilities to incorporate nuclear data covariance into radiation transport simulations:** The standard methodology for determining nuclear data uncertainty from stochastic sampling approaches is discussed in Chapters 2 and 4. This work utilized an approach to encompass the full range of available uncertainty data in nuclear reactions when sampling from a multivariate normal distribution thereby generating a more accurate depiction of the resultant uncertainty to benchmark ETA experimental outcomes.

3. **Developed and characterized unique irradiation environments:** The ATHENA and ATHENA-II design development and characterization represents a stepping stone in nuclear certification testing for providing a time- and energy-relevant neutron environment.The increases in the efficiency of the design over ETA enables radiation effects on microelectronic testing where the previous ETA design was below the threshold for observable damage.

4. **Improved neutron spectrum unfolding techniques:** This work provided a heuristic baseline for neutron spectrum unfolding methods where none or limited models are available. Various methods exist to deconvolve a neutron spectrum from activation products; however, the advances here fully capture the statical

and systematic uncertainties and improve upon the methods available through regularization.

5. **Contributed to future improvements of radiation transport validation:** The ETA and ATHENA radiation transport point designs and experimental measurements were conducted in a manner to either limit or quantify relevant uncertainties. The high fidelity measurements offer a unique environment for validation of codes such as MCNP and SCALE. Additionally, feedback was provided to Oak Ridge National Laboratory (ORNL) for future improvements to the SCALE package including inconsistent uncertainties from published data, the need for parallelization in individual Monte Carlo simulations, and the need for a high-energy, fine-group structure with covariance data.

II. Background

This chapter outlines the major nuclear science and engineering theory relevant to spectral shaping and analysis of ETA. First, the basic neutron interaction theory that impacts the ability of a source to be shaped into an objective spectrum is discussed. Next, the nuclear fission process is outlined with a primary focus on fission product generation. After, fundamental aspects of nuclear data and their application in Monte Carlo neutron transport codes and an associated stochastic sampling approach utilizing nuclear data covariance matrices are outlined. Finally, neutron activation foil theory relevant to the unfolding of a neutron spectrum is examined.

2.1 Neutron Interactions with Matter

Neutron interaction mechanisms with matter serve as a physical constraint to spectral shaping of a neutron flux spectrum. Neutron interactions can act to moderate, absorb, or even emit more neutrons. The major reaction mechanisms available in the range of fast to thermal energies that are relevant to nuclear weapon environments are elastic scattering, inelastic scattering, radiative capture, and the release of 'x' neutrons (n,xn) through neutron evaporation. Fission reactions are an extremely important reaction mechanism for the formation of synthetic weapon debris; however, fission does not contribute significantly to the spectral modification problem for this application. A diagram summarizing the important neutron reactions is shown in Figure 2.1.

The neutron interaction probability is described by the neutron microscopic reaction cross section (σ_{rxn}), which is a function of the target isotope and incident neutron energy (E_n). The microscopic cross section multiplied by the atomic

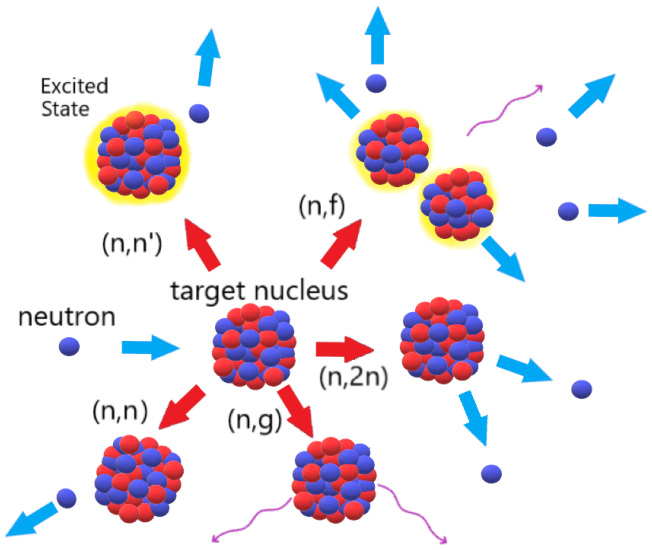

Figure 2.1. Diagram of selected neutron reactions of importance to spectral shaping and fission product generation. The red arrows indicate labeled reaction channels on the target nucleus. The blue arrows indicate the emission and movement of additional particles following the reaction.

number density, N, provides the macroscopic cross section, Σ_{rxn}, a measure of the interaction probability in bulk material per unit path length traveled.

2.1.1 Elastic Scattering (n,n).

Elastic scattering (n,n) is an extremely important reaction for lowering the average energy of the neutron population by downscattering [53]. An elastic collision does not place the target nucleus in an excited state, which allows for the simplified use of conservation of energy and momentum to describe the interaction. A selected group of elastic scattering cross sections relevant to the application in the ETA design are shown in Figure 2.2.

The maximum energy lost in a neutron elastic collision with a nucleus is a function of the target isotope atomic mass (M). Elastic scattering with higher mass isotopes produce a smaller energy loss per collision compared to interactions with lower atomic mass nuclei. Elastic scattering can transfer nearly all of a neutron's kinetic energy

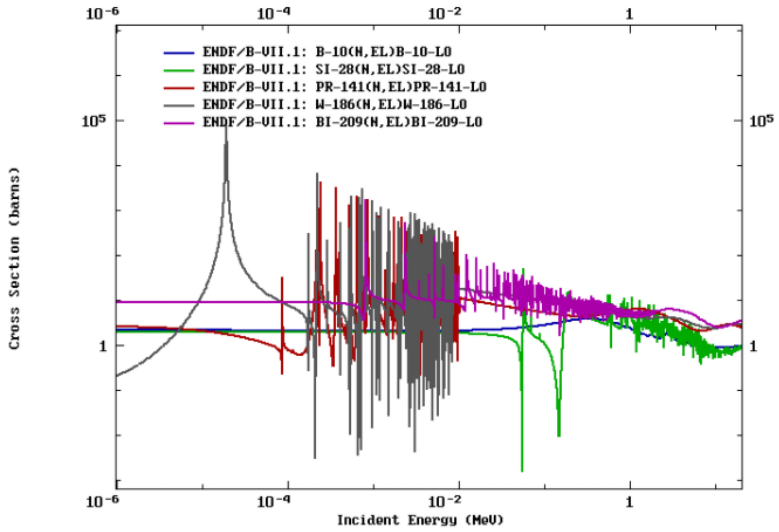

Figure 2.2. Comparison of various elastic scattering cross sections for materials in ETA [46].

with a collision on hydrogen, while scattering off bismuth will produce very little energy loss. The maximum energy transfer, Q, to the target nucleus per collision is given by

$$Q_{max} = \frac{4ME_n}{(M+1)^2}. \tag{2.1}$$

2.1.2 Inelastic Scattering (n,n').

Inelastic scattering is similar to the reaction dynamics of elastic scattering; however, the target nucleus is placed in an energetically excited state after the impact [53]. The energy of the excited states are governed by quantum mechanics and are unique to particular isotopes. An incident neutron, or other particle, can transfer energy to the target nucleus and populate an excited state of the atom. For inelastic scattering, this is typically one of the lower discrete energy levels.

Inelastic scattering is a threshold reaction, meaning an incident neutron must have a minimum amount of energy to enable the reaction channel. Additionally, neutrons generally lose more energy per collision with high Z isotopes if the interaction is

inelastic compared to elastic scattering. The energy that would normally be conserved in an elastic collision is reduced in the conservation equations by the energy of the excited state populated. Examples of inelastic scattering cross sections are shown in Figure 2.3.

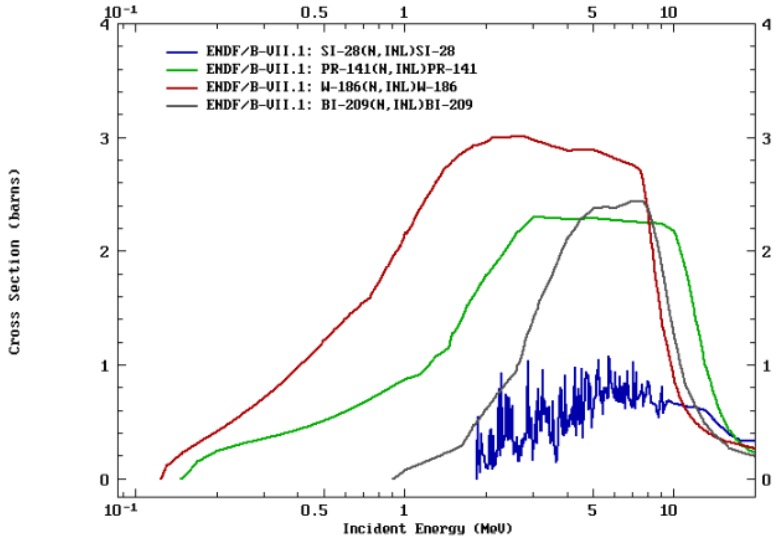

Figure 2.3. Comparison of inelastic scattering cross sections for materials in ETA [46].

Inelastic scattering is one of the lower threshold energy neutron reactions. As shown in Figure 2.3, there is no general functional form of the threshold energy to enable the reaction by atomic mass. For example, the incident neutron threshold energy to cause inelastic scattering with ^{27}Al, a lighter isotope, is between ^{184}W and ^{208}Pb; although the general trend is lower excited state threshold energies for heavier nuclei. These cross sections indicate the energy levels of the nucleus itself, and the threshold and particular states populated, are reflective of the structure of the nucleus.

The excited nucleus can de-excite via γ-ray emission or other channels if above the threshold for particle emission. The excited nucleus usually decays in a short time; however, metastable isomeric states can be populated with inelastic scattering and can have half-lives on the order of hours or much longer [54]. These isomeric states

have applications in foil activation experiments used for neutron spectrum unfolding, where it may take some time to start measuring the foil activity. An energy level and decay mode diagram of ^{115}In is shown in Figure 2.4. This isotope is chosen as a representative example because it was used as an activation foil reaction in the modeled ETA results. The metastable state at 336 keV with spin parity $J^{\pi} = 1/2^{-}$ is important for foil activation experiments for the higher epithermal region.

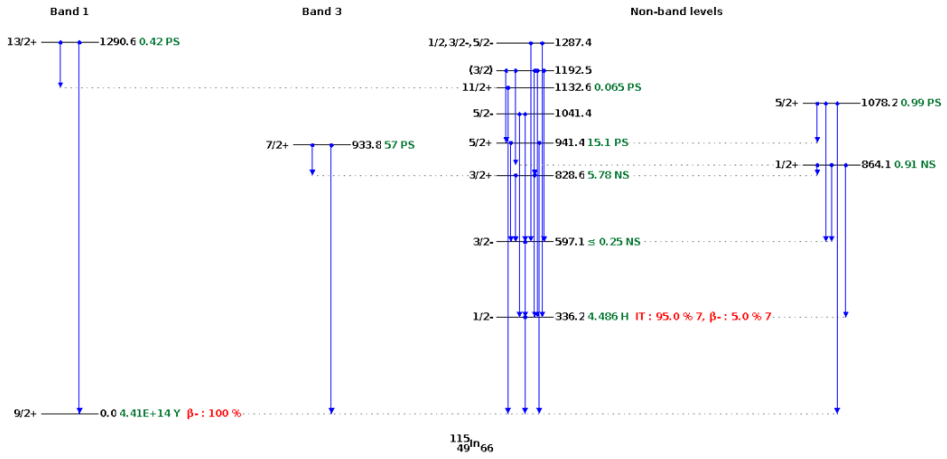

Figure 2.4. ^{115}In energy level and decay mode diagram truncated at 1.3 MeV. Plots produced using the Online Service retrieval code package written by C. L. Dunford, National Nuclear Data Center, Brookhaven National Laboratory.

2.1.3 Neutron Evaporation (n,xn).

A neutron can interact with a nucleus and eject additional neutrons. The (n,xn) reactions such as (n,2n) and (n,3n) require a threshold energy to separate the neutron from the original nucleus, appropriately called the neutron separation energy. Neutron separation energies are on the order of a few MeV to tens of MeV [54, 55]. Increasing the incident neutron energy allows for the evaporation of more neutrons from the nucleus.

The (n,xn) mechanism can occur as a direct reaction, where the incident neutron interacts with only a few particles in the nucleus, or as a compound reaction, where

the incident neutron interacts with the entire nucleus and is absorbed [53]. Example (n,2n) reactions are shown in Figure 2.5. The cross section threshold is generally lower for higher atomic mass isotopes, which have neutrons that are not as tightly bound to the nucleus.

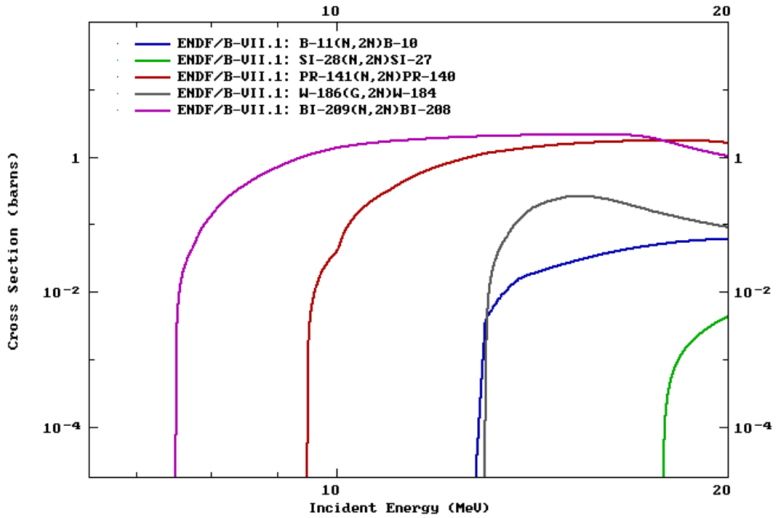

Figure 2.5. Comparison of (n,2n) cross sections for materials in ETA [46].

In the context of spectral shaping, (n,xn) reactions are significant for two reasons. First, the interaction increases the total neutron population by sacrificing a high-energy neutron. Second, the neutron energies are lower post-reaction because the reaction is required to overcome the potential barrier and losses through γ-ray emission. The lowered neutron energy is beneficial for building up lower energy neutron populations. Additionally, this reaction mechanism has applications in foil activation experiments for determining the high-energy neutron population.

2.1.4 Radiative Capture (n,γ).

Radiative capture, labeled (n,g) and (n,γ) in literature, is a reaction mechanism most prominent at low energies where an incident neutron is absorbed into the nucleus and a γ-ray is emitted [54]. At low energies (below approximately 1 keV, isotope dependent) the absorption cross section follows the "1/v" law, so the probability

increases with the inverse of the square of E_n [53]. Figure 2.6 provides examples of selected (n,γ) cross sections.

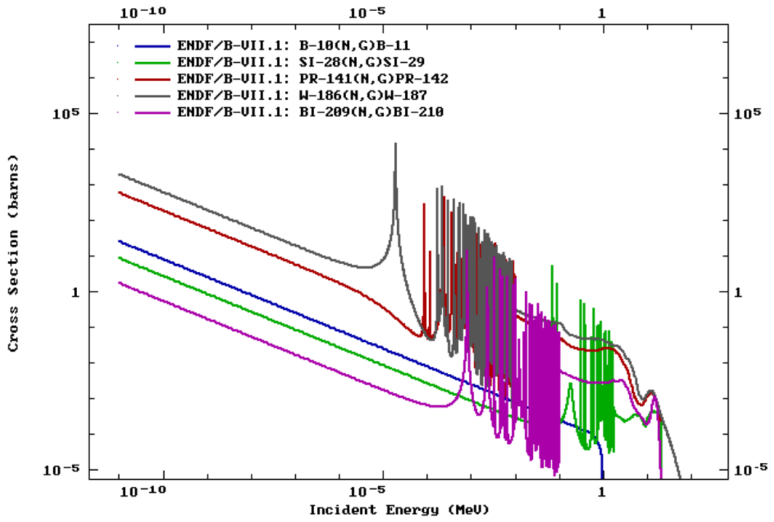

Figure 2.6. Comparison of various (n,γ) cross sections for materials in ETA [46].

Radiative capture is an important absorption reaction mechanism in a few ways. The (n,γ) reactions are of interest to foil activation experiments, specifically for determining the thermal spectrum. The resonance structure of the cross section in the epithermal region can also be used to generate a unique response. Radiative capture is generally undesirable for spectral shaping, acting as a poison to the neutron economy. Fortunately, the 14 MeV NIF source is not largely impacted by radiative capture until the neutrons have been moderated, but the (n, γ) reaction can be used to absorb excess thermal neutrons [4, 54].

2.2 Nuclear Fission

2.2.1 Fission Theory.

In nuclear fission an excited nucleus breaks up into two or more fission fragments. Fission releases a large amount of energy, which is distributed as kinetic energy in the fission fragments, neutrons, γ-ray, and delayed decay energy. The amount of energy

liberated is dependent on the specific reaction products and incident neutron energy, an average of approximately 200 MeV. The delayed decay energy is associated with the decay of the unstable fission products, which includes energy in the form of β particles, additional γ-rays, anti-neutrinos, and neutrons. A schematic of the fission process is shown in Figure 2.7.

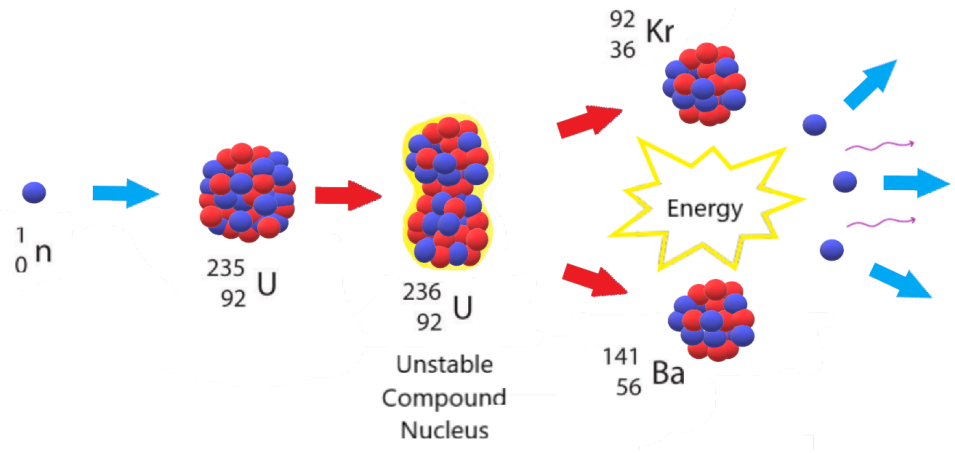

Figure 2.7. Schematic overview of ^{235}U neutron induced fission.

Fission occurs most often in high atomic mass nuclei, such as ^{235}U, ^{238}U, or ^{239}Pu; however, most isotopes can be fissioned at large enough incident energies. The fissioned isotope separates into two, or occasionally three, nuclei [40]. Fissionable isotopes like ^{238}U, ^{240}Pu, and ^{242}Pu have a significant fission barrier and are incapable of sustaining a nuclear chain reaction. Fissile isotopes like ^{235}U and ^{239}Pu are capable of sustaining a nuclear chain reaction and have cross sections with similar characteristics to the radiative capture cross section shown in Figure 2.6.

The unstable compound nucleus can be modeled at high excitation energies, well above the fission barrier, as an incompressible liquid drop [54, 56, 57]. The deformation of the nucleus causes increased surface energies, which are balanced with the Coulomb force charge repulsion, the strong nuclear force, and shell pairing effects. The perturbation creates an increase in the surface energy and decrease in

the Coulomb repulsion because the charge is spread out [58]. During the fission process, the evolving compound nucleus can emit pre-fission neutrons, known as multi-chance fission [58]. First-chance fission is the emission of no neutrons, second-chance fission is the emission of one neutron, and so on. Multi-chance fission is of particular importance to the mass chains observed in the fission product distribution.

Immediately following the fission event, the fission fragments are in a highly excited state. Fission fragments are generally very neutron rich compared to the valley of stability. The excited fragments emit photons to de-excite and may have enough energy to evaporate more neutrons [58]. The prompt fission product yield is the distribution of products post-neutron evaporation from the fission fragments. The fission process releases 2-3 neutrons on average, and this average increases with incident neutron energy due to multi-chance fission and an increase in fission fragment excitation energy, allowing de-excitation through neutron emission.

2.2.2 Fission Products.

The fission product distribution of thermally-induced fission tends to be centered around isotopes with closed nuclear shells. These isotopes have a "magic number" of protons and neutrons, similar to the filled electron structure of the noble gases. The fission fragment distribution from thermal neutrons incident on ^{235}U is shown in Figure 2.8.

Low-Z stable nuclei have approximately equal numbers of protons and neutrons, but larger nuclei require more neutrons to mitigate the Coulomb repulsion of protons [54]. Most of the decay products following fission are beta emitters, which occurs because the products are neutron-rich and become more stable upon the conversion of a neutron to a proton. Figure 2.9 shows the primary decay modes of

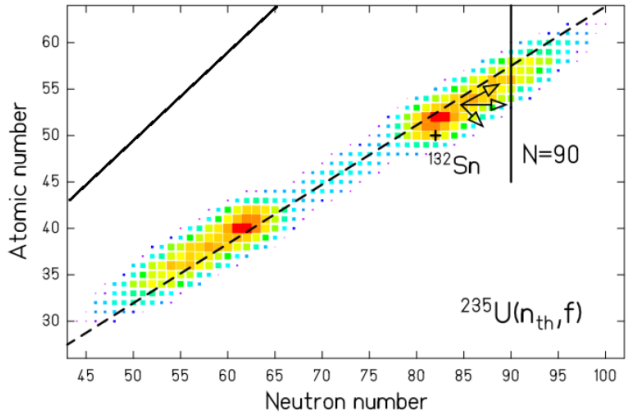

Figure 2.8. GEF calculated ^{235}U thermal fission product distribution prior to prompt neutron emission. The dashed line is the neutron to proton ratio of ^{235}U prompt fission products, and the solid line in the upper left is a ratio of 1 [59].

radionuclides as they decay to the valley of stability. In the region of fission products, the primary competing decay mode to $\beta-$ is neutron emission, resulting in cross-mass chain transfers after the initial fission process.

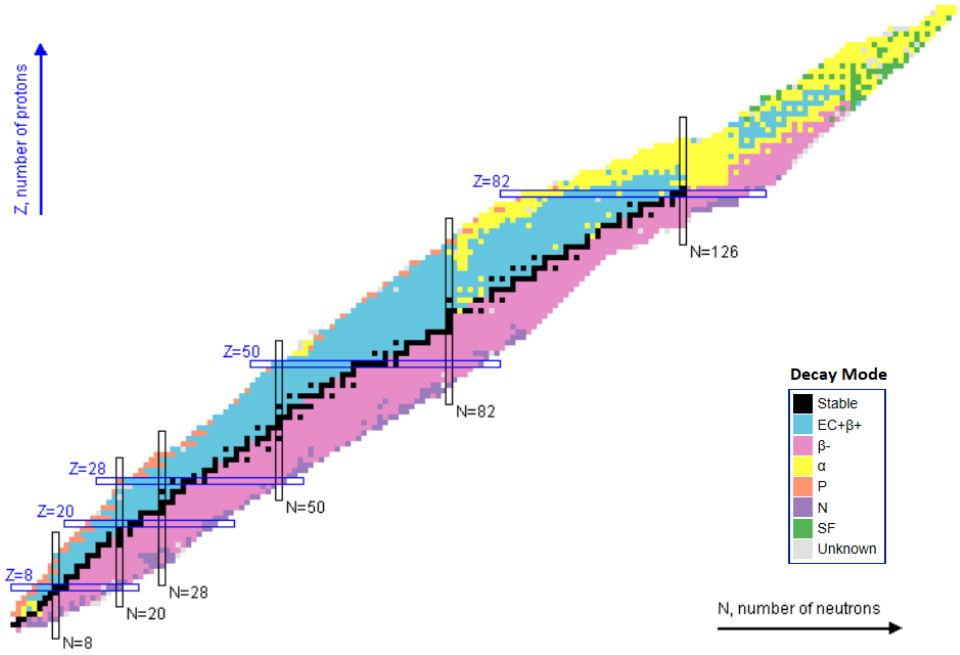

Figure 2.9. Primary decay modes of isotopes. Plots produced using the Online Service retrieval code package written by C. L. Dunford, National Nuclear Data Center, Brookhaven National Laboratory.

Fission yields can be described by the independent, cumulative, and chain yields.

The independent yield, Y_{ind}, is the prompt fission product distribution directly after the fission event before successive decay [60]. Y_{ind} for ^{235}U thermal fission is shown in Figure 2.10. The independent isomeric yield is defined as [61]

$$Y_{ind}(A, Z, I) = Y(A) \quad f(A, Z) \quad R(A, Z, I), \tag{2.2}$$

where the sum yield, $(Y(A))$, is the sum of all independent fission products for a given mass, A, the isomeric yield ratio, $R(A, Z, I)$, is the production of each isomer, I, for a given independent yield, and the fractional independent yield, $f(A, Z)$, defines the yield of a particular isotope.

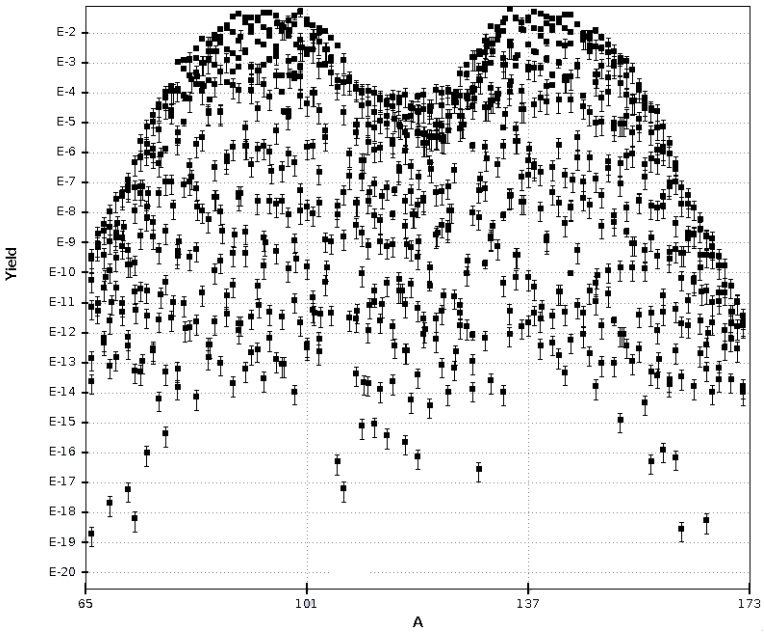

Figure 2.10. Independent fission product yield of thermal fission of ^{235}U. Plots produced using the Online Service retrieval code package written by C. L. Dunford, National Nuclear Data Center, Brookhaven National Laboratory.

The independent yield produces a cascade of decay chains leading to the cumulative yield, $Y_c(A, Z, I)$. Y_c represents the production of an isotope over time after all prompt and delayed emissions and decays. Y_c is normally the quantity that is measured in experiments. The cumulative yield is given as [62]

$$Y_c(A, Z, I) = Y_{ind}(A, Z, I) + \sum_{j=0}^{N} Y_c(A_j, Z_j, I_j)\, b_j, \tag{2.3}$$

where b_j represents the branching ratio from isotope j into the cumulative yield and N defines the total number of decay channels into the cumulative yield isotope. The cumulative yields for thermal, fast, and high-energy fission of ^{235}U are shown in Figure 2.11.

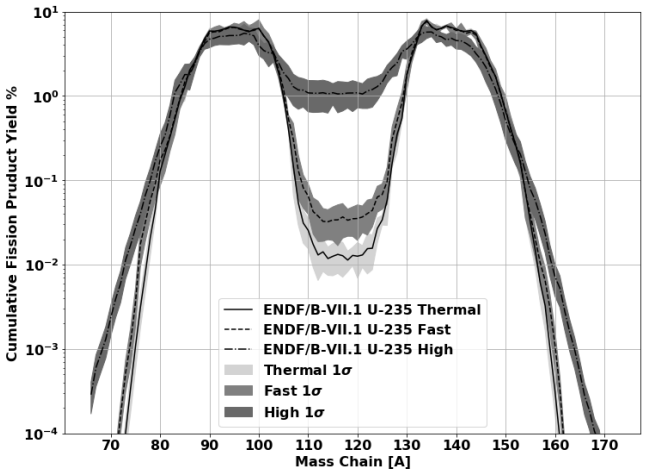

Figure 2.11. Comparison of energy dependent ^{235}U cumulative fission product distributions from ENDF/B-VII.1 [46].

As shown in Figure 2.11, fission product yields are dependent on the energy of the incident neutron. The ^{235}U fission products populate one heavy and one light peak, the region between the peaks is referred to as the valley, and the low population tails falling off either peak are the wings. As the energy of the incident neutron is increased for a given fissioning system, the valley and wings of the fission product distribution are raised because the fission process becomes more symmetric [56]. The uncertainty in the evaluated fission product yields varies significantly; the fission spectrum or fast fission relative uncertainty ranges from 1.6% for mass chain 137 to 64% for mass chain 109 [46]. The uncertainty for each fission product is represented at the 1σ level as bands in Figure 2.11.

Finally, the chain yield for a particular mass chain is defined as the sum of the independent yields to the final decay in that mass chain [60]. The chain yield leads to the cumulative distribution accounting for branching in and out of a mass chain through neutron emission. In particular, the chain yield equals the cumulative yield for the last stable member of a decay chain. An example is shown in Figure 2.12 for the A = 89 mass chain, where the stable isotope is ^{89}Y [63].

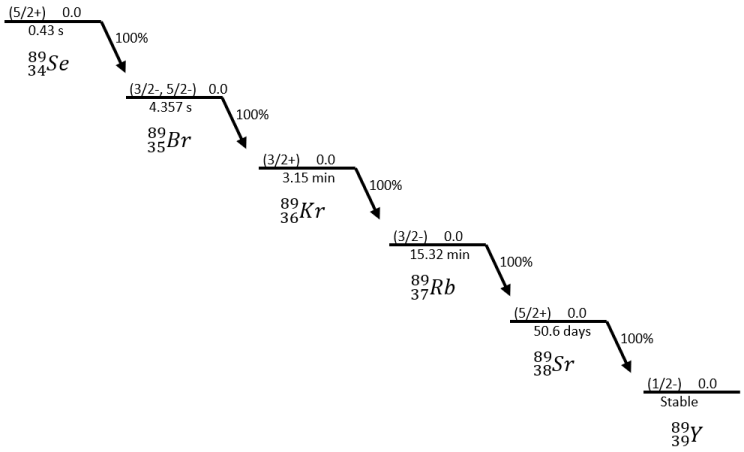

Figure 2.12. Simplified neutron rich decay scheme for mass chain A=89. The ^{89}Sr decay to ^{89}Y represents the final decay to the stable isotope [63].

2.2.3 Nagy Fits for Fission Product Isotopes.

The three fissioning energies provided in ENDF describe part of the behavior of the fissioning system as a function of neutron energy. However, including fits to experimental data enables better energy resolution and predictions that are consistent with observed experiments. Empirical relations developed by Nagy *et al.* provide an approach to predict the fission product yield as a function of energy given sufficient yield measurement data [51]. Nagy fits the fission product experimental data to an exponential equation

$$Y(E_n) = Y_0 e^{bE_n}, \tag{2.4}$$

where the fitting parameters b and Y_0 represent the slope of the function in logarithmic form and thermal fission yield, respectively [51]. The slope is the primary measure of the energy dependency of the fission-product yield, which requires modifications for multi-chance fission. First chance fission is dominant up to 5.5 MeV, and second-chance fission up to 14.1 MeV [51]. Multi-chance fission effects on the fission product yield are less pronounced in asymmetric regions but can have a large impact in symmetric fission, where $109 \leq A \leq 129$ [4, 51].

It is important to note that data-based phenomenological models are not perfect predictors of determining fission products *a priori*. In particular, recent publications have findings that cannot be accurately modeled with current theoretical approaches [56]. In general, there are large uncertainties in the predictive power of calculating energy-dependent fission-product yields. Still, this type of empirical fit has lower predicted error than GEF for individual isotopes where sufficient energy-dependent measurements exist.

2.3 Nuclear Data

2.3.1 Nuclear Data Libraries.

Nuclear data relevant to neutrons have been collected for the better part of the last century. Nuclear data available for modeling and simulations are collected and published in evaluated data files. There are many versions of evaluated nuclear data, which all aim to characterize the relevant physics backed by experimental results. For example, the primary U.S.-based nuclear data file is the Evaluated Nuclear Data File (ENDF). Other nations or organizations also have independent evaluations of the available nuclear data. Examples of other nuclear data libraries are the Russian National Library of Nuclear Data (ROSFOND), the European Joint Evaluated Fission and Fusion (JEFF) Nuclear Data Library, Japanese Evaluated Nuclear Data Library

(JENDL), Chinese Evaluated Nuclear Data Library (CENDL), and the International Reactor Dosimetry and Fusion File (IRDFF).

Figure 2.13 shows the evaluation of ^{197}Au(n,2n) reaction for various libraries. In some cases, the evaluation can be drastically different. Other times, the libraries are using the same evaluation from another library, which can be noted by the overlapping evaluations.

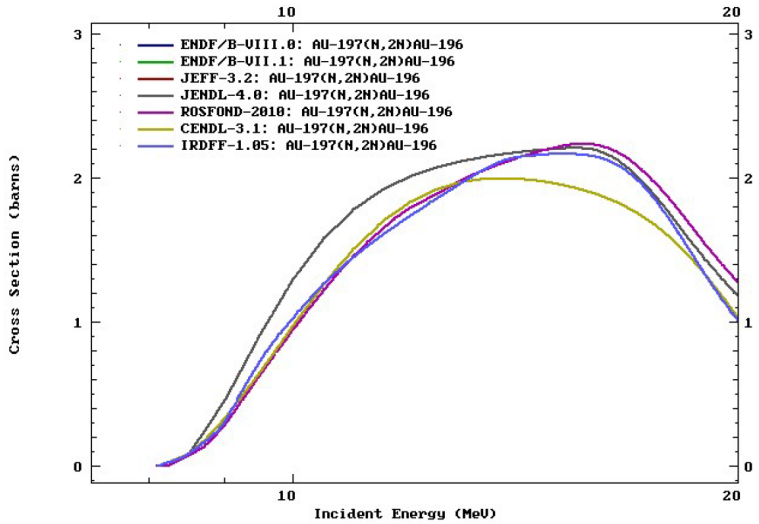

Figure 2.13. Comparison of various library evaluations of the ^{197}Au (n,2n) cross section [46].

The experimental data that feeds into ENDF is contained in EXchange FORmat (EXFOR), where the experiment uncertainty, if available, is tracked. Nuclear data evaluators need reaction models to fill in the gaps where experimental data does not exist. For example, experiments with sub-electron-volt neutron energy resolution are not feasible at the present time. ENDF relies on evaluations of EXFOR data based on experimental quality, statistics, and theoretical basis to fill in areas lacking experimental data [64]. ENDF then stores the underlying nuclear data (cross sections, angular distributions, half-lives) that can be used in simulations.

Benchmarking the evaluated nuclear data is done primarily through testing integral results, such as the effective neutron gain-to-loss ratio, k_{eff}, of a critical

assembly [64]. These integral measurements provide a more accessible measurement that can be done with high precision and accuracy, as precise as a relative error of 0.01%, to validate microscopic cross sections. The use of integral benchmark experiments is important for comparing the net result of the nuclear data; however, there are uncertainties and correlations in the independent reactions that combine to create the integral results.

Validation experiments, applications, studies, and integral benchmarks performed increase the base and accuracy of the nuclear data [64]. However, it is important to note that the experiments used to measure nuclear data may have uncertainties that vary by orders of magnitude. An interesting feature of this fact is that the relative nuclear data uncertainty does not always decrease between successive library versions. One example is the increase in uncertainty in the neutrons released per thermal fission of ^{235}U, which increased from 0.311% to 0.385% between ENDF/B-VII.0 to VII.1 [65]. Another example demonstrating the change in nuclear data uncertainty over time is that evaluated ^{6}He half-life has changed by approximately 5% with large increases in the relative error over the last 50 years [66].

Another prevalent issue is that the majority of accurate measurements were performed for nuclear reactor studies, which limits accessibility to reliable data in different energy domains. As a consequence of this, ENDF only contains fission production data at thermal, fast fission spectrum (average 0.5 MeV), and high-energy (14 MeV). To combat this challenge, smaller, more application-specific libraries have been developed.

The International Atomic Energy Agency (IAEA) provides data to the benchmarked neutron dosimetry reaction IRDFF library [48]. This library is noted because it is used in the PNNL STAYSL code system, discussed in Section 2.6. The IRDFF v.1.05 and IRDFF-II libraries contains "state-of-the-art" covariance

information and have improvement through testing and integral experiments [67, 68].

The IRDFF library also includes feed through from fast decaying excited states to metastable states for important dosimetry reactions. An example is the ^{115}In(n,n')^{115m1}In reaction; the ^{115m1}In decay scheme is depicted in Figure 2.4. The first metastable state at 336 keV (spin parity $J^{\pi} = 1/2^{-}$) has a half-life of 4.5 hours, which makes it a good candidate reaction for foil activation experiments [69]. The IRDFF v.1.05 library contains reaction data that includes the decay of additional metastable states and higher excited states into ^{115m1}In. Under standard measurement timing conditions, all of the higher energy ^{115}In states will have decayed, thus contributing to the activity measured for the first metastable state.

2.3.2 Nuclear Data Covariance.

Covariance arises in nuclear-related experiments when one process affects another or the nuclear data measurement energy ranges are correlated. Unfortunately, nuclear data covariance analysis is not standard to historical experimental analysis. Often errors are attributed to model fidelity, measurement, or setup problems when nuclear data covariance may have been the root cause [70]. In many nuclear decay processes, the correlation between decays is unity because the decays happen in a series. Correlation can also occur if there is branching from a radioactive state. Covariance is defined with the expectation values, $\langle X \rangle$, and mean value, μ, providing for the covariance between variables X and Y as

$$cov(X, Y) = \langle XY \rangle - \mu_X \mu_Y. \tag{2.5}$$

A correlation matrix combined with the uncertainty in the nuclear data can be used to form the covariance matrix. The diagonal of the correlation matrix is 1, so the diagonal of the covariance matrix is the variance for the group. As such, the

covariance of an observable compared to itself reduces to the variance

$$cov(X,X) = \langle X^2 \rangle - \langle X \rangle^2 = \sigma_X^2, \tag{2.6}$$

and the conversion from a correlation matrix to a covariance matrix is given by

$$cov(X,Y) = corr(X,Y)\sigma_X\sigma_Y. \tag{2.7}$$

Instead of the covariance matrix, nuclear data often stores the correlation matrix in a group structure format, as shown in Figure 2.14. In general the largest correlations occur in nearby energy groups, where the experimental uncertainty in the incident E_n is largest. Correlations also exist between reactions, in addition to correlations in a single energy-dependent reaction channel, but these data are rarely quantified.

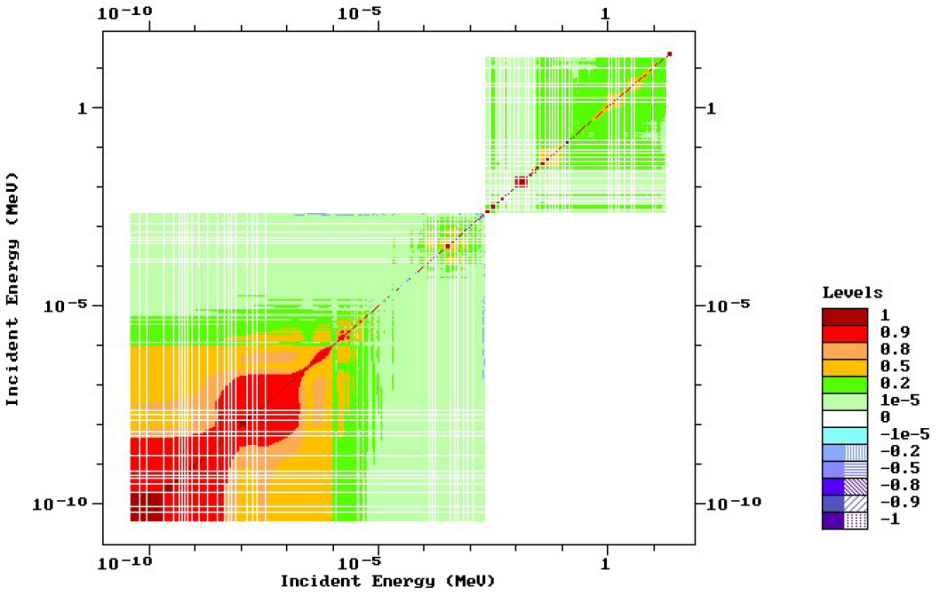

Figure 2.14. ^{235}U(n,f) correlation matrix [46].

Integral experiments are extremely dependent on the underlying reactions that make up the net result. Therefore, there are generally larger variances in the reactions that are part of the total cross section. Figure 2.15 displays the relative uncertainty of

the ^{235}U(n,f) cross section compared to the total cross section. Figure 2.16 displays the relative uncertainty of the total cross section of ^{209}Bi compared to the (n,2n) reaction cross section.

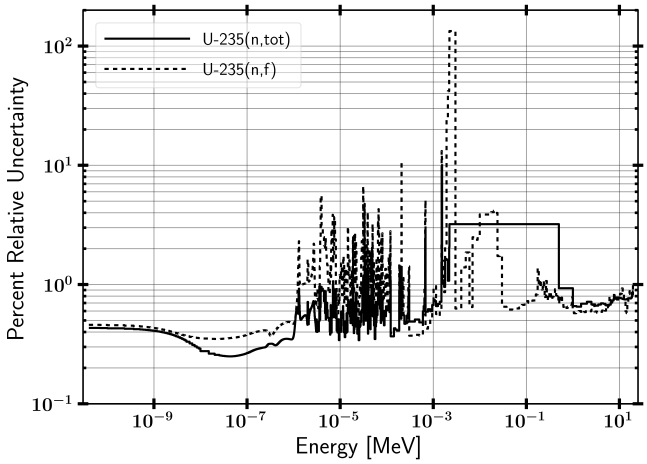

Figure 2.15. Percent relative uncertainty in ^{235}U(n,f) cross section compared to ^{235}U(n,tot) cross sections [46].

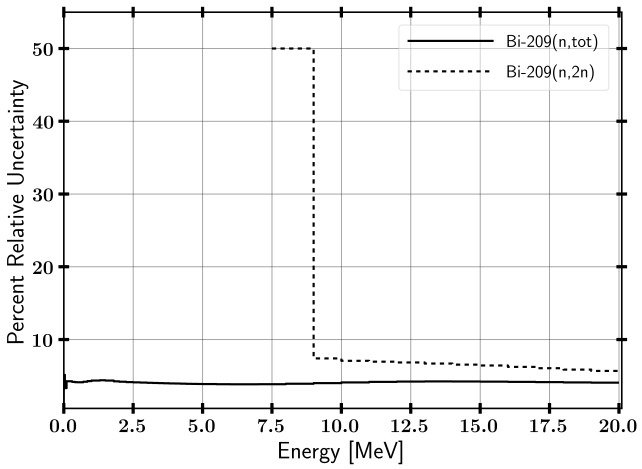

Figure 2.16. Percent relative uncertainty in ^{209}Bi(n,2n) cross section compared to ^{209}Bi(n,tot) cross sections [46].

The uncertainty in ^{235}U(n,f) and ^{209}Bi highlight a couple key attributes relevant to nuclear data. First, the component reactions that make up the total cross section almost always have a higher relative uncertainty because integral cross section experiments can more accurately be measured through attenuation of a "beam" of

neutrons. The underlying reactions cross sections are generally more difficult to characterize. Second, the ^{235}U(n,f) cross section relative uncertainty near 2.2 keV is 133.6%. This large uncertainty implies that the cross section must go negative to capture the full distribution of possible total cross sections within a given confidence interval when utilizing a Gaussian distribution. This suggests that the confidence intervals are not symmetric and points to utilizing alternative functional forms for the cross section probability distribution functions. Negative cross sections are obviously non-physical; however, it gives scope to the magnitude of the uncertainty in the underlying cross sections over difficult experimental energy ranges. Next, the ^{235}U reactions are more thoroughly studied as compared to ^{209}Bi. Over the majority of the energy range, the uncertainty in the ^{235}U cross section is below one percent relative error, largely driven down by thermal nuclear reactor experiments, while ^{209}Bi cross section has a larger error around 5%. Finally, areas where the cross sections are low have representative larger relative errors; this is the case near the threshold of the ^{209}Bi (n,2n) reaction as shown in Figure 2.16.

2.3.3 Nuclear Data Stochastic Sampling.

The two primary methods that exist for uncertainty quantification of radiation transport simulations are linear perturbation and stochastic sampling Monte Carlo [71]. First order linear perturbation theory is not always adequate for large uncertainties or incorporating second-order effects from the uncertainty in the neutron transport; however, it does have broad uses in the reactor community. Stochastic sampling has grown in popularity as computational resources have improved. Stochastic methods rely on performing independent neutron transport calculations with perturbed nuclear data libraries sampled based on the covariance of the cross sections using the multivariate normal distribution to build a

distribution of responses [72]. The generalized multivariate normal distribution is a function of the nuclear cross section mean values, $\boldsymbol{\mu}$, length k, random solution vector, $\boldsymbol{X}$, covariance matrix, $\boldsymbol{\Lambda}$, and is given by

$$f(\boldsymbol{X}) = \frac{exp(-0.5(\mathbf{X}-\boldsymbol{\mu})^T\boldsymbol{\Lambda}^{-1}(\mathbf{X}-\boldsymbol{\mu}))}{\sqrt{(2\pi)^k \mid \boldsymbol{\Lambda} \mid}}. \tag{2.8}$$

Several Monte Carlo sampling methods have been created to capture the effect of nuclear data covariance on nuclear engineering problems, including SCALE Sampler, NUSS, and SHARK-X [45, 72–74].

Deficiencies with the stochastic sampling approach are generally associated with the nuclear data libraries and the sampling method. First, nuclear data uncertainty is often above 100% in energy regions where measurements do not exist, so the value of the cross section is not well characterized. Second, the nuclear data uncertainty is assumed to be normally distributed; however, alternative forms may be more appropriate. In stochastic sampling approaches, these two factors lead to truncation of large uncertainties to prevent performing neutron transport calculations with negative cross sections. Although negative cross sections are non-physical, the truncation may underestimate the calculated uncertainty, which can have an effect if the experiment is performed in these energy domains when using the Gaussian distribution. Finally, component cross sections that make up the total cross section are constrained to sum to the total cross section. This is generally a reasonable assumption as the total cross section is well-known, but it ignores the correlations between the individual component reactions in making the adjustments.

2.4 Monte Carlo Neutron Transport

2.4.1 Monte Carlo Neutron Transport Theory.

Monte Carlo methods for neutron transport leverage pseudo-random sampling, nuclear data, and material specifications to build a simulation of the particle transport in space, direction, energy, and time [75]. Neutron interactions are sampled with probability distribution functions (PDFs) for aspects such as path length traveled and interaction type [76]. An objective of a neutron transport calculation is to determine the average behavior of particles within the system. This can be captured with the volume averaged scalar flux, $\bar{\phi_V}$, defined as

$$\bar{\phi_V} = \frac{1}{V}\int_V dV \int_t dt \int_E dE\, \phi(\vec{r}, E, t), \tag{2.9}$$

where $\bar{\phi_V}$ is given as a function of energy, E, position, $\vec{r}$, and time, t. Monte Carlo methods approximate the scalar flux with either track length or collision estimates [76]. The track length estimator is

$$\bar{\phi_V} = \frac{W\, T_l}{V\, N}, \tag{2.10}$$

where the path length score for the flux is based on the distance traveled, T_l, and is normalized by the particle weight, W, cell volume, V, and number of histories sampled (N).

Statistics often drive the uncertainty in a Monte Carlo simulation as systematic uncertainties are *generally* not considered due to computational costs. The "true" mean value, μ, of a response PDF is the expectation value, $E(x)$, which is estimated with a sample mean, $\bar{x}$. According to the Central Limit Theorem, the sample mean approaches the real mean as the number of samples, N, goes to infinity, and the distribution of the means of sampled x_i follows a Normal distribution. The sample

mean can be calculated as

$$\bar{x} = \frac{1}{N} \sum_{i=1}^{N} x_i. \tag{2.11}$$

Therefore, sample variance, S_x^2, can be computed as

$$S_x^2 = \frac{1}{N-1} \sum_{i=1}^{N} (x_i - \bar{x})^2, \tag{2.12}$$

and the variance of the mean, $S_{\bar{x}}^2$, is simply

$$S_{\bar{x}}^2 = \frac{S_x^2}{N}, \tag{2.13}$$

where S_x^2 is defined as the sample variance. Therefore, the statistical uncertainty in the results decreases with $\sqrt{N}$. The precision of the result can be improved with more histories, shrinking the spread in x_i. However, the accuracy cannot be improved. Accuracy is impacted by systematic errors, such as uncertainty in the nuclear data.

2.4.2 Comparison of Monte Carlo Neutron Transport Results.

The results from different Monte Carlo simulation codes often produce slightly different results. The outputs are generally in better agreement for criticality calculations of critical assemblies and nuclear reactor analysis. It is important to gauge the effect of utilizing different transport codes to see how much variance is expected. Some of the differences that effect Monte Carlo simulations are within the structure of the code itself, statistical error, or different starting seeds, while others are based on the nuclear data that may be altered, geometry or source implementation, and/or user error.

Criticality is a well-understood nuclear engineering problem that the nuclear data libraries are commonly validated against. Wang *et al.* conducted a study on a high

temperature pebble-bed reactor and compared SCALE's CSAS6 module for criticality calculations to MCNP5's kcode [77]. The results there, in addition to a similar study conducted by Johnson *et al.* of a pebble-bed reactor, determined that the difference in k_{eff} in MCNP to SCALE was near half a percent [78]. This variance can easily be handled for reactor operations; however, this highlights that even well-understood problems do have differences based on the simulation code itself.

In another study, Chen *et al.* compared the average γ-ray dose outside of a spent nuclear fuel cask [79]. The dose rates predicted by SCALE and MCNP simulations varied as much as 27%. Again, this shows that the less well-benchmarked studies can have large code-to-code disagreements.

2.5 Foil Activation

2.5.1 Foil Activation Theory.

Foil activation is a method of characterizing an incident neutron flux through unfolding the response of the foils using the energy-dependent nuclear reaction channels in the foil. Activation experiments are essential for testing that requires small geometries or where electronic equipment used in measuring techniques will be damaged.

Activation foils produce measurable radioactive isotopes during the course of an irradiation. The production rate of radioactive isotopes is negated by radioactive decay processes, which place an upper limit, the saturation activity, on the radioactivity of a foil [80]. The saturation activity

$$A_\infty = R = \int_{E1}^{E2} \phi(E)\Sigma(E)_{act}V \tag{2.14}$$

is equivalent to the reaction rate, R, which is a function of the energy dependent flux,

ϕ, the macroscopic reaction activation cross section, $\Sigma(E)_{rxn}$, and the volume of the foil, V. The energy term, $E1$, is zero in many cases; however, threshold reactions require the incident neutron to be of higher energy to enable the reaction channel.

When six half-lives have elapsed, a foil will have reached approximately 98% of its saturation activity, neglecting spatial and energy self-shielding effects [80]. When the activation is not sufficient to fully saturate the foil, a correction needs to be made. The activation of the foil for a given irradiation time, t_i is given as

$$A_0 = A_\infty(1 - e^{-\lambda t_i}), \tag{2.15}$$

where λ is of the decay constant of the radioactive product.

The formula can be simplified in the limit of irradiation times much less than the half-life of the activation products. In this case, the production rate is much larger than the decay from radiation, so the rate of production of the radioisotope is driven only by the reaction rate. The neutron pulse length at the NIF is on the order of shakes (1 shake = 10 nanoseconds), while the reaction channels of interest have half-lives on the order of an hour or longer. Therefore this approximation can be made for the foil activation. The time integrated flux, or neutron fluence, Φ, can be used to determine the total reactions, R_{total}, over an irradiation period, given by

$$R_{total} = \int_{E1}^{E2} \Phi(E)\Sigma(E)_{act} V \, dE. \tag{2.16}$$

Experimental measurements of the activity must be corrected to deduce the original activity of the foil, A_0, immediately after irradiation as shown in Equation 2.17. The activity is corrected for the radioactive decay occurring between the end of irradiation and the start of counting, t_d. A similar correction factor based on the count time, t_c, provides a correction for radioactive decay during counting

that can result in a reduction of counting rates by the end of the counting period. Additionally, the detector efficiency for the given γ-ray energy, ϵ, and relative γ-ray intensity, I_γ, must be taken into account. The γ-ray intensity may also include a branching ratio if applicable to the decay mechanism. Finally, the measured counts, C, is reduced by the background counts, B. All corrections included, less self-shielding effects, provide a formulation for converting counts to post-irradiation activity as

$$A_0 = \frac{\lambda(C - B)e^{\lambda t_d}}{\epsilon(1 - e^{-\lambda t_c})I_\gamma}. \tag{2.17}$$

2.5.2 Selection of Experimental Foils.

The method of foil activation has been studied in-depth in the nuclear sciences and engineering community. A list of the various requirements that are of importance for a neutron activation foil experiment with neutron energies in the range of thermal to approximately 20 MeV are summarized below [75, 80, 81].

- The reaction neutron cross section is extremely important for foil activation, and there are a few key parameters that should be considered. First, the magnitude of the cross section determines the reaction rate of the product nuclides. A large cross section allows for more activation, and therefore, better results when analyzing the activation foils. Second, the uniqueness of the cross section shape is used to unfold the incident neutron energy spectrum. An (n,γ) cross section may peak in a particular region, which is essential to providing information of the neutron flux in that energy region. Alternatively, a threshold reaction, such as an (n,2n), is important for providing information about the flux at higher energies. Third, activation of the selected foils for an experiment should cover the entire energy range of the incident neutrons. Finally, the cross section must

be well characterized with low uncertainty over the neutron energy range of interest.

- The range of activation product half-lives applicable for a particular experiment depends on availability of detectors and the time before counting the foils post-irradiation. A long-lived radioisotope will be available for counting for longer times at the expense of the total activity. The opposite is true for short half-lives. Half-lives on the order of an hour to a few years are generally used; however, the half-life must also be balanced with the production of the radioisotope to understand the entire picture.

- The elemental, isotopic, and chemical purity of the activation foil should be well known. An unknown composition foil can produce erroneous results.

- Interfering reaction channels and decay emissions should be avoided. An example of this is natural copper, which has multiple 511 keV emissions from different reaction channels. It is difficult to distinguish these γ-rays to determine activation in counting. Similar problems arise in multi-isotope materials that have multiple reactions producing the same nuclide. For example, the ^{106}Cd(n,γ) reaction produces the same isotope as a ^{108}Cd(n,2n) reaction, which complicates spectral unfolding.

- The activation foil should be optically thin to not cause perturbations of the neutron flux. An additional benefit of relatively thin foils is that the γ-ray emissions for detection are not significantly attenuated through self-shielding. In general, adding additional foils helps to improve the unfolding results, as long as the entire foil set remains generally optically thin [82].

- The decay nature of the product nuclide should preferably be a γ-ray emitter, as its detection can provide fine energy resolution to determine activation.

The discrete γ-ray emissions provide a means of determining the source and magnitude of the foil activation. The energy of the γ-ray is also of importance. Semiconductor detection methods have a peak intrinsic efficiency near 100 keV with some variance depending on whether the semiconductor is p-type or n-type. Beta spectrometry is also a potential option that may be considered; however, the resolution is not as good as γ-ray spectroscopy.

2.6 Neutron Energy Spectrum Unfolding

Foil activation experiments are a well-documented method for determining an incident neutron energy spectrum [80]. The foils are irradiated under a nearly equivalent neutron flux, which serves to activate the foil samples through nuclear reaction channels, each of which has a unique response function with respect to the neutron flux. The nuclear data and activities of the foils can be used to unfold the incident neutron energy spectrum.

In an ideal situation, the number of foil reactions, i, would be selected based on the number of energy groups, j, required, and the problem would be formulated as [75, 82],

$$A_i = \sum_{j=1}^{N} \Sigma_i(E_j)\ \Phi(E_j)\ V, \quad i = 1..m. \tag{2.18}$$

In practice, this formulation of the unfolding problem is not used as it often provides non-physical results. The issue is caused by the similar shapes of reaction cross sections, which create a poorly constructed matrix and a limit on the number of foils that can be used at a time to prevent changing the neutron flux. There are many methods that aim to provide solutions to the generally degenerate neutron spectrum.

A few examples of unfolding methods include matrix inversion, least-squares spectral adjustment, and stochastic algorithms [83]. Direct matrix inversion was

previously discussed in the setup of the unfolding problem. Matrix inversion is generally seen as "ill-posed" and can lead to non-physical results, such as negative fluxes [82, 83]. Stochastic methods rely on random sampling to derive a best-fit or average over a group of reasonably well-fitting spectra; however, the main disadvantage is preventing oscillatory solutions [83]. The least-squares method minimizes the chi-square based on a guess spectrum, activation information, and nuclear data [84]. The least-squares method is also known as spectral adjustment and can incorporate more information, most notably the underlying energy-dependent nuclear data, into the determination of the resultant spectrum [84].

The general formulation of the least-squares method is derived in this case by minimizing the error between activation results to the nuclear data convolved with the guess neutron spectrum [84]. The chi-square, χ^2, is given as per degrees of freedom, ν, as a function of the uncertainty, activation rates A_i, nuclear data, and measured results. The χ^2 formulation of the least-squares approach can be reduced if there is no time dependence of the neutron flux as

$$\frac{\chi^2}{\nu} = \frac{1}{\nu} \sum_{i=1}^{m} \frac{(\sum_{j=1}^{N} \Sigma_i(E_j)\ \Phi(E_j) - \frac{A_i}{V_{Foil}})^2}{\sigma_i^2} \quad . \tag{2.19}$$

The uncertainty for each measurement, σ_i, can include components for the measurement uncertainty and the model covariance to include activation cross section and neutron flux, where the measurement uncertainty is not correlated with the model uncertainty. In many implementations, σ_i is solely based on measurement uncertainty; however, solution methodologies such as PNNL STAYSL include the full covariance matrices for the model and sensitivity matricies for the measurement of a generalized least square solution. The χ^2 statistic can also be used in the context of comparing two normal distributions, where

$\sigma_i = \sqrt{\sigma^2_{i,model} + \sigma^2_{i,measurement}}$ [85].

Providing an initial spectrum is generally required for the unfolding methods. The activities produced for the foils is often highly degenerate, where an infinite number of spectra could provide the same observable end-point. The initial spectrum allows for the insertion of more physics-based results into the unfolding. For neutron spectra, an initial guess spectrum is often created with a particle transport code or a deterministic solution. Alternatively, an initial spectrum could be selected from published results [86].

2.7 Radiation Effects on Electronics

Radiation effects on electronics is an extremely large field of study with applications ranging from device hardness, space environments, to basic physics experiments [87]. This section focuses on displacement damage caused primarily by neutrons and ionization doses as applicable.

2.7.1 Neutron Displacement Damage.

Neutron displacement damage in a lattice of atoms is a direct consequence of neutron interactions with matter described in Section 2.1. An incident neutron can interact with an atom, creating a primary knock-on atom (PKA) in a collision. The energy of the PKA is governed by conservation of energy and momentum of the interaction system. For a spectrum of neutrons, various reactions can contribute to the displacement of atoms. The displacement of an atom leads to the production of Frenkel pairs, or a combination of an interstitial atom that has been displaced and a vacancy from the displacement site. The Frenkel pair defect is primarily considered because it is the most energetically favorable; however, more complicated defect structures can be present in irradiations [88].

Figure 2.17 displays the recoiling PKA spectrum for a lattice of silicon under a 14 MeV and TN+PFNS calculated with the SPECTER code [89]. There are two groupings of recoiling PKA kinetic energies. The lower energy peak corresponds to elastic scattering, where a maximum of 0.48 MeV can be transferred to a ^{28}Si atom. Threshold reactions for inelastic and (n,2n) functions result in the larger energy peak. Radiative capture γ-rays can also cause displacement of a recoiling atom; where, ^{28}Si(n,γ) results in approximately 1 keV recoiling ^{29}Si atom. The recoiling PKA can go on to cause many more displacements.

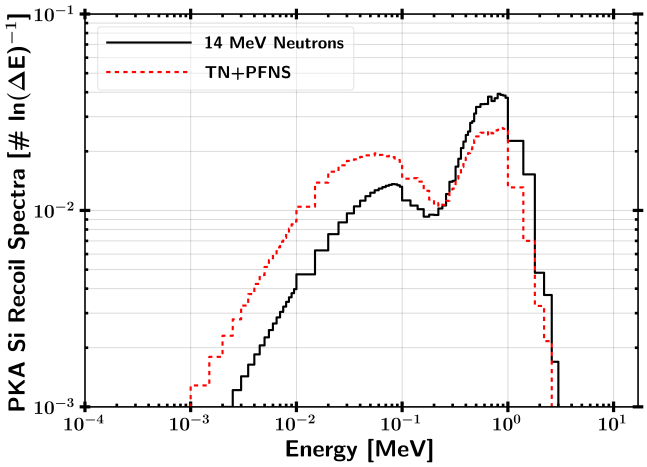

Figure 2.17. Recoil Si spectra for incident 14 MeV neutrons and TN+PFNS neutrons internal to ATHENA caulcated with the SPECTRE code [89]. The ATHENA spectrum is lower energy than 14 MeV on average, so less energy is available to produce PKAs. The peak beginning near 0.3 MeV corresponds to the maximum energy transfer for elastic scattering, while the peak at 1 MeV primarily includes higher energy inelastic and (n,2n) reaction channels.

Neutron environments have historically been represented as collapsed equivalent fluence at a mono-energetic energy, often 1 MeV neutrons. ASTM E722−19 is the most recent released document describing the formulation of the engineering level metrics for environments where the displacement damage is primarily from neutrons above 10 keV [19, 90]. Several assumptions must be made for an equivalent fluence, which are not always present in practice such as charged particle equilibrium. The displacement damage function, $F_{D,material}$, can be used to relate an observable effect,

such as the gain degradation of a silicon based transistor. For example, the 1-MeV neutron equivalent fluence for elemental silicon is given by

$$\Phi_{eq,1-MeV,Si} = \frac{\int_0^\infty \Phi(E) F_{D,Si}(E) dE}{F_{D,1-MeV,Si}}, \tag{2.20}$$

where the neutron fluence, $\Phi(E)$, is convolved with $\mathrm{F}_{D,Si}$ and normalized by a reference value of 95 MeV$-$mb for the 1 MeV neutron damage function. $\mathrm{F}_{D,Si}$ was calculated in the ASTM standard for ENDF/B-VIII.0 cross sections in natural silicon using the Robinson energy partition function [19]. Additionally, the hardness of a spectrum, which signifies the representative energy of a neutron spectrum for irradiation, is scaled by the integral of $\Phi(E)$ over all energies with

$$H_{1-MeV,Si} = \frac{\Phi_{eq,1-MeV,Si}}{\int_0^\infty \Phi(E) dE}. \tag{2.21}$$

Several energy partition functions exist, which split the kinetic energy released per unit mass (kerma) into, customarily, an ionization and displacement component [91]. The kerma in a material includes subsequent decays and radiated energy. The microscopic displacement kerma in particular uses the energy partition function to split the energy imparted into the material which produces displacement or non-ionizing energy.

Similar to the ASTM derivation, the Nortgett, Robinson, and Torrens (NRT) damage energy normalization can be used to account for the threshold recoiling ion energy to cause a displacement (E_d) from a lattice site [92]. The NRT damage energy is determined in the same manner as ASTM 722$-$19 but includes integrating over the threshold required to produce a Frenkel pair in the lattice [91,93]. The ASTM 722$-$19 displacement kerma and NRT damage energy function are shown in Figure 2.18 for comparison. Under NRT, $2E_d/\beta$ of incident neutron energy is required to produce

a Frenkel pair, where 20.5 eV is an experimentally measured and angular integrated reference for E_d [94]. β is an displacement efficiency term equal to 0.8 [92].

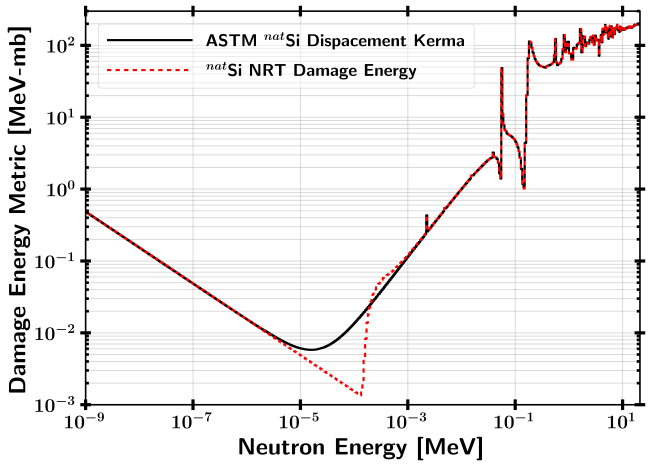

Figure 2.18. ASTM 722−19 and the NRT damage energy functions. The NRT damage energy exhibits a reduction for contributing reaction channels below the threshold energy. At energies above the NRT threshold, there is no difference.

Similar to activation foil cross sections, the NRT damage energy has been assessed for covariance based on the damage response function for nuclear data, threshold E_d, displacement model, interaction potential, and model defects such as non-negative constraints. A model for ^{28}Si, the primary Si constituent, NRT damage energy was derived at Sandia National Laboratories and is shown in Figure 2.19 [93]. The primary sources for the correlation matrix structure is the interaction potential and nuclear data for the component reactions.

2.7.2 Ionization Dosimetry.

Ionizing radiation is also an important characteristic for dosimetry and radiation effects on electronics. γ-ray energies up to approximately 20 MeV are present in neutron environments in materials through radiative capture [95]. Additionally from neutrons, γ-ray population can be produced through fission, inelastic neutron interactions, or (n,xn) reactions. Ionizing radiation can be measured with various

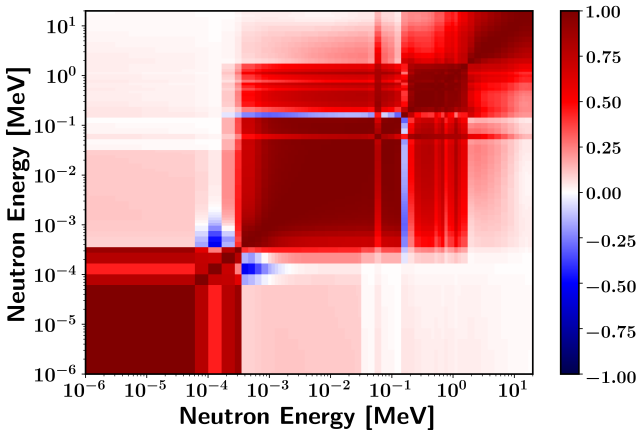

(a) Correlation matrix

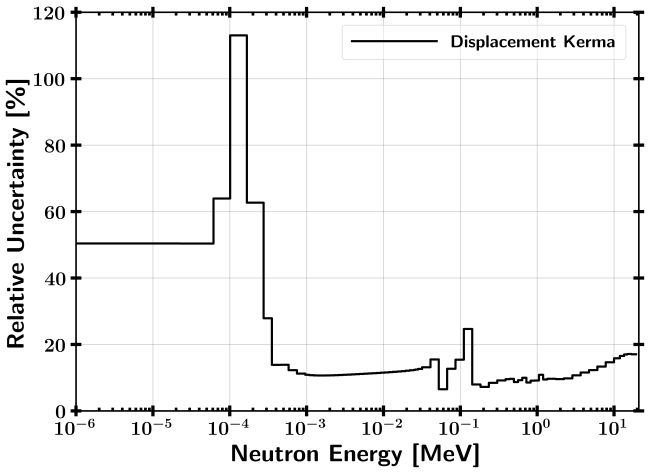

(b) Relative Uncertainty

Figure 2.19. NRT damage energy covariance matrix parameters [93].

detectors; however, thermoluminescent dosimetry is considered in this work to measure the absorbed ionizing dose.

2.7.2.1 Ionizing Radiation.

γ-ray environments can produce ionization through three primary mechanisms in the energy range of interest. In order of increasing energy required [53],

1. the photoelectric effect is the ejection of an electron following γ absorption,

2. the Compton effect is a γ-ray scattering off atomic electron,

3. and pair production can produce an electron/positron pair if a γ-ray energy is greater than 1.022 MeV.

The three primary interactions' magnitude are material dependent and act to attenuate γ-rays, producing electrons and/or lower energy photons in the process.

The mass attenuation coefficient, μ/ρ, is a notation for the density-normalized macroscopic cross section of a material for photon interactions with matter that captures the contributions of the photoelectric effect, Compton effect, and pair production. Figure 2.20 displays μ/ρ for natural silicon. In the low energy region where the photoelectric effect dominates, the K-shell atomic orbital electron at 2 keV results in a step function increase past the threshold energy. μ_{en}/ρ, the mass energy absorption coefficient, accounts for the energy that can escape the system or is emitted below the ionization threshold or re-radiated.

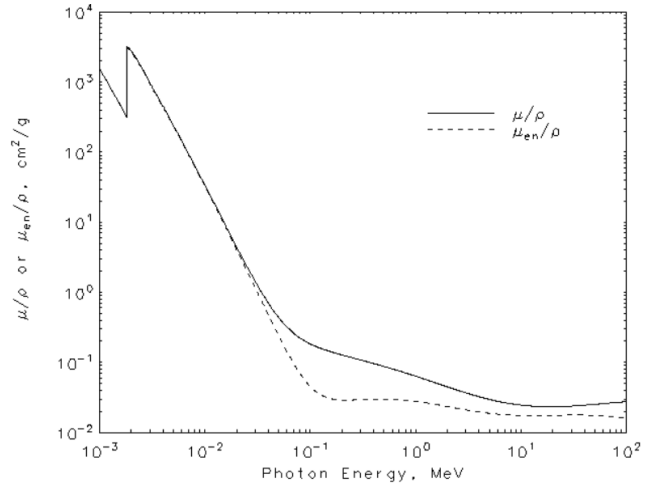

Figure 2.20. Silicon mass and mass energy absorption coefficients [96].

.

The ionizing radiation dose is the kerma of energy that contributes to ionization in a material with units of energy per unit mass. One important aspect to ionization dose and the mass energy absorption coefficient is charged-particle equilibrium for a cell under ionization, meaning that the electron current entering a

cell is equivalent to the electron current exiting the cell. There are several reasons why charged-particle equilibrium may not exist, such as a non-optically thin cell. One major source of non-equilibrium conditions occurs at material interfaces which have largely different atomic numbers, altering the rate of ionization and can lead to non-equilibrium conditions.

2.7.2.2 Thermoluminescence.

Thermoluminescent (TL) dosimetry is a developed mechanism to experimentally determine the total ionizing dose in a material. A generic TL process is graphically shown in Figure 2.21 [80]. A TL material is doped with impurities to add electron and hole traps to the electronic band structure. Under the presence of ionizing radiation, a valence electron can increase in energy up into the conduction band and end in an electron trap with some probability and an associated vacancy hole trap. Depending on the stability of these traps, the concentration of trap sites builds up in a TL material. Several TL dosimeters (TLDs) have been studied with more popular commercial materials being LiF:Mg,Ti and CaF_2:Mn. Some ideal material properties for TL devices include limited "fading" or decay of traps on a long time period, atomic number similar to what dose is being predicted for, and optimized flourescent characteristics.

The TL process relies on increasing the temperature or energy of the valence band, which increases the transition rate for trap centers to re-radiate back to the valence band. Depending on the relative trap energy depths, an electron can be raised to the conduction band and subsequently combine with a trapped hole site. Alternatively, a hole site can migrate to a trapped electron and emit a photon. TL materials are chosen so that the emitted photons are detectable with a detector, usually the visible light spectrum.

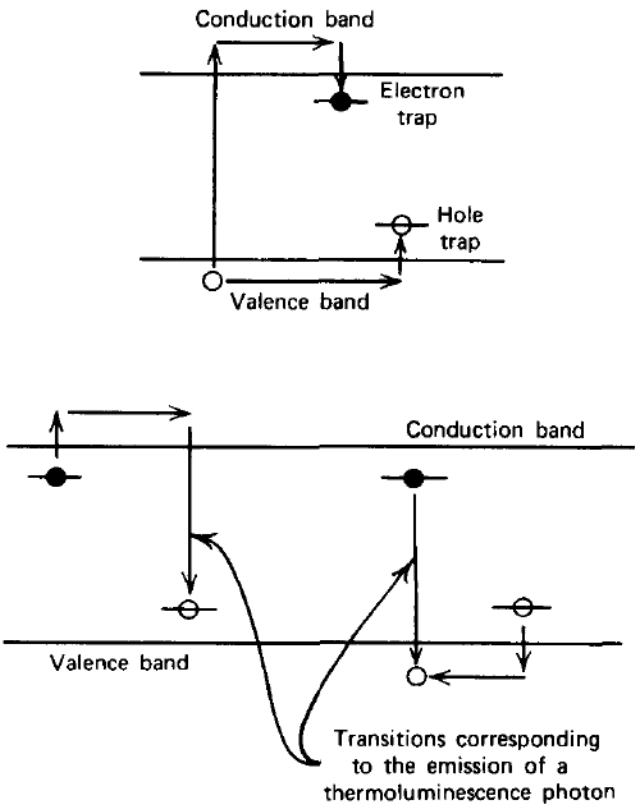

Figure 2.21. TL and heating diagram showing the production of traps and emission of photons from trap sites [80].

The measurement of TLD materials includes a reference dose and time-temperature-profile (TTP). TLD readers can be used to heat the material according to a TTP where either the integral or max of the number of counts as a function of temperature is normally used to measure the dose. Characterized sets of TLD crystals can be measured relative to a reference dose, where a known source is used to expose the TLD. TLD materials generally have a region of linear relation between dose and TL. The reference dose can be used to normalize an experimental dose TL curve due to this linearity and determine experimental ionizing dose radiation conditions.

III. Radiation Environment Monte Carlo Characterization

This chapter was derived from a paper published in March 2020 with *IEEE Transactions on Nuclear Science* titled "Nuclear Data Covariance Analysis in Radiation Transport Simulations Utilizing SCALE Sampler and the IRDFF Nuclear Data Library [97]." The author list included Nicholas J. Quartemont, Abigail A. Bickley, and James E. Bevins, all affiliated with AFIT. The article has been modified to fit this dissertation format; however, the content was unchanged.

This article serves as the generalized framework for modeling the effects of nuclear data uncertainty and correlations to observable metrics for neutron radiation experiments. The generalized goal was to develop an understanding of the range of possible outcomes for the original ETA experiment and in the future lead to the determination of a neutron flux covariance matrix for neutron flux unfolding of the experimental measurements. The concept of an ETA is introduced as an example problem here, where follow-on chapters provide a more robust approach to the ETA modeling efforts.

3.1 Abstract

This paper describes the nuclear data covariance analysis of an experimental design for a neutron energy tuning assembly created to shape a 14 MeV neutron point source to an objective spectrum. Underlying nuclear data uncertainties play a large role in the radiation transport and reaction rates for the range of responses to be expected from an experiment. The methodology leveraged the SCALE Sampler module to determine the uncertainty in the neutron transport. The reaction uncertainty was perturbed with the International Reactor Dosimetry and Fusion File v.1.05 uncertainty, correlation matrix, and reaction cross section through

multivariate normal distribution sampling to provide a final response metric. The resultant neutron fluence uncertainty for the energy tuning assembly ranged from 2.7 to 6.2% in the energy range from 1.28 keV to 14.1 MeV, which contains 99.99% of the neutron fluence. The integrated uncertainties, including statistical and systematic nuclear data uncertainties, for reaction products analyzed were 2.33 to 4.84% for most reactions, but ^{55}Mn(n,γ), a less well characterized reaction occurring in an energy domain with high flux uncertainty, was 19.7%. The mean of the reaction distributions was within 1.1% of the unperturbed nuclear data simulation. The experiment is planned for late 2019 where the predicted results will be compared against the experimental outcomes. The methodology presented can be utilized with alternate nuclear libraries in SCALE to develop uncertainty bounds and neutron flux spectra for many radiation transport problems.

3.2 Introduction

Nuclear data covariance analysis is an important modeling technique to consider when simulating the expected outcomes from one-off, high-cost experiments, the range of operating conditions that can lead to safety considerations in reactors, or criticality safety in enriched uranium or plutonium operations [98, 99]. Including nuclear data covariance in the analysis allows the simulation to better quantify the underlying uncertainties and range of possible outcomes that often far exceed the statistical uncertainties associated with Monte Carlo simulations and (frequently unquantified) discretization uncertainties relevant to deterministic simulations [100]. This work outlines a framework for further incorporating a nuclear data covariance analysis into a Monte Carlo simulation of an energy tuning assembly (ETA) designed to convert a source neutron spectrum into an objective spectrum.

The two primary methods that exist for uncertainty quantification are linear

perturbation and stochastic sampling Monte Carlo approaches [71]. First order linear perturbation theory is not always adequate for large uncertainties or incorporating second order effects from the uncertainty in the neutron transport; however, it does have broad uses in low uncertainty core physics applications [101]. Stochastic sampling has grown in popularity as computational resources have improved. Stochastic methods rely on performing independent neutron transport calculations with perturbed nuclear data libraries sampled based on the covariances of the cross sections to build a distribution of responses [72]. Several Monte Carlo sampling methods have been created to capture the impact of nuclear data covariance on nuclear engineering problems, including SCALE Sampler, NUSS, SHARK-X, among others [45, 72–74, 102]. Many collections of software capable of performing these types of uncertainty quantification are not available for distribution or focus solely on nuclear reactors.

The majority of uncertainty analyses to date focus on integrated quantities such as the effective criticality of a nuclear reactor [101, 103]. Integrated values can be important observable quantities, but individual reaction channel rates that directly affect the observable outcomes are more important in other applications. For example, radionuclide production often relies on a single reaction channel that is observed, which can have much larger uncertainties than noted in integral quantities. However, in the majority of uncertainty analyses, insight into the underlying distribution of reactions is often not explicitly determined. Additionally, the energy dependence of the response can also be important to assess, but it is traditionally not included in the uncertainty analysis. However, the energy dependence of systematic uncertainties has key applications such as the development of a guess spectrum for neutron flux unfolding techniques.

While the stochastic sampling approach can address many of the shortcomings

of perturbation theory, it is not without its own deficiencies including computational cost, the dependence on nuclear data libraries, and the sampling method [101]. The nuclear data uncertainty is typically assumed to follow a normal distribution, and a multivariate normal distribution approximation has historically been utilized to perturb the underlying nuclear data in stochastic sampling codes [104, 105]. This approximation is accurate when the uncertainty is small compared to the mean value. However, nuclear data uncertainty can be above 100% in energy regions where a measurement has never been taken. With high uncertainties, especially those approaching 100%, sampled non-physical negative cross sections are possible when a normal distribution is assumed. Varying forms of the nuclear data have been considered and are not always normally distributed [105, 106]. In fact, the evaluated data contained in ENDF specifically states that it is not necessary to assume the probability density functions are normal in shape [46, 107].

To prevent performing neutron transport calculations with negative cross sections, most stochastic sampling approaches truncate the uncertainty or re-sample when presented with negative values [104]. The underlying data are also constrained to meet the requirements of a covariance matrix such as being positive semi-definite, which is not always present with the evaluated data. Although negative cross sections are non-physical, the truncation underestimates the uncertainty, which can have an impact if the experiment is performed in these high uncertainty regions.

Evaluated uncertainties may also be underestimates of the general nuclear data uncertainty [65]. Capturing the full nuclear data uncertainty is essential because it is often a dominant unknown in nuclear applications [108]. Furthermore, every reaction and uncertainty of interest may not be available in the same nuclear data library, which motivates a need to include additional libraries to meet experimental modeling requirements.

However, it is essential to note that there is no inherent uncertainty to nuclear data [45]. Instead, the uncertainties and correlations are an evaluation based on experimental data and models, and not always a direct quantification of the uncertainty. Stochastic sampling uncertainty quantification approaches are state-of-the-art for an estimation of the uncertainty that is consistent with published evaluated data. This work utilizes SCALE 6.2 along with the International Reactor Dosimetry and Fusion File (IRDFF) v.1.05 reaction cross section library [45, 48]. MCNP5 is utilized to perform continuous energy neutron transport simulations that were mapped to the SCALE MAVRIC sequence [44, 45]. This transformation of Monte Carlo code systems was necessary to leverage the SCALE Sampler sequence but results in variations in the mean value based on the different implementation of the neutron transport algorithms, nuclear data, geometry specification, and source definition. Comparisons between Monte Carlo radiation transport codes have shown variations outside the associated Monte Carlo statistical uncertainty. For example, integral results, such as the effective criticality of a nuclear reactor, have been compared between versions of equivalently modeled continuous energy MCNP and SCALE calculations [77, 78, 109]. Each study reported near a 1% or less difference between the calculated values for the differing codes. Alternatively, a study of radiation dose rates from spent fuel storage observed differences on the order of several percent between SCALE and MCNP [79].

The proposed methodology leverages the SCALE Sampler sequence around the MAVRIC neutron transport code with post-processing of the reaction rates produced with the IRDFF nuclear data library. The SCALE MAVRIC module is used for continuous energy and multi-group Monte Carlo neutron transport. The SCALE Sampler sequence is a general purpose total Monte Carlo approach and is utilized to assess systematic uncertainties for a given radiation transport simulation

that can include nuclear data, material specification, and geometry. The resultant uncertainties from the Sampler multi-group neutron transport calculation are utilized to quantify uncertainties in a continuous energy neutron transport simulation modeled using MCNP5.

This paper is organized as follows. Section 3.3 briefly describes an example Monte Carlo problem utilized in this work. Section 3.4 provides the methodology including nuclear data libraries and models to generate uncertainties around integral and energy dependent responses. Section 3.5 outlines the simulation results. Finally, Section 3.6 summarizes the uncertainty quantification techniques and provides a path forward for future work.

3.3 Example Problem Description

To illustrate the approach for quantifying nuclear data covariance on reaction rates and determining a guess neutron flux for unfolding techniques, an example problem was analyzed for this work. The chosen problem was an energy tuning assembly (ETA) for an experiment to be performed at the National Ignition Facility (NIF). The planned ETA experiment at NIF is of relatively large cost, so capturing the impact of nuclear data covariances are important to understanding the range of potential experimental outcomes. This problem is interesting for this work because the experimental outcomes are dependent on the several individual reaction channels and a neutron spectrum spanning seven orders of magnitude in intensity and energy. The combination of these factors lends itself well to a stochastic sampling approach.

Additionally, this problem is useful for highlighting three deficiencies in current stochastic sampling software, and provides an approach to address these shortcomings. First, the nuclear data covariance cross section libraries that have been developed for SCALE Sampler are limited and currently do not include a

group structure well suited for high-energy neutron applications [45]. Second, even if high-energy group structures existed in Sampler, other codes may adopt different group structures leading to a mismatch that must be addressed. For the ETA case, the use of PNNL STAYSL to unfold the neutron energy spectrum from the foil activities is one such example [110]. Finally, benchmarked simulation sequences exist in codes other than MAVRIC, necessitating the ability to combine results from multiple simulations. In this example, a full-scale NIF simulation exists in MCNP5.

The ETA, shown in Figure 3.1, was previously designed to produce a notional thermonuclear and prompt fission neutron spectrum (TN+PFNS) [4, 37]. The TN+PFNS is an unclassified representation of a boosted nuclear weapon based on the Godiva critical assembly [111]. The ETA design is 28 cm in diameter and approximately 24 cm in height. The NIF source was located 15 centimeters below the base of the cone and was modeled as a D-T Polar Drive Exploding Pusher (PDXP) target with a nominal yield of 3.7×10^{15} neutrons with an initial energy of 14 MeV [112]. The ETA consists of cones and cylinders of boron carbide, praseodymium, bismuth, tungsten, silicon, 409 stainless steel, and lead. Each ETA part is manufactured with three or four nines pure material and sub-mm tolerances thereby limiting other sources of systematic uncertainty in the model. The ETA surroundings are filled with vacuum pressure nitrogen. The ETA is to be fielded with a activation foil pack and a highly enriched uranium (HEU) foil, depicted as item six in Figure 3.1, to infer the neutron fluence spectrum achieved in the ETA. The foils are placed in the sample cavity where the objective neutron spectrum is achieved. The sample cavity is enclosed in a lead filled aluminum drawer for extraction post-experiment. The ETA was modeled with the drawer facing up, so gravity skewed the mass distribution slightly away from the drawer insert as shown in Figure 3.1.

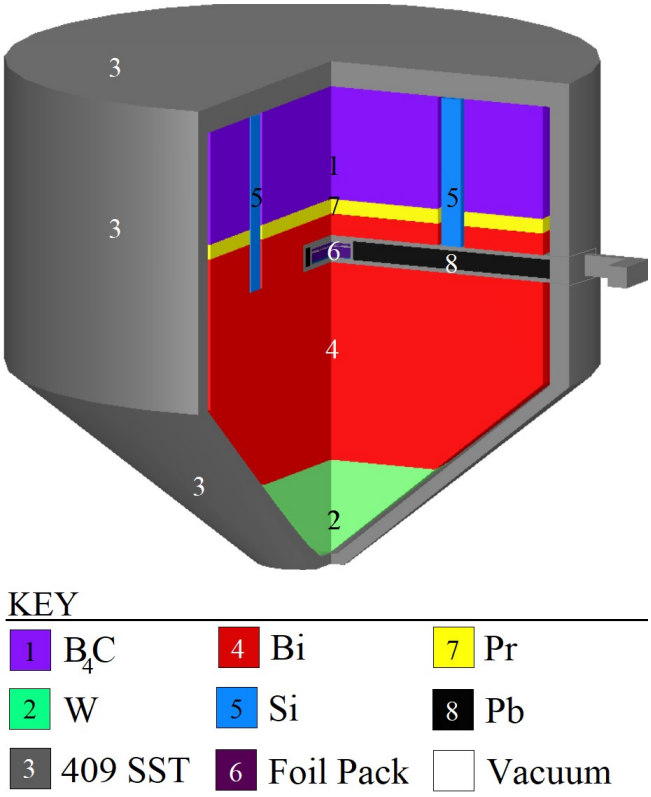

Figure 3.1. (Color online) The ETA is designed to achieve an objective TN+PFNS through spectral modification of the NIF neutron source.

The activation foils chosen are natural indium, aluminum, nickel, zirconium, gold, manganese, and tungsten. Each foil has threshold and non-threshold reactions that span the range of interest for the TN+PFNS energy spectrum, which can be used to unfold the incident neutron energy spectrum to validate the ETA performance [37, 80, 82]. The HEU sample is enriched to 93.15% ^{235}U. All foils are placed in the removable drawer. The modeling objective is to have an expectation for the impact of nuclear data covariances on the foil activation rates, fission yield, and neutron energy spectrum in the sample region.

3.4 Description of Work

The methodology used to perform this uncertainty analysis is shown in Figure 3.2. There are three key contributions to the uncertainty in this radiation transport simulation. First, there is uncertainty in the neutron transport between the neutron source and the region of interest, defined for this problem as the drawer containing the foil pack. The second contribution results from the uncertainty in the cross section due to the interaction of the neutron flux with the foils to form the reaction tally. In most uncertainty quantification analyses, these two nuclear data uncertainties are treated at the same time; however, it is important to note that nuclear data uncertainties impact the problem from multiple perspectives to form the overall nuclear data systematic uncertainty σ_{sys}. This analysis neglects other forms of systematic uncertainty such as material composition, geometry, and source characterization. Last, every Monte Carlo based result has statistical uncertainty σ_{stat}, which can be driven to negligible values with sufficient computational resources.

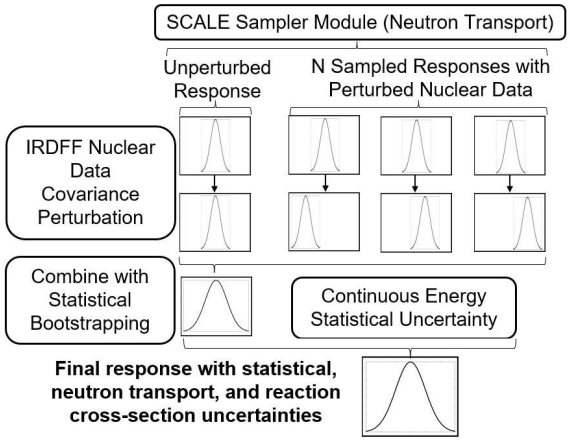

Figure 3.2. Methodology flowchart to determine nuclear data uncertainty for a single reaction channel from alternative library into SCALE.

The SCALE Sampler module was used to assess the neutron transport response

uncertainty by building a distribution of responses using the pre-built set of 252-group nuclear data libraries sampled from ENDF/B-VII.1 consistent with the underlying nuclear data covariances [46]. 182 Monte Carlo simulations were completed with Sampler to provide enough sets of data for convergence of all responses with the uncertainty bounded within 1% of the total uncertainty. Each of Sampler's independent sample simulated fluences in each activation foil were convolved with the IRDFF nuclear data covariance sampled reaction cross sections separately from the perturbation in SCALE. In cases such as ^{55}Mn(n,γ), ^{186}W(n,γ), and U(n,f), ENDF data were utilized because they were consistent with IRDFF [46]. The resultant responses were combined using statistical bootstrapping as the final response distribution was assumed to be non-normally distributed. Bootstrapping is a process of randomly selecting with replacement data from a sampled distribution to create a probability distribution representative of the underlying distribution [113]. Finally, some applications required a group structure different than what is available in Sampler, which can be accomplished with a continuous energy neutron transport calculation. The bootstrapped σ_{sys} was mapped to the alternate group structure, and the Sampler σ_{stat} was replaced by the continuous energy σ_{stat} by adding σ_{sys} and σ_{stat} in quadrature.

3.4.1 Nuclear Data Libraries.

Three nuclear data libraries were utilized in this analysis. First, the continuous energy neutron transport simulations performed in MCNP and SCALE utilized the ENDF/B-VII.1 library [46]. ENDF is a comprehensive nuclear library which contains the data necessary for the transport calculation. ENDF/B-VII.1 was chosen for the radiation transport simulations to maintain consistency given the limitation of SCALE. The systematic nuclear data uncertainties in this work are

thereby limited to the nuclear data available for sampling in ENDF/B-VII.1. The covariance information included in ENDF/B-VII.1 relevant to this application includes the total cross sections, the (n,γ) cross sections, the (n,2n) cross sections, the fission cross sections, the (n,n) cross sections, and the (n,n') cross sections. ENDF/B-VIII.0 was released in 2018 and contains new or updated evaluations with full covariance information such as inelastic scattering and angular distributions [114]. However, Oak Ridge National Laboratory is still testing to include ENDF/B-VIII.0 in a future update of SCALE [115].

The multi-group nuclear data transport calculations were performed with the 252-group SCALE library based on ENDF/B-VII.1. This was the highest fidelity multi-group library distributed with SCALE and contains nuclear data covariance sampled libraries for use in Sampler. The group structure covariance libraries were largely developed from ENDF/B-VII.1, but additional information has been included from ENDF/B-VI, ENDF/B-VII.2 (proposed at the time), JENDL-4.0, working groups, and collaboration with U.S. National Laboratories [45].

It is worth noting that mutli-group neutron transport can change the results of a Monte Carlo simulation. A study compared criticality for mixed oxide fuel thermal nuclear reactors using SCALE version 6.1 and 6.2 with the available continuous energy and higher fidelity multi-group neutron cross section evaluation and demonstrated agreement within 1% [116]. The spent fuel storage study also reported that differences between multi-group nuclear data libraries in SCALE ranged from 1% to 50% for their problem. Finally, a study evaluated the activation of materials with a neutron source between various group structures [79]. The reported differences ranged between approximately 5 to 50%, which was directly attributed to the generation of the cross section [117].

The activation foil reactions utilized the IRDFF v.1.05 library, and

ENDF/B-VII.1 was used for response functions not available in IRDFF. The International Atomic Energy Agency provides data for the IRDFF library, which contains benchmarked neutron dosimetry reactions [48]. The IRDFF v1.05 library contains "state-of-the-art" covariance information and has improved through testing and integral experiments, but it does not contain a comprehensive collection of nuclear data for all isotopes [52]. The IRDFF library is also extremely valuable in that some reaction cross sections are available for the energy-dependent population of metastable isomeric states, important for activation experiments. SCALE cannot directly load nuclear data libraries; however, the IRDFF library can be incorporated by providing user defined response functions.

The IRDFF library is also used in the PNNL STAYSL code system, and all of the foil activation reactions used for this experiment have nuclear data within the IRDFF [110]. STAYSL performs least-square spectral adjustment to unfold the neutron flux from activation foil activities, nuclear data, and nuclear data covariance [84]. STAYSL is not discussed further here, but it was a driver for utilizing the IRDFF library.

The ^{197}Au(n,γ) example shown in Figure 3.3 shows the use of the same uncertainty among all evaluated libraries up to approximately 1 keV. However, the IRDFF v.1.05 evaluation has a much larger uncertainty from 1 to 4 keV, and the SCALE 252-group library drops to zero uncertainty after approximately 2.5 MeV. Some of these deviations are based on the group structure utilized, but others are due to incomplete nuclear data covariance information, which necessitated the effort noted above to generate complete libraries for use with stochastic sampling and necessitated the use of multiple libraries to incorporate the best covariance information available.

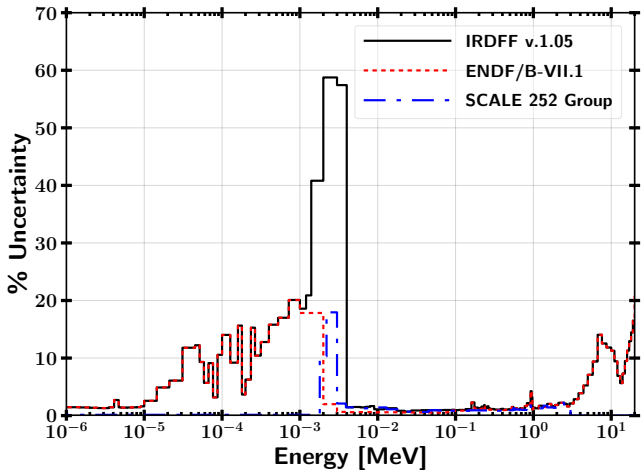

Figure 3.3. (Color online) Comparison between IRDFF v.1.05, ENDF/B-VII.1, and SCALE 252-Group ENDF/B-VII.1 ^{197}Au(n,γ) reaction cross section uncertainties.

3.4.2 MCNP and SCALE MAVRIC Model.

A continuous energy radiation transport simulation of the NIF experiment was performed in MCNP5 in collaboration with Lawrence Livermore National Laboratory. The NIF model in MCNP5 has been utilized for numerous experiments and moving from MCNP to other radiation transport codes is cumbersome due to the high fidelity model that has been developed and validated. The ETA was modeled in the full NIF chamber including the target positioner (TARPOS), target and diagnostic manipulator (TANDM), polar diagnostic instrument manipulator and the first panel walls [118]. The ancillary equipment and surroundings must be incorporated into the model to account for neutron 'room return' in the NIF chamber. The source D-T fusion neutrons were modeled as mono-energetic 14.03 MeV, which is a zero plasma temperature model that has previously been used at the NIF.

A surface source write file was created to use for a surface source read (SSR) to expedite the radiation transport analysis of the ETA. The SSR file contains all of the particle histories that cross defined surfaces [44]. By utilizing these files, the

transport from the source to ETA is fully defined and contains source particles to use in further simulations starting from the surfaces where the file was scored [119]. The surfaces scored were a disk at the top and bottom of ETA 17.5 cm in diameter and a connecting cylinder. The front disk surface was utilized to capture all of neutrons travelling toward the ETA cone. The surface neutron current distributions at the front (source facing), back, and cylindrical surfaces are shown in Figure 3.4. The back and cylindrical surfaces solely represent the room return, while the front surface source is dominated by source neutrons. The total fluence of neutrons based on the neutron current tally through the front, back, and cylindrical surfaces were 6.5×10^{14}, 3.5×10^{12}, and 2.4×10^{12} neutrons, respectively.

The neutron current on the SSR surfaces was mapped to SCALE for use in MAVRIC and Sampler by source definitions to approximate the behavior of MCNP's surface source. The front source was modeled as a point source at the location of the PDXP target. The point source strength was 3.72×10^{15} neutrons to include the room return component based on the solid angle between the front surface and the point source. The back source was modeled as a disk, and the cylinder was approximated as four line sources facing ETA and emitting in 2π.

3.4.3 Sampling Nuclear Data Covariance Libraries.

User-defined response functions in Sampler are not sampled with a covariance matrix as built-in nuclear data in SCALE. There are options to perturb a variable inside of Sampler; however, there are presently no methods to include correlations to create the covariance. Instead, the reaction rates were determined in post processing by perturbing each Sampler reaction rate for each activation foil. This methodology to re-sample the reaction rate for a response assumes that the nuclear data follow a correlated multivariate normal distribution [74, 120, 121]. Multivariate

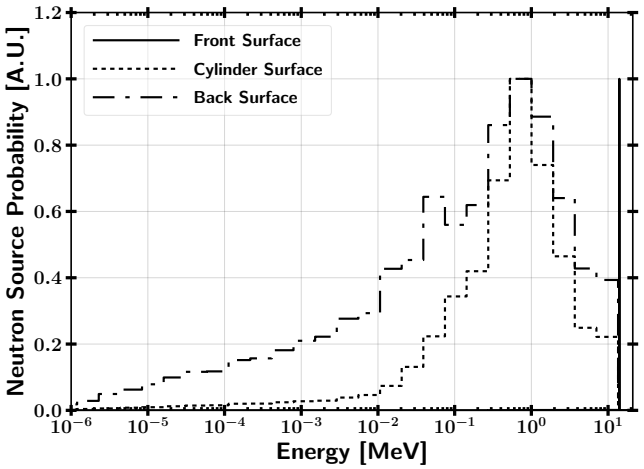

Figure 3.4. Neutron current distributions at the front, back, and cylindrical components of the SSR file. The front surface (solid line) is almost entirely unscattered 14.03 MeV neutrons.

normal distributions require an expectation value and a covariance matrix that is positive semi-definite.

The IRDFF nuclear cross sections were converted to SCALE's 252-group format, while the uncertainties were converted by linear interpolation of the midpoint bin energies. The uncertainty is generally slowly changing over small energy ranges making a linear interpolation a reasonable approximation of the group-wise uncertainty as discussed further in Section 3.4.5. Alternatives to this approach include cross section uncertainty processing to a 252 group format or assuming a flux weighted ratio of uncertainties to create a new bin uncertainty.

The IRDFF nuclear data and uncertainty were sampled from the multivariate normal distribution for each independent Sampler trial. The reaction tally, R, result was perturbed by the ratio of the macroscopic cross section, Σ, before and after multivariate random sampling to create group-wise perturbation parameters, Q, with the neutron flux, ϕ, over 252 groups, g.

$$R = \sum_{g=1}^{252} \phi_g \, \Sigma_g \, Q_g \tag{3.1}$$

The net result modified the microscopic cross section to form the perturbed R. The multivariate normal distribution sampled data act as a set of constants that are multiplied to each energy group [121]. The sampled reaction trials were combined with bootstrapping where random samples were drawn with replacement to determine the mean and standard deviation of the distribution.

3.4.4 Validating the Use of the Multivariate Normal Distribution.

Common practices for stochastic sampling approaches are built around the multivariate normal distribution, which has a very straightforward way to sample nuclear data covariance matrices. However, the log-normal distribution is more appropriate for physical properties that cannot take on negative values such as neutron reaction cross sections [105]. The log-normal distribution and normal distribution produce similar approximations for small relative uncertainties, but the distributions diverge significantly for large variances. Sampling from a normal distribution is not the optimal solution when the uncertainty in the data is larger than 30% relative error [122]. For example, the ^{55}Mn(n,γ) reaction has large uncertainty at higher neutron energies. The evaluated cross section and experimental data informing the (n,γ) reaction cross section near 14 MeV in ENDF/B-VII.1 are shown in Figure 3.5.

The experimental data are spread over an order of magnitude, but are most dense around the evaluated cross section, thereby supporting the use of a log-normal distribution over the normal distribution. Sampling of the nuclear data covariance matrices assuming a log-normal distribution instead of a normal distribution can produce drastically different results in radiation transport simulations.

The methodology utilized by Sampler employs a multivariate normal distribution with negative values truncated [108]. The impact from choosing a normal distribution

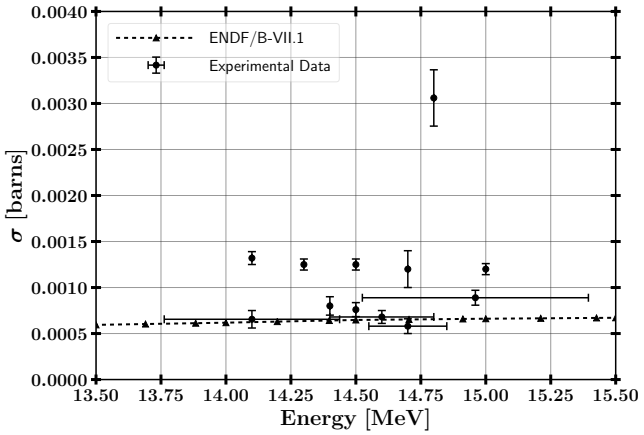

Figure 3.5. Experimental nuclear data informing the ^{55}Mn(n,γ) reaction in comparison with the evaluated nuclear data contained in ENDF/B-VII.1 [123–129].

with negative value rejection is mitigated because uncertainties are generally larger in regions where the reaction cross section is lower, so the net result on the problem may be reduced. Additionally, the truncated multivariate normal distribution has been shown to produce greater or equivalent entropy in comparison to the log-normal distribution. The methodology for sampling the nuclear data libraries in this analysis utilized the multivariate normal distribution to maintain consistency with Sampler. The impact to this research is that an estimation of the uncertainty is determined. The quality of that estimation is high for well-studied cross sections and diminishes as the nuclear data uncertainty increases and is a fundamental limitation of current methodologies [101, 108].

3.4.5 Mapping Nuclear Data Systematic Error to Alternate Group Structures.

Nuclear data group structures are essential to the accuracy of a group discretized transport simulation. A notable issue with utilizing a single group structure for all applications is the weighting function to process the continuous energy cross sections. If the flux is dramatically different from the weighting function, then the simulation

can result in erroneous results. Ideally, multi-group cross sections would be generated for each individual problem. However, even in the ideal case, complex problems with dramatic changes in the neutron spectrum in different regions of a problem can result in non-ideal behavior. In practice, pre-compiled multi-group libraries for common problems are often distributed with deterministic codes.

In contrast, it has been shown that the integral group-wise cross section uncertainty is relatively insensitive to the group structure used [120]. Any error associated with the group structure is minimized due to the (sometimes large) uncertainty in published cross section uncertainties and the general linear trend in evaluated uncertainties over small energy ranges. The integrated uncertainty for a given group structure and the differential cross section both play an important role in the results, but need to be handled differently.

The SCALE Sampler sequence is limited to a 56 and 252-group structure approach for sampling nuclear reaction cross sections. Ideally the continuous energy libraries would be perturbed; however, the group-wise transport method is still a powerful tool. The associated libraries contain 1,000 pre-sampled neutron cross sections. The weighting functions for SCALE's library are a Maxwellian from 10^{-5} eV to 0.1 eV, a $1/E$ between 0.1 eV to 80 keV, a Watt Fission spectrum from 80 keV to 10 MeV, and a $1/E$ between 10 to 20 MeV.

A test case for the ^{58}Ni(n,2n) reaction is used to demonstrate the impact of the weighting function and group structure on the uncertainty results. The ^{58}Ni(n,2n) reaction ENDF interpolation scheme is linear in energy and in cross section which makes analytic solutions straightforward. The cross sections from ENDF/B-VII.1 available in SCALE are shown in Figure 3.6 along with the SCALE relative uncertainty of the reaction cross section. As shown in Figure 3.6, the $1/E$ weighting function slightly shifts the 252-group cross section to lower energies in this energy

range.

The test case utilizes a normalized flux weighted by the bin width from the threshold energy of 12.4 MeV up to 20 MeV. This flux profile, shown in Figure 3.7, was chosen to eliminate bias from the energy bin sizes for the 252-group structure.

Neglecting self-shielding effects in the calculation, the 252-group structure underestimated R by 0.4% for the test case. The reaction rate for the continuous energy cross section resulted in 0.005117 ± 3.255% reactions/cm^3-s, while the 252 group structure cross section resulted in 0.005095 ± 3.244% reactions/cm^3-s. More importantly, the reaction uncertainty differed by 0.2% which suggests at first order that uncertainties may differ from a continuous energy solution by approximately the same magnitude that R is different.

The differential uncertainties were treated as being a function of energy through linear interpolation of the midpoint bin energies. This approach provides an approximation of the total uncertainty for the target STAYSL 129-group structure. The 252-group structure results were assumed to be a combination of σ_{sys} and σ_{stat} through quadrature as

$$\sigma_{total} = \sqrt{\sigma_{sys}^2 + \sigma_{stat}^2}. \tag{3.2}$$

This allowed σ_{sys} to be determined for each energy group. The reverse treatment was performed to add in σ_{sys} from the continuous energy MCNP5 simulation to the target group structure.

3.5 Results and Discussion

The fluence per unit lethargy for the nominal 252-group and the bootstrapped 182 252-group Sampler simulations are compared in Figure 3.8 to the target 129-group STAYSL structure. This shows the overall shape and characteristics of the TN+PFNS

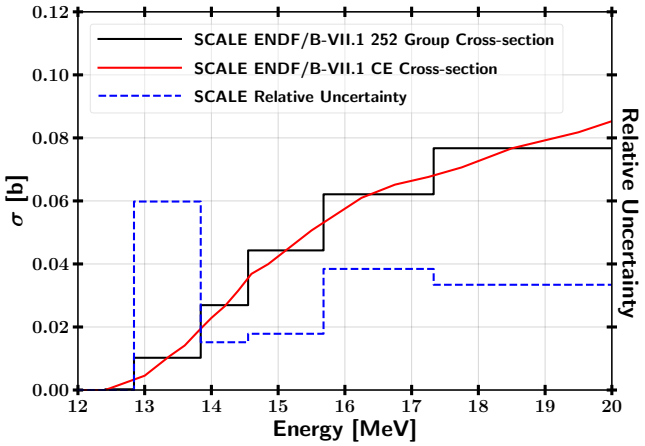

Figure 3.6. (Color online) Comparison between ^{58}Ni(n,2n) continuous energy (CE) and 252-group $1/E$ weighted cross sections. The relative uncertainty of the reaction cross section is shown.

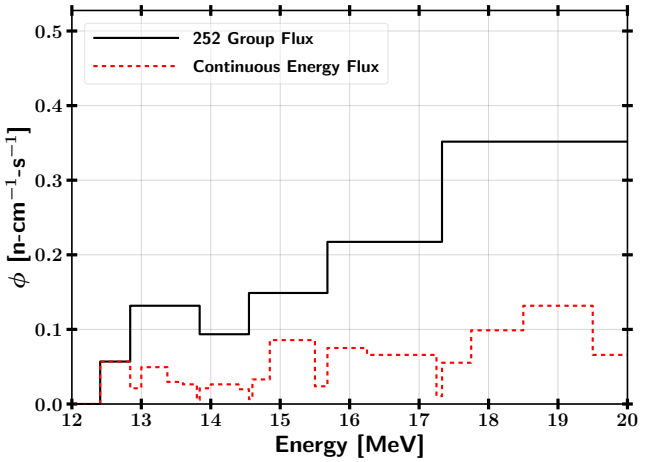

Figure 3.7. (Color online) ^{58}Ni(n,2n) case study constant differential flux.

produced by ETA in the sample cavity, but due to the large range in intensity and energy, it is difficult to see the impact from quantifying the nuclear data uncertainty using Sampler.

The results of the mapped fluence uncertainty from Sampler to the continuous energy MCNP5 simulation using the 129-group STAYSL structure are shown in Figure 3.9. The integral fluence above 1.28 keV, the point where the systematic uncertainty begins to dominate the statistical uncertainty, is 99.99% of the total. The fluence uncertainty from 1.28 keV to 14.1 MeV ranged from 2.7 to 6.2%. The

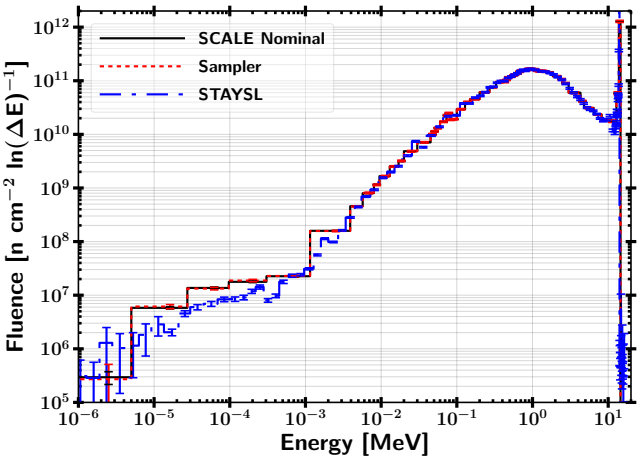

Figure 3.8. (Color online) Comparison of the simulated fluence in the ETA foil pack for the nominal 252-group and bootstrapped 182 252-group Sampler simulations in comparison to the target 129-group STAYSL structure.

systematic differential fluence uncertainty in this region is a property of the neutron transport and not sensitive to the neutron energy. Below 1.28 keV, the statistical contribution increased rapidly and was similar in magnitude to the overall systematic uncertainty.

The fluence shown in Figure 3.8 and the uncertainty in Figure 3.9 were combined with the sampled IRDFF cross section as described in Section 3.4.3 using Equation 3.1 to predict the reaction rates in each of the foils located in the ETA experimental cavity. The results comparing the integral activation reaction products and fissions from the original MCNP5 SSR model, the continuous energy MAVRIC model with the SSR mapped as described in Section 3.4.2, and the 252-group Sampler bootstrapped model are shown in Table 3.1.

The MCNP5 and SCALE Mavric calculations of the activation product reactions for the continuous energy solutions produced the same reaction yield, within ± 2.8%, for the reaction channels studied. The two simulations produce results that do not overlap within statistical uncertainty. This is attributed to the use of different transport algorithms and the source transformation utilizing the SSR. The

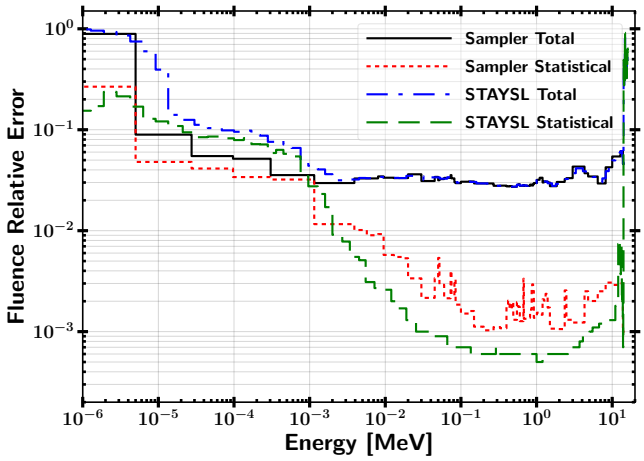

Figure 3.9. (Color online) Sampler neutron fluence uncertainty mapped to STAYSL bin structure.

Table 3.1. Activation foil results and HEU fissions predicted with bootstrapped nuclear data covariance uncertainty.

	MCNP SSR	SCALE MAVRIC CE		SCALE Sampler 252-Group	
Reaction	Reactions ± σ_{stat} [#]	Reactions ± σ_{stat} [#]	Percent Change Relative to MCNP	Reactions ± σ_{total} [#]	Percent Change Relative to MCNP
^{90}Zr(n,2n)^{89}Zr	1.89E+9 ± 2.5E+6	1.91E+9 ± 1.4E+6	1.5	2.06E+9 ± 9.6E+7	9.0
^{58}Ni(n,2n)^{57}Ni	1.87E+8 ± 2.4E+5	1.90E+8 ± 1.4E+5	1.4	2.21E+8 ± 1.1E+7	17.8
^{58}Ni(n,p)^{58}Co	6.54E+9 ± 5.2E+6	6.64E+9 ± 1.5E+5	1.5	6.66E+9 ± 1.7E+8	1.7
^{197}Au(n,2n)^{196}Au	2.91E+9 ± 3.8E+6	2.91E+9 ± 2.5E+6	-0.1	2.94E+9 ± 1.4E+8	1.0
^{197}Au(n,γ)^{198}Au	1.00E+9 ± 8.0E+5	1.02E+9 ± 1.5E+6	2.0	9.88E+8 ± 2.5E+7	-1.2
^{115}In(n,n')^{115}In^{m1}	3.81E+9 ± 1.9E+6	3.82E+9 ± 1.7E+6	0.0	3.85E+9 ± 9.0E+7	1.0
^{115}In(n,γ)^{116}In^{m1}	5.14E+9 ± 2.6E+6	5.19E+9 ± 4.4E+6	1.0	5.12E+9 ± 1.8E+8	-0.3
^{27}Al(n,a)^{24}Na	1.08E+9 ± 1.3E+6	1.08E+9 ± 7.7E+5	0.0	1.07E+9 ± 4.9E+7	-0.9
^{186}W(n,γ)^{187}W	7.21E+8 ± 7.2E+5	7.30E+8 ± 1.6E+6	1.2	7.08E+8 ± 2.9E+7	-1.9
^{55}Mn(n,γ) ^{56}Mn	3.14E+8 ± 3.1E+5	3.23E+8 ± 4.7E+5	2.8	2.67E+8 ± 5.3E+7	-14.9
^{235}U(n,f)	1.94E+9 ± 1.2E+6	1.96E+9 ± 8.2E+5	0.5	1.95E+9 ± 2.1E+7	0.0
^{238}U(n,f)	2.70E+7 ± 2.4E+4	2.67E+7 ± 1.6E+4	-1.1	2.70E+7 ± 4.6E+5	0.0
Total Fissions	1.99E+9 ± 1.2E+6	2.00E+9 ± 8.4E+5	0.5	1.99E+9 ± 2.1E+7	0.0

statistical uncertainty related to Monte Carlo based results is largely arbitrary as it can be driven to negligible values with sufficient computational resources. The observed differences between MCNP5 and SCALE Mavric for the reaction yields of channels of interest are consistent with previous observations reported in literature [77–79]. This result indicates that no significant bias was introduced that would impact the determination of systematic uncertainty from the nuclear data covariances.

The 252-group Sampler total reactions and fissions were similar to the MCNP5 and Mavric results, as quantified in Table 1. The differences relative to the MCNP results were consistent in comparison to literature with three main exceptions, ^{89}Zr, ^{57}Ni, and ^{56}Mn production. The primary reason for the difference is the non-optimal weighting functions for the generation of the multi-group cross sections described in Sections 3.4.2 and 3.4.5 and highlighted in [117]. The underestimation of the ^{89}Zr and ^{57}Ni production cross sections by the SCALE Sampler 252-group simulation results from the $1/E$ flux weighting of the 13.8 to 14.6 MeV group utilized. The 252 group ^{55}Mn reaction difference of -14.9% from MCNP was caused by the flux weighting used to create the group cross section, and the bulk of the difference occurs below 80 keV where a large resonance in ^{55}Mn(n,γ) is present.

The convergence of ^{56}Mn production, which was the largest uncertainty and least converged, is shown in Figure 3.10. In all cases, the bootstrapped mean value is within 1% of the unperturbed nuclear data starting sample. The mean should stay relatively constant as all data were sampled from a multivariate normal distribution.

The contribution to the total uncertainty from neutron transport, as manifested in the fluence uncertainty, and reaction cross section uncertainty is determined for the reactions that utilized the IRDFF nuclear data. Reactions that were completed solely in Sampler have this information convolved in the results and are not included in Table 3.2. Table 3.2 reflects the neutron fluence uncertainty and reaction cross section uncertainty contributions to the total uncertainty.

The uncertainties with only the transport uncertainty included are determined by running the post-processing script with and without sampling the reaction cross sections. The baseline case without sampling the reaction cross section reflects the uncertainty due to solely transport related uncertainties. Likewise, the transport uncertainty convolved with the reaction uncertainty are determined by including the

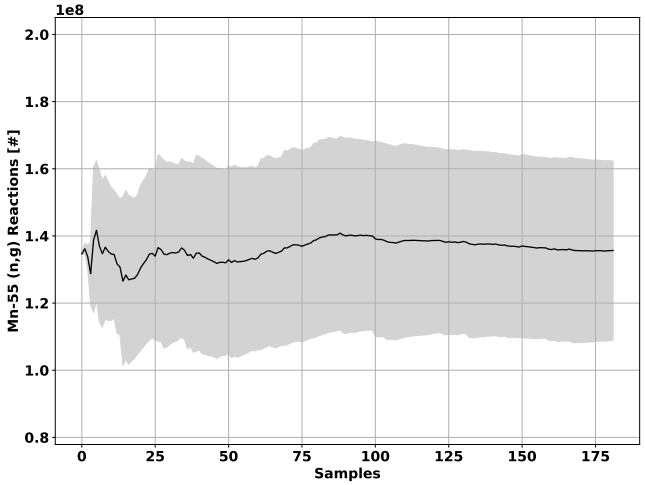

Figure 3.10. Cumulative moving average ^{56}Mn production vs sample number.

Table 3.2. Contributions to total uncertainty for activation reactions utilizing IRDFF nuclear data.

Reaction	Total Uncertainty [%]	Transport Uncertainty Contribution [%]	Reaction cross section Uncertainty Contribution [%]
^{90}Zr(n,2n)^{89}Zr	4.66	4.60	0.78
^{58}Ni(n,2n)^{57}Ni	4.76	4.57	1.34
^{58}Ni(n,p)^{58}Co	2.50	2.14	1.29
^{197}Au(n,2n)^{196}Au	4.84	4.63	1.42
^{115}In(n,n')^{115}In^{m1}	2.33	1.85	1.42
^{115}In(n,γ)^{116}In^{m1}	3.45	2.59	2.28
^{27}Al(n,a)^{24}Na	4.62	4.59	0.45

reaction perturbation. The reaction uncertainty is determined by adding the transport uncertainty and reaction cross section uncertainty in quadrature based on the relative errors. The uncertainty contributions are dominated by the fluence uncertainty as expected since the reactions were chosen for low uncertainty over the activation range. The fluence uncertainty was within 0.2% for all high energy threshold reactions covering the TN portion of the spectrum, which is caused by all

four reactions having a very similar functional form and energy coverage. In general, non-threshold reactions experienced lower transport uncertainty because the reaction occurs over all energy ranges which reduces volatility in the integral reaction mechanism. The uncertainty in the continuous energy solution can be directly inferred from the multi-group approach with the knowledge of the uncertainty having some variability based on the group structure.

3.6 Conclusions and Future Work

Nuclear data covariance analysis of radiation transport simulations is an important technique that would be beneficial to perform for all nuclear related experiments. Quantifying uncertainties is useful for the design of experiments and understanding where basic research is necessary. The vast majority of radiation transport simulations stop at Monte Carlo statistical uncertainty; however, nuclear data covariances play a large role in Monte Carlo simulations. This work quantified the nuclear data covariance utilizing the SCALE Sampler module with additional post-processing to incorporate the integral reaction uncertainty with the IRDFF v.1.05 library.

A major objective of the example problem was to determine the expected experimental outcomes and the neutron fluence energy spectrum to use in an unfolding technique to validate the neutron fluence environment post-experiment. The ETA fluence uncertainty from 1.28 keV to 14.1 MeV ranged from 2.7 to 6.2%. At lower energies, the statistical uncertainty contribution at 1.28 keV was 1.1% and increased to 26.7% at 5 eV. The neutron fluence uncertainty, shown in Figure 3.9, decreases the ability to accurately predict the neutron energy spectrum to use as a starting spectrum for unfolding techniques. Using the nominal neutron fluence energy spectrum with nuclear data uncertainty and uncertainty bounds calculated

with Sampler enables a higher fidelity neutron flux unfolding input.

Additionally, the variance in the neutron energy spectrum in combination with uncertainty in the activation cross section have a direct relationship with the uncertainty in the activation foil activities. The activation foil reactions in Table 3.1 provide an assessment of the range of possibilities for the experimental foil activities. The resultant reaction products had integrated uncertainties as low as one percent to tens of percent. Nuclear data uncertainties in the neutron transport were generally the largest contribution to the integral activation uncertainty. The activation foils were chosen based on confidence in the underlying nuclear data, so the activation foil reaction cross section uncertainty was not the largest component in any of the activation foil results. The ETA contains non-traditional materials, so it was not suprising that the transport was largest source of uncertainty.

These results highlighted radiation transport, statistical, and reaction cross section as three major contributors to uncertainty of a radiation transport simulation. In a well controlled experiment, nuclear data may be the dominant uncertainty. It is important to capture as much of the uncertainty as possible to have the ability to predict the results of an experiment. The detail and confidence in the nuclear data are essential for the ETA, as for most nuclear related experiments, so it is important to capture the nuclear data piece in the analysis.

The ETA experiment is planned for late 2019. Future work related to the analysis performed here will compare the experimental outcomes to the predicted reactions and create a verification of the nuclear data covariance analysis technique utilized. The methodology presented can be directly applied to derive uncertainty bounds for other nuclear engineering problems utilizing any nuclear data library available.

3.7 Acknowledgment

This research was supported in part by the U.S. Air Force Technical Application Center (AFTAC) under the AFIT/AFTAC Endowed Term Chair MOA#: 212196 and the Defense Threat Reduction Agency under grant HDTRA-18-27434. Oak Ridge and Lawrence Livermore National Laboratory's support was invaluable for the completion of the Sampler and MCNP5 NIF model runs performed, respectively.

IV. ETA Analysis

This chapter was derived from a paper published in March 2020 with *Journal of Radiation Effects Research and Engineering* titled "Analysis of an Energy Tuning Assembly for Simulating Nuclear Weapon Environments at the National Ignition Facility [130]." The author list included Nicholas J. Quartemont and James E. Bevins, Rachel Slaybaugh, and Lee Bernstein. The article has been modified to fit this dissertation format; however, the content was unchanged.

This work provided the foundation for analyzing an ETA from a modeling perspective to predict observables such as activation and fission products. The modeling methodology includes Monte Carlo radiation transport simulations, neutron flux unfolding, and fission product estimation techniques. An important note that was updated in future chapters was that the radiation transport simulation was performed with a surface source, meaning that the source neutrons were transported up to a geometry near the problem area. Although the mean value of the responses modeled was unaffected, the nuclear data covariance up to this point was not included in the simulations here. The results presented here highlight the expected results from the ETA experiment provided in Chapter 5.

4.1 Abstract

An energy tuning assembly was developed to spectrally shape the National Ignition Facility deuterium-tritium fusion neutron source to a notional thermonuclear and prompt fission neutron spectrum. The spectrally-shaped neutron environment can be used to create synthetic post-detonation relevant weapon debris that contain spectrally accurate fission products across all mass chains to enhance U.S. technical nuclear forensic capabilities for nuclear weapon attribution and device

reconstruction. This research performed nuclear data covariance analysis through stochastic sampling techniques to predict the performance of an energy tuning assembly to create the objective thermonuclear and prompt fission neutron spectrum, assess anticipated experimental outcomes, and determine the expected fission products to be produced in a highly enriched uranium foil in the sample cavity. It was found that the nuclear data covariance affected the neutron fluence energy distribution by less than 5 percent for neutron energies above 1 keV in the sample region. The foil activation resulting from the perturbed fluence distribution was found to generally vary on the order of 3-5% but was as high as 20%. The range of foil activation outcomes was used to show that neutron flux unfolding techniques provided broad spectral agreement between the energy tuning assembly and objective spectrum and resulted in an 80+% probability of successful unfolding using STAYSL given the range of expected foil activities. This energy distribution was achieved at a total fluence of 4.9×10^{11} n cm^{-2} $\pm$ 1.4% in a 10 shake neutron pulse. More than 1 billion fissions, approximately of the order collected in nuclear forensics ground samples, were generated with a cumulative fission product distribution that matched the objective within current predictive capabilities. The analysis performed in this research enables the development of a NIF validation experiment, enhances confidence in the experimental outcomes, and further develops a unique capability for the nuclear security community.

4.2 Introduction

Generating neutron environments has broad application to the nuclear forensics, medical, national security, and nuclear data communities [34, 131, 132]. The neutron energy spectrum is important for many applications such as the survivability of electronics in strategic environments, and deviations from the threat environment

for testing has many implications for the certification of nuclear components [133]. Additionally, accurate neutron energy distributions are critical to the production of accurate fission product samples that have a direct impact on the deterrence of potential nuclear terrorism through the development and improvement of nuclear attribution capabilities [1]. However, no capability exists to replicate nuclear weapon neutron environments in the absence of full-scale testing [11]. Alternative methods of creating fission product debris have been explored to include sample doping, direct production using fission converters, or surrogate methods [4]. Each of these methods are limited in their ability to correctly reproduce the expected fission product distribution resulting from the neutron environment experienced in a nuclear weapon.

An alternative approach is to develop a neutron energy spectrum representative of an objective neutron energy spectrum. This can be accomplished through targeted modification of a source neutron energy distribution, a non-trivial process for neutrons. To automate the process for designing energy tuning assemblies (ETAs), the Coeus metaheuristic optimization software package was developed to convert a facility's characteristic source spectrum to an user-defined objective spectrum [35, 134]. Coeus enables fast and accurate design of ETAs to spectrally shape a given neutron spectrum into a desired neutron environment. As an example, the generation of a notional thermonuclear and prompt fission neutron spectrum was chosen to be used for the production of realistic fission debris. Coeus was used to develop an ETA with the objective spectrum to produce accurate fission products to advance the technical nuclear forsenics field. The ETA is planned for a proof of concept experiment at National Ignition Facility (NIF).

Initial validation of the spectral shaping and ETA concept were performed at the 88-Inch cyclotron at Lawrence Berkeley National Laboratory. While this experiment

demonstrated the concept, the 88-Inch cyclotron source spectrum differed significantly from the NIF. This differing energy range covered nuclear data and reactions not applicable with the NIF D-T source and changed the relative weighting of the reaction channels important to the resulting neutron spectrum [36]. This is important because the spectral shaping concept breaks from traditional integral nuclear validation efforts in that the measurable outcomes are heavily dominated by specific reaction channels that vary based on material position in the ETA [135]. As such, while the 88-Inch provided the first validation of the concept, it provided little direct evidence of the performance of the ETA at the NIF. This is further compounded by the use of non-traditional nuclear materials in the ETA design, where the nuclear data quality may be poor. Therefore, this work sought to characterize the nuclear data uncertainty and its effect on the experimental observables of the ETA to better assess the performance of the system.

Unfortunately, quantifying the impact of nuclear data on complex systems with multiple observable signatures of interest is a non-trivial problem. Variance in the nuclear data affects the neutron transport simulation and the resulting modified neutron spectrum obtained after the source spectrum is modified through nuclear reactions. The resulting variance in the obtained neutron spectrum is then propagated to the observable reaction rates in the sample region inside of ETA. This analysis incorporated nuclear data covariance into the simulated results through stochastic sampling of the underlying nuclear data to build a distribution of responses [97]. The cross section libraries used in this work were ENDF/B-VII.1 for the neutron transport and the IRDFF v.1.05 library for foil activation cross sections [46, 48].

Previous work completed the design of an ETA for the production of spectrally accurate fission product generation, initial experimental validation, and techniques

to quantify the effect of nuclear data covariance [36, 38, 97]. The objective of this work is to model the ETA capability to tailor the NIF neutron energy spectrum and generate fission products for technical nuclear forensics applications, including reporting progress since previous work.

This paper is organized as follows. First, the problem description of the ETA and design are provided. The next section provides the methodology for the main components of this research, including the Monte Carlo simulation, neutron fluence unfolding, and fission product estimation. Next, the results of the neutron transport calculation, unfolded spectrum, and fission product distributions are provided. Finally, the last section summarizes the major findings and provides a path forward for future work.

4.3 Model Description

The objective spectrum chosen for the production of synthetic weapon fission product debris was a thermonuclear and prompt fission neutron spectrum (TN+PFNS), relevant to production of synthetic nuclear weapon fission product debris. The representative neutron spectrum was produced with MCNP6.1 using transport in a bare Godiva sphere of a Watt fission spectrum and a 14.1 MeV source to model the deuterium-tritium (D-T) fusion neutrons [4, 47]. For the purposes of this study, several fission isotope yields of interest are selected from the wings, valley, and peaks of fission product distribution for ^{235}U. Each fission product has energy-dependent data in the literature [46, 51, 136–143].

The source selected was a NIF D-T Polar Drive Exploding Pusher (PDXP) target with a nominal yield of 3.7×10^{15} neutrons from laser driven inertial confinement fusion [112]. The D-T fusion produces 14 MeV energy neutrons that fill in the thermonuclear component of the objective spectrum, and the prompt fission

portion is built-up with neutron interactions in the ETA. The prompt nature of the irradiation negates decay and in-growth errors associated with long irradiation times.

The ETA produced with Coeus to meet the objective notional TN+PNFS is shown in Fig 4.1 [4]. The NIF source was located 15 centimeters below the base of the cone. The ETA was constructed with cones and cylinders using materials of boron carbide, praseodymium, stainless steel, and pure elements of bismuth, tungsten, silicon, stainless steel, and lead. The external portions of ETA and surroundings were filled with vacuum pressure nitrogen below 10^{-4} torr [144]. The ETA sample cavity, labeled 6 in Fig 4.1., was encased in a lead-filled removable drawer, labeled 8 in Fig 4.1., for rapid sample extraction post-irradiation. The ETA was modeled with the drawer facing up, so that the direction of gravity skewed the mass distribution away from the drawer insert.

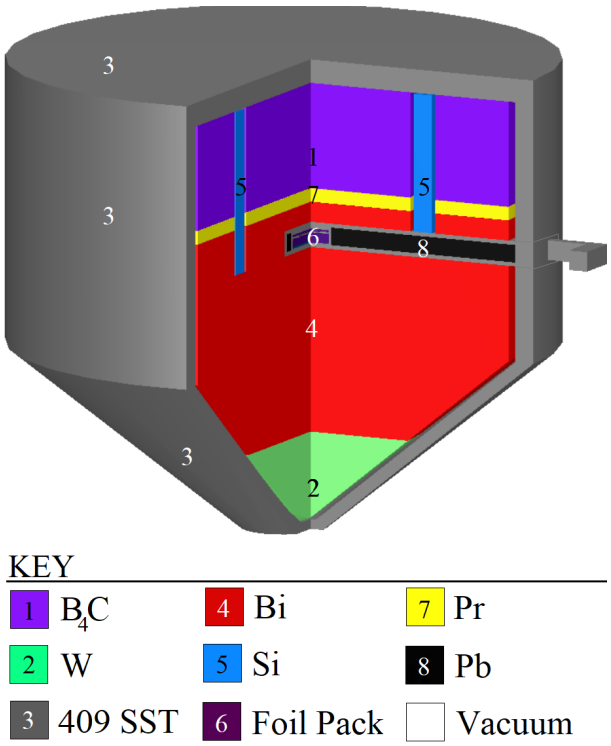

Figure 4.1. ETA produced by Coeus to reproduce an objective notional TN+PFNS [4].

The ETA sample cavity is designed to hold several activation foils and a highly enriched uranium (HEU) sample in a Target Option Activation Device (TOAD). The foils chosen were natural indium, aluminum, nickel, zirconium, gold, tungsten, and manganese. These foils have threshold and non-threshold reactions that span the range of interest from the TN+PFNS energy spectrum, which can be used to unfold the incident neutron energy spectrum to validate the ETA performance [80, 82]. The HEU sample is enriched to 93.15% and is the source of the fission products.

A summary of the foil characteristics for the reactions chosen for the simulated NIF experiment are shown in Table 4.1. The Zr, Ni, In, Al, W, and Mn foils were all 1 mm in thickness and 2.5 cm in radius. The foils were selected to cover threshold energy reaction channels and thermal reactions which inform lower energy neutron flux environments. The Au foil was 0.0254 mm thick with a radius of 2.004 cm. The HEU foil not shown was 2.004 cm in radius and 0.0508 mm in thickness.

Table 4.1. Selected activation foil information for simulated NIF experiment.

Reaction	Threshold [MeV] (@ 10 mb)	Decay Radiation [keV] (Intensity)
^{90}Zr(n,2n)	12.1 (12.1)	909.2 (0.9904)
^{58}Ni(n,2n)	12.4 (13.3)	1,378 (0.817)
^{58}Ni(n,p)	0.4 (1.3)	810.8 (0.9945)
^{197}Au(n,2n)	8.1 (8.3)	355.7 (0.87)
^{197}Au(n,g)	Thermal	411.8 (0.9562)
^{115}In(n,n')	0.336 (0.597)	336.24 (0.459)
^{115}In(n,g)	Thermal	1293.56 (0.848)
^{27}Al(n,a)	3.25 (6.7)	1368.63 (0.9999)
^{186}W(n,g)	Thermal	685.51 (0.332)
^{55}Mn(n,g)	Thermal	846.8 (0.9885)

4.4 Description of Work

This section describes the overarching methodology for the radiation transport simulation and the quantification of nuclear data uncertainty. Additionally, the technique used to unfold the neutron fluence from the modeled activation foil activities is presented. Finally, two methods for predicting fission products are outlined.

4.4.1 Neutron Transport Simulations.

The simulation methodology to propagate nuclear data covariance through the ETA design included neutron transport calculations in MCNP5 and the Standardized Computer-Analysis for Licensing Evaluation (SCALE) code package [44, 45]. Additional systematic uncertainties due to materials and geometry were limited through the use of 99.5+% pure components and sub-mm machining tolerances on each component in the constructed ETA. MCNP5 was used for continuous energy Monte Carlo neutron transport, which was used to benchmark continuous energy Monte Carlo neutron transport in SCALE MAVRIC. The SCALE MAVRIC sequence was utilized for Monte Carlo radiation transport in continuous energy to validate the model to MCNP and also used in a 252 energy group structure with the SCALE Sampler module to assess the effect of nuclear data covariance [45]. Finally, the activation foil uncertainties were sampled with a multivariate normal distribution to incorporate the reaction cross section uncertainty consistent with the IRDFF v.1.05 nuclear data library [48, 97].

The SCALE Sampler module enabled analysis of nuclear data covariance through pre-built libraries based on stochastic sampling of the nuclear data and was distributed with a 252 and 56 energy group structure [45]. The covariance libraries were largely developed from ENDF/B-VII.1; however, additional information was

been included from collaborative research between Brookhaven National Laboratory, Los Alamos National Laboratory, and Oak Ridge National Laboratory. Additionally, the nuclear data covariance libraries include information completed in the Working Party on International Nuclear Data Evaluation Cooperation Subgroup-26 [45]. The impact of nuclear data covariance was addressed for the neutron energy spectrum, foil activation rates, and fission product production rates. The output from Sampler was used with the IRDFF covariance matricies to generate final response metrics with systematic uncertainty from the radiation transport and reaction cross sections [97]. The IRDFF library contains benchmarked neutron dosimetry reactions and "state-of-the-art" covariance information [52].

A validated full-scale NIF model did not exist for the SCALE package, but significant development and validation of the full NIF model has been performed in MCNP5 [44]. As such, the ETA was modeled in MCNP5 with a surface source read (SSR) file generated using a 14.03 MeV neutron point source, which is the zero ion-temperature mean energy [145]. NIF neutron emissions are extremely short duration, on the order of 300 picoseconds, so the neutrons were modeled as all being generated at the same time [112]. The SSR source included a full system model of NIF that included the target positioner, ETA, ETA diagnostic instrument manipulator (DIM), snout DIM, and target chamber support structures. The SSR file reads in a formatted file that contains all of the particle histories that cross defined surfaces, thereby allowing for accelerated transport in regions of interest [44, 119]. This allowed the Sampler models to capture the impact of room return without requiring the creation of a full NIF model in SCALE.

The SSR file surfaces used were two disks at the front and back of the ETA and a connecting cylinder surrounding the ETA. The SSR generated in MCNP was

mapped to probability distribution functions with relative strengths for each primary surface. The surface neutron current distributions at the front (source facing), back, and cylindrical surfaces are shown in Figure 4.2. The back and cylindrical surfaces solely represented the room return, while the front source was dominated by source neutrons. The total fluence of neutrons through the front, back, and cylindrical surfaces were 6.5×10^{14}, 3.5×10^{12}, and 2.4×10^{12} neutrons, respectively.

The neutron current on the SSR surfaces in MCNP5 was mapped to SCALE for use in MAVRIC and Sampler by source definitions to approximate the behavior of MCNP's surface source. The front source was modeled as a point source at the location of the PDXP target. The point source strength was 3.72×10^{15} neutrons, which included the room return component, based on the solid angle between the front surface and the point source. Cylindrical neutron sources could not be adapted to Cartesian coordinate direction vectors, so the cylindrical SSR surface was approximated. The back source was modeled as a disk, and the cylinder was approximated as four line sources placed symmetrically at the same distance from the ETA as the original SSR cylindrical source facing the ETA and emitting in 2π.

The MCNP5 model was compared to the continuous energy MAVRIC sequence to benchmark the sources used for MAVRIC and the 252 group Sampler values. The resultant model for the continuous energy SCALE MAVRIC sequence was converted to the 252 group SCALE Sampler sequence, where the nuclear data covariance was assessed. The 252 group structure was built for nuclear reactor applications, which is non-ideal for this application and resulted in some discrepancies near bin boundaries [97]. However, the 252 group was the best nuclear data covariance library available for SCALE Sampler at the time of this research. The Sampler values were collapsed at lower energy to create a 66 group structure.

The results of each of the models were used to assess the foil reactions and HEU

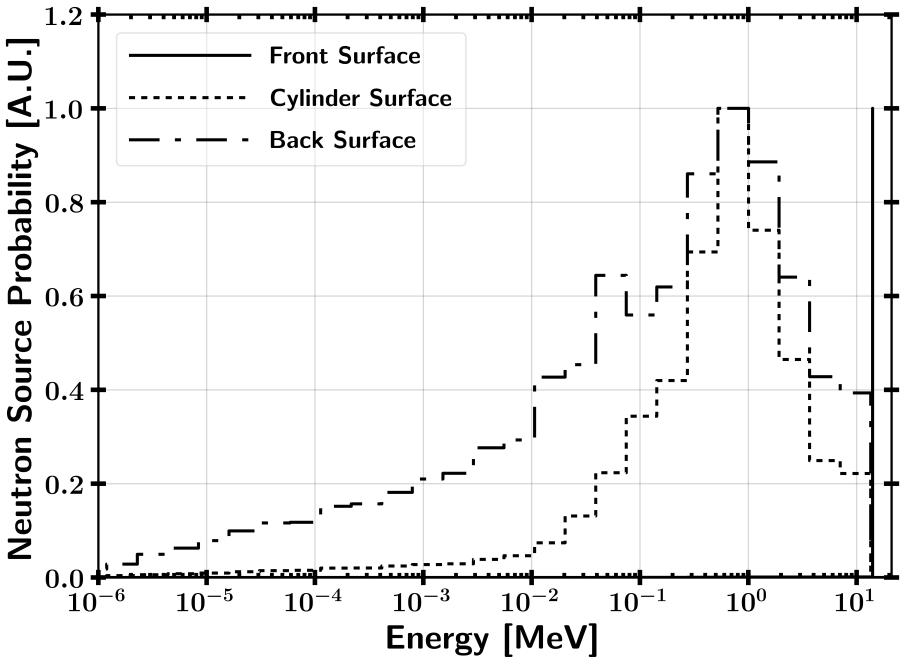

Figure 4.2. Surfaces source probability distribution functions generated from the MCNP SSR for use in SCALE. The distributions were normalized to a peak value of 1.

fissions achieved in the ETA platform. Since the total neutron fluence time is much less than the half-lives of the fission and activation products for the foils, this removes any uncertainty from in-growth and decay during the experiment. The resultant responses were combined using statistical bootstrapping, where confidence bounds were determined by randomly selecting with replacement data from the sampled distributions to create a probability distribution representative of the underlying distribution [113].

Sampler was used to generate 182 trials to provide converged results for all of the activation foil reactions, HEU fissions, and neutron fluence, including the post-processing perturbations with the IRDFF nuclear data covariance. The convergence of ^{56}Mn production, which contained the largest uncertainty and was least converged so represents the worst-case performance, is shown in Figure 4.3. In all cases, the bootstrapped mean value was within 1% of the unperturbed nuclear

data starting sample. The response values from Sampler and MCNP5 for the activation foil reactions, neutron fluence, and HEU fissions were determined with the continuous energy values from MCNP5 and the uncertainty bounds given by the quadrature addition of the MCNP5 statistical error and Sampler systematic error attributed to nuclear data covariance.

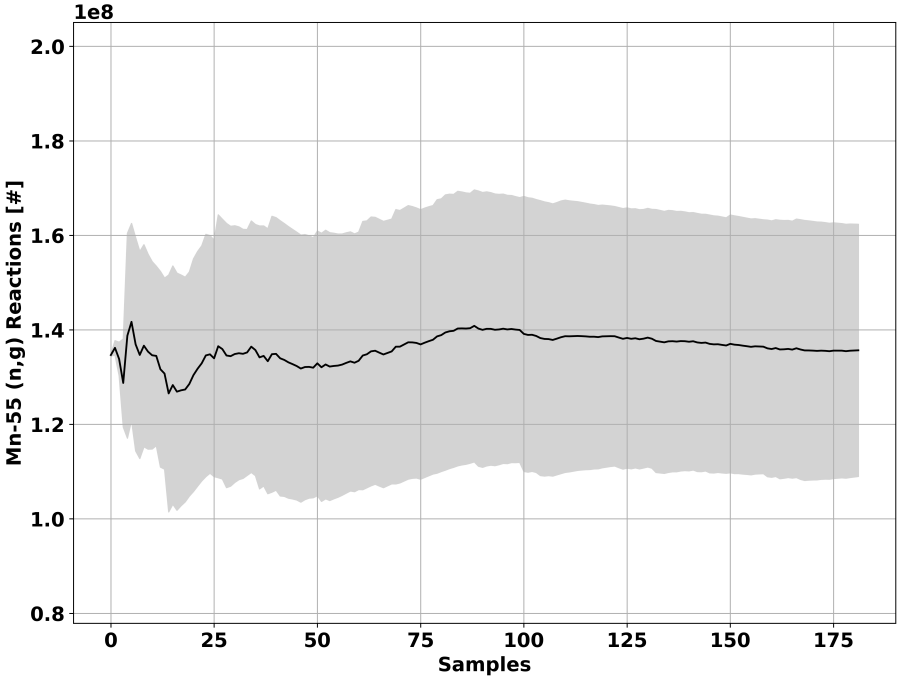

Figure 4.3. Cumulative moving average ^{56}Mn production vs sample number with starting value shown as the black solid horizontal line.

Finally, the reaction results from Sampler were again sampled with a multivariate normal distribution to perturb the data consistent with the IRDFF v.1.05 library [97]. The user defined responses used in Sampler were not modified in the Monte Carlo simulations, so the uncertainty in the foil reaction cross sections needed to be taken into account in post-processing due to limitations in SCALE. ENDF data were utilized for ^{55}Mn(n,g), ^{186}W(n,g), and U(n,f) because it was consistent with IRDFF [46, 48]. The reaction cross section was modified in the execution of Sampler for these 3 reactions sets and required no subsequent post-processing [46].

4.4.2 Neutron Spectra Statistical Tests.

The results of the Monte Carlo simulations were compared to the TN+PFNS though the Pearson correlation coefficient and the Kolmogorov-Smirnov (K-S) statistic. The Pearson correlation coefficient provides a measure of the linear relationship between two sets of data and is often used for comparative signal analysis. The formula for the Pearson correlation coefficient is given as a function of "n" data points for two distributions defined by points x_i and y_i as

$$r = \frac{n\sum x_i y_i - (\sum x_i \sum y_i)}{\sqrt{n\sum x_i^2 - (\sum x_i)^2}\sqrt{n\sum y_i^2 - (\sum y_i)^2}}. \tag{4.1}$$

The null hypothesis of the Pearson correlation coefficient is that there is no correlation between the two datasets. The p-value indicates the probability of an uncorrelated system producing a correlation coefficient at least as large in magnitude. Small p-values (<0.05) indicate a statistically significant Pearson correlation coefficient.

The K-S two-sample statistic compares the cumulative distribution functions (CDF) between two sets of data. The K-S statistic provides information on the relative magnitude of the distributions, so it is useful in combination with the Pearson correlation coefficient to quantify the similarity between two distributions. The K-S statistic is given as a function of the supremum (maximum) difference between the expected and observed CDF as shown in (4.2). The null hypothesis for this test is that the two samples were drawn from the same distribution. Unlike the Pearson Correlation Coefficient, a large p-value (> 0.05) from the K-S statistic fails to reject the null hypothesis.

$$D = \sup_x \mid CDF_{exp}(x) - CDF_{obs}(x) \mid \tag{4.2}$$

4.4.3 Neutron Fluence Unfolding.

The modeled foil activities were used with the underlying IRDFF nuclear data to unfold the neutron spectrum using STAYSL [110]. STAYSL determines the incident neutron flux using a generalized least-squares spectral adjustment based on a χ^2 comparison of the measured activities and the activities calculated from an adjusted flux [52]. STAYSL utilizes activity information, A°, a neutron flux, a nuclear data matrix, P, and covariance matrices in the formulation of the χ^2 statistic. The χ^2 is minimized based on the STAYSL minimized activity information, $\bar{A}$, and the STAYSL calculated neutron flux convolved with the IRDFF nuclear data parameters, $\bar{P}$. The χ^2 statistic utilized in STAYSL is given by [84];

$$\chi^2 = \begin{bmatrix} P - \bar{P} \\ A^\circ - \bar{A} \end{bmatrix}^\dagger \bullet \begin{bmatrix} N_P & 0 \\ 0 & N_{A^\circ} \end{bmatrix}^{-1} \bullet \begin{bmatrix} P - \bar{P} \\ A^\circ - \bar{A} \end{bmatrix} \tag{4.3}$$

where N_P is the covariance matrix from the flux and nuclear data and N_{A° is the activity covariance matrix. For this work, the 129 group IRDFF v.1.05 library was used, which is ideal for dosimetry applications for the range of energies considered in this work [48].

The activities produced for a given set of foils are often degenerate, where an infinite number of spectra could provide the same distribution of measured activities. To overcome this, STAYSL requires an initial guess neutron spectrum to introduce a Bayesian prior, allowing for physics and modeling to guide the overall solution space. The initial guess spectrum used for STAYSL was the nominal MCNP-calculated neutron fluence in the HEU foil, and the specified uncertainty includes both the statistical and systematic nuclear data uncertainty.

The reduced chi-squared statistic, χ^2, was used to interpret the unfolded neutron flux agreement with the set of results from Sampler. The reduced χ^2, as used in the

foil activation neutron flux unfolding, is [146]

$$\frac{\chi^2}{\nu} = \frac{1}{\nu}\sum_{i=1}^{N}(\frac{R_{Trial} - R_{STAYSL}}{\sigma_{rxn}})^2, \tag{4.4}$$

where the degrees of freedom, ν, are the number of activation foil reactions, N, minus one, σ_{rxn} is the modeled systematic and statistical uncertainty, R_{STAYSL} is the unfolded STAYSL activation foil activity, and R_{Trial} is the Sampler trial foil activity.

The null hypothesis for the χ^2 statistic is that the two sets of data are governed by the expected distribution, and the test of independence shows the probability of rejecting this null hypothesis. The p-value, the probability of finding a larger χ^2/ν given the calculated result, can be used to compare the results of the expected distribution to the calculated χ^2/ν. A small p-value (<0.05) signifies there is a strong significance level for the results not being governed by the expected distribution. P-values above the cutoff significance level fail to reject the null-hypothesis.

4.4.4 Fission Product Estimation.

The energy spectrum of neutrons causing fission was used to determine the fission product yield with a phenomenological fit and the General Description of Fission Observables (GEF) code [50]. The distribution of neutrons causing fission is proportional to the fission cross section times the neutron flux. Including fits to experimental data enables better energy resolution and predictions that are consistent with observed experiments where experimental data exists, while GEF enables predictions for mass chains lacking sufficient energy-dependent data. Empirical relations developed by Nagy *et al.* provide an approach to predict the fission product yield as a function of energy given sufficient yield measurement data [51]. Nagy fits the fission product experimental data to the exponential equation

$$Y(E_n) = Y_0 e^{bE_n}, \tag{4.5}$$

where the fitting parameters b and Y_0 represent the slope of the function in logarithmic form and thermal fission yield, respectively [51]. The slope is the primary measure of the energy dependence of the fission product yield, which requires modifications for multi-chance fission. Modifications were performed to incorporate first and second chance fission, which are the most dominant modes up to 14.1 MeV. First chance fission is dominant from up to 5.5 MeV, and second-chance fission up to 14.1 MeV [51]. Multi-chance fission effects on the fission product yield are less pronounced in asymmetric regions but can have a large impact in symmetric fission ($109 \leq A \leq 129$) [4, 51].

GEF is applicable over a wide range of fissioning systems, including isotopes with atomic numbers from 80 to 112 [50]. The underlying model has been shown to have good predictive power, albeit with relatively large uncertainties due to GEF containing up to 50 free parameters used for the potential energy surfaces of the fission barrier of the fissioning system, fission theory, and adjustments based on empirical parameters [50,59]. GEF incorporates covariance information of the fissioning system, multi-chance fission, and many other unique features.

The values for the mass chain yield distribution calculated by GEF were determined using separate calculations for each energy group defined by the midpoint bin energy of the fissioning system, ^{236}U for neutron induced ^{235}U fission. The uncertainty reported includes a combination of the GEF Monte Carlo statistical and systematic uncertainty and the systematic uncertainty from the Sampler results for the fissioning neutron energy distribution.

4.5 Results

Using the methodology outlined above, the ETA was simulated to determine the impact of nuclear data on the overall performance and experimental observables. First, the results of the neutron transport are presented including the overall ETA fluence distribution, the foil activation, and the timing profile. Next, the results of the modeled neutron flux unfoldings are provided for each of the trials completed in Sampler. Last, the predicted fission product distribution for selected cumulative yield fission products and the mass chain fission product yield for the ETA neutron spectrum produced fissions are presented.

4.5.1 Neutron Transport Results.

A summary of the activation foil reactions and fissions in the HEU foil are given in Table 4.2. A bias of approximately 1% was observed for the reaction rates from the continuous energy MAVRIC simulation, a result consistent with previous code comparison results [77–79]. However, there were some important discrepancies that are caused by the 252 group structure. The 252 group Sampler mean total reactions were generally in agreement with the continuous energy solutions with three exceptions: ^{89}Zr, ^{57}Ni, and ^{56}Mn. The first two threshold reactions were attributed directly to the flux weighting of the 13.8 to 14.6 MeV group used in the energy region where the reaction occurred. The 252 group ^{55}Mn reaction difference from MCNP was caused by the flux weighting used to create the group cross section, and the bulk of the difference occurs below 80 keV. The 252 group library performed well for the majority of the reactions because many of the activation reactions are saturated by the PFNS, which was used to generate the cross section weighting for the intended nuclear reactor applications of this group structure.

The continuous energy solutions in Table 3.1, MCNP SSR and SCALE MAVRIC

Table 4.2. Activation foil reaction results and HEU fissions modeled results from MCNP5, SCALE MAVRIC, and SCALE Sampler.

	MCNP SSR	SCALE MAVRIC CE		SCALE Sampler 252-Group	
Reaction	Reactions [#]	Reactions [#]	Percent Change Relative to MCNP	Reactions [#]	Percent Change Relative to MCNP
^{90}Zr(n,2n)^{89}Zr	1.89E+9 ± 2.5E+6	1.91E+9 ± 1.4E+6	1.5	2.06E+9 ± 9.6E+7	9.0
^{58}Ni(n,2n)^{57}Ni	1.87E+8 ± 2.4E+5	1.90E+8 ± 1.4E+5	1.4	2.21E+8 ± 1.1E+7	17.8
^{58}Ni(n,p)^{58}Co	6.54E+9 ± 5.2E+6	6.64E+9 ± 1.5E+5	1.5	6.66E+9 ± 1.7E+8	1.7
^{197}Au(n,2n)^{196}Au	2.91E+9 ± 3.8E+6	2.91E+9 ± 2.5E+6	-0.1	2.94E+9 ± 1.4E+8	1.0
^{197}Au(n,g)^{198}Au	1.00E+9 ± 8.0E+5	1.02E+9 ± 1.5E+6	2.0	9.88E+8 ± 2.5E+7	-1.2
^{115}In(n,n')^{115}In^{m1}	3.81E+9 ± 1.9E+6	3.82E+9 ± 1.7E+6	0.0	3.85E+9 ± 9.0E+7	1.0
^{115}In(n,g)^{116}In^{m1}	5.14E+9 ± 2.6E+6	5.19E+9 ± 4.4E+6	1.0	5.12E+9 ± 1.8E+8	-0.3
^{27}Al(n,a)^{24}Na	1.08E+9 ± 1.3E+6	1.08E+9 ± 7.7E+5	0.0	1.07E+9 ± 4.9E+7	-0.9
^{186}W(n,g)^{187}W	7.21E+8 ± 7.2E+5	7.30E+8 ± 1.6E+6	1.2	7.08E+8 ± 2.9E+7	-1.9
^{55}Mn(n,g)^{56}Mn	3.14E+8 ± 3.1E+5	3.23E+8 ± 4.7E+5	2.8	2.67E+8 ± 5.3E+7	-14.9
^{235}U(n,f)	1.94E+9 ± 1.2E+6	1.96E+9 ± 8.2E+5	0.5	1.95E+9 ± 2.1E+7	0.0
^{238}U(n,f)	2.70E+7 ± 2.4E+4	2.67E+7 ± 1.6E+4	-1.1	2.70E+7 ± 4.6E+5	0.0
Total Fissions	1.99E+9 ± 1.2E+6	2.00E+9 ± 8.4E+5	0.5	1.99E+9 ± 2.1E+7	0.0

continuous energy (CE), only capture statistical uncertainty in their results. The 252 group SCALE Sampler results capture statistical and bootstrapped systematic nuclear data uncertainty from the Sampler results. As can be seen, the systematic nuclear data uncertainty greatly exceeds the contribution of the statistical uncertainty to the overall uncertainty of the simulated results. Inclusion of nuclear data uncertainty results in relative errors less than 5% for most reactions; however, ^{56}Mn production has a relative error of 19.7%.

The neutron fluence results of the continuous energy MCNP5 and SCALE MAVRIC sequence in comparison to the notional objective TN+PFNS are shown in Fig 4.4. Overall, there is broad neutron spectral agreement between the TN+PFNS and ETA fluence and between MCNP5 and SCALE. Comparing the nominal values, there are a few main areas of disagreement between the ETA result and TN+PFNS. First, below 50 keV, there is an increase in thermal neutrons in the ETA simulations relative to the objective spectrum; however, this portion of the spectrum only represents ∼1% of the ETA fluence. The NIF room return and low-A spectral shaping components, necessitated by NIF weight constraints used in the design,

contribute to the majority of this fluence. Additionally, from 7 to 14 MeV there are relatively large differences caused by the method used to generate the TN+PFNS. Godiva, composed solely of HEU, has very few pathways to populate this energy region. The primary energy loss mechanisms in Godiva, inelastic scattering and (n,xn) reactions, are limited in their ability to populate the 7 to 14 MeV energy range, and there would need to be many elastic scattering events to populate this energy range from the 14 MeV fusion source given the high-A of the Godiva assembly. The 14 MeV region disagreement is caused by the lack of attenuation of the source neutrons; the weight constraints of the ETA design for the NIF facility meant that additional attenuating material could not be added. Further, above 14 MeV there is a severely depressed neutron flux in the ETA. A portion of this disagreement was caused by the mono-energetic source implementation instead of a more realistic ion temperature broadened distribution, which was chosen for consistency with previous NIF MCNP modeling work [145].

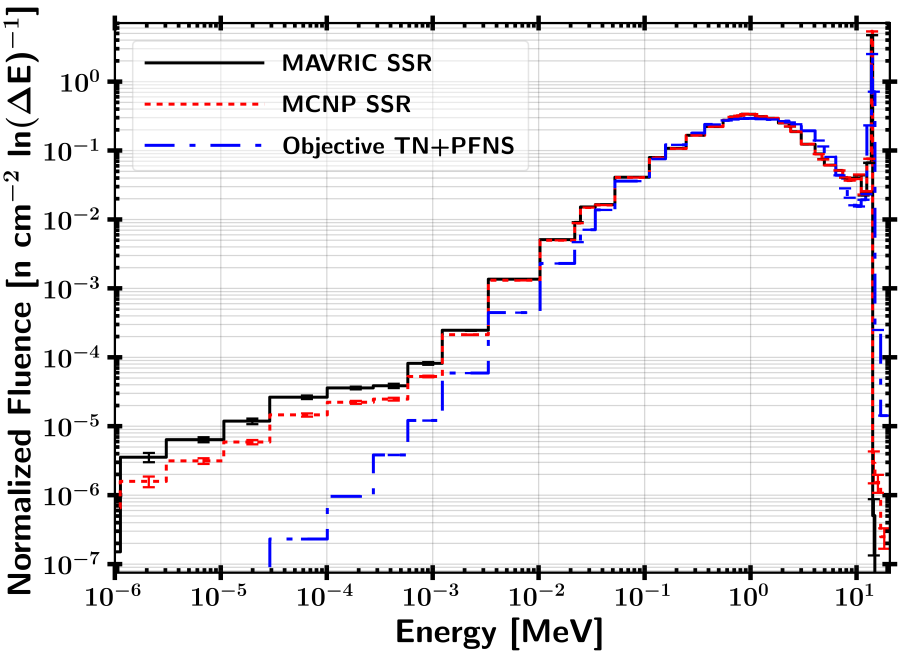

Figure 4.4. Normalized continuous energy MCNP5 SSR and SCALE mapped SSR fluence per unit lethargy spectra comparison to objective TN+PFNS.

The results of the nuclear data covariance fluence spectra are shown in Fig 4.5. The SCALE results were calculated with the 252 group structure and 182 samples from Sampler, while the MCNP5 results were performed with a continuous energy calculation using mapped systematic nuclear data uncertainties from Sampler. The nuclear data covariance increases the flux uncertainty more significantly at lower energies where the transport is dominated by a cascade of multiple reactions. In general, the mean of the flux accounting for nuclear data covariance with Sampler is comparable to flux with the nominal nuclear data. Most of the difference in the mean value is due to differences in the underlying codes, as shown in Fig 4.4, not due to a shift induced by the distribution of the nuclear data covariance captured in the Sampler results. Including the nuclear data covariance increases the range of potential values, approximately 3-5% above 1 keV and 7-100% below 1 keV.

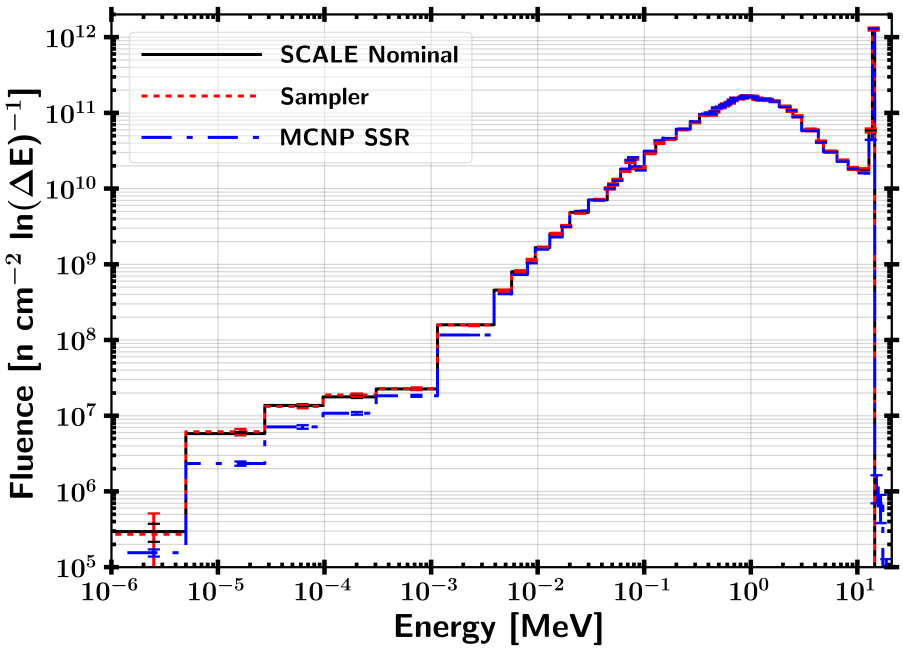

Figure 4.5. Comparison of MCNP SSR to SCALE 252 group unperturbed nuclear data and Sampler perturbed nuclear data at the ETA activation and HEU foils.

The Pearson correltation coefficient and K-S two-sample statistic were used to test the statistical significance of the correlation between the ETA-generated spectrum

and the objective TN+PFNS. Comparing the objective TN+PFNS to the continuous energy MCNP results yields a Pearson correlation coefficient of 0.90 ($p \ll 0.05$) and K-S statistic of 0.11 (p=0.11). The Pearson correlation coefficient result indicates that no correlation between the data sets can be rejected with strong significance, and the K-S statistic indicates the null hypothesis that the samples were drawn from the same distribution could not be rejected. The results indicate that Coeus generated ETAs are able to succeed in closely replicating the TN+PFNS neutron environment based on the simulated results.

The incident fluence on the HEU foil for the modeled ETA experiment is 4.9×10^{11} n cm$^{-2} \pm 1.4\%$. The neutron fluence per unit area from an unshaped point source with a strength of 3.7×10^{15} neutrons at 29 centimeters (distance from the source to the ETA foils) is 3.5×10^{11} n cm^{-2}. This implies that the net neutron population with ETA is increased from the spherical divergence approximation, primarily due to reflection and (n,2n) reactions. The cumulative fluence on the HEU foil as a function of time is shown in Fig 4.6.

The total neutron pulse length in the ETA cavity is approximately 10 shakes (100 nanoseconds). As expected based on the prompt nature of the NIF source, the total pulse length is much less than than the half-lives of the activation products used in the unfolding, so the in-growth and decay during the irradation can be neglected. The uncollided source neutrons arrive at the foil in approximately 0.6 shakes, consistent with the time required for a 14.03 MeV neutron to travel from the source to the HEU foil.

The activation foil activities are summarized in Table 4.3. The mean value presented is the mean from the MCNP continuous energy results. The uncertainty presented is the statistical uncertainty of the MCNP continuous energy results combined in quadrature with the nuclear data uncertainty from the Sampler results.

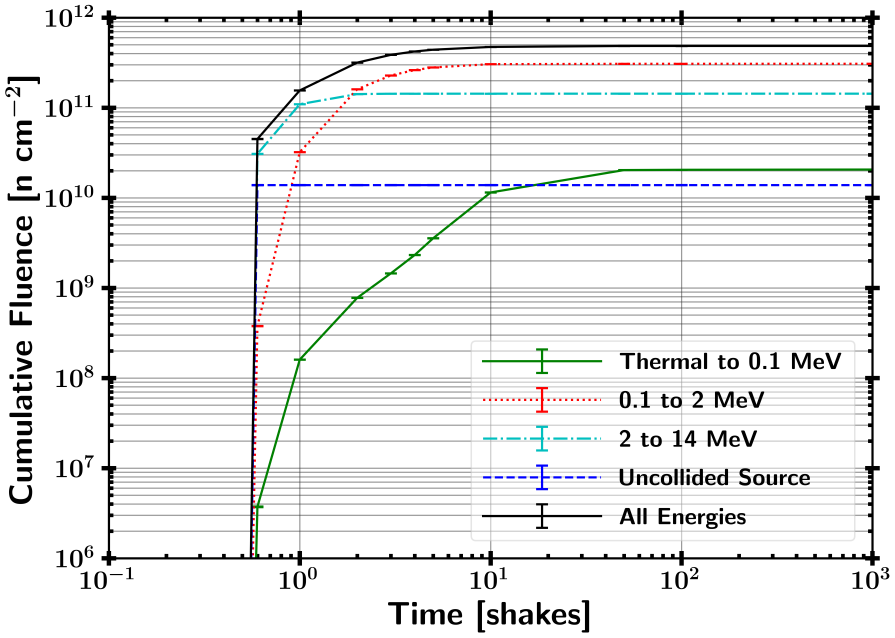

Figure 4.6. Cumulative neutron fluence on HEU foil as a function of time broken into four broad energy groups.

Uncertainty in the half-lives and branching ratios were small and could be neglected.

4.5.2 Neutron Flux Unfolding Results.

STAYSL was executed on all 182 sets of foil activities from Sampler to build a distribution of modeled experimental outcomes. The 129 group STAYSL unfolded results are shown in Fig 4.7. The largest χ^2 trial and bootstrapped neutron fluence from all trials were added to Fig 4.7 for comparison with the initial-guess MCNP spectrum with unperturbed nuclear data on the activation foil activities. The boostrapped neutron fluence χ^2 represents the average value for the 182 trial samples. Additionally, the 5-95% activation ranges for each reaction are shown, indicating the region informed in the unfolding procedure by a given reaction.

The χ^2 results, derived from the unfolded activities, provide strong confidence in the ability to unfold the neutron spectrum from the foil activities with the degree of nuclear data covariance. The null hypothesis, that the two sets of data were governed

Table 4.3. Foil activities predicted with bootstrapped nuclear data covariance uncertainty.

Product	$t_{1/2}$	Initial Activity [kBq]	$\Delta t = 2hr$ Activity [kBq]	Relative Error [%]
^{89}Zr	78.41 hrs	4.63	4.55	4.7
^{57}Ni	35.6 hrs	1.01	0.97	4.8
^{58}Co	70.86 days	0.74	0.74	2.5
^{196}Au	6.17 days	3.78	3.75	4.8
^{198}Au	2.69 days	2.98	2.92	2.6
$^{115}In^{m1}$	4.49 hrs	164	120	2.3
$^{116}In^{m1}$	54.29 min	1094	236	3.4
^{24}Na	15 hrs	13.8	12.6	4.6
^{187}W	24 hrs	5.79	5.46	4.1
^{56}Mn	2.58 hrs	23.5	13.7	20.0

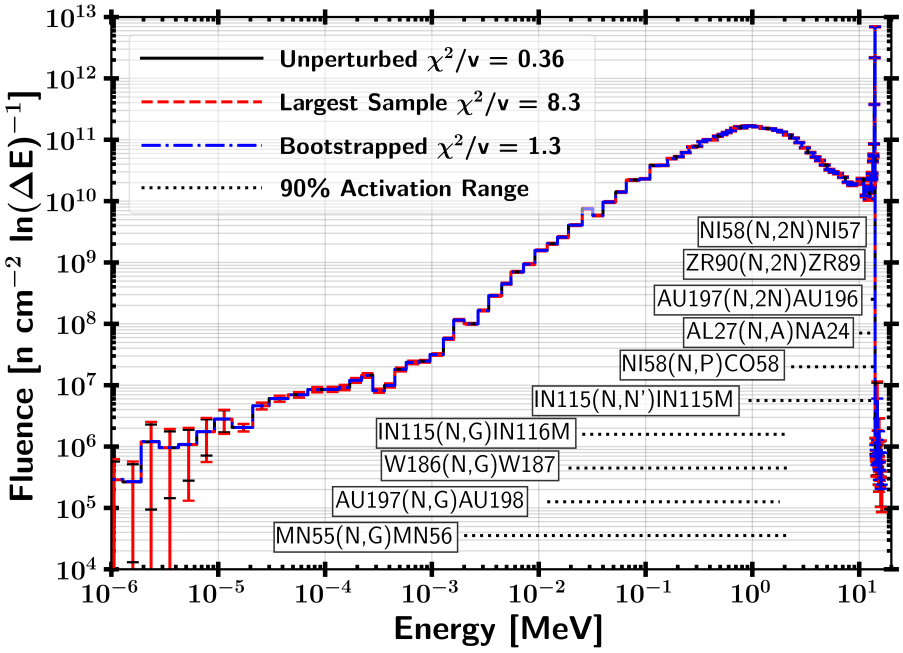

Figure 4.7. STAYSL unfolded spectra per unit lethargy for unperturbed nuclear data, largest deviation, and bootstrapped values.

from the expected distribution, could not be rejected for most of the trials with high confidence. The χ^2 for the nominal guess, largest sample, and bootstrapped unfolded activities are 0.36, 8.3, and 1.3 with p-values of 0.96, $\ll 0.05$, and 0.22, respectively. The p-values indicate the probability of achieving a larger χ^2 given the results, so the

nominal case is within reasonable expectations, while the largest χ^2 value is rejected with strong significance. The bootstrapped activity p-value is closer to the rejection value of 0.05, but the p-value is large enough to not reject the unfolded activities. The distribution of χ^2/ν values for the set of trials is shown in Fig 4.8.

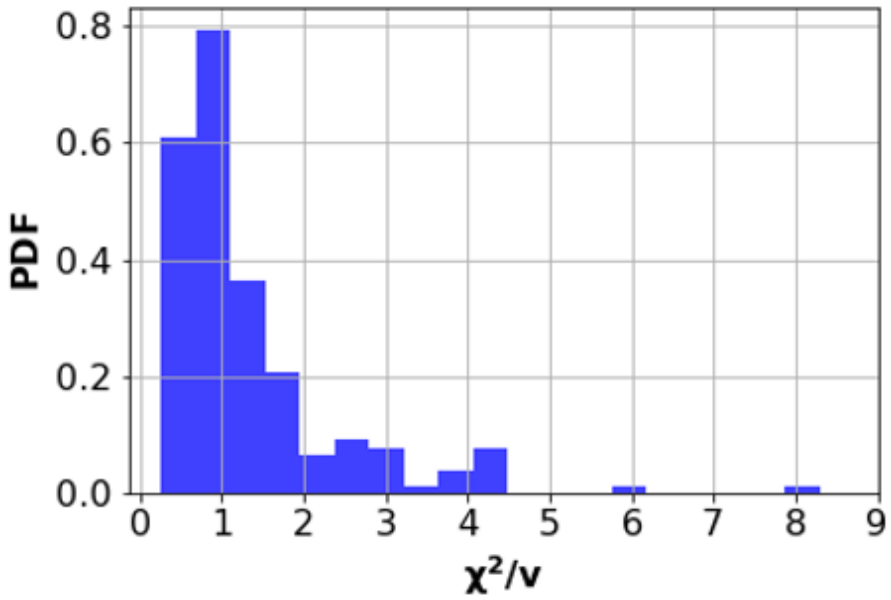

Figure 4.8. Probability density function of STAYSL unfolded ETA spectrum χ^2.

Of the 182 trials, the hypothesis that activities come from the expected distribution was not rejected 81.9% of the time with 95% confidence. The distribution of χ^2 values peaks near 1; however, a non-negligible portion of the unfolding calculations provide results that rejected the null hypothesis.

It is nevertheless worth noting that even the rejected trials result in unfolded neutron energy spectra that are very similar, as shown for the largest sample χ^2 in Fig 4.7. As described next, these small perturbations in the neutron energy spectra result in negligible changes to the overall fission products produced in the HEU sample.

4.5.3 Fission Product Estimation Results.

Table 4.4 displays the fission product production in the HEU foil using Nagy fits of experimental data. The uncertainties capture the uncertainties in the underlying energy-dependent fission product yield data, the uncertainties in the fit, the Monte Carlo statistical uncertainties, and the systematic nuclear data uncertainties from Sampler. The TN+PFNS objective spectrum fission products are consistent with the fission product production achieved in the ETA within uncertainty associated with the modeled results. The Nagy and GEF models produce similar results, albeit with much higher uncertainty for the GEF results.

The resultant GEF mass chain distribution for the ETA and the original objective TN+PFNS are displayed in Fig 4.9. Overall, there is large agreement in reproducing the fission product distribution expected from the TN+PFNS. The high uncertainty reflects the large parameter uncertainty in the GEF fission models that limit the ability to predict mass chain fission products *a priori* across all mass chains.

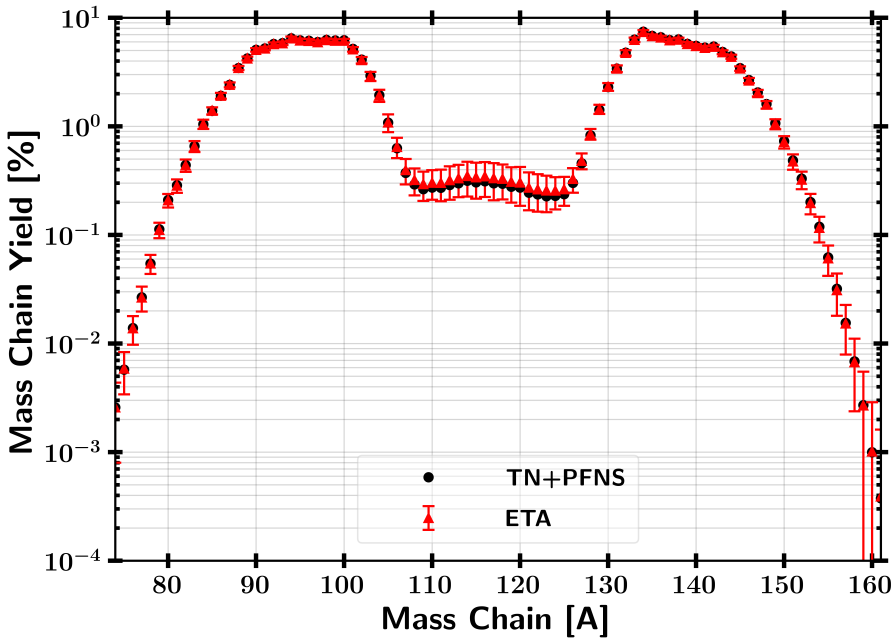

Figure 4.9. TN+PFNS versus ETA fission product mass chain distributions calculated with GEF values.

Table 4.4. ETA and TN+PFNS produced Nagy fit cumulative fission product yield from simulated data.

Fission Product	Fission Product Yield [%]	
	ETA	TN+PFNS
^{91}Sr	5.34 ± 0.15	5.37 ± 0.08
^{92}Sr	5.38 ± 0.16	5.41 ± 0.10
^{95}Zr	6.03 ± 0.15	6.05 ± 0.06
^{97}Zr	5.71 ± 0.16	5.74 ± 0.08
^{99}Mo	5.62 ± 0.16	5.65 ± 0.08
^{103}Ru	3.20 ± 0.09	3.21 ± 0.05
^{105}Ru	1.41 ± 0.05	1.39 ± 0.04
^{109}Pd	0.32 ± 0.02	0.29 ± 0.02
^{111}Ag	0.28 ± 0.01	0.25 ± 0.01
^{112}Pd	0.27 ± 0.01	0.23 ± 0.01
^{113}Ag	0.20 ± 0.01	0.18 ± 0.01
^{115g}Cd	0.28 ± 0.01	0.25 ± 0.01
^{132}Te	4.32 ± 0.13	4.33 ± 0.07
^{140}Ba	5.56 ± 0.15	5.60 ± 0.07
^{141}Ce	5.46 ± 0.17	5.49 ± 0.10
^{143}Ce	5.06 ± 0.15	5.11 ± 0.09
^{144}Ce	4.69 ± 0.16	4.75 ± 0.11
^{147}Nd	2.08 ± 0.06	2.10 ± 0.03
^{149}Pm	1.01 ± 0.04	1.01 ± 0.03
^{151}Pm	0.47 ± 0.02	0.46 ± 0.02
^{153}Sm	0.18 ± 0.01	0.18 ± 0.01
^{156}Eu	0.028 ± 0.001	0.027 ± 0.001
^{161}Tb	0.0013 ± 0.00006	0.0011 ± 0.00004

The mass chain relative residual yields comparing the ETA to the objective spectrum are shown in Fig 4.10. There are a few areas of disagreement between the mean value of the ETA and the TN+PFNS. The symmetric valley fission products are systematically larger because of the increased high energy flux produced in ETA. Accordingly, there is an decrease in yield for asymmetric fission products'

mass chains in ETA. However, the differences in the symmetric valley and asymmetric fission products are not substantial compared to the uncertainty in the fission product yield calculations.

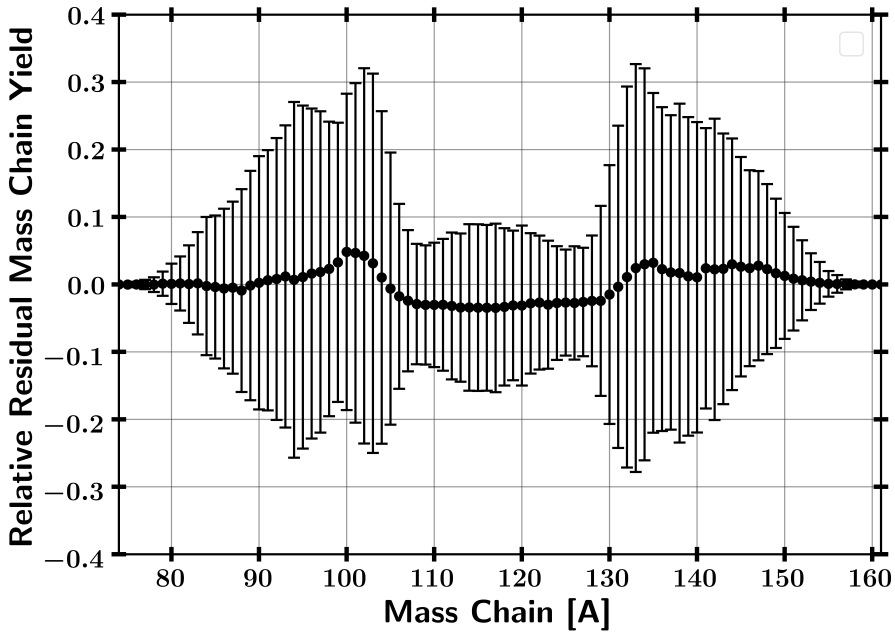

Figure 4.10. Relative residual mass chain yields of ETA compared to TN+PFNS from GEF values.

4.6 Conclusions

This work describes the continued development, analysis, and support of the capability of producing spectrally-accurate neutron environments through the use of an ETA. The application of this work focused on the production of fission fragment debris through targeted modification of the NIF source spectrum. The ETA design developed using Coeus replicates the neutron environment and fission product distributions of interest to technical nuclear forensics and provides a step forward to generating synthetic debris. The results model the full range of experimental outcomes and incorporate nuclear data covariance analysis to further bound the range of possible experimental outcomes for this novel approach to generating

high-fidelity neutron environments.

The primary objective of the ETA research was to determine if the TN+PFNS neutron energy distribution can be produced using spectral modification with an ETA at the NIF. This research showed computationally that the ETA concept can fill the technical nuclear forensics and neutron environment capability gaps. The Pearson correlation coefficient and K-S two-sample statistic used to compare the TN+PFNS to the modeled achieved neutron spectrum were 0.9 and 0.11, signifying that there is large spectral agreement in reproducing the objective neutron fluence environment.

The ETA uses non-tradiational nuclear materials and the measured results depend on independent channels in a weighting disproportional to the relative cross section intensities. Therefore, SCALE Sampler was used to asses the impact of the nuclear data uncertainty on the measurable experimental outcomes. Using this approach, the nuclear data uncertainty and covariance on the ETA performance was found to be non-negligible. Nuclear data covariance increased the energy-dependent neutron fluence uncertainty in the ETA sample cavity to approximately 3-5% above 1 keV and 7-100% below 1 keV. The resultant nuclear data uncertainty, including the foil reaction cross section uncertainty resulted in uncertainties on the order of a few percent for all but the ^{55}Mn(n,γ) reaction where the systematic uncertainty was found the be 19.7%.

The foil activities and fission products produced in the ETA cavity are within measurable limits for radiochemistry and γ-ray spectrometry. The measured fission products are used to unfold the neutron enery spectrum observed in the experimental cavity using STAYSL. The STAYSL unfolded results on each of the 182 Sampler trials provide an 80+% probability of being able to perform a statistically-significant unfold of the neutron spectrum given a set of activation measurements and the modeled spectrum, based on the χ^2 of each unfolded trial.

In the context of technical nuclear forensic and attribution capabilities associated

with device reconstruction, an observable quantity of interest is the fission product distribution created from the neutron flux interaction with the fissile material. The ETA's modeled performance produces $2 \times 10^9 \pm 1\%$ fissions, which is near the order of those collected in forensics ground samples. Selected fission products analyzed with the General Description of Fission Observables (GEF) code and experimental data from the literature were used to create energy dependent Nagy fits. The fission products produced in the HEU with the ETA's spectral shaping capability have an equivalent cumulative fission product yield distribution to the objective TN+PFNS within current fission product yield modeling capabilities.

The capability of producing objective neutron spectra has wide reaching significance to further leverage operating neutron source facilities into new areas of research and support key capability needs. The ETA designed in this research effort contributes to further enable enhancements to nuclear attribution and has potential use for the certification of electronic components in neutron threat environments.

The future work related to the analysis performed here will compare the experimental outcomes to the predicted reactions and methodology used in this research. Although the ETA is a huge step forward for developing synthetic weapon debris, improvements will be made to develop a second generation ETA to generate a more representative neutron spectrum. Additionally, facility improvements to the NIF and updated constraints will be incorporated to increase the optimization with the objective of increasing the efficiency of the ETA to produce 10^{11} fissions, which is essential to achieve better detection of low yield fission products. Finally, real-world scenario nuclear fallout includes fractionation based on the physical properties and chemistry of the fission products. A fractionation technique can most readily focus on refractory fission products with low condensation points, as opposed to volatile mass chains as many of these are gases that may be lost in

chemical separations. Incorporating the fractionated synthetic fission product debris into a matrix representative of a nuclear forensic collection would be of great benefit to technical nuclear forensic training and exercises.

4.7 Acknowledgment

This material is based upon work supported in part by the National Science Foundation Graduate Research Fellowship under Grant No. NSF 11-582. This work is also supported by the U.S. Air Force Technical Application Center (AFTAC) under the AFIT/AFTAC Endowed Term Chair MOA#: 212196 and the Defense Threat Reduction Agency under grant HDTRA-18-27434. The views expressed in this article are those of the authors and do not necessarily reflect the official policy or position of the United States Air Force, the Department of Defense, or the United States Government.

V. ETA Experiment

This chapter was derived from a paper published in July 2021 with *Applied Radiation and Isotopes* titled "Uranium Integral Fission Product Yields for a Spectrally-shaped 14.1 MeV Neutron Source at the National Ignition Facility" [39]. The author list included Nicholas J. Quartemont, Narek Gharibyan, Ken Moody, and James E. Bevins. The article has been modified to fit this dissertation format; however, the content was unchanged.

This part of the research effort demonstrated ETA's capbility to produce fission products under the integral TN+PFNS at the NIF. The analysis framework was outlined in Chapters 3 and 4, so readers familiar with those topics will find Section 5.5 of more interest where the fielded ETA experiment environment and fission product observables are highlighted. The experiment performed was the first novel use of an ETA at the NIF, where fission products were produced from the TN+PFNS with the instantaneous source D-T fusion neutrons.

5.1 Abstract

This paper describes the experimental results for an energy tuning assembly created to modify the National Ignition Facility deuterium-tritium fusion neutron source into a notional thermonuclear and prompt fission neutron spectrum, which has applications in integral measurements, nuclear data benchmarks, and radiation effects on microelectronics. The Monte Carlo neutron transport utilized MCNP5 to estimate the ETA-modified fluence using the ENDF-B/VIII.0 and IRDFF-II continuous energy nuclear data libraries, and SCALE Sampler was used to estimate the systematic nuclear data covariance using ENDF-B/VII.1 and IRDFF-II in a 252-group structure. The experiment fielded eight activation foils and a highly

enriched uranium sample. This provided fifteen reaction channels that were used in a forward-fit comparison to the modeled results and to unfold the neutron spectrum using STAYSL. γ-ray spectrometry was performed on the activation and highly enriched uranium foils, and the reduced χ^2 between the modeled and experimental values was 1.21. The results from the STAYSL unfold, reduced $\chi^2 = 1.62$, indicated that the modeled neutron spectrum was achieved and the systematic nuclear data uncertainty associated with the neutron transport and activation product cross sections was representative of the experiment. Integral cumulative fission product yield data were collected for 37 mass chains with a combination of γ-ray spectrometry and radiochemical analysis. Fission product analysis was generally in agreement with two models using a semi-empirical fit and the General Observables of Fission code, with the exception of mass chains 88, 109, 111, 112, 113, 129, 139, 142, 144, 151, and 156.

5.2 Introduction

An energy tuning assembly (ETA) experiment was performed at the National Ignition Facility (NIF) to spectrally shape the deuterium-tritium (D-T) 14.1 MeV fusion neutron spectrum into a modified thermonuclear (TN) and prompt fission neutron spectrum (PFNS). Customizable neutron environments offer increased access to unique neutron energy spectra, which can provide data on integral measurement needs and activation dosimetry validation [68, 147]. Many testing facilities targeting integral measurements focus on nuclear reactor spectra, the Watt fission spectrum, and the 14.1 MeV D-T fusion process. Accelerators can also provide a nearly mono-energetic neutron source for discrete energy measurements [138].

Utilizing different neutron spectra can identify nuclear data gaps and inaccurate evaluations that feed into nuclear data libraries used in modern radiation transport

simulations [148]. In particular, integral fission product yield (IFY) measurements inform nuclear data libraries and models, which are essential knowledge for nuclear reactor operations, international nuclear treaty monitoring, and technical nuclear forensics. The NIF has a unique capability as a high-density D-T prompt neutron source that can be used to produce nearly instantaneous fission products under the appropriate neutron spectrum distribution without any saturation or decay effects common with nuclear reactor or accelerator production. The ETA, or similar platform, could also be utilized to study radiation effects on electronics and create environments for nuclear data benchmarks.

The ETA design [4] considered in this work was previously tested at the Lawrence Berkeley National Laboratory (LBNL) 88-Inch Cyclotron to validate initial modeling concepts and neutron spectrometry techniques [37]. The modeling of the expected experimental outcomes and uncertainties was improved by accounting for nuclear data covariance analysis, which improved the quality of the foil activation spectrometry used to measure the ETA-generated neutron environment [97].

This work describes the first ETA experimental results from the NIF to generate a TN+PFNS neutron environment. The experimental design, modeling, and results from activation analysis and the unfolding of the the neutron fluence with Pacific Northwest National Laboratory's (PNNL's) STAYSL [110] are described. Finally, results of 47 cumulative and independent IFY across 37 mass chains for a highly enriched uranium sample are presented.

5.3 Experiment

The ETA, shown in Figure 5.1, was designed to produce a notional thermonuclear and prompt fission neutron spectrum (TN+PFNS) relevant to the production of surrogate post-detonation weapon debris [37]. The ETA design is 28

cm in diameter and approximately 24 cm in height. The ETA consists of cones and cylinders of boron carbide, aluminum, bismuth, tungsten, silicon, 316 stainless steel, and lead. Each ETA part is manufactured with three or four nines pure material and sub-mm tolerances thereby limiting sources of systematic uncertainty.

The ETA was fielded with an activation foil pack and a HEU foil placed in the sample cavity, item 6 in Figure 5.1, where the objective TN+PFNS neutron spectrum was achieved. ETA was fielded with eight activation foils, summarized in Table 5.1. Each activation foil had a radius of 2.5 cm with the exception of manganese and the HEU. The manganese foil was a 2.5 cm side length square foil. The HEU (93.217 wt%) utilized for the experiment consisted of three disk samples (HEU1, HEU2, and HEU3) weighing 0.3675, 0.3549, and 0.3550 g with a maximum weight uncertainty of 0.2% with areas of 4.99, 4.72, and 4.88 cm^2. The HEU samples were encased in a hermetically sealed Target Option Activation Device (TOAD) [149]. The TOAD was positioned between indium and tungsten as depicted in Table 5.1.

Table 5.1. Summary of experimental activation foils and reactions selected to unfold the neutron energy spectrum. The order of the foils was in the listed order with Au-1 closest to the NIF source.

Foil (Thickness)	Mass [g]	Reaction [IRDFF v.1.05 Reaction Number]	Threshold [MeV] (@ 10 mb)	Primary Radiation [keV] (Intensity)	$t_{1/2}$	Decay Data
Au-1 (0.09 mm)	3.718	^{197}Au(n,2n) ^{196}Au^{g+m1} [16]	8.1 (8.3)	355.7 (0.87)	6.17 days	[150]
		^{197}Au(n,g)^{198}Au [102]	Thermal	411.8 (0.9562)	2.69 days	[151]
Zr (0.97 mm)	12.683	^{90}Zr(n,2n)^{89}Zr [16]	12.1 (12.1)	909.2 (0.9904)	78.41 hrs	[152]
Mn (1.12 mm)	5.028	^{55}Mn(n,2n)^{54}Mn [16]	10.4 (10.6)	834.85 (0.99976)	312.2 days	[153]
		^{55}Mn(n,g)^{56}Mn [102]	Thermal	846.8 (0.9885)	2.58 hrs	[154]
In (1.03 mm)	14.811	^{113}In(n,n')^{113}In^{m1} [11004]	0.4 (0.7)	391.7 (0.6494)	99.5 min	[155]
		^{115}In(n,n')^{115}In^{m1} [11004]	0.3 (0.6)	336.24 (0.459)	4.49 hrs	[156]
		^{115}In(n,g)^{116}In^{m1} [11102]	Thermal	1293.56 (0.848)	54.29 min	[157]
HEU (0.12 mm)	1.0774	^{238}U(n,g)^{239}Np [102]	Thermal	106.36 (0.202)	2.356 days	[158]
W (1.02 mm)	37.964	^{186}W(n,g)^{187}W [102]	Thermal	685.51 (0.332)	24 hrs	[159]
Ni (1.12 mm)	14.316	^{58}Ni(n,2n)^{57}Ni [16]	12.4 (13.3)	1378 (0.817)	35.6 hrs	[160]
		^{58}Ni(n,p)^{58}Co^{g+m1} [103]	0 (1.3)	810.8 (0.9945)	70.86 days	[161]
Al (1 mm)	5.428	^{27}Al(n,a)^{24}Na [107]	3.2 (6.7)	1368.63 (0.9999)	15 hrs	[162]
Au-2 (0.09 mm)	3.692	^{197}Au(n,2n)^{196}Au^{g+m1} [16]	8.1 (8.3)	355.7 (0.87)	6.17 days	[150]
		^{197}Au(n,g)^{198}Au [102]	Thermal	411.8 (0.9562)	2.69 days	[151]

The NIF source for shot N191020-001 was located 15 cm below the base of the cone and was a D-T Polar Drive Exploding Pusher (PDXP) target [163]. The source configuration utilized a 64/36 D-T mix capsule with a 1.44 mg mass, 29 μm thick,

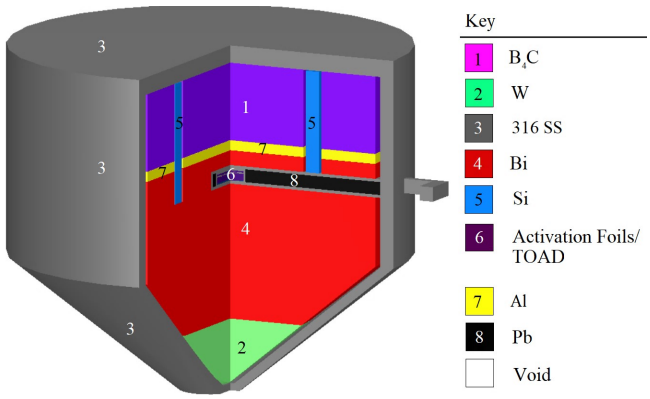

Figure 5.1. (Color online) The ETA designed to achieve the TN+PFNS via spectral modification of the NIF neutron source.

and 4.05 mm outer diameter. The PDXP shot delivered 1.56 MJ of laser energy, enabling thermonuclear fusion with a nominal yield of $1.08 \pm 0.04 \times 10^{16}$ neutrons over 424 ps with a minimum plasma ion temperature of 8.36 keV [164]. The ETA experiment was fielded on a Target and Diagnostic Manipulator (TANDM) as an additional experiment to the Energetic Neutron Platform (ENP). The ETA, ENP, and target positioner (TARPOS) experimental configuration is shown in Figure 5.2.

5.4 Analysis methods

The primary analysis techniques utilized in this work were Monte Carlo simulation, γ-ray spectrometry, modeling of fission products, neutron spectrum unfolding, and radiochemistry. The modeled neutron environment with MCNP and SCALE was used to predict the neutron environment and resulting observable products such as activation or fission products [44, 45]. Experimental measurements of the products included γ-ray spectroscopy and radiochemistry on the fission products. The primary codes and data utilized are summarized in Table 5.2. A repository containing the primary model inputs and outputs utilized in this work can be accessed here [165].

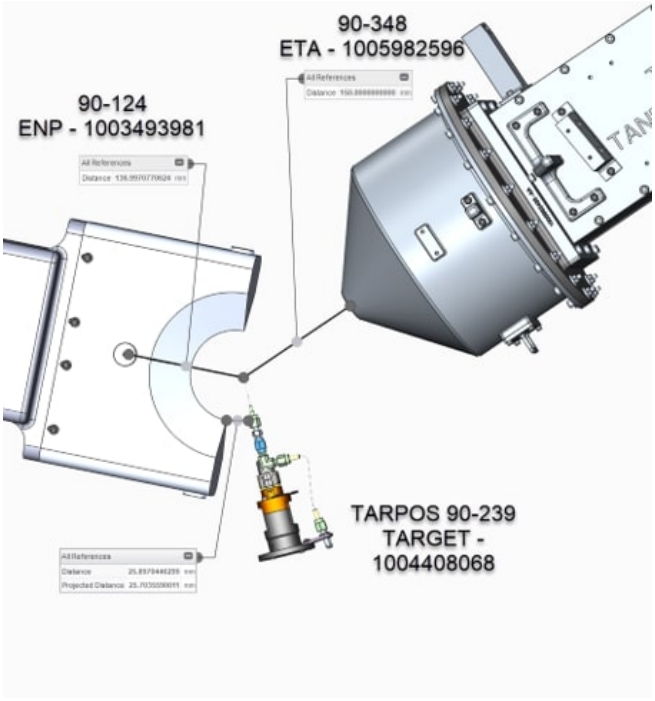

Figure 5.2. (Color online) NIF chamber experimental configuration of TARPOS, ENP, and ETA.

Table 5.2. Primary codes and methods utilized.

Purpose	Code/Method (Library)
Monte Carlo Neutron Transport	MCNP5 (ENDF/B-VII.1 and ENDF/B-VIII.0)
	SCALE MAVRIC and Sampler (ENDF/V-VII.1 252-group)
γ-ray Spectrometry	GAMANAL
	PeakEasy 4.97
Fission Product Estimation	GEF
	Semi-empirical fits
Neutron Flux Spectrum Unfolding	PNNL STAYSL (IRDFF v.1.05 129-group)

5.4.1 Monte Carlo Simulation.

The ETA neutronics design was modeled in MCNP5 to determine the expected neutron environment in the sample cavity and in SCALE MAVRIC with Sampler to

propagate nuclear data covariance in the transport model [44, 45]. MCNP5 was used for continuous energy (CE) MC neutron transport and to benchmark MC neutron transport in CE SCALE MAVRIC. The MAVRIC MC simulation was then used in a 252 energy group structure with the SCALE Sampler module to assess the effect of nuclear data covariance through stochastic sampling of the ENDF-B/VII.1 nuclear data library [46]. Finally, the activation foil covariances were sampled with a multivariate normal distribution to incorporate the reaction cross section uncertainty with an interpolation scheme described with the IRDFF-II nuclear data library [68]. Previous work has described the methodology in detail to characterize the effect of nuclear data covariance for NIF ETA simulations [97, 130].

The MCNP5 ETA model was created with a surface source read (SSR) file generated using a neutron point source with a mean energy of 14.07 MeV [145]. The SSR, a box around ETA, was made with a validated full-scale NIF model including the TARPOS, ETA, TANDM (90-348), snout diagnostic instrument manipulator (DIM), Sandia ENP experiment, TANDM (90-124), and target chamber support structures and used the ENDF/B-VII.1 library [46]. Time dependence in the neutron source was neglected because NIF neutron emission generations are approximately 300 picoseconds [164]. The ENDF/B-VIII.0 nuclear data library was used for the neutron transport inside the SSR source, and the IRDFF-II library was used for the activation cross sections [166]. The difference in transport libraries after the SSR was created was a limitation of NIF-validated model.

A lower fidelity SCALE MAVRIC model was also created for the experimental setup of the NIF. The MAVRIC model with Sampler included a full fidelity model of ETA and representative geometry for the remainder. The source specifications were identical to MCNP5; however, only the ENDF/B-VII.1 library was available in SCALE [45]. The results from 285 samples in Sampler running MAVRIC in the 252-

group structure were characterized with statistical bootstrapping to determine a 1-σ uncertainty in the reaction products and fluence distribution. The Sampler transport uncertainty and flux correlation matrix are shown in Figure 5.3.

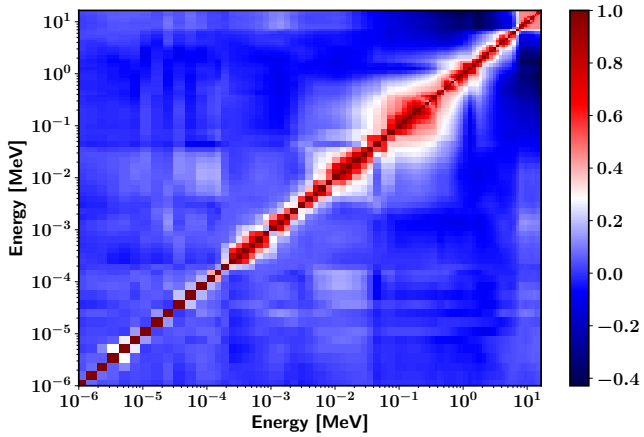

(a) Correlation matrix

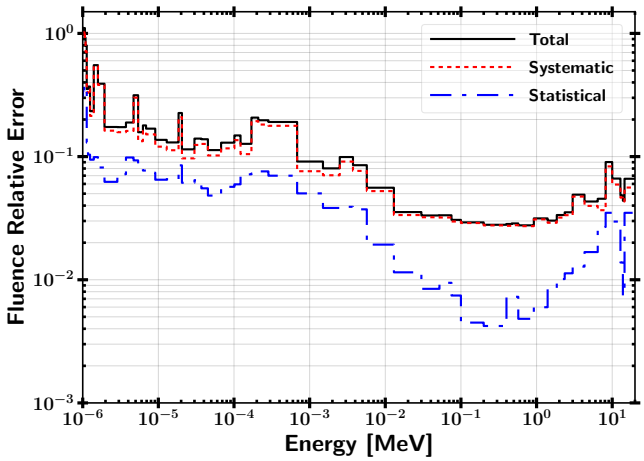

(b) Relative Uncertainty

Figure 5.3. (Color online) ETA Neutron fluence covariance parameters in ETA sample cavity showing the a) correlation matrix and b) relative statistical and systematic uncertainty as a function of energy.

The resulting correlation matrix and uncertainty were used in the unfolding routine in STAYSL to bound the possible outcome. The correlation matrix indicated nearby energy group correlations and an anti-correlation between the TN neutrons near 14 MeV and peak of the PFNS near 1 MeV because removal

mechanisms – such as (n,2n) and (n,n') – in the TN region are needed to populate the PFNS. The associated neutron fluence uncertainty was 5.3% at 14.1 MeV, due to the uncertainty in tungsten and bismuth attenuation coefficients. The uncertainty at 1 MeV was 2.9% because there are multiple paths to down-scatter the source neutrons, including spallation (n,2n) reactions primarily on W and Bi components in addition to successive inelastic scattering events. At 1.3 eV, the uncertainty reached 67% due to the large number of interactions required to moderate D-T neutrons to low energy. The low energy neutron distribution is not well described by a normal distribution, and this creates a limitation of assumed normally distributed uncertainties in STAYSL at low energy [104].

5.4.2 Activation Analysis.

Activation analysis was performed with γ-ray spectrometry using three high purity germanium (HPGe) and multi-channel analyzer systems in the LLNL counting facility on the activation foils and HEU1 sample [149]. Two methods were performed to analyze the energy dependent counts, GAMANAL, which was created for analysis of fission product spectra, and PeakEasy 4.97, which was also used for peak fitting [167]. The fission product nuclear data utilized in this analysis was from literature, the Table of Isotopes, 8th Edition [168] and data retrieved from the National Nuclear Data Center Chart of the Nuclides Online Data Service. GAMANAL was calibrated with standard calibration sources to determine the efficiency as a function of sample position, energy, and detector geometry. GAMANAL performed γ-ray attenuation corrections and counting of peaks using multiple linear regression least squares with smoothed Gaussian peak fits [167].

Measurements of the activity were decay corrected to the reaction product atoms, N_0, immediately after irradiation by

$$N_0 = \frac{(C - B)e^{\lambda t_d}}{\epsilon(1 - e^{-\lambda t_c})I_\gamma}, \tag{5.1}$$

where the measured counts, C, were reduced by the background counts, B, and corrected for decay between the end of irradiation and the start of counting, t_d. A correction factor was used for radioactive decay during counting time, t_c. The detector efficiency for the given γ-ray energy, ϵ, was determined with GAMANAL to include γ-ray self-shielding. Finally, the relative γ-ray intensity, I_γ, for each decay was taken into account.

Each foil was counted until approximately 10,000 counts were detected from the reaction products. All reactions did not require in-growth corrections, with the exception of the $^{196}\mathrm{Au}^{g+m1}$ reaction product. The $^{58}\mathrm{Co}^{m1}$ reaction product is not suitable for γ-ray spectrometry, so the sample was allowed to decay for two weeks prior to the measurement of $^{58}\mathrm{Co}^{g+m1}$. Similarly, ^{239}Np was measured after the short-lived decay of ^{239}U.

A variance-based weighted average was taken for each decay γ-ray associated with a product nuclei for each measurement of that decay mode [43]. The final weighted average of each γ-ray decay mode measurement was then done to determine N_0 for each product. Radioactive decay uncertainties were added after accounting for the statistical error and a 2% systematic error [43]. Uncertainties associated with the weight and size of the activation foils were neglected as negligible in this work with respect to the measurement uncertainty.

5.4.3 Fission product models.

The modeled neutron fluence was convolved with the fission cross section to produce the expected experimental fission product production from ^{235}U and ^{238}U

with two techniques. First, the energy spectrum of neutrons causing fission was used to determine the fission product yield with a phenomenological fit and the General Description of Fission Observables (GEF) code [49]. Second, semi-empirical relations developed by Nagy *et al.* were used to predict the fission product yield as a function of energy given sufficient yield-dependent fission product measurement data [51].

GEF is applicable over a wide range of fissioning systems, including isotopes with atomic numbers from 80 to 112 [49]. GEF incorporates covariance information of the fissioning system, multi-chance fission, and many other unique features. The values for the mass chain yield distribution calculated by GEF were determined using separate calculations for each energy group defined by the midpoint bin energy of the fissioning system, ^{236}U for neutron-induced ^{235}U fission and ^{239}U for neutron-induced ^{238}U fission. The uncertainty reported in this work includes GEF statistical, GEF systematic covariance, and the Sampler systematic uncertainty for the fissioning neutron energy distribution.

The semi-empirical formula for estimating fission product yield is given by

$$Y(E_n) = Y_0 e^{bE_n}, \tag{5.2}$$

where the fitting parameters b and Y_0 represent the slope of the function in logarithmic form and thermal fission yield, respectively [51]. The slope is the primary measure of the energy dependence of the fission product yield, which requires modifications for multi-chance fission. First chance fission is dominant up to 5.5 MeV and second-chance fission up to 14.1 MeV [51], requiring modifications to incorporate first and second chance fission in this work. Correlations between fission product yield as a function of energy were not captured because data were not available.

The measured fission products were compared through relative fission yields, R values [169]. The R value was used to remove unknown systematic errors and is a ratio given by

$$R = \frac{A_i^{f,e} \Big/ A_{97}^{f,e}}{A_i^* / A_{97}^*} = \frac{N_i^{f,e} \Big/ N_{97}^{f,e}}{N_i^* / N_{97}^*} = \frac{N_i^{f,e} \Big/ N_{97}^{f,e}}{Y_i^* / Y_{97}^*}, \tag{5.3}$$

where the activity ratio between the i^{th} measured fission product or mass chain time-corrected atoms, $N_i^{f,e}$, to the measured $A = 97$ mass chain atoms, $N_{97}^{f,e}$, was normalized by the ENDF-B/VIII.0 ^{235}U thermal fission product yield ratio of the i^{th} fission product mass chain, Y_i^*, to the yield for the $A = 97$ mass chain, Y_{97}^*. The $A = 97$ mass chain was chosen because ^{97}Zr provided a strong γ-ray for measurement and is a well-characterized peak fission product.

5.4.4 Neutron Spectrum Unfolding.

The measured foil activation products were used with an average foil pack MCNP5 CE fluence and SCALE Sampler neutron fluence covariance to unfold the neutron spectrum using STAYSL with the IRDFF v.1.05 129-energy group structure. The most current version of STAYSL did not include IRDFF-II, where the reaction cross section and covariance matrix for ^{197}Au(n,γ) and ^{238}U(n,γ) were updated. The 129-group cross section library was derived for D-T neutron experiments; however, the cross section integrating function results in increased radiative capture reactions compared to the CE solution. For example, the ^{197}Au(n,γ) was 29% higher and ^{186}W(n,γ) was 53% higher in the 129-group STAYSL library than the CE solution. The STAYSL (n,γ) microscopic cross sections were re-calculated with MCNP5 with IRDFF-II data in the 129-group STAYSL structure to correct the cross section integrating function. This allowed the

use of IRDFF-II ^{197}Au(n,γ) and ^{238}U(n,γ) reaction cross sections in STAYSL. However, the IRDFF v.1.05 covariance matricies for ^{197}Au(n,γ) and ^{238}U(n,γ) were still used. The 129-group cross sections are shown in Figure 5.4.

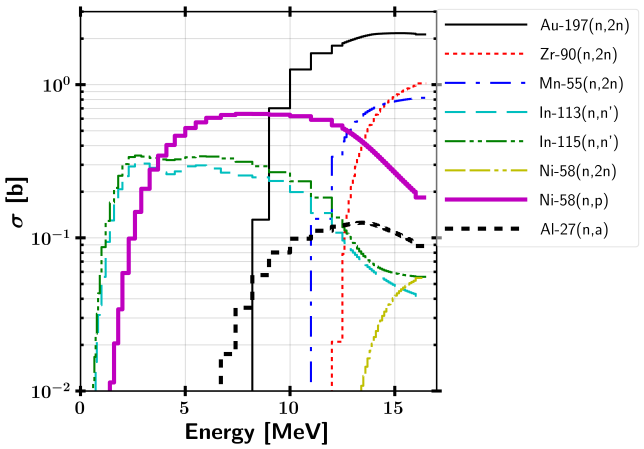

(a) Threshold reactions

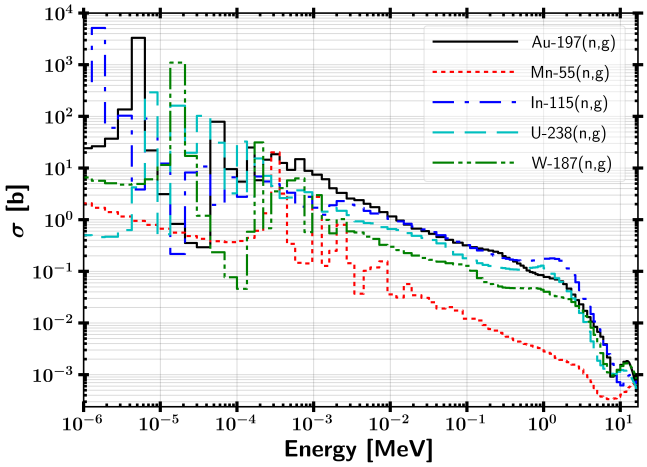

(b) Thermal reactions

Figure 5.4. (Color online) Neutron activation cross sections used in STAYSL for the a) threshold and b) thermal reactions. The reaction cross sections indicate coverage of the energy range of interest with unique and overlapping measurements.

MCNP5 was used to generate energy-dependent neutron self-shielding factors to account for attenuation within and across the foil pack in a mixed neutron field and beam environment similar to other thick-foil techniques [82]. The self-shielding factors were required for modification of the neutron flux throughout the foil pack due to the

relatively large size of the foils used resulting in non-negligible attenuation as shown in Figure 5.5.

STAYSL determines the incident neutron flux using a generalized least-squares spectral adjustment based on a χ^2 comparison of the measured activation products and the activities calculated from an adjusted flux [52]. The activity information, A°, a neutron flux, a nuclear data matrix, P, and covariance matrices are used in the formulation of the χ^2 statistic. The χ^2 is minimized based on the STAYSL minimized activity information, $\bar{A}$, and the STAYSL calculated neutron flux convolved with the IRDFF nuclear data parameters, $\bar{P}$. The χ^2 statistic utilized in STAYSL is given by

$$\chi^2 = \begin{bmatrix} P - \bar{P} \\ A^\circ - \bar{A} \end{bmatrix}^\dagger \bullet \begin{bmatrix} N_P & 0 \\ 0 & N_{A^\circ} \end{bmatrix}^{-1} \bullet \begin{bmatrix} P - \bar{P} \\ A^\circ - \bar{A} \end{bmatrix} \tag{5.4}$$

where N_P is the covariance matrix from the flux and nuclear data and N_{A° is the activity covariance matrix [84].

Additionally, STAYSL requires an initial guess spectrum as the activities produced for the foils are often degenerate with multiple creation environments. However, the initial spectrum allows for a physics- and modeling-based result to guide the overall result. The initial guess spectrum was created with the mean value from MCNP5 over the entire activation foil pack volume and a neutron fluence covariance matrix as derived with Sampler [97]. The 252-group Sampler covariance matrix was mapped to the 129-group STAYSL structure through linear interpolation of the systematic uncertainties and correlation based on the midpoint of the energy bins for each structure.

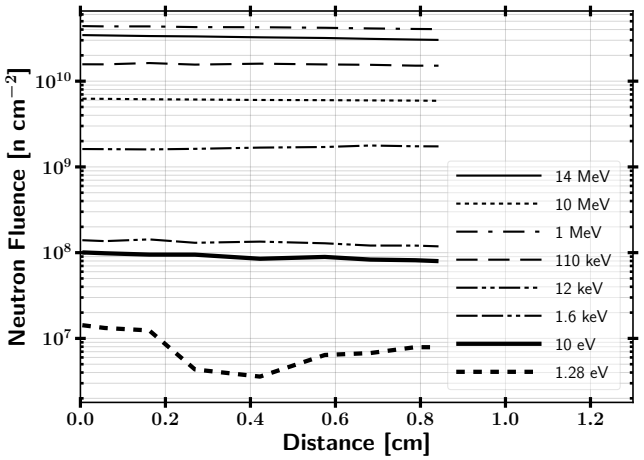

Figure 5.5. Neutron fluence in ETA sample cavity showing exponential attenuation at high energy and nuclear resonance self-shielding at low energies.

5.4.5 Radiochemistry.

Radiochemistry was performed to separate lower yield fission products that would not be observed in the bulk sample with γ-ray spectrometry. Radiochemistry procedures were adopted from standard fission-product separation procedures found in their respective radiochemistry chapters and commonly utilized distribution tables [170–173]. The radiochemical procedures of HEU2 included dissolution in 9M HCl with 8M HNO_3 to remove the rare-earth (RE) fission products from the bulk HEU and subsequent separations to isolate desired elements [174]. A mixed lanthanide-yttrium RE carrier and aliquots of barium and cesium were added to HEU2 for chemical yielding and improved chemical performance. Additionally, a ^{237}Np tracer was added for yielding of ^{239}Np.

The neptunium fraction was eluted from an anion-exchange column. The RE fission products were separated into three fractions containing the light (La-Pr), medium (Nd-Pm) and heavy (Sm-Tb, containing Y) fractions after elution with a mixture of HNO_3 and methanol from an anion-exchange column. The dried fractions were dissolved in 10 ml of water, transferred to Prindle γ-ray vials

(cylindrical plastic vial with 10 cm^2 area), and analyzed with γ-ray spectrometry. The fractions were counted on coaxial and planar HPGe detectors and evaluated by the GAMANAL code as described in Section 5.4.2 with decay-curve analysis to verify the half-life of the fission-product measurement. Chemical yielding was performed with inductively-coupled plasma mass spectrometry (ICP-MS), where the tracer isotope concentration was used to determine chemical efficiency during separations for the measured radioisotopes.

Separations were performed on HEU3 after dissolution with the addition of palladium, cadmium, and silver carriers. An Ag_2S precipitate was formed to recover the silver fraction, and the palladium fraction was recovered with Pd-dimethylglyoxime precipitation. The cadmium fraction was taken after precipitation of uranium hydroxide as the effluent with an anion-exchange column. Each sample was collected in a Prindle vial and analyzed with γ-ray spectrometry. An aliquot from each sample (Ag/Pd/Cd) along with a separate set of carrier solutions representing 100% yield were used for ICP-MS measurements to determine chemical recovery yields with yielding uncertainty from repeated sampling. The total uncertainty for the measured fission products includes nuclear data uncertainty in $t_{1/2}$ and γ-ray intensities, counting statistics, chemical recovery uncertainty, and weighted averaging for repeated measurements.

5.5 Results and Discussion

5.5.1 Activation Foils.

The decay-corrected activation products compared to the modeled results and the χ^2 per degree of freedom, ν, are summarized in Table 5.3. The individual χ^2 contribution for a reaction included both modeled and measurement uncertainty added in quadrature. The experiment average activation product measurement is an

average of the GAMANAL and Peak Easy fits with correlated uncertainties. The Peak Easy results were 0.4% to 1.9% larger due to the differences in the peak fitting routine compared to GAMANAL. The measured activation products were used to scale the MC derived reactions to the experimental total fluence from the NIF source environment. The total fluence from the source was determined with χ^2 minimization and was 1.13×10^{16} neutrons.

Table 5.3. Activation product measurements compared to modeled values.

Reaction Product	GAMANAL	Peak Easy	Experiment Average	Modeled
$^{196}Au^{g+m1}$	5.74E+9 ± 3.57%	5.75E+9 ± 3.67%	5.75E+9 ± 3.62%	5.85E+9 ± 4.48%
^{198}Au	2.24E+9 ± 2.01%	2.25E+9 ± 2.03%	2.25E+9 ± 2.02%	2.27E+9 ± 3.64%
^{89}Zr	5.81E+9 ± 2.02%	5.83E+9 ± 2.03%	5.82E+9 ± 2.03%	5.96E+9 ± 4.43%
^{54}Mn	8.65E+9 ± 3.82%	8.65E+9 ± 3.55%	8.65E+9 ± 3.69%	9.24E+9 ± 4.52%
^{56}Mn	3.33E+8 ± 2.12%	3.33E+8 ± 2.06%	3.25E+8 ± 2.09%	4.20E+8 ± 11.79%
$^{113}In^{m1}$	4.50E+8 ± 2.74%	4.50E+8 ± 2.70%	4.49E+8 ± 2.72%	4.46E+8 ± 2.11%
$^{115}In^{m1}$	1.18E+10 ± 5.40%	1.16E+10 ± 5.43%	1.17E+10 ± 5.42%	1.22E+10 ± 2.38%
$^{116}In^{m1}$	1.76E+10 ± 2.35%	1.83E+10 ± 3.06%	1.80E+10 ± 2.71%	1.70E+10 ± 3.41%
^{239}Np (Radiochemistry)	6.77E+6 ± 5.09%	N/A	6.77E+7 ± 5.09%	7.99E+6 ± 3.80%
^{187}W	2.41E+9 ± 2.53%	2.49E+9 ± 3.17%	2.45E+9 ± 2.85%	2.39E+9 ± 3.43%
^{57}Ni	5.55E+8 ± 3.39%	5.85E+8 ± 5.28%	5.70E+8 ± 4.34%	5.65E+8 ± 4.53%
$^{58}Co^{g+m1}$	1.63E+10 ± 2.04%	1.65E+10 ± 2.05%	1.64E+10 ± 2.05%	1.88E+10 ± 2.53%
^{24}Na	3.33E+9 ± 2.35%	3.40E+9 ± 2.06%	3.37E+9 ± 2.21%	3.34E+9 ± 4.34%
$^{196}Au^{g+m1}$	5.00E+9 ± 3.57%	5.05E+9 ± 3.67%	5.03E+9 ± 3.62%	5.15E+9 ± 4.46%
^{198}Au	2.01E+9 ± 2.01%	2.03E+9 ± 2.02%	2.02E+9 ± 2.02%	2.03E+9 ± 2.73%
$\chi^2/\nu = 2.31$ (excluding $^{58}Co^{g+m1} = 1.21$)				

The modeled results with MCNP5, including systematic uncertainty quantified with Sampler, show overall agreement with the exception of $^{58}Co^{g+m1}$, where including $^{58}Co^{g+m1}$ results in a χ^2/ν of 2.31 ($p = 0.004$). Similar research at the NIF has also found a suppression of nearly 27% production of $^{58}Co^{g+m1}$ [175]. $^{58}Co^{g+m1}$ was removed from the unfolding dataset due to these inconsistencies; removing that reaction produces a χ^2/ν of 1.21 ($p = 0.267$). The $^{58}Co^{g+m1}$ product indicates either decreased neutron fluence over the reaction range or the reaction uncertainty was underestimated. There is some evidence to support this may be the case as the ENDF-B/VII.1 uncertainty for this reaction at 14 MeV is ∼9x greater than the uncertainty in IRDFF-II, which was used in Sampler to obtain the integral

uncertainty of 2.53%.

5.5.2 Unfolding.

Table 5.4 summarizes the STAYSL changes to the ETA foil pack activation products following spectral adjustment and the individual χ^2 contributions. The neutron flux environment was constrained by the uncertainty and covariance matrix shown previously in Figure 5.3. The resultant neutron fluence in the sample cavity was $1.49 \pm 0.01 \times 10^{12}$ neutrons cm^{-2}. ^{239}Np and ^{56}Mn had activation product changes of over 10%. ^{56}Mn was in a region of relatively large transport uncertainty as a thermal reaction but also has larger nuclear data uncertainty, reaching 24% at 0.125 MeV. Numerical precision, an inherent feature of the STAYSL code, was also a minor issue as noted in the negative χ^2 contribution for ^{89}Zr. The STAYSL-unfolded spectrum had a $\chi^2/\nu = 1.62$ ($p = 0.071$), which indicates that the modeled spectrum and covariance was in agreement with the experiment for these reaction products.

Table 5.4. STAYSL modifications to reaction products and χ^2 contributions.

Reaction Product	**STAYSL Adjusted % Difference from Measured Reactions**	**χ^2 Contribution**
^{196}Au^{g+m1}	0.74	0.08
^{198}Au	0.83	0.22
^{89}Zr	-0.09	-0.03
^{56}Mn	30.13	1.67
^{113}In^{m1}	-1.88	0.56
^{115}In^{m1}	4.66	0.61
^{116}In^{m1}	-5.20	2.59
^{239}Np	16.80	11.14
^{187}W	-1.22	0.10
^{57}Ni	-3.02	0.32
^{24}Na	-1.77	0.33
^{196}Au^{g+m1}	2.98	0.84
^{198}Au	0.34	0.05
$\chi^2/\nu = 1.62$ ($p = 0.071$)		

Neutron fluence results were compared though the Pearson correlation coefficient

(PCC) and the Kolmogorov-Smirnov (K-S) statistic. The PCC metric, r, provides a measure of the linear relationship between two sets of data. The null hypothesis of the PCC is that there is no correlation between the two datasets. The p-value indicates the probability of an uncorrelated system producing a correlation coefficient at least as large in magnitude. Small p-values (<0.05) indicate a statistically significant PCC.

The K-S two-sample statistic, D, compares the cumulative distribution functions (CDF) between two sets of data. The K-S statistic provides information on the relative magnitude of the distributions and is calculated by the maximum difference between the expected and observed CDF. The null hypothesis for this test is that the two samples were drawn from the same distribution. Unlike the PCC, a large p-value (> 0.05) from the K-S statistic fails to reject the null hypothesis.

The STAYSL unfolded neutron spectrum is shown in Figure 5.6. Activation ranges for several products overlap with the discarded $^{58}Co^{g+m1}$, most notably the threshold indium reactions. The modeled neutron fluence was in agreement with the STAYSL unfolded results with $r = 1$ ($p \sim 0$) and $D = 0.04$ ($p = 1.00$), indicating that the Sampler methodology was representative of the neutron environment covariance matrix. The primary differences in the χ^2 values based on the MC models and STAYSL were the mismatch of group structures, representative environment in Sampler, use ENDF-B/VII.1 in Sampler transport, and numerical precision in STAYSL. Overall, the unfolded neutron spectrum indicates that the modeled neutron spectrum is in strong agreement with the experiment.

5.5.3 Fission Products.

The R_{97} distribution as a function of mass chain for cumulative yield fission products is shown in Figure 5.7. The $N_i^{f,e} \Big/ N_{97}^{f,e}$ values for the distribution, including independent yields not graphed, are provided in Table 5.5 of the 5.6, along

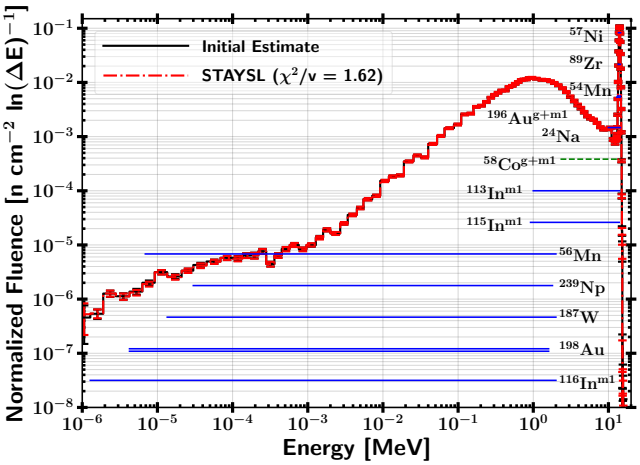

(a) Logarithmic energy scale

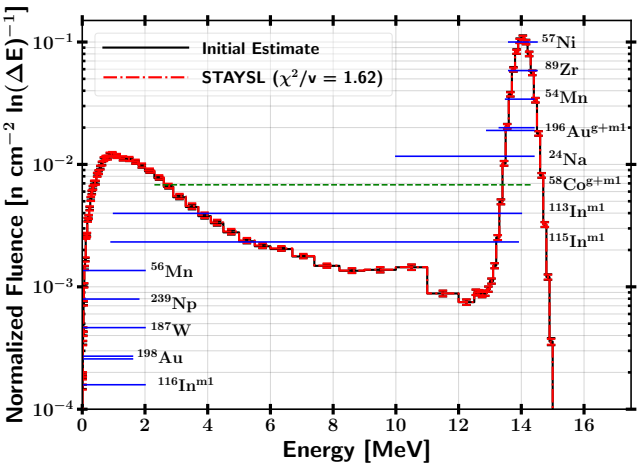

(b) Linear energy scale

Figure 5.6. (Color online) Neutron fluence per unit lethargy for the initial guess and STAYSL unfolded result in a) logarithmic energy scale and b) linear energy scale. The horizontal lines indicate the 5-95% activation ranges. The ^{58}Co^{g+m1} dotted horizontal line was not included in the unfold.

with the modeled neutron fluence in the HEU foils in Table 5.6. The modeled neutron fluence was used instead of the measured fluence due to the optical thickness of the foils resulting in non-negligible attenuation throughout the foil pack as shown in Figure 5.5. Using the benchmarked model allowed the extraction of the fluence at the HEU foils thereby providing a more accurate assessment the neutron fluence seen by the HEU foils. The experimental measurements included 15 mass

chains after radiochemical processing and 21 mass chain measurements by direct γ-ray spectrometry. The cadmium radiochemistry was not successful and was removed from solution with the precipitation of uranium hydroxide.

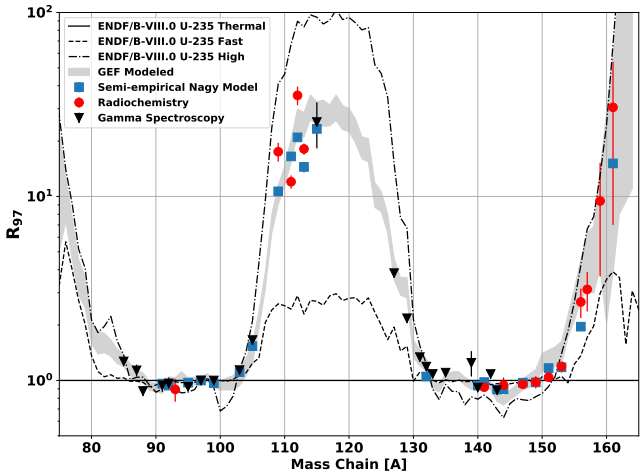

Figure 5.7. (Color online) Comparison between the experimentally measured fission product yields and the modeled GEF and semi-empirical fit. ENDF-B/VIII.0 R values are provided as a reference.

The results show moderate predictive capabilities to reproduce the experimental results. The χ^2/ν for the GEF and semi-empirical fits for the entire distribution were 1.58 and 2.50, respectively. The GEF results that contributed over 2.00 to the χ^2/ν were mass chains 88 ($\chi^2 = 3.5$), 109 (9.1), 111 (4.3), 112 (2.8), 113 (2.7), 129 (6.0), 139 (2.3), 142 (5.2), and 144 (2.3). The semi-empirical fit results, which were only possible for mass chains with sufficient energy-dependent fission product yield data, that contributed more than 2.00 to the χ^2/ν were 109 (10.2), 111 (13.7), 112 (11.3), 113 (5.1), 151 (2.4), and 156 (2.0). The semi-empirical fits had similar performance to GEF. The missing correlation between the energy dependence of fission yields would improve the semi-empirical results if available.

The valley fission product mass chain region between $A = 109 - 113$ were inconsistent with the model. The peak fission products with an R value close to 1 were well modeled; however, the fission product yield is not highly energy

dependent. There are several possible causes for the inability to accurately model mass chain fission product yields. First, there may be an unknown source of systematic uncertainty. Second and related to the radiochemically processed mass chains, the final solutions may contain precipitate particulates which would result in systematically biased recovery yield measurements. Third, recent publications have measured fission product yield as a function of energy that contradict current models for ^{235}U(n,f) [176] and ^{239}Pu(n,f) [138]; therefore, more IFY experiments testing first- and second-chance fission models would be beneficial.

5.6 Conclusions

This work described the capability to modify the NIF D-T neutron spectrum to a moderated TN+PFNS. Customizable neutron spectra allow for increased access to study basic nuclear data such as integral fission product yields and dosimetry cross sections as well as develop integral benchmark experiments. The ETA experiment measured activation reaction products to quantify the experimental environment. IFY were obtained for neutron-induced fission of 93.217% ^{235}U HEU for 36 mass chains and include 47 independent and cumulative yields.

The neutron spectrum was modeled in MCNP5 using ENDF-B/VIII.0 and IRDFF-II nuclear data libraries. Systematic nuclear data uncertainties were calculated through stochastic sampling in SCALE Sampler using an ensemble of 285 realizations of the 252-group ENDF-B/VII.1 library. The CE MCNP5 mean results were used with the multi-group Sampler covariance results as an *a priori* guess spectrum for STAYSL to characterize the neutron flux in the ETA sample cavity with foil activation spectroscopy.

The 15 activation products produced in an activation foil pack were consistent with the model ($\chi^2/\nu = 1.21$) with the exception of ^{58}Co^{g+m1}, which was excluded

from the analysis due to large inconsistencies, which have been reported elsewhere for this reaction channel at the NIF. The $^{58}Co^{g+m1}$ discrepancy will require additional research to resolve. The unfolded neutron spectrum was consistent with the model and passed statistical testing with $\chi^2/\nu = 1.62$ ($p = 0.071$). This indicates that the combination of MCNP5 and SCALE Sampler was adequate for the analysis; however, the model would benefit from improvements to the Sampler multi-group cross section libraries for higher energy environments.

Fission product measurements indicate general agreement between the measurements and the models resulted from GEF and semi-empirical fits. However, silver and palladium valley fission products, along with several others, were not consistent and resulted in large individual χ^2 contributions. A repeated experiment and measurement of these mass chains would be ideal to provide benchmarks for model improvement. The semi-empirical fit performed worse than GEF; however, improvements can be made if fission product yield incident neutron energy correlations were available.

Future work aims to improve upon the ETA design to better match the NIF configuration constraints and increase the neutron fluence in the sample cavity. Additionally, $^{58}Co^{g+m1}$ measurements at NIF are planned to be taken under the D-T environment in addition to a similar moderated spectrum to further explore the large, yet consistent, discrepancies between modeled and experimental results at NIF.

Acknowledgments

This research was supported in part by the U.S. Air Force Technical Application Center (AFTAC) under the AFIT/AFTAC Endowed Term Chair MOA#: 212196 and the Defense Threat Reduction Agency under grant HDTRA-18-27434 and 19-29109.

This work was performed under the auspices of the U.S. Department of Energy by Lawrence Livermore National Laboratory under Contract DE-AC52-07NA27344.

Additionally, the authors would like to thank Todd Woody, Keenan Thomas, Sam Glover, Brent Blue, and Charles Yeamans (Lawrence Livermore National Laboratory), Douglas Peplow and William Wieselquist (Oak Ridge National Laboratory), Larry Greenwood (Pacific Northwest National Laboratory), and Glenn Sjoden (Air Force Technical Applications Center) for their invaluable support of this research.

Appendix: Measured $N_i^{f,e} \Big/ N_{97}^{f,e}$ Values and Neutron Environment

Table 5.5 provides the $N_i^{f,e} \Big/ N_{97}^{f,e}$ values measured for the ETA experiment based on a measured 2.90E+08 ± 2.1% ^{97}Zr atoms per gram of HEU sample. The associated modeled HEU neutron fluence in the STAYSL 129-group structure is shown in Table 5.6. Mass chain yields for A of 92, 131, 132, and 135 were calculated as the sum of both fission products in the respective mass chains. Fission products uncertainty includes nuclear data uncertainty, counting statistics, chemical recovery uncertainty, and weighted averaging for repeated measurements. Large uncertainties above $A = 156$ are primarily due to counting statistics.

Table 5.5. Cumulative (C) and independent (I) $N_i^{f,e} \Big/ N_{97}^{f,e}$ HEU foil fission product values measured directly via γ-ray spectrometry or after radiochemical processing (RC).

Isotope	Measurement Type	Yield Type	$N_i^{f,e} \Big/ N_{97}^{f,e}$	% Error	Isotope	Measurement Type	Yield Type	$N_i^{f,e} \Big/ N_{97}^{f,e}$	% Error
Kr-85m	γ-spectrometry	C	2.79E-01	3.9	I-132	γ-spectrometry	I	2.67E-02	15.8
Kr-87	γ-spectrometry	C	4.84E-01	7.2	I-133	γ-spectrometry	C	1.21E+00	4.2
Kr-88	γ-spectrometry	C	5.22E-01	5.7	I-135	γ-spectrometry	C	1.01E+00	3.0
Sr-91	γ-spectrometry	C	9.15E-01	7.5	Xe-135	γ-spectrometry	I	1.88E-01	5.4
Sr-92	γ-spectrometry	C	9.16E-01	6.9	Cs-136	γ-spectrometry	I	1.04E-02	25.4
Y-92	γ-spectrometry	I	5.20E-02	57.9	Ba-139	γ-spectrometry	C	1.33E+00	15.6
Y-93	γ-spectrometry	C	1.07E+00	14.2	Ba-140	γ-spectrometry	C	9.48E-01	3.4
Y-93	RC	C	9.46E-01	14.3	Ba-140	RC	C	1.03E+00	6.3
Zr-95	γ-spectrometry	C	1.00E+00	3.3	Ce-141	RC	C	8.96E-01	3.3
Zr-97	γ-spectrometry	C	1.00E+00	0.0	La-142	γ-spectrometry	C	1.06E+00	3.3
Mo-99	γ-spectrometry	C	1.02E+00	3.7	Ce-143	γ-spectrometry	C	8.78E-01	3.2
Ru-103	γ-spectrometry	C	5.75E-01	3.4	Ce-143	RC	C	8.56E-01	3.3
Rh-105	γ-spectrometry	C	2.71E-01	5.5	Ce-144	RC	C	8.65E-01	10.2
Ru-105	γ-spectrometry	C	2.66E-01	3.7	Nd-147	γ-spectrometry	C	3.56E-01	8.9
Pd-109	RC	C	9.11E-02	11.7	Nd-147	RC	C	3.57E-01	4.8
Ag-111	RC	C	3.49E-02	8.2	Pm-149	RC	C	1.77E-01	7.6
Pd-112	RC	C	7.71E-02	11.7	Pm-151	RC	C	7.28E-02	5.1
Ag-113	RC	C	4.29E-02	7.1	Sm-153	RC	C	3.15E-02	3.5
Cd-115	γ-spectrometry	C	5.32E-02	27.9	Sm-156	RC	C	6.61E-03	18.2
Sb-127	γ-spectrometry	C	1.00E-01	4.8	Eu-156	RC	C	3.78E-03	27.2
Sb-129	γ-spectrometry	C	1.97E-01	4.6	Eu-157	RC	C	3.21E-03	24.2
I-131	γ-spectrometry	C	5.37E-01	3.8	Gd-159	RC	C	1.59E-03	61.1
Te-131m	γ-spectrometry	C	1.08E-01	8.4	Tb-161	RC	C	4.34E-04	77.1
Te-132	γ-spectrometry	C	8.29E-01	4.9					

Table 5.6. Energy distribution of neutron fluence in HEU sample.

Upper Energy [MeV]	$n - cm^{-2}$	**Relative Error**	**Upper Energy [MeV]**	$n - cm^{-2}$	**Relative Error**	**Upper Energy [MeV]**	$n - cm^{-2}$	**Relative Error**
1.00E-09	0.00E+00	21.34	1.90E-02	1.88E+09	0.04	7.40E+00	7.41E+09	0.05
1.00E-08	8.48E+03	7.91	2.55E-02	4.31E+09	0.04	8.20E+00	6.44E+09	0.06
2.30E-08	1.67E+05	7.25	3.20E-02	4.24E+09	0.03	9.00E+00	5.28E+09	0.08
5.00E-08	7.72E+05	4.69	4.00E-02	3.92E+09	0.03	1.00E+01	6.04E+09	0.09
7.60E-08	8.97E+05	3.12	5.25E-02	8.38E+09	0.03	1.10E+01	5.68E+09	0.08
1.15E-07	1.14E+06	2.83	6.60E-02	9.94E+09	0.03	1.20E+01	3.17E+09	0.07
1.70E-07	1.33E+06	2.02	8.80E-02	1.73E+10	0.03	1.25E+01	1.28E+09	0.06
2.55E-07	1.62E+06	1.10	1.10E-01	1.60E+10	0.03	1.26E+01	2.98E+08	0.06
3.80E-07	2.98E+06	0.94	1.35E-01	2.22E+10	0.03	1.27E+01	2.86E+08	0.06
5.50E-07	3.79E+06	1.20	1.60E-01	1.92E+10	0.03	1.28E+01	2.80E+08	0.06
8.40E-07	5.23E+06	0.64	1.90E-01	2.59E+10	0.03	1.29E+01	2.90E+08	0.06
1.28E-06	3.59E+06	1.11	2.20E-01	2.33E+10	0.03	1.30E+01	3.02E+08	0.06
1.90E-06	4.02E+06	0.51	2.55E-01	2.74E+10	0.03	1.31E+01	3.34E+08	0.05
2.80E-06	1.71E+07	0.20	2.90E-01	2.85E+10	0.03	1.32E+01	4.59E+08	0.05
4.25E-06	1.75E+07	0.19	3.20E-01	2.47E+10	0.03	1.33E+01	7.73E+08	0.05
6.30E-06	1.75E+07	0.28	3.60E-01	3.21E+10	0.03	1.34E+01	1.55E+09	0.05
9.20E-06	2.89E+07	0.18	4.00E-01	3.17E+10	0.03	1.35E+01	3.16E+09	0.05
1.35E-05	4.90E+07	0.14	4.50E-01	3.56E+10	0.03	1.36E+01	6.30E+09	0.05
2.10E-05	5.45E+07	0.17	5.00E-01	3.68E+10	0.03	1.37E+01	1.16E+10	0.05
3.00E-05	5.08E+07	0.12	5.50E-01	3.50E+10	0.03	1.38E+01	1.84E+10	0.05
4.50E-05	6.69E+07	0.14	6.00E-01	3.47E+10	0.03	1.39E+01	2.54E+10	0.05
6.90E-05	8.69E+07	0.12	6.60E-01	4.11E+10	0.03	1.40E+01	3.08E+10	0.05
1.00E-04	8.49E+07	0.13	7.20E-01	4.05E+10	0.03	1.41E+01	3.25E+10	0.04
1.35E-04	7.01E+07	0.15	7.80E-01	3.82E+10	0.03	1.42E+01	2.98E+10	0.04
1.70E-04	5.72E+07	0.14	8.40E-01	3.56E+10	0.03	1.43E+01	2.36E+10	0.04
2.20E-04	7.07E+07	0.21	9.20E-01	4.61E+10	0.03	1.44E+01	1.63E+10	0.05
2.80E-04	8.47E+07	0.22	1.00E+00	4.26E+10	0.03	1.45E+01	9.75E+09	0.05
3.60E-04	3.70E+07	0.20	1.20E+00	8.96E+10	0.03	1.46E+01	5.21E+09	0.05
4.50E-04	4.91E+07	0.20	1.40E+00	7.25E+10	0.03	1.47E+01	2.35E+09	0.05
5.75E-04	8.25E+07	0.19	1.60E+00	6.19E+10	0.03	1.48E+01	8.94E+08	0.05
7.60E-04	1.14E+08	0.16	1.80E+00	5.17E+10	0.03	1.49E+01	3.37E+08	0.06
9.60E-04	8.22E+07	0.13	2.00E+00	4.29E+10	0.03	1.50E+01	9.50E+07	0.09
1.28E-03	1.13E+08	0.10	2.30E+00	5.18E+10	0.03	1.51E+01	2.41E+07	0.16
1.60E-03	1.35E+08	0.09	2.60E+00	3.99E+10	0.03	1.52E+01	5.43E+06	0.30
2.00E-03	1.87E+08	0.08	2.90E+00	3.02E+10	0.04	1.53E+01	3.90E+06	0.51
2.70E-03	1.79E+08	0.09	3.30E+00	2.94E+10	0.04	1.54E+01	1.88E+05	0.87
3.40E-03	2.30E+08	0.10	3.70E+00	2.18E+10	0.05	1.55E+01	6.88E+03	1.00
4.50E-03	4.15E+08	0.09	4.10E+00	1.64E+10	0.05	1.56E+01	6.37E+04	0.68
5.50E-03	4.03E+08	0.09	4.50E+00	1.30E+10	0.05	1.57E+01	3.21E+04	0.73
7.20E-03	8.17E+08	0.08	5.00E+00	1.24E+10	0.05	1.58E+01	9.86E+03	1.00
9.20E-03	8.31E+08	0.06	5.50E+00	9.51E+09	0.04	1.59E+01	0.00E+00	0.06
1.20E-02	1.68E+09	0.05	6.00E+00	7.89E+09	0.04	1.60E+01	0.00E+00	0.06
1.50E-02	1.71E+09	0.05	6.70E+00	9.44E+09	0.04	1.65E+01	5.29E+04	1.00

VI. ATHENA Experiment

This chapter was derived from a manuscript submitted in June 2021 with *Nuclear Instruments and Methods in Physics Research Section A* titled "ATHENA: A Unique Radiation Environment Platform at the National Ignition Facility [39]." The author list included Nicholas J. Quartemont, George Peterson, Adib Samin, Darren Holland, James C. Petrosky, and James E. Bevins from AFIT/ENP, Colton Moran and Buguo Wang from the Department of Engineering Physics at Wright State University, and Charles Yeamans and Brandon Woodworth from LLNL. Sections 6.5.2.2 and 6.5.2.1 contain analysis not performed by the main author.

The article has been modified to fit this dissertation format; however, the content was unchanged. The ATHENA platform was developed as a next generation ETA, where the efficiency was increased both from an efficiency of spectral shaping and facility constraints. The ATHENA platform drawer was demonstrated to have a 3.6×10^{12} $\frac{n}{cm^2}$ at a stand-off of 6 cm for a 10^{16} yield NIF shot, while the ETA platform would perform slightly less efficient at 2.6×10^{12} $\frac{n}{cm^2}$. ATHENA represents a 2.7 times more efficient device, as the ETA platform was only able to attain a stand-off from the NIF source of 15 cm, leading to a reduced 1.3×10^{12} $\frac{n}{cm^2}$. Furthermore, the ATHENA platform has enhanced flexibility to act as an active diagnostic platform.

6.1 Abstract

This paper describes the ATHENA platform, an energy tuning assembly, which was developed to spectrally shape the National Ignition Facility (NIF) deuterium-tritium fusion neutron source to a thermonuclear (fusion) plus prompt fission neutron spectrum. This unique, otherwise inaccessible radiation environment complements existing experimental facilities and capabilities. The flexible ATHENA

irradiation positions were modeled in Monte Carlo simulations to characterize the radiation environments on the platform. Validation of the internal neutron spectrum produced from fielding ATHENA at the NIF occurred through neutron flux unfolding with 20 measured activation products. The modeled neutron flux distribution was determined via stochastic sampling of the radiation transport cross sections. The STAYSL unfolded neutron flux resulted in a reduced χ^2 value of 1.4 with a larger contribution from ^{46}Ti(n,2n) reaction channel. The NIF experiment demonstrated that ATHENA is capable of producing a thermonuclear and prompt fission neutron spectrum with a 50 nanosecond pulse width and a 1-MeV equivalent neutron fluence of 3.6×10^{12} $\frac{n}{cm^2}$ with strong radial uniformity over the sample volume. Example case studies of ATHENA for integral experiments and microelectronic device responses are also presented.

6.2 Introduction

Customizable neutron source development through energy tuning assemblies (ETAs) provides a capability to explore inaccessible radiation environments by spectrally modifying existing neutron facilities [4, 37, 97, 177]. These unique environments can have key applications in nuclear sciences and engineering such as nuclear data and validation experiments to benchmark integral experiment models. Additionally, these customizable radiation sources can be used to further radiation effects on electronics testing to provide a spectrally accurate source term on relevant timescales. Current and past sources for neutron testing have limitations on the neutron energy spectrum, timing, and γ-ray contributions to the radiation environment, a long standing challenge for the community [178]. Fast burst reactors such as the dismantled Sandia Pulse Reactor-III or at White Sands Missile Range have proved to be the gold standard for prompt fission spectrum neutron irradiation

with 5×10^{14} 1-MeV(Si) $\frac{n}{cm^2}$ over longer nuclear weapon relevant time-scales [20, 21]. However, due to concerns over special nuclear material and increased development, other types of facilities have seen an increase in utilization as neutron sources for national security experiments.

Facilities such as the National Ignition Facility (NIF) can provide a clean source of 14.1 MeV neutrons from deuterium-tritium (D-T) fusion reactions above 10^{13} 1-MeV(Si) $\frac{n}{cm^2}$ with little γ-ray contamination [22]. The 1-MeV(Si) fluence, a common equivalency used for radiation effects testing, is represented as a weighted integration of neutron fluence with the weighting function based on the equivalency of energy-dependent displacement damage as outlined in ASTM $19-722$ [19]. Spallation neutron sources like the Los Alamos Neutron Science Center (LANSCE) can provide 2×10^{12} 1-MeV(Si) $\frac{n}{cm^2}$ over a short 100+ ns timescale with a low γ-ray environment, but the neutron spectrum is spread over a much larger and higher range of neutron energies [179]. Ion beam sources can produce near 5×10^{13} 1-MeV(Si) $\frac{n}{cm^2}$ over a moderate 40 μs timescale, but they also require an equivalence factor between ion and neutron damage [179, 180]. Nuclear reactors such as the Annular Core Research Reactors can produce in excess of 10^{15} 1-MeV(Si) $\frac{n}{cm^2}$ over a longer 6 ms timescale in pulsed mode; however, they include a larger ionizing dose with a thermalized neutron spectrum [23].

The ATHENA platform was designed as an ETA to produce a thermonuclear and prompt fission spectrum (TN+PFNS) through spectral modification of the NIF D-T neutron source. The payload is a second-generation design to the precursor ETA proof-of-concept platform. The original ETA design, fielded at the NIF to measure highly enriched uranium fission products, produced a prompt TN+PFNS and validated the modeling methodology [177]. Improvements to the ATHENA platform from the original ETA include an optimized physical geometry that allows for a

6 cm standoff range to the NIF source (compared to the previous 15 cm), improved efficiency (higher fluence at the target position), and reduced weight allowing more flexible implementation. Additionally, the experimental irradiation volume has been expanded to a 7 cm diameter, 8 cm high cylindrical irradiation configuration with an external primarily D-T irradiation position to allow for multiple, larger experiments to be conducted on one platform. The enhanced capability on ATHENA can provide up to 3.6×10^{12} 1-MeV(Si) $\frac{n}{cm^2}$ for a 10^{16} source neutron D-T shot yield on a 50 ns timescale.

This paper is organized as follows. Section 6.3 describes the optimization and design of the ATHENA payload and supporting diagnostic equipment available. Section 6.4 outlines the radiation environment, modeling methodology, and provides validation of the ATHENA resulting source environment during a NIF shot. Section 6.5 provides use-cases for the ATHENA platform to include integral nuclear data measurements and microelectronic device responses under the unique ATHENA environment. Finally, Section 6.6 summarizes the uncertainty quantification techniques and provides a path forward for future work.

6.3 Experimental Setup

This section describes the optimization of the internal ATHENA neutron spectrum, mechanical hardware, and supporting diagnostics for experiments. The experimental concept allows for an internal spectrally-shaped neutron spectrum and optional externally-mounted irradiation position, which adds to the experimental efficiency to take multiple, equivalent 1-MeV(Si) fluence, measurements on the ATHENA platform. The internal radiation environment cavity utilizes a removable plug to add the larger irradiation volume for the spectrally-modified neutron source, and the internal neutron environment is characterized with an drawer containing

activation foils. The ATHENA validation experiment, discussed further in Section 6.4.2.1, is shown in Figure 6.1 for an experimental validation of the internal radiation environment created 9 cm from the NIF target chamber center (TCC) during NIF shot N201128-001, where the experiment was not performed at the smallest distance of 6 cm. A repository containing the ATHENA design, materials, and models used in this work was made available here [181].

6.3.1 Design Optimization.

ATHENA was designed with the ETA software, Coeus V1.0 [35], leveraging the Gnowee metaheuristic optimization algorithm [182]. Coeus functions as a wrapper to call MCNP [47] neutron transport simulations for candidate ETA designs provided by Gnoewee. Each candidate ETA design was defined with an outer design envelope containing cylinders and cones that are filled with materials to spectrally modify the NIF point neutron source into a target neutron spectrum. The population-based Gnowee algorithm optimized the ATHENA geometry and materials based on a set of objectives and constraints with heuristic search strategies described in previous work [182].

The objective function was defined as a desired TN+PFNS relevant to nuclear neutron environments within the ATHENA sample drawer shown in Figure 6.1. A combination of 85% volume distributed fission spectrum neutrons and 15% D-T point source neutrons were transported within a 10.2 cm beryllium reflected highly enriched uranium (HEU) critical assembly [183]. The volume-averaged neutron flux within the critical assembly was used for the objective TN+PFNS.

Two general constraints were applied to the ATHENA optimization. First, candidate designs required a minimum threshold neutron fluence of 3×10^{12} n-cm^{-2} in the drawer sample cavity. Second, there were several NIF facility constraints

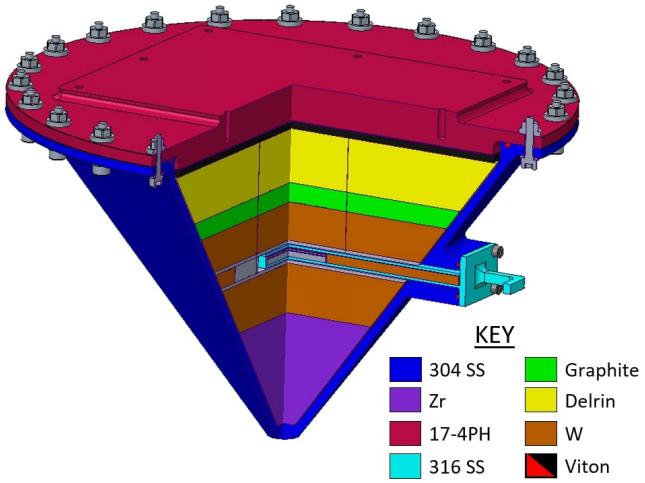

Figure 6.1. (Color online) N201129-001 NIF shot ATHENA platform. The ATHENA neutron spectral-shaping package was mounted on diagnostic instrument mount 90-348 and the D-T capsule target was at the end of the target positioner, 9 cm from the base of ATHENA.

including the weight and ATHENA geometry envelope. The weight was constrained to a maximum of 120 kg; the fluence and weight constraint were implemented by discarding a candidate design if the constraint was not met. The design was set 6 cm from the D-T source at target chamber center (TCC) based on the facility's laser exclusion zones, and the design was constrained to a maximum diameter of 30 cm based on the available ports to field the platform.

The Coeus resultant ATHENA design with engineering modifications and additional manufacturing detail is shown in Figure 6.1. Engineering modifications were made to the design to remove non-contributing components and increase the thermal neutron population with the addition of the back polyoxymethylene (Delrin) thermoplastic layer, leading to the final ATHENA hardware discussed in Section 6.3.2. Isotopic concentration uncertainty was limited by utilizing materials between 99 to 99.95% purity. The front zirconium and tungsten layers provide the primary inelastic and (n,2n) reaction channels as a source term for the PFNS. The back carbon and Delrin layers increase the low-energy neutron population in the assembly while also acting as a reflector to increase the overall fluence in the

experimental cavity.

The available irradiation positions on ATHENA are highlighted in Figure 6.2. The spectrally shaped internal radiation environment includes a drawer sample region and removable plug cylindrical volume. The external environment, with minimal spectral shaping, is positioned to face the target chamber center (TCC), which is the source position of the D-T fusion neutrons.

6.3.2 Mechanical Hardware.

The internal ATHENA cavity was created with a removable plug past the primary spectral modification material, allowing for an expanded device irradiation volume and room for connecting electronics. A rapidly-extractable sample drawer is positioned containing neutron activation foils and thermoluminescent dosimeters (TLDs) to measure the neutron and ionizing radiation environment, respectively. The internal cavity region is accessible post-shot through a port in the back of the platform.

The external region contains a removable sled that is also accessible through the port, and a second diagnostic set of activation foils and TLDs can be positioned here. Retrieval times are dependent on facility safety constraints based on the achieved source yield for a shot; samples for a 1×10^{16} neutron yield can typically be recovered for analysis within a couple of hours.

The ATHENA platform was designed with re-usable internal components, but they can be replaced for quasi-customizable environments within the assembly's defined outer-envelope. Additionally, replacing spectral modification material layers could directly test specific isotopic reaction contributions to the integral result in validation experiments.

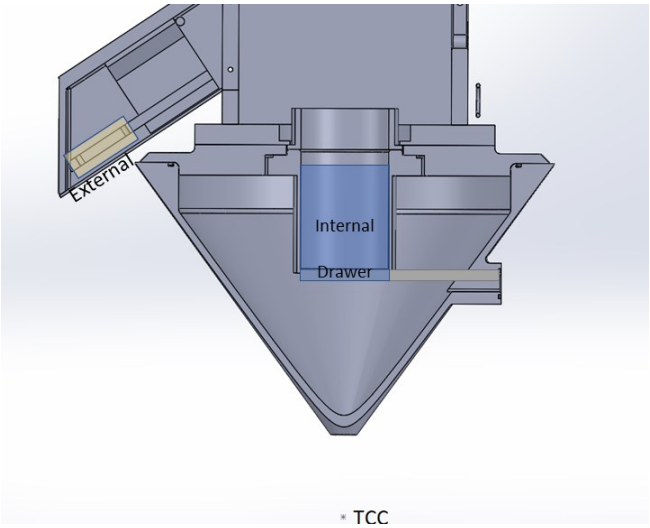

Figure 6.2. (Color online) ATHENA platform with internal drawer, internal cavity, and external arm irradiation positions.

6.3.3 Diagnostics.

Radiation environments can be characterized with both passive and active diagnostics to benchmark models and inform on experimental conditions. Two passive diagnostics utilized on the ATHENA platform are activation foils and TLDs, to measure the integral neutron and ionizing radiation environments, respectively. Active diagnostics can include radiation measurement devices such as chemical vapor deposition diamond detectors or powered semiconductor component devices.

The neutron diagnostic activation foils fielded for the ATHENA environment validation experiment are summarized in Table 6.1. Each of the reactions are included in the International Reactor Dosimetry and Fusion File (IRDFF) nuclear data library and have half-lives to allow post-experiment spectroscopy from several hours to days [48]. The materials and reactions were chosen to cover the broad energy range of the modified neutron spectrum, while maintaining an optically "thin" foil stack. The measured resulting activation products were used to unfold the experimental neutron energy spectrum.

The internal drawer of ATHENA also has positions for eight 3.2x3.2x0.89 mm

Table 6.1. Neutron spectrum unfolding activation foils and reactions utilized for ATHENA irradiation positions.

Foil (Thickness)	Mass [g]	Reaction	Threshold [MeV] (@ 10 mb)	Primary Radiation [keV] (Intensity)	$t_{1/2}$	Decay Data
Au-1 (0.05 mm)	1.883	^{197}Au(n,2n)^{196}Au^{g+m1}	8.1 (8.3)	355.7 (0.87)	6.17 days	[150]
		^{197}Au(n,γ)^{198}Au	Thermal	411.8 (0.9562)	2.69 days	[151]
Ni (0.23 mm)	4.073	^{58}Ni(n,2n)^{57}Ni	12.4 (13.3)	1,378 (0.817)	35.6 hrs	[160]
		^{58}Ni(n,p)^{58}Co^{g+m1}	0 (1.3)	810.8 (0.9945)	70.86 days	[161]
In (0.27 mm)	3.665	^{113}In(n,n')^{113}In^{m1}	0.4 (0.7)	391.7 (0.6494)	99.5 min	[155]
		^{115}In(n,n')^{115}In^{m1}	0.336 (0.597)	336.24 (0.459)	4.49 hrs	[156]
		^{115}In(n,γ)^{116}In^{m1}	Thermal	1293.56 (0.848)	54.29 min	[157]
Al (0.73 mm)	3.793	^{27}Al(n,a)^{24}Na	3.25 (6.7)	1368.63 (0.9999)	15 hrs	[162]
Ti (0.25 mm)	2.112	^{46}Ti (n,2n) ^{45}Ti	13.5 (14)	511.0 (1.696)	184.8 min	[184]
		^{nat}Ti(n,x)^{46}Sc	2.1 (6)	1120.5 (0.9999)	83.79 days	[185]
		^{nat}Ti(n,x)^{47}Sc	0.8 (10.5)	159.38 (0.683)	3.3492 days	[186]
		^{nat}Ti(n,x)^{48}Sc	3.3 (7.5)	1312.1 (1.001)	43.67 hrs	[187]
W (0.12 mm)	4.304	^{186}W(n,γ)^{187}W	Thermal	685.51 (0.332)	24 hrs	[159]
Zr (0.27 mm)	3.083	^{90}Zr(n,2n)^{89}Zr	12.1 (12.1)	909.2 (0.9904)	78.41 hrs	[152]
Mg (0.09)	0.318	^{24}Mg(n,p)^{24}Na	4.9 (6.4)	1368.63 (0.9999)	15 hrs	[162]
Au-2 (0.05 mm)	1.884	^{197}Au(n,2n)^{196}Au^{g+m1}	8.1 (8.3)	355.7 (0.87)	6.17 days	[150]
		^{197}Au(n,γ)^{198}Au	Thermal	411.8 (0.9562)	2.69 days	[151]

Thermo Fisher Scientific TLD-400 and/or TLD-100 chips for a passive integral ionizing dose measurement. Similar to the activation foils, the same capability to field eight TLD chips also exists for the external position. For the ATHENA-I experiment four TLD-400 chips were fielded.

Active diagnostics within the NIF facility are also important for modeling the radiation environment for these types of experiments. The D-T shot yield to scale modeling results can be determined with neutron activation spectrometers relying on ^{90}Zr(n,2n) to determine the primary D-T yield [188]. The emission neutron energy spectrum, total yield, and the plasma ion temperature can be measured with neutron time-of-flight (nTOF) scintillators available within the chamber [189]. Additionally the source emission angular distribution, which is generally considered as an isotropic point source, can be assessed with pinhole neutron topography measurements [190].

6.4 Environment Characterization

The ATHENA radiation environment was characterized with Monte Carlo radiation transport codes, and the internal neutron and γ-ray fields were experimentally validated during an integral measurement experiment. MCNP6 was used to model the continuous energy radiation transport environment, and the SCALE 6.3 Beta 14 MAVRIC and Sampler modules were used to assess the effect of nuclear data covariance on the neutron transport throughout the geometry [45, 47]. The internal ATHENA irradiation position in the drawer was validated using temporal and energy integrated activation foils to unfold the neutron fluence spectrum. Additionally, TLD-400s (CaF_2:Mn) were fielded to provide an integrated ionizing dose measurement inside the sample cavity.

6.4.1 Simulation Methodology.

The modeling and nuclear data covariance methodology have been introduced in previous work on the original ETA [97, 177]. The as-fielded ATHENA platform and the surrounding NIF equipment were modeled in MCNP6 to obtain the continuous energy radiation environments in the sample irradiation positions using a full-scale NIF model. SCALE 6.3 Beta 14 MAVRIC-shift with Sampler was used to propagate nuclear data covariance in the neutron transport model to bound the neutron spectrum for unfolding with STAYSL [45, 47]. MAVRIC simulations were then used in a 1597 energy group structure with the SCALE Sampler module to assess the effect of nuclear data covariance through stochastic sampling of the neutron energy group ENDF-B/VIII.0 nuclear data library [166].

The IRDFF nuclear data library was used for activation foil reaction cross sections and covariance matrices [48, 68]. The IRDFF v.1.05 library was used here due to compatibility with the currently obtained release of STAYSL; however,

minimal changes for the chosen reactions have been updated in the IRDFF-II library. Updated reactions include ^{197}Au(n,γ)^{198}Au. Additionally, the updated IRDFF-II library includes natural titanium reaction products that have multiple production pathways. Not using the IRDFF-II library resulted in negligible impact to the experiment analysis, but not having the natural target reaction product measurements required splitting the contributions for scandium reaction products based on the modeled reactions.

6.4.2 Neutron Environment.

The polar-direct-drive exploding pusher (PDXP) neutron source fielded for the ATHENA experiment, one of the available targets at the NIF, utilizes a gas filled D-T mixture without a hohlraum [191]. Capsules typically have low mass which significantly reduces down-scattering within the target area resulting in a nearly pure D-T fusion neutron spectrum [192]. The laser driven targets can achieve neutron yields on the order 10^{16} with an ion-temperature of approximately 10 keV and an emission time near 300 ps.

The ATHENA shot source utilized a 50/50 D-T mix capsule with a 1.96 mg mass, 23 μm thick, and 4.95 mm outer diameter. The NIF laser system delivered 1.58 MJ of laser energy yielding $6.35 \pm 0.24 \times 10^{15}$ neutrons over 500 ps [193]. The NIF source was modeled based on the nTOF signal located at position 116-316, the most closely positioned detector to ATHENA, for the initial ATHENA experiment position at 90-348. The neutron spectrum in the room does have anisotropies, so using the closest diagnostic is important to capture some of the energy dependence as a function of position in the chamber. The experimental neutron spectrum, depicted in Figure 6.3, was calculated based on the nTOF signal using a linear least squares fit to the convolution of the neutron spectrum with the nTOF instrument response

function and detection efficiency [189].

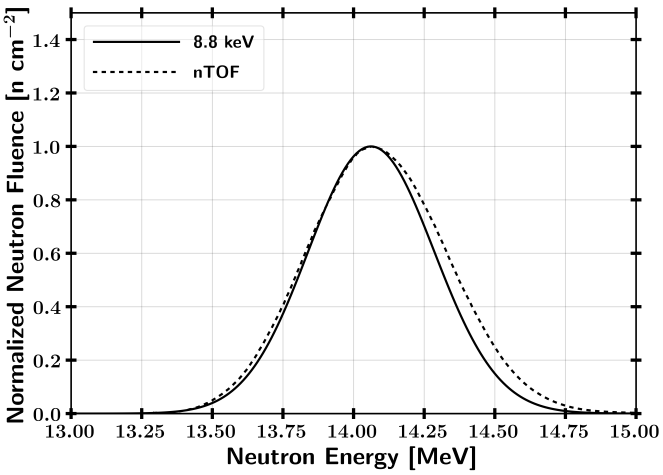

Figure 6.3. NIF shot N201128-001 calculated neutron spectrum on nTOF 116-316 in comparison to a theoretical 8.8 keV ion-temperature model [194].

The experimental source spectrum was generally in agreement with a theoretical plasma distribution with a 8.8 keV ion-temperature plasma based on [145]; however, there was an increase in high energy neutron population due to upscattering reactions within the source itself. Also noteworthy is that the increase in high energy neutrons was not seen on nTOF 90-174, further indicating the angular asymmetry of the PDXP source. Time dependence in the neutron source was neglected in the Monte Carlo simulations due to short emissions relative to the neutron transport component within ATHENA [164].

Figure 6.4 highlights the simulated induced neutron environments, where the plug is removed. The drawer and center cavity results indicate that the internal environments produced during a NIF shot provide a nearly uniform TN+PFNS, where the thermal population of neutrons increases farther back in the cavity. The external neutron spectrum is primarily uncollided source neutrons with a scattered PFNS contribution from the central ATHENA platform itself.

The simulated neutron fluence covariance results for the internal drawer neutron spectrum from 300 samples in Sampler running MAVRIC with the 1597-group

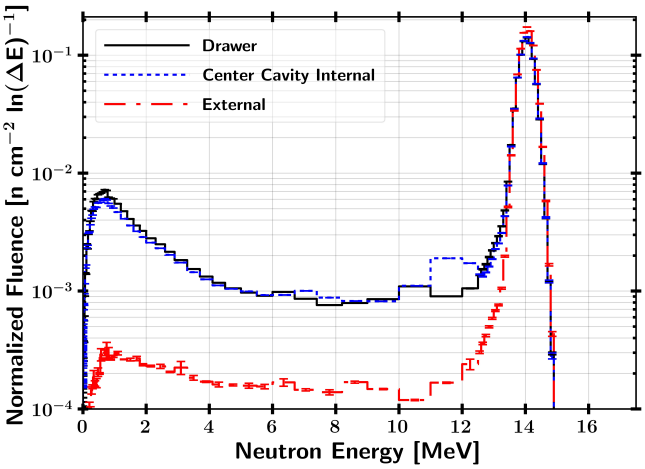

(a) Linear Energy Scale

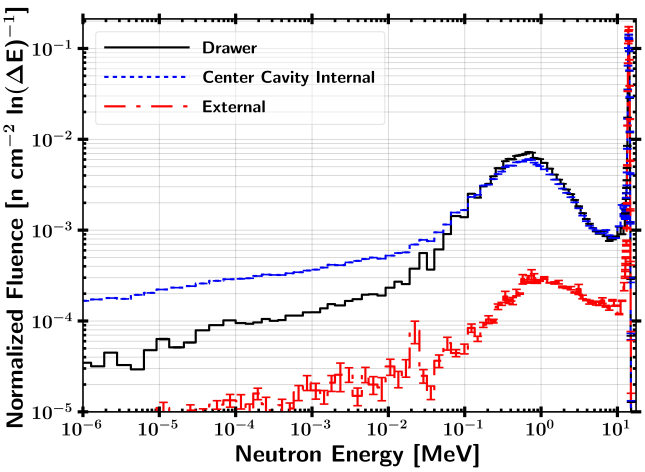

(b) Logarithmic Energy Scale

Figure 6.4. (Color online) ATHENA internal drawer, center cavity, and external neutron spectra highlighting the spectrally shaped neutron and external D-T neutron environments achievable for testing.

structure were characterized with statistical bootstrapping to determine a 1-σ uncertainty in the fluence distribution mapped to the 129-group STAYSL structure. The Sampler neutron transport uncertainty and flux correlation matrix for the internal cavity spectrum are shown in Figure 6.5. The resultant covariance matrix was used in STAYSL to bound the neutron flux distribution.

At energies approaching the source D-T neutrons, the uncertainty is approximately 1-2%. Near 1 MeV, the uncertainty was lower than the source region

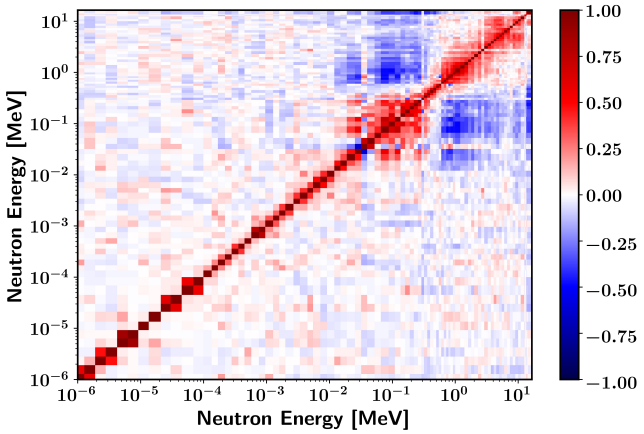

(a) Correlation matrix

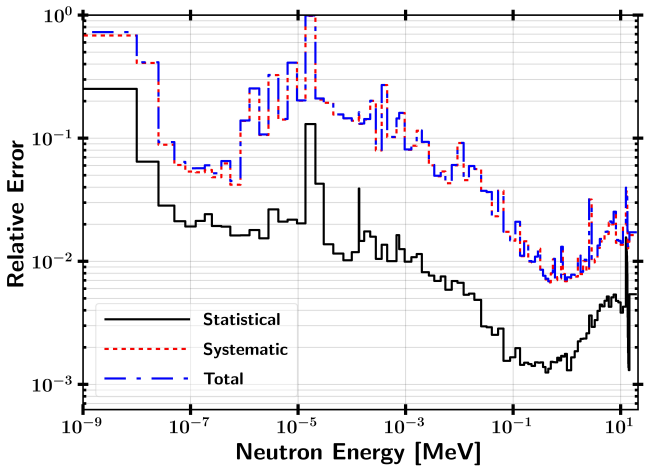

(b) Relative Uncertainty

Figure 6.5. (Color online) Neutron fluence covariance parameters for internal ATHENA sample cavity showing the a) correlation matrix and b) relative statistical and systematic uncertainty as a function of energy. The covariance matrix formed from the correlation matrix and relative uncertainty was used to bound the neutron spectrum unfolding in STAYSL.

because multiple reactions paths over few interactions are able to populate this region. At lower energies, the uncertainty grows to nearly 100% due to the large amount of scattering reactions required to reach these energies. Additionally, the radiative capture resonances in the tungsten layer cause large uncertainty near 10 eV, where even small uncertainties can compound over the tens to hundreds of mean free paths required to pass into the sample drawer. Note, the ENDF-B/VIII.0

library, which was the source of the nuclear data covariance, did not include W(n,2n) reaction uncertainty. Thus, the results underestimate the uncertainty and correlation between the TN and PFNS components.

6.4.2.1 ATHENA-I Validation.

ATHENA was fielded at 9 cm from TCC on diagnostic instrument manipulator (DIM) 90-348. This position is 3 cm farther from the minimum distance that the platform can be placed due to an external flange obstructing the laser paths, and the design has been updated for future experiments to remove this piece, as shown when comparing Figures 6.1 and 6.2. The activation analysis performed was similar to the method outlined in previous research on the ETA experiment [177]. Post-shot activation analysis was performed on the activation foils with γ-ray spectrometry using three high purity germanium (HPGe) and multi-channel analyzer systems in the Lawrence Livermore National Laboratory counting facility [30]. PeakEasy 4.99 was used for peak fitting with energy-dependent counts and efficiency as calculated with GAMANAL [167, 195]. Standard calibration sources were used to determine each HPGe detector's efficiency as a function of sample position, energy, and detector geometry.

Each foil was counted until approximately 10,000 counts were detected, and the activity measurements were decay corrected to the reaction product atoms immediately after irradiation. A variance-based weighted average was taken for each decay γ-ray associated with a product nuclei for each measurement of that decay mode [43]. The final weighted average of each γ-ray decay mode measurement was then completed to determine the amount of each product. Radioactive decay uncertainties were added in quadrature after accounting for the statistical error and a 2% detection systematic error [43].

The measured foil activation products were used with the modeled MCNP6 neutron fluence and SCALE Sampler neutron fluence covariance to unfold the neutron spectrum using STAYSL with the IRDFF v.1.05 129-energy group structure. STAYSL determines the incident neutron flux using a generalized least-squares spectral adjustment based on a χ^2 comparison of the measured activation products and the activities calculated from an adjusted flux [52]. Additionally, STAYSL requires an initial guess spectrum as the activities produced for the foils are often degenerate with multiple possible creation environments. However, the initial spectrum allows for a physics and modeling-based result to guide the overall result.

The neutron irradiation time is much shorter than the half-lives of the product isotopes, so the effects of saturation and decay during irradiation are negligible. Reaction channels with multiple feeding paths were split based on the modeled contributions. Activation foil self-shielding correction factors were created based on the MCNP6 model [177].

The experimental results for 20 activation products used in STAYSL are summarized in Table 6.2. For each reaction, the saturation activity, σ-ϕ, and associated measurement error are given. The saturation activity utilized the short-pulse approximation, where the value reflects the equivalent total number of atoms produced divided by the total target atoms. STAYSL χ^2 contributions include the difference from the measurement to the optimized modeled solution with covariance information from the measurement, neutron fluence, and activation cross sections. Additionally, the percent error relative to the measurement and 5 - 95% activation range where the activation product informs the unfolding procedure are provided.

The STAYSL unfolded neutron spectrum for the internal drawer of ATHENA is

Table 6.2. ATHENA validation experiment reaction channels for STAYSL unfolding with measured value and error. The χ^2 contribution to the total and percent error from the model are also given, where negative percent errors represent that an activation product was under-produced at the experiment. The 5 - 95% activation energy range corresponds to the energy interval where the activation products inform the unfold.

Measured Reaction	Measurement [σ-ϕ]	Measurement Error [%]	STAYSL Adjusted χ^2 Contribution	Percent Error [%]	5 - 95% Activation Energy Range [MeV]
^{197}Au(n,2n)^{196}Au^{g+m1}-1	8.803E-13	3.90	0.3	2.3	13.2 - 14.4
^{197}Au(n,γ)^{198}Au-1	9.017E-13	2.10	0.1	0.7	5E-8 - 0.60
^{58}Ni(n,2n)^{57}Ni	9.543E-15	5.50	1.1	-5.7	13.6 - 14.5
^{58}Ni(n,p)^{58}Co^{g+m1}	2.040E-13	2.00	2.0	3.6	2.9 - 14.3
^{113}In(n,n')^{113}In^{m1}	1.098E-13	2.40	0.6	-1.9	0.92 - 14.2
^{115}In(n,n')^{115}In^{m1}	1.439E-13	5.60	2.1	-8.2	0.84 - 14.2
^{115}In(n,γ)^{116}In^{m1}	1.272E-12	3.40	0.0	-0.5	5E-8 - 0.84
^{27}Al(n,a)^{24}Na	5.082E-14	2.10	0.6	1.7	12 -14.4
^{46}Ti(n,2n)^{45}Ti	6.482E-15	2.70	8.5	-20.9	13.8 - 14.5
^{46}Ti(n,p)^{46}Sc	1.120E-13	2.40	1.7	4.2	7.4 - 14.4
^{47}Ti(n,x)^{46}Sc	1.412E-14	2.40	0.7	6.4	13.6 - 14.5
^{47}Ti(n,p)^{47}Sc	6.662E-14	2.60	0.7	-3.5	2.9 - 14.4
^{48}Ti(n,x)^{47}Sc	2.568E-15	2.60	0.0	-0.7	13.6 - 14.4
^{48}Ti(n,p)^{48}Sc	2.603E-14	2.30	0.0	-0.5	12.8 - 14.4
^{49}Ti(n,x)^{48}Sc	1.174E-15	2.30	1.7	16.0	13.6 - 14.5
^{186}W(n,γ)^{187}W	2.000E-13	3.30	1.9	4.6	2.3E-8 - 1.0
^{90}Zr(n,2n)^{89}Zr	2.382E-13	2.30	0.3	-1.2	13.6 - 14.4
^{24}Mg(n,p)^{24}Na	8.392E-14	2.30	3.6	-4.3	11 - 14.4
^{197}Au(n,2n)^{196}Au^{g+m1}-2	8.450E-13	8.40	0.1	2.6	13.2 - 14.4
^{197}Au(n,γ)^{198}Au-2	1.156E-12	2.00	0.3	-1.1	5E-8 - 0.50

shown in Figure 6.6. The STAYSL χ^2 per degree of freedom was 1.38, indicating general agreement with the modeled neutron flux and covariance. The ^{46}Ti(n,2n)^{45}Ti reaction showed the largest deviation from the model, where the other high energy reaction products aside from ^{45}Ti agreed with the model. The NIF neutron source is not isotropic, and the nTOF detectors are not perfectly aligned with the experimental platforms. It is possible that the neutron spectrum at the ATHENA platform on 90-348 was different than on 116-316. Additionally, the missing covariance information for W(n,2n) reactions underestimated the uncertainty, which would require evaluated data available in SCALE to remedy.

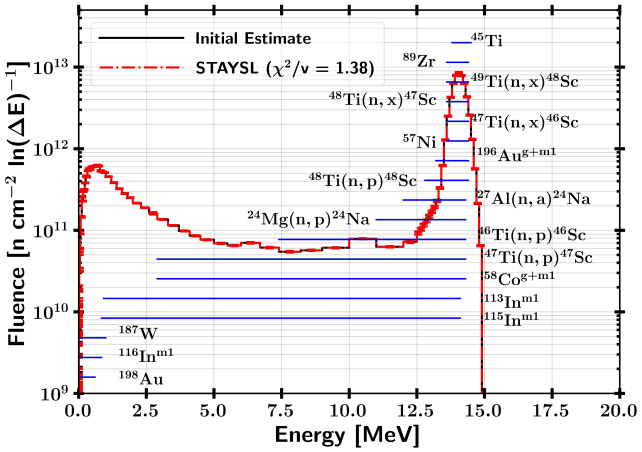

(a) Linear Energy Scale

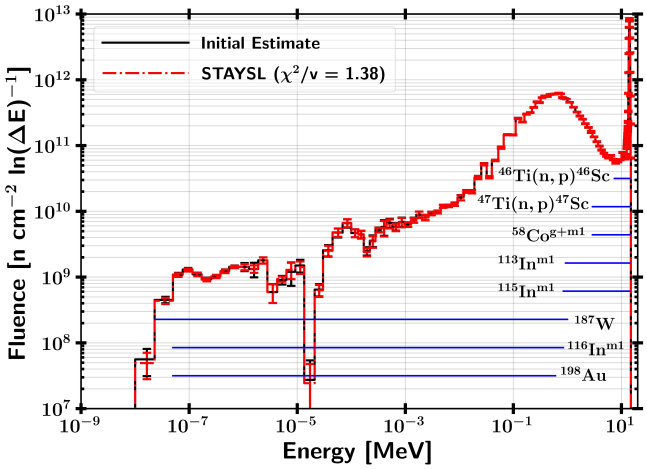

(b) Logarithmic Energy Scale

Figure 6.6. (Color online) STAYSL unfolded ATHENA internal drawer neutron spectrum for the validation shot with a) linear and b) logarithmic energy scales. The blue horizontal lines indicate the 5 to 95% activation range where the activation product informs the unfolded neutron spectrum.

6.4.2.2 Neutron displacement damage.

Neutron displacement damage and related effects are also an important characteristic of the ATHENA environments. Engineering-level neutron environmental metrics have been historically used to define a neutron spectrum and fluence in terms of mono-energetic neutrons defined in ASTM E722−19 [19, 90]. These metrics are applicable when the majority of displacement damage is from

neutrons above 10 keV and assumes charged particle equilibrium. For example, the displacement damage function, $F_{D,material}$, can be used to relate an observable effect, such as the gain degradation of a silicon-based transistor. For example, the 1-MeV neutron equivalent fluence for elemental silicon is given by,

$$\Phi_{eq,1-MeV,Si} = \frac{\int_0^\infty \Phi(E) F_{D,Si}(E) dE}{F_{D,1-MeV,Si}}, \tag{6.1}$$

where the neutron fluence ,$\Phi(E)$ is convolved with $\mathrm{F}_{D,Si}$ and normalized by a reference value of 95 MeV$-$mb for the 1 MeV neutron damage function. $\mathrm{F}_{D,Si}$ was calculated using the ASTM standard for ENDF/B-VIII.0 cross sections in natural silicon using the Robinson energy partition function [19]. Additionally, the hardness of a spectrum, which signifies the representative energy of a neutron spectrum for irradiation, is scaled by the integral of $\Phi(E)$ over all energies with

$$H_{1-MeV,Si} = \frac{\Phi_{eq,1-MeV,Si}}{\int_0^\infty \Phi(E) dE}. \tag{6.2}$$

Similarly, the Nortgett, Robinson, and Torrens (NRT) damage energy normalization can be used to account for the threshold recoiling ion energy to cause a displacement, E_d, from a lattice site [92]. The NRT damage energy was provided and calculated in the same manner as ASTM 722$-$19 but includes integrating over the threshold required to produce a Frenkel pair in the lattice [91, 93]. The ASTM 722$-$19 displacement kerma and NRT damage energy function are shown in Figure 6.7 for comparison.

Under NRT, $2E_d/\beta$ of incident neutron energy is required to produce a Frenkel pair, where 20.5 eV was used as an experimentally measured angular-integrated reference for E_d [94]. β is a displacement efficiency term equal to 0.8 [92]. The NRT damage energy also can be scaled to quantify the initial Frenkel pair density from

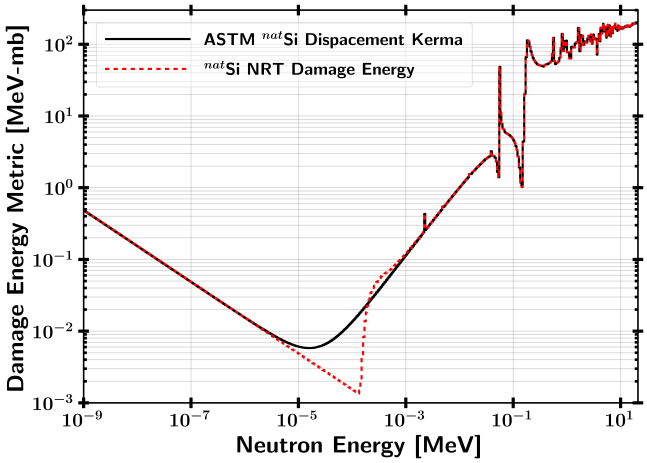

Figure 6.7. (Color online) ASTM 722−19 and the NRT damage energy functions. The NRT damage energy exhibits a reduction for contributing reaction channels below the threshold energy. At energies above the NRT threshold, there is no difference.

displaced atoms by multiplying by $\beta/\ 2E_d$, which correlates with the displacements per atom (DPA) in a material [93, 196]. Second order and more complicated defect structures are also present under neutron irradiation in silicon and should be considered for a more in depth analysis, which is one reason that a spectrally-accurate experimental environment such as ATHENA fills a gap in the radiation effects community [88].

Table 6.3 provides a summary of the irradiation environments on the ATHENA platform calculated with the methods provided above. The NIF source was modeled at a strength of 1×10^{16} neutrons, where the PDXP sources used for ATHENA are capable of producing source yields from approximately 10^{15} - 2×10^{16} neutrons with a ion temperature near 10 keV [22].

Additionally, the uncertainty term for the NRT damage energy was determined using the covariance information in the formulation derived at Sandia National Laboratories [93]. Uncertainty was taken in the damage response function for nuclear data, threshold E_d, displacement model, interaction potential, and model defects such as non-negative constraints. The covariance matrix was only derived

for ^{28}Si, which is the dominant silicon natural isotope. This uncertainty can also be used as a lower estimate for the integral initial Frenkel pair density.

The uniformity of the internal neutron spectrum is demonstrated by the similar values of $H_{1-MeV,Si}$. As noted in Section 6.4.2, the thermal neutron proportion of the neutron spectrum increases father back in the cavity resulting in the lower $H_{1-MeV,Si}$ for the center internal cavity. Figure 6.8 highlights the general uniformity of the neutron fluence and $H_{1-MeV,Si}$ over the internal cavity volume. The largest radial difference in Φ was 3% for a centered, 2.5 cm radius sample, and 7% for a maximum 3.7 cm radius.

6.4.3 γ-ray Environment.

The ionizing radiation environment was modeled at each position in MCNP6 with integral validation using TLD reference doses. The MCNP6 model in Section 6.4.2 was used to model secondary γ-ray and electron energy deposition. The prompt ATHENA

Table 6.3. ATHENA irradiation position neutron environment metrics for a 10^{16} neutron shot yield.

Position	Drawer Cavity	Center Internal Cavity	External
Φ $[\frac{n}{cm^2}]$	3.61E+12	2.32E+12	1.00E+12
$\Phi_{eq,1-MeV,Si}$ $[\frac{n}{cm^2}]$	3.64E+12	1.99E+12	1.75E+12
NRT Damage Energy [MeV-mb]	3.46E+14 ± 11.2%	1.90E+14 ± 11.6%	1.66E+14 ± 16.4%
Integral Si Frenkel Pairs $[\frac{\#}{\mu m^3}]$	337	185	162
$H_{1-MeV,Si}$	1.0	0.90	1.75
Neutron Pulse Length [ns]	50	50	10
Prompt Rad(Si) - (γ / e^-)	620	170	31
Total Rad(Si) - (γ / e^-)	630	238	133

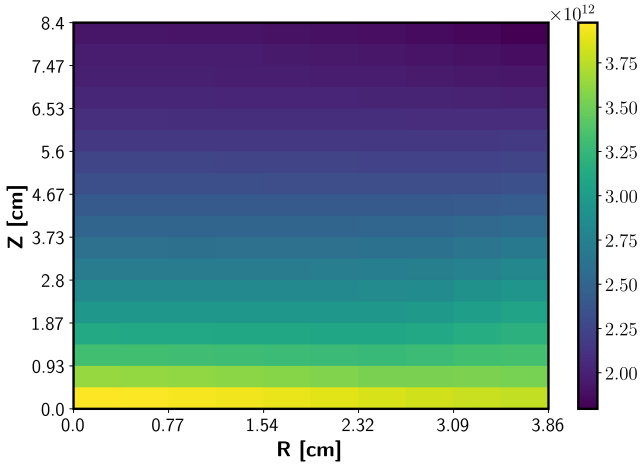

(a) Φ

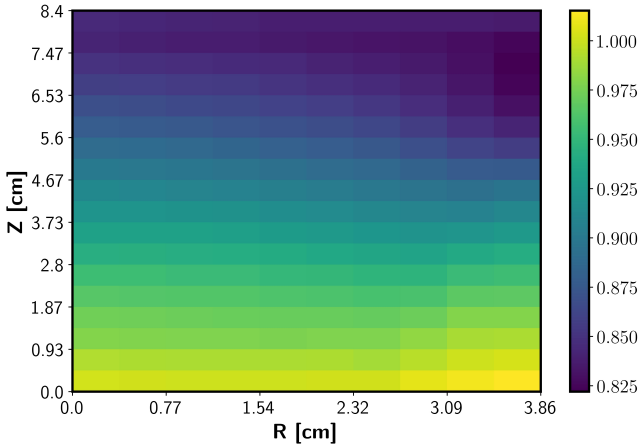

(b) $H_{1-MeV,Si}$

Figure 6.8. (Color online) Two-dimensional histogram of Φ and $H_{1-MeV,Si}$ within the internal cavity volume. Spherical divergence of Φ contributes to the reduction at larger z, while the fluence is similar radially.

γ-ray population was created through inelastic nuclear reactions between the higher energy incident neutrons and radiative capture events throughout the assembly and to a lesser extent through inelastic collisions with the PDXP source capsule [197]. The total ionizing dose with late-time decay radiation produced through activation of the materials within the NIF and ATHENA platform was modeled with a four-hour integration time including all delayed particle half-lives. The 16.67 MeV γ-rays associated with the $4.2 \pm 2.0 \times 10^{-5}$ branching ratio for D-T fusion were neglected due

to limited contribution to the total ionizing dose, approximately 1 mRad(Si) internally and 0.2 Rad(Si) in the external position [198]. An electron energy deposition tally was used to estimate the expected ionizing dose from the incident particles to account for a lack of charge equilibrium. Electrons were created in the model using the default physics packages including production by γ-rays, coherent scattering, bremsstrahlung, straggling, and a 1 keV electron energy cutoff [47].

Experimentally, four 3.2x3.2x0.89 mm Thermo Fisher Scientific TLD-400 chips were irradiated in the internal drawer of ATHENA. Four Thermo Fisher Scientific TLD-400 chips were also exposed to 500 and 1,000 rads(TLD-400) from a reference ^{60}Co γ-ray irradiation at an exposure rate of 54 rad(TLD-400)/minute. Each set of TLDs was measured with a Harshaw 3500 TLD reader, and the integral of the thermoluminescent (TL) curve was used to provide a measurement of the ionizing dose, scaled by a reference light efficiency. The manufacturer recommended time-temperature profile (preheat to 50 °C, followed by a 20 second acquisition of counts with a temperature rate of 25 °C/s and a maximum temperature of 400 °C) was used to heat the TLD-400 chips. The 500 and 1,000 rad reference exposures were confirmed to have a linear response between counts and dose to within 1%.

For the internal ATHENA spectrum validation shot, the modeled integral dose was 290 ± 4.6% rads(TLD-400), compared to a measured dose of 515 ± 7.9% rads(TLD-400). The ionizing dose calculated with γ-ray energy deposition was 329 ± 0.1% rads(TLD-400), in general agreement with the electron results. The γ-ray based dose differs from the electron due to non-equilibrium charge caused by differing material interfaces near the TLD chips. Additionally, the γ-ray spectrum cannot be determined with this integral measurement, so changes in the energy dependency were possible. One possible explanation for the discrepancy between modeled and experimental results is that there is little experimental data for

inelastic neutron cross-sections and secondary γ-ray production on the higher mass Zr and W layers. Recent coupled neutron and γ-ray studies have noted discrepancies between experiments and modeled γ-ray or ionizing dose environments [199–202]. Also, (n,xγ) reactions have been identified as a broad nuclear data need for experimental data collection [203]. In particular, W and compositions of steel, utilized in the ATHENA platform, would benefit from additional γ-ray production cross-section measurements and integral benchmark experiments [204]. Additionally, MCNP does not include correlations or conservation of energy on an individual interaction basis, and therefore can only be used to estimate the γ-ray environment, which is solely due to secondary γ-ray production. Improvements to this treatment in MCNP include MCNP-Polimi [205] and the cascading gamma-ray and multiplicity (CGM) model [206]. MCNP-PoliMi includes drastically improved event-by-event correlations and conservation of energy at each interaction, which may improve the modeled results. Similarly, the CGM option enables correlations between γ-rays produced through individual reaction channels.

A separate simulation in MCNP version 6.1.4, the last working MCNP CGM option available, was completed with CGM. The CGM model resulted in a total ionizing dose of 163 $\pm$ 8.0% rads(TLD-400), which was in less agreement than the original model. Additionally, the neutron energy spectrum and activation product production for the energy range of the PFNS was greatly suppressed in MCNP6.1.4, which did not agree with the measured activation products like MCNP6.2. Therefore, the primary results results reported in this work are based on the MCNP6.2 output without CGM.

The integral ionizing radiation for each region outlined in Table 6.3 was generally too small to be relevant for effects testing. This is a benefit over traditional testing

environments that are not truly a combined effects test but also have significant compounding effects from the ionizing γ-ray environment. However, the rate of the energy deposition was seen as a potential additional application to the ATHENA platform. The ATHENA modeled time-dependent dose are shown in Figure 6.9 for a 10^{16} neutron shot yield, which created dose rates on the order of 10^{10} to 10^{11} Rad(Si)-s^{-1} due to the prompt nature of the modified NIF source. While ATHENA was not optimized for the γ-ray environment, this could be explored in future design modifications.

6.5 Application Simulations

The ultimate objective of the ATHENA platform is to provide a unique radiation environment to explore the impact of the spectrum, timing, and intensity in a mixed neutron and ionizing radiation environment. As such, the ATHENA platform has several key applications and use cases for radiation effects testing and producing experimental measurements for validation of codes and nuclear data. In this section, example applications and simulations are outlined as use-cases being explored for ATHENA.

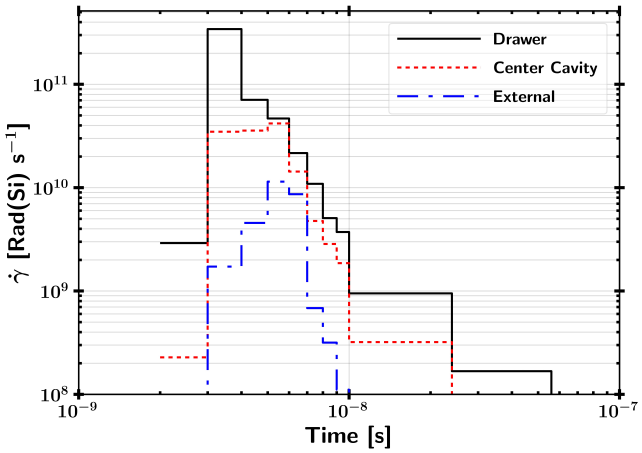

Figure 6.9. (Color online) Ionization energy deposition rate in ATHENA's experimental positions for a 10^{16} neutron shot yield.

6.5.1 Integral Nuclear Data and Modeling Validation.

Different facilities produce environments with various physics fidelity and induced nuclear test environment relevancy. Figure 6.10 displays relevant U.S. testing facilities' neutron energy spectra with respect to the objective TN+PFNS. The ATHENA results indicate how this platform produces a unique environment, which spans the same energy ranges and provides capabilities within current gaps.

Additionally, the short pulse duration provides the opportunity for fission product and integral benchmarking in time-dependent, non-steady state environments. Fission product generation under a similar TN+PFNS at the NIF was demonstrated in previous work is shown in Figure 6.11 [177]. The R_{97} distribution is given as the activity ratio between the i^{th} measured fission product or mass chain time-corrected atoms to the measured $A = 97$ mass chain atoms which was normalized by the ENDF-B/VIII.0 ^{235}U thermal fission product yield ratio of the i^{th} fission product mass chain to the yield for the $A = 97$ mass chain [169]. The fission product inventories were modeled in the General Observables of Fission

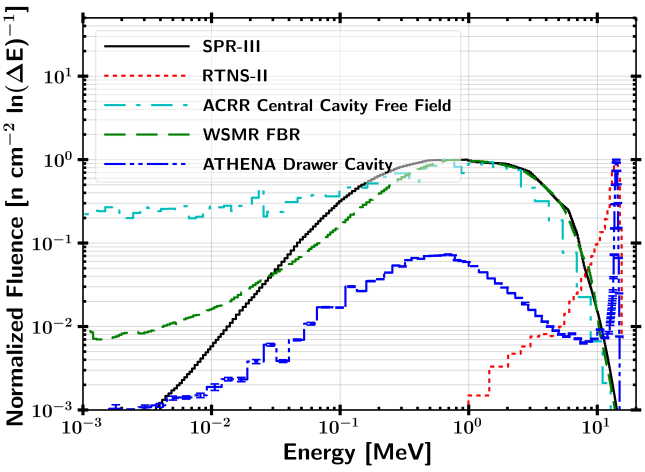

Figure 6.10. (Color online) Comparison of the ATHENA-I internal validation neutron energy spectrum to that of various spectra utilized for large scale radation effects testing in the U.S. Where, the ATHENA spectrum allows for a combined fission like spectrum coinciding with the high energy D-T fusion neutron component.

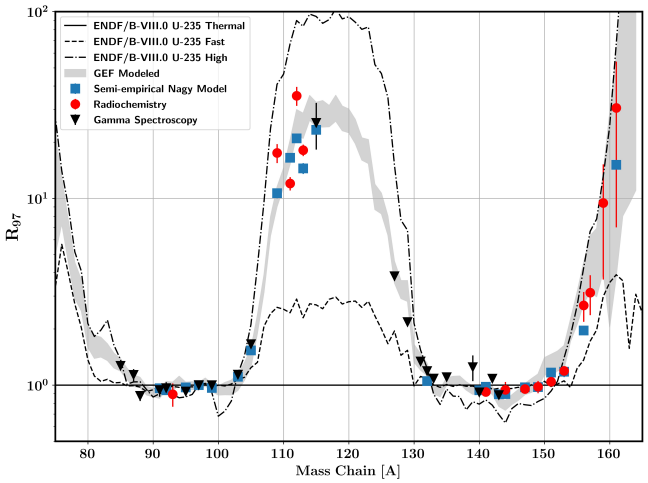

Figure 6.11. (Color online) NIF ETA experiment demonstrated production of TN+PFNS fission products in highly enriched uranium sample. The modeled results were performed with the GEF code and a semi-empirical fit. ENDF-B/VIII.0 R values are provided as a reference.

(GEF) code [49] in addition to semi-empirical fits to experimentally measured energy dependent fission products [51]. The reduced χ^2 for the GEF and semi-empirical fits for the entire distribution were 1.58 and 2.50, respectively.

The controlled experimental conditions provide reduced complexity and relatively rapid production of new environments by modifying ATHENA's internal materials and geometry. This allows for customized validation experiments to be conducted to supplement traditional criticality benchmarks for nuclear data evaluation and model validation suites thereby improving performance of both in non-reactor/criticality applications [14,15]. These experiments would be similar in nature to the pulse-sphere experiments, but would rely on integral measurements in a varying, and customized, environment and set of materials [207–209].

6.5.2 Microelectronic Device Environment and Response.

ATHENA enables experiments with a TN+PFNS on short times-scales for exploring spectral and temporal impacts on the response of microelectronic components. Figure 6.12 displays the neutron flux and initial Frenkel pair

production rate densities in a modeled silicon sample in the ATHENA internal cavity for illustration. The neutron flux at early times is dominated by TN neutrons (red line) because of the faster velocities and less interaction time in ATHENA. At later times, the peak of the PFNS (blue line) dominates as the slower neutrons take longer time to arrive at the sample area. The Frenkel pair production is proportional to the time-dependent $\Phi_{eq,1-MeV,Si}$ as described in Section 6.4.2.2, where the late-time lower energy neutrons (green line) contribute less to the displacement damage in a sample. The internal drawer environment is similar to the internal cavity results shown in Figure 6.12, while the external experiment volume has a larger contribution from the source D-T neutrons leading the start of the defect generation.

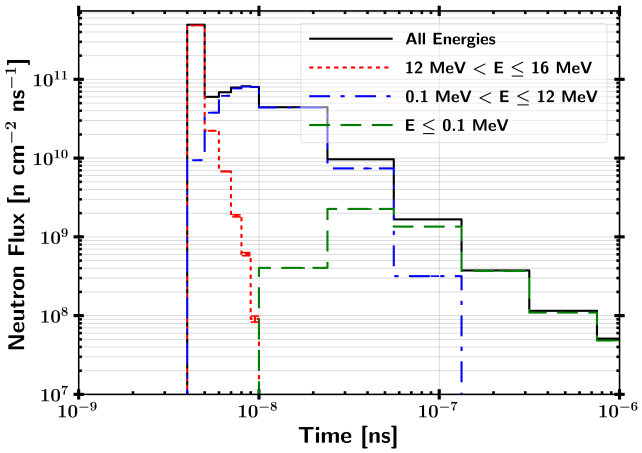

Figure 6.12. Internal ATHENA environment neutron flux for a 10^{16} neutron shot yield.

Compared with current facilities, the ATHENA platform also offers a different radiation spectrum with a short-pulse ($\leq$ 50 ns) capability. Larger device damage rates and magnitudes could be achieved at the NIF without spectral modification; however, the neutron energy spectrum produced can be used to explore and validate spectral equivalency models commonly used for radiation effects on electronics. The combination of a tunable, prompt neutron environment with spectral and timing characteristics not available anywhere else in the world allows ATHENA to be used for

unique validation experiments for time-evolution of defects in semiconductor materials and microelectronic device response.

6.5.2.1 Defect Characterization.

ATHENA offers unique environments to explore defect types and concentrations as a function of time and spectral intensity. To illustrate the differences in defects in Si from different irradiation environments, a model was adopted from mean field theory [210]. Si was chosen because of the extensive literature and experimental history.

A coupled system of ordinary differential equations was created describing the formation of concentrations of point defects including interstitial Si atoms, C_{int}, and vacancies, C_v. Additionally, size n clusters of interstitial, $C_{int,n}$, and vacancy, $C_{v,n}$, concentrations up to n=9 were tracked for convergence with $C_{v,10} = C_{int,10} = 0$. For simplicity, it was assumed that the radiation only produces point defects, that point defects are the only mobile species, and that all clusters are immobile.

The system of differential equations was first discretized by implementing implicit time-stepping and the resulting discrete equations were solved iteratively using the Newton-Raphson method. The concentration of defects was tracked throughout the irradiation of ATHENA's internal cavity as described in Sections 6.4.2 and 6.5.2. A reference case with a constant 10^{-5} DPA-s^{-1}, analogous to longer period nuclear reactor irradiations, was selected for comparison at longer irradiation times. The resulting summation of all cluster sizes are shown in Figure 6.13, where the model parameters required are summarized in Table 6.4.

The modeled vacancy and interstitial distributions highlight that short-pulse neutron environments where the crystal lattice is not allowed to relax to equilibrium between events can produce drastically different results in the observable defect

Table 6.4. Mean field theory model parameters [211–216]

Parameter	Symbol	Value
Temperature	T	300 K
Boltzmann constant	k_b	8.617E-5 eV/K
Atomic Volume	V_{at}	0.02 nm^3
Burgers vector	b	0.384 nm
Vacancy formation energy	E_f^v	3.96 eV
Interstitial formation energy	E_f^i	3.8 eV
Hop Frequency	v	1E12 Hz
Hop distance	d	0.235 nm
Vacancy diffusion prefactor	D_o^v	5.52E10 nm^2 s^{-1}
Interstitial diffusion prefactor	D_i^v	5.52E10 $nm^2 s^{-1}$
Vacancy migration energy	E_m^v	0.35 eV
Interstitial migration energy	E_m^i	0.07 eV
Di-vacancy binding energy	$E_b^{2v} = E_f^v$-E_f^{2v}	2.4 eV
Di-interstitial binding energy	$E_b^{2i} = 2E_f^i$-E_f^{2i}	1.9 eV
hline Dose rate	Γ(t)	Varied
The cascade efficiency	η	0.4
The fraction of point defects produced during irradiation	ϵ_{PD}	1
Recombination coefficient	$\mu_R = \frac{4\pi(r_i+r_v)}{V_{at}}$	277 nm−2
Dislocation density	ρ_d	3E-4 nm^{-2}
Capture efficiency for SIA clusters	Z_i	1.2

concentrations. In the ATHENA internal cavity results, recombination is less prevalent at these short time-scales, as the population of interstitial sites does not equilibrate prior to the creation of additional defects. The net result increases the proportion of interstitial sites post-irradiation compared to the case of the fixed dose rate relevant to longer irradiation pulses, where the interstitials have a longer time period to recombine and reach an approximately steady-state distribution. Experimentally, sample 2N2222 bipolar junction transistor (BJT) devices were irradiated at the Ohio State University Research Reactor (OSURR) to demonstrate the observable defects between $\Phi_{eq,1-MeV,Si}$ of 10^{12} to 10^{14} $\frac{n}{cm^2}$ $\frac{n}{cm^2}$. Deep-level transient spectroscopy (DLTS) was performed on the devices to characterize the charge carrier traps. The DLTS measurements are provided in Fig. 6.14.

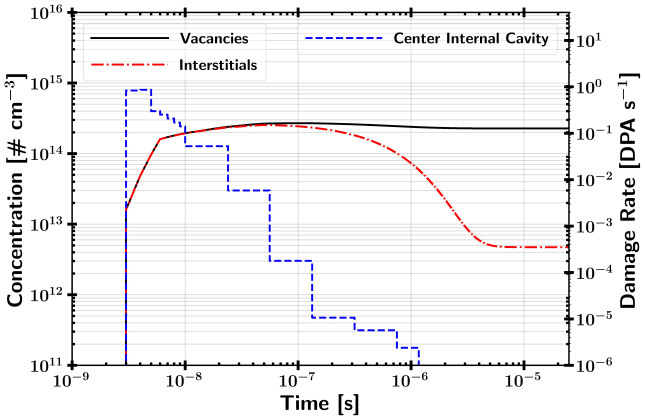

(a) NIF ATHENA Internal Cavity

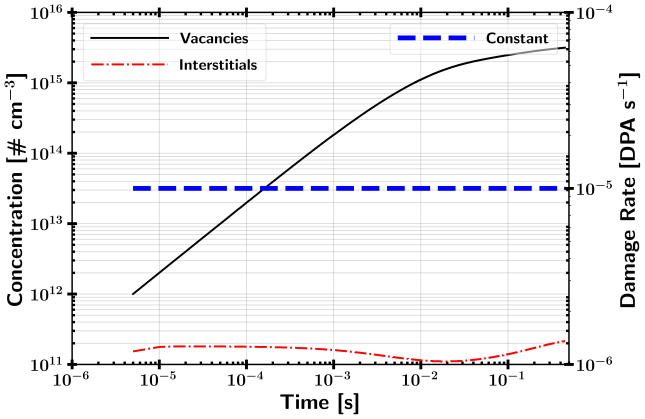

(b) Constant 10^{-5} DPA-s^{-1}

Figure 6.13. (Color online) Mean field theory results for the summation of all cluster sizes of interstitial (sum of C_{int} through $C_{int,9}$) and vacancy (sum of C_v through C_{v9}) defects for the a) ATHENA internal cavity and b) constant displacement damage rate showing that the temporal aspects to an irradiation can create significantly different defect concentrations in the device.

Electron traps included interstitial carbon, C_i, vacancy-oxygen pairs, $V-O$, di-vacancy centers, $V_2(=/-)$, $E4$ centers, and $E5$ centers. Although the defect concentration is predicted to be low, defects were able to be measured at similar $\Phi_{eq,1-MeV,Si}$ levels to the expected ATHENA environment. The $\Phi_{eq,1-MeV,Si}$ of 10^{14} $\frac{n}{cm^2}$ was used to help resolve the scaled $\Phi_{eq,1-MeV,Si}$ of 10^{12} $\frac{n}{cm^2}$ environment, where there was shown to be a non-linear growth of the traps.

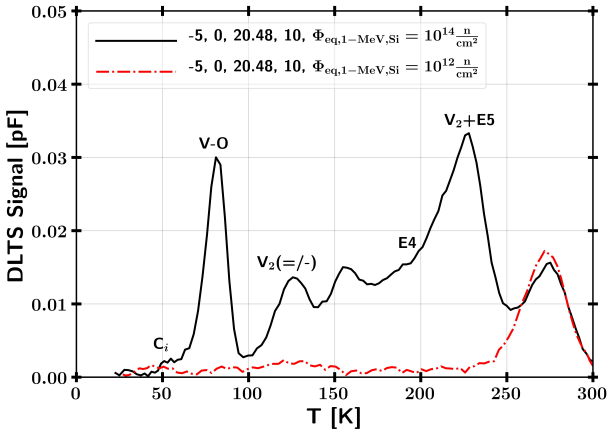

Figure 6.14. (Color online) DLTS base-collector measurements of 2N2222 devices irradiated at the OSURR showing the major electron traps and associated identified defect formations. Non-identified peaks correspond to hydrogen-related defect complexes. The DLTS labels correspond to the device reverse bias [V], pulsing bias [V], rate window [ms], and pulse width [ms], and $\Phi_{eq,1-MeV,Si}$ $[\frac{n}{cm^2}]$, respectively.

6.5.2.2 BJT Device Response.

The device response of components such as a silicon-based bipolar junction transistor (BJT) is dependent on the radiation environment. Testing of these types of devices under different conditions is important to determine the response of the device to assess performance in a radiation environment. Originally posed by Messenger and Spratt [217], the current gain before irradiation, β_0, and after irradiation, β_f, of a transitor can be described by a linear relationship to the total fluence under a given neutron spectrum, $\Phi(E)$, given by,

$$\frac{1}{\beta_f} = \frac{1}{\beta_i} + K(E)\Phi(E), \tag{6.3}$$

where, a proportionality constant, $K(E)$, can be defined for a particular device and environment. During irradiation, the Frenkel pair defect generation can create band levels below the conduction band for Si. The defects ultimately reduce device performance by reducing carrier lifetimes through reduction of mobility, leading to gain degradation.

Short irradiation pulses result in non-equilibrium defect generation and present a different set of environmental conditions that can result in a different observable effect in device response. $K(E)$ has been shown experimentally to be a function of the radiation flux environment, where larger flux rates lead to higher damage coefficients [218]. Larger fluxes lead to more severe short-term damage under fast-burst fission reactor conditions; however, BJT devices sustained less damage after long term annealing. Higher initial damage in high flux environments is likely due to a combination of metastable defect states and shorter annealing time [218]. Additionally, the suppressed damage after long annealing times is possibly linked to higher concentrations of interstitial and vacancy sites, leading to higher levels of recombination before stable defects can form.

Figure 6.15 highlights a few radiation effects testing sources in comparison to the ATHENA environment. Testing environments are relevant to different nuclear scenarios, where each exists to test different corners of the domain. Characterizing different calibration points is essential to validate pre-dominant semi-empirical models used to assess device performance under neutron and surrogate neutron irradiation. Increasing testing of the space can increase confidence in predictive models that allow enhanced confidence to extrapolate into environments where testing is not currently feasible. Furthermore, having a flexible testing capability to inform first-principle models is essential as devices deviate farther from historical testing data and to new device architectures [219]. Smaller physical size as well as drift BJTs have been shown to deviate from the original implementation of the Messenger-Spratt relationship [220, 221].

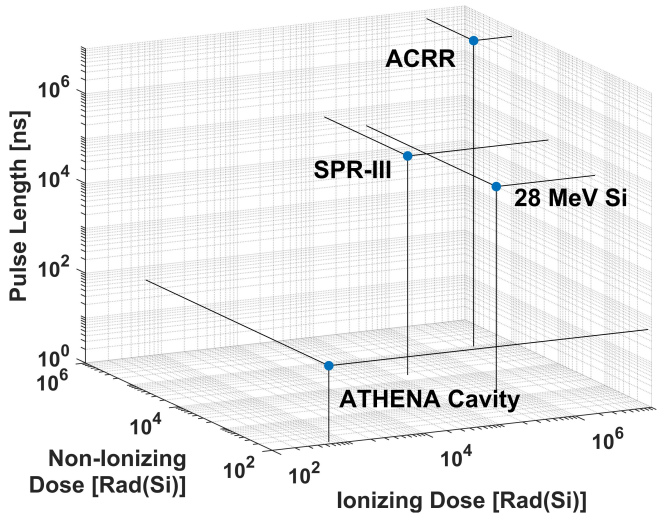

Figure 6.15. ATHENA internal environment characteristics in comparison to the ACRR, SPR-III, and representative 28 MeV Si ion beam [21,23,179]. ATHENA enables an experimental condition with a TN+PFNS in prompt time-scales.

6.6 Conclusion and Perspectives

The ATHENA platform has been designed as a flexible spectral modification platform with a capability to act as a short-pulse neutron and intense γ-ray dose rate source at the NIF. Coupled with data available at currently operational facilities, the ATHENA prompt thermonuclear and prompt fission spectrum environment increases the environmental domain to test devices and validate nuclear data and physics models in a highly-controlled facility platform. ATHENA also provides updates from the ETA platform for an expanded diagnostic region, which is essential for active experimentation on electronics components or with detector systems, and a secondary external platform for direct comparisons between environment conditions.

Integral validation of the ATHENA internal radiation environment provided a clearer understanding of the experimental capabilities and uncertainty analysis of the platform. The environment was modeled in MCNP6 using ENDF-B/VIII.0 and IRDFF v.1.05 nuclear data libraries with systematic nuclear data uncertainties

calculated through stochastic sampling in SCALE Sampler using an ensemble of 300 realizations of the 1597-group ENDF-B/VIII.0 library. A total of 20 activation products were measured at the initial validation shot, and the reduced χ^2 was = 1.38, indicating general agreement with the modeled results. The total ionizing dose was measured to be 515 ± 7.9% rads(TLD-400), whereas the modeled values indicated a lower value of 290 ± 4.6% rads(TLD-400). The discrepancy requires additional research to determine the origin as being dominated by either nuclear data and radiation transport models or measurement.

Future work on the ATHENA platform will be scoped to test 2N2222 BJT devices at NIF. These components have a extensive history of radiation environment characterization, and they offer a starting benchmark experiment before moving toward more exotic devices. The ATHENA platform's utility lies in the unique calibration point to validate models for surrogate sources and enhance understanding of radiation effects experiments.

6.7 Acknowledgment

This work is supported by the National Nuclear Security Administration (NNSA) under grant NA000103 and the Defense Threat Reduction Agency under grant HDTRA-1033292. Some of this work was performed under the auspices of the U.S. Department of Energy by Lawrence Livermore National Laboratory under Contract DE-AC52-07NA27344. The views expressed in this article are those of the authors and do not necessarily reflect the official policy or position of the United States Air Force, the Department of Defense, or the United States Government.

Additionally, the authors would like to thank Todd Wooddy, Keenan Thomas, Sam Glover, and Brent Blue (Lawrence Livermore National Laboratory), Cihangir Celik and William Wieselquist (Oak Ridge National Laboratory), and Pat Griffin

(Sandia National Laboratories) for their invaluable support of this research.

VII. Heuristic Neutron Flux Unfolding Optimization

This chapter was derived from a manuscript submitted in June 2021 with *Transactions on Nuclear Science* titled "Regularized Heuristic Method for Activation Monitor Neutron Spectrum Unfolding." The author list included Nicholas J. Quartemont and James E. Bevins.

The article has been modified to fit this dissertation format; however, the content was unchanged. Neutron flux spectra were determined heuristically from activation foil based dosimetry measurements with a regularization penalty function. In the context of the first ETA experiment, this method was used to determine the possible neutron spectrum or activation energy range which was depressed from the model discrepancy compared to the measured ^{58}Ni(n,p)^{58}Co^{g+m1} reaction products.

7.1 Abstract

This paper describes an activation foil measurement based neutron flux unfolding method utilizing a heuristic optimization approach. A regularization parameter based on the differential neutron flux was introduced into the optimization cost function to remove large nonphysical oscillations in the unfolded neutron energy spectrum. The procedure was completed for two example case studies ranging from thermal energies up to 20 MeV demonstrating recovery of neutron flux energy information on radiation environments where a model was partially missing or there was a discrepancy in a reaction channel. The unfolded results provided a distribution of unfolded spectra that conformed to the activation products but indicated degenerate solutions to the general activation problem. Additionally, increasing the fidelity of initial estimate on the neutron spectrum reduced the degeneracies and lowered the uncertainty in the unfolded spectrum, even in a low-fidelity, physics-based estimate of the neutron

spectrum. Epithermal neutron energies, where few nuclear reactions are available to inform the neutron flux, were shown to be the most difficult region. This method can be extended to other heuristic optimization routines and offers an alternative option for traditional activation dosimetry neutron flux unfolding techniques while improving the characterization of the neutron flux in applications with poor initial models of the environment.

7.2 Introduction

Neutron flux unfolding with activation reactions is an essential method for the measurement and validation of modeled neutron environments with applications in dosimetry and source characterization such as spallation neutron beam lines, research reactors, and medical isotope production optimization [222–224]. Neutron flux deconvolution from measured dosimetry activation products enables measurements where larger neutron detectors may not physically fit in an experiment [177]. Recent work in neutron flux unfolding techniques have adopted a heuristic approach to solving for a neutron environment [225–227]. Heuristic methods offer a significant advantage in that an initial estimate is not required, and the determined neutron spectrum is directly dependent on activation nuclear data and characterized uncertainties.

The majority of neutron flux unfolding codes require an initial characterization of the neutron spectrum, normally calculated with a Monte Carlo or a multi-group discrete ordinate neutron transport code. However, if a dosimetry reaction is not well characterized by the model, unfolding techniques can fail to produce a neutron spectrum that conforms with the measured activation products. As a solution, these reactions are sometimes omitted from the final unfold, thereby potentially removing valuable information about the neutron environment [227–230]. A heuristic method

can address potential issues common with other approaches including an ill-defined source definition or difficulties modeling part of the environment. For example, room return neutrons are a systematic concern for neutron experiments, especially at low energy. Estimating the population of these neutrons as a function of room size, shape, and materials are an active field of study to attempt to alleviate the issue; however, characterizing the uncertainty is difficult [231, 232].

This work examines the uncertainties in heuristic neutron flux unfolding techniques that have not been addressed in most heuristic or stochastic optimization routines [225, 227, 233–235], as well as improvements in a regularization parameter. The optimization routine has been created to account for nuclear data covariance of the reaction products in the formulation of a χ^2 statistic. Additionally, the χ^2 statistic has incorporated a penalty term for large oscillations in nearby neutron energy groups, which has not been included in the recent stochastic approaches. This method is then demonstrated for two case studies from thermal to 20 MeV neutron energies to highlight potential applications.

7.3 Neutron Spectrum Unfolding

Activation based neutron spectrum unfolding relies on monitor reactions to inform the neutron energy spectrum for a range of energies. The activation product activity reaction rate, R, is given as

$$A_\infty = R = \int_0^\infty \phi(E)\Sigma_{act}(E)V dE, \tag{7.1}$$

where the saturation activity, A_∞, in the limit at long, steady-state irradiation times, over a given volume, V, is a function of the neutron flux, $\phi(E)$, and the energy-dependent macroscopic activation cross section, $\Sigma_{act}(E)$, for a given reaction channel [80]. The activity after an irradiation time interval, t, is given as

$$A_0 = A_\infty(1 - e^{-\lambda t}). \tag{7.2}$$

The post-irradiation activity, A_0, builds to A_∞ as a function of the product decay constant, λ. In the limit of $t << t_{1/2}$, where there is negligable decay during irradiation, the activation can be simplified with the temporally-integrated neutron fluence, Φ.

In practice, $\phi(E)$ and the microscopic cross sections, $\sigma(E)$, are represented in a flux-energy-integrated multi-group structure. The matrix representation is a matrix-vector product, $\boldsymbol{A}\vec{\phi} \approx \vec{b}$, with "$m$" measurements and "$n$" energy groups. $\boldsymbol{A}$ is a $[m \times n]$ matrix with the multi-group microscopic reaction cross section, σ_g, corresponding to each measured reaction as rows. $\vec{\phi}$ is multi-group vector representation of ϕ, and b contains the measured A_∞ per target atom. Key information on the experiment includes nuclear data, irradiation duration and intensity, integrating function for creating group averaged values, and neutron self-shielding correction factors for the activation materials. For a given neutron spectrum, an individual σ_g is calculated with the expectation value over the energy interval given by,

$$\sigma_g = \frac{\int_{E_{Lower}}^{E_{Upper}} \phi(E)\sigma(E)dE}{\int_{E_{Lower}}^{E_{Upper}} \phi(E)dE}. \tag{7.3}$$

The energy-integrated reaction cross sections are an important aspect of neutron flux unfolding, and the activation foil reactions utilized in this work were from the IRDFF v.1.05 library distributed with STAYSL [48, 52]. The International Atomic Energy Agency provides data for the IRDFF library, which contains benchmarked neutron dosimetry reactions [48]. The IRDFF v1.05 library contains "state-of-the-art" covariance information and has been improved through testing

and integral experiments, but it does not contain a comprehensive collection of nuclear data for all isotopes [52]. The IRDFF library is also extremely valuable in that some reaction cross sections are available for the energy-dependent population of metastable isomeric states, important for activation experiments.

Figure 7.1 highlights the available benchmarked nuclear reaction channels within the IRDFF v.1.05 library in the 129-group STAYSL structure. Reactions at low energy or energy group are dominated by radiative capture, with substanital increases in the cross section at energies below the resonance region. Additionally, many threshold reactions are available past energy group 80. However, there is a general gap in nuclear data for dosimetry reactions in the epithermal neutron energy range near energy groups 40 through approximately 60, where nuclear processes are limited for activation dosimetry applications. The measurable quantity in Figure 7.1 is the product of the neutron flux with the reaction cross section, and the low sensitivity of activation reactions over this energy range limits the sensitivity of reaction products to inform on the neutron flux in this region.

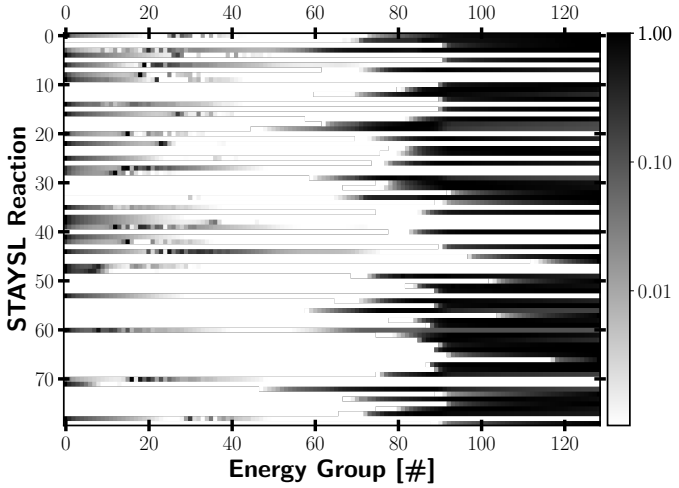

Figure 7.1. STAYSL 129-group energy structure available reactions normalized to the reaction peak cross section value [52]. This particular group structure covers 10^{-10} to 16.5 MeV and highlights the amount of threshold and radiative capture reactions for activation based measurements within the IRDFF v.1.05 library [48]. Energy groups 40, 60, and 80 correspond to 7.2 keV, 40 keV, and 3.7 MeV for reference.

Several codes have been validated for unfolding neutron flux spectra from modeled data; STAYSL and SAND-II are two commonly-used examples in the literature for unfolding activation measurements [52, 236]. PNNL STAYSL determines the incident neutron flux using a generalized least-squares spectral adjustment based on a χ^2 statistic of the measured activation products with the IRDFF nuclear data parameters, calculated activities, and neutron flux covariance information [48, 52]. SAND-II utilizes an iterative approach to adjust a trial neutron spectrum to converge to an optimum solution, and evaluations have been performed starting from a constant initial spectrum [236, 237].

7.4 Description of Work

This section provides the general methodology for regularizing the neutron flux throughout the optimization routine. Additionally, a simple algorithm is provided to optimize based on a proposed cost function, where the heuristic optimizer could be based on a multitude of potential heuristic and stochastic search strategies. Finally, the methods utilized to characterize optimized sets of unfolded spectra are shown.

7.4.1 Regularization.

Constraints on the continuity of a neutron spectrum are necessary to maintain a physically reasonable solution and remove degenerate neutron flux environments that can lead to similar activation foil measurements. One method to provide a physics-based constraint is to use a modeled neutron environment as a prior estimate to guide neutron flux unfolding techniques. However, without an adequate model for part of the problem, regularization can be used to constrain the neutron flux in regions where little information is available to inform a physically-reasonable solution. Common regularization schemes utilized in unfolding techniques are 1-D

smoothing functions, Gaussian formulation for correlation of nearby energy groups, and constraining the nearby differential flux of adjacent bins [52, 225, 227, 233, 236]. However, these techniques may be inappropriate for the problem, or, in the case of smoothing filters, are regularly performed after the optimization is complete, which can lead to changes in the activation rates.

The continuity constraint utilized here was an adjusted formulation of one originally posed by Sen *et al.* for a convex optimization function approach, given as [238]

$$C = \sum_{g=1}^{n} (log \frac{\varphi_{g-1}\varphi_{g+1}}{\varphi_g^2})^2, \tag{7.4}$$

where a ratio is taken of nearby differential neutron flux bins, $\varphi_g = \frac{\phi_g}{E_g - E_{g-1}}$. The original implementation of this continuity constraint also divided the summation terms by the change in lethargy given by $log \frac{E_{g+1}}{E_g}$. This lethargy term was removed because the differential flux already accounted for the energy bin widths and reduced the constraint on individual terms' dynamic range. This continuity constraint penalizes large oscillations in nearby flux bins; however, it does have the distinct disadvantage of possibly removing neutron resonances, a common artifact of regularization.

7.4.2 Optimization Routine.

The objective function, f, to be minimized was based on a traditionally-utilized reduced χ^2 metric and on the differential flux regularization parameter as function of candidate solution neutron energy spectrum, $\vec{\phi}$, given as

$$f(\phi) = \frac{\chi^2(\vec{\phi})}{\nu} + \max(1, \lambda_c C(\vec{\phi})), \tag{7.5}$$

where ν is the degrees of freedom and λ_c is the constraint weighting parameter. The reduced χ^2 form was the square of the difference between the trial activation products and measured, b_i, divided by the corresponding covariance in the i^{th} measured reaction product, Σ_i, given as

$$\frac{\chi^2(\vec{\phi})}{\nu} = \frac{1}{m-1}\sum_{i=1}^{m}\frac{(\sum_{g=1}^{n}\sigma_{i,g}\phi_g - b_i)^2}{\Sigma_i}. \tag{7.6}$$

Σ_i included measurement uncertainty contributions and nuclear data activation product covariance from the IRDFF v.1.05 nuclear data library added in quadrature [48]. This provides a statistic to compare two distributions with uncertainty in each distribution [85]. Under this approach, no assumptions or inclusion of the neutron flux covariance was included. λ_c, a function of the irradiation environment and group structure size, can be iteratively determined or informed by neutron transport models to estimate the neutron environment. λ_c should be chosen to be the reciprocal of an estimate for $C(\vec{\phi})$ to normalize the regularization parameter.

The candidate solution, $\vec{\phi}$, considered for this work was a constrained integral neutron flux with the values of ϕ_g ranging from physically realizable values of $(0, 1]$. The energy group structure was chosen so that physically unrealistic energy groups that cannot contribute to the solution were removed prior to unfolding. Neutron energies down to thermal energies can occur in nearly all neutron experiments; however, there is typically a physics limitation to the upper bound of what neutron energies can be expected. Removing neutron energy groups decreases the optimization space and reduces the number of degenerate solutions.

The neutron spectrum was normalized to unity to be multiplied by the flux magnitude, ($\|\phi\|_1$), with error, ϵ_ϕ. Utilizing a constrained integral neutron flux for all energy groups helps to eliminate degenerate solutions. Alternatively, if no

information on the flux magnitude can be made available, an unbounded positive value optimization of each ϕ_g has been utilized in other works [225].

The algorithm summary provided in Algorithm 1 shows the general framework for the heuristic-based unfolding method implemented in this work. First, the population is created, potentially with an initial estimate if information, such as a radiation transport model, is available to inform the solution space. The convergence criteria utilized here was a value of 2.0, which allows for a solution space with reduced χ^2 contributions less than 1.0 and solution regularization consistent with estimated values. Many heuristics exist to generate trial samples for this approach, and the GNOWEE algorithm, a population-based metaheuristic technique, was used for this work [182]. A similar algorithm capable of generating trial neutron spectra such as a genetic algorithm would also be suitable [83].

Algorithm 1: Heuristic Unfolding Algorithm

```
Generate Population(Seed Population);
for i = 0 : N do
    while f(φ⃗) ≥ Convergence Criteria do
        χ² minimization of ‖φ‖₁ ± ε_φ;
        Evaluate χ²(φ⃗) + max(1,λ_c C(φ⃗));
        Population Update;
    end
end
```

The procedure was repeated and parallelized on individual runs to build a set of neutron spectra that conform to the measurements. The convergence criteria for the objective function was set to a value of 2.0, which allows for a balance of smoothing and agreement of the $\vec{\phi}$ with measured activation products. The regularization term was set to a minimum value of 1.0 to not over-smooth trial $\vec{\phi}$.

7.4.3 Spectrum Characterization.

The set of neutron spectra that conform to the activation product and regularization requirements were characterized for individual convergence, convergence of individual neutron flux bins, and for how the data was distributed. A converged cost function was required to add a trial neutron spectrum into the set. Figure 7.2 displays the convergence properties for the first example case with no estimate described in Section 7.5.1. This convergence plot was representative of all heuristic convergence trends performed with the only change that adding an initial estimate to the population shifted the onset of the decrease in the cost function. Solutions far from the solution space exhibited a worse convergence rate than $\mathcal{O}(N^{-0.5})$, leading to approximately $\mathcal{O}(N^{-0.5})$ convergence near the local minimum, where N is the number of function evaluations.

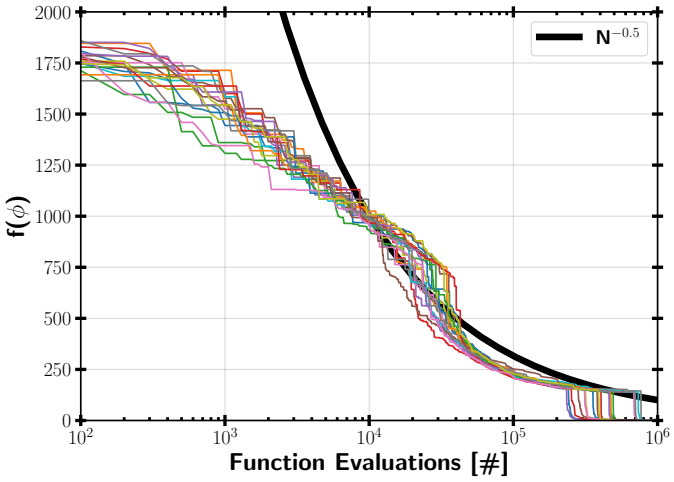

Figure 7.2. (Color online) Cost function convergence as a function of function evaluations, N, for a regularized heuristic unfold algorithm. Individual solution convergences for a sample problem are shown along with a bolded $N^{-0.5}$ convergence for comparison.

Figure 7.3 highlights the distribution of a high- and low-energy neutron fluence bin for the example case described in Section 7.5.1 with a partial estimate at high energy. This case was chosen to demonstrate the common trends of the

heuristic-based unfolded distribution, where large uncertainties resulted in a more log-normal distribution. The log-normal distribution is more appropriate for physical properties that cannot take on negative values such as neutron reaction cross sections [97, 105]. The log-normal distribution and normal distribution produce similar approximations for small relative uncertainties, but the distributions diverge significantly for large variances. Although other distributions are possible, the normal and log-normal distribution are typically used in literature and practice for neutron flux unfolding techniques. The high-energy bin demonstrates that with model predictions, the uncertainty was more normally distributed because the candidate solution is already in the vicinity of a solution minimum.

Figure 7.4 highlights the convergence trends for the individual energy bins shown in Figure 7.3. Attaining approximately a couple hundred samples provided convergence for the distribution of unfolded results. However, the number of unfolded spectra in the sample set could be extended or reduced for computational purposes and yield similar results.

7.5 Results

Two example unfolds with varying levels of fidelity for an initial estimate of the neutron environment are highlighted here. The neutron energy range covered from thermal to 20 MeV with broad coverage of neutron activation reactions over the neutron fluence. The first example provides a mixed thermonuclear (TN) and prompt-fission neutron spectrum (PFNS), where there is a moderate degree of oscillation in the measured neutron spectrum. The second unfold illustrates an experimentally-based neutron time of flight (nTOF) measurement combined with simulated unknown levels of room return and source characterization below the nTOF detector threshold. A repository containing the input and required codes used in this work is made

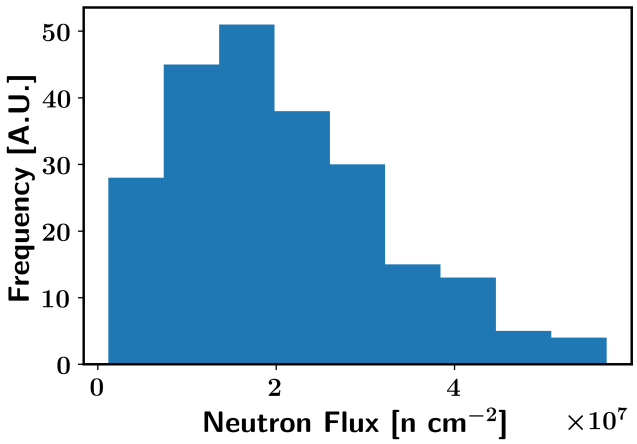

(a) 1 eV

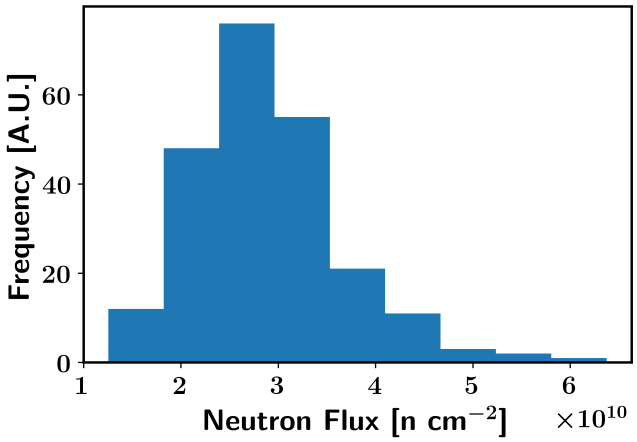

(b) 14.1 MeV

Figure 7.3. Frequency histogram of high- and low-energy heuristic based unfolding energy bins. The low-energy case was not informed by an initial estimate, leading to larger range of possible solutions that leads to a log-normal distribution. The high-energy bin received a partial estimate and was more normally distributed.

available here [239].

7.5.1 Neutron energy tuning assembly.

As a first example, a neutron energy tuning assembly (ETA) that was experimentally tested to create a TN+PFNS based on spectral modification of the National Ignition Facility source deuterium-tritium (DT) neutrons was used. This problem covers a relatively large range of experimental neutron energy conditions

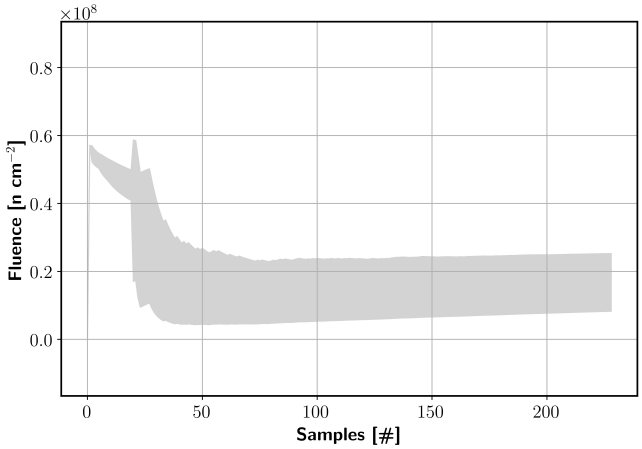

(a) E = 1 eV

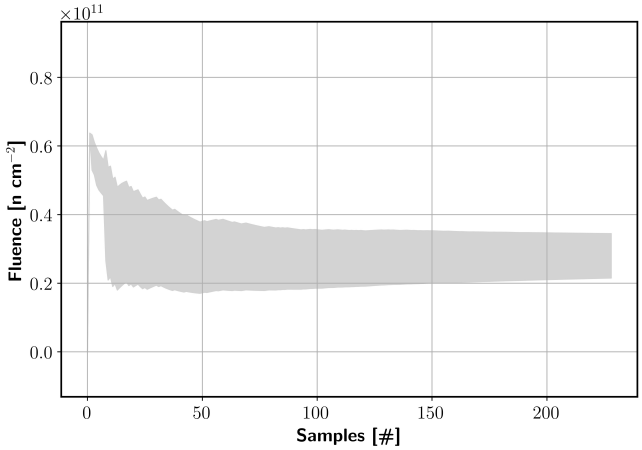

(b) E = 14.1 MeV

Figure 7.4. Convergence of a high- and low-energy heuristic-based unfolding energy bin. After 100 to 200 samples, there was general convergence of individual energy bins.

from thermal to 16.5 MeV, and has been documented in previous work [130, 177]. The experiment was modeled in MCNP5 to determine the continuous energy solution and SCALE MAVRIC with Sampler to determine the neutron flux covariance in the activation foil region [44, 45]. The neutron fluence covariance was calculated through stochastic sampling of the radiation transport cross sections based on the ENDF-B/VII.1 nuclear data library, and the activation reaction uncertainty was calculated with the IRDFF v.1.05 nuclear data library covariance matrices added in quadrature to the neutron fluence covariance [46, 48]. However,

the uncertainty in the evaluated nuclear data covariance matrices often are not supported by experimental data, which can under-predict the uncertainty in radiation transport simulations.

Previously, the ETA neutron spectrum was unfolded with PNNL STAYSL using the modeled estimate and 129-group STAYSL structure in STAYSL, where the cross sections are shown in Figure 7.5 [177]. However, the ^{58}Ni(n,p)^{58}Co^{g+m1} reaction product, of 15 measured reactions, was in fairly large disagreement with the model with a χ^2 contribution of 22.5. This result provides an example where there was a disagreement between the measured and modeled results that the STAYSL spectral adjustment did not account for as the experimentally measured ^{58}Co^{g+m1} was 13% lower than the predicted activation rate from the STAYSL-adjusted spectrum. The measured activation products used in the unfold are provided in Table 7.1.

Table 7.1. Experimental σ-ϕ and measurement error used to unfold the ETA neutron spectrum.

Reaction	**Measurement** [σ-ϕ]	**Measurement Error** [%]
^{197}Au(n,2n)^{196}Au^{g+m1}	5.090E-13	3.6
^{197}Au(n,g)^{198}Au	1.990E-13	2.0
^{90}Zr(n,2n)^{89}Zr	1.351E-13	2.0
^{55}Mn(n,2n)^{54}Mn	1.569E-13	3.7
^{55}Mn(n,g)^{56}Mn	5.891E-15	2.1
^{113}In(n,n')^{113}In^{m1}	1.348E-13	2.7
^{115}In(n,n')^{115}In^{m1}	1.573E-13	5.4
^{115}In(n,g)^{116}In^{m1}	2.420E-13	2.7
^{238}U(n,g)^{239}Np	1.373E-13	5.1
^{186}W(n,g)^{187}W	6.938E-14	2.9
^{58}Ni(n,2n)^{57}Ni	1.358E-13	2.0
^{58}Ni(n,p)^{58}Co^{g+m1}	4.710E-15	4.3
^{27}Al(n,a)^{24}Na	2.778E-14	2.2
^{197}Au(n,2n)^{196}Au^{g+m1}	4.422E-13	3.6
^{197}Au(n,g)^{198}Au	1.775E-13	2.0

The heuristic unfold was performed with four cases: without a starting estimate (randomly generated), a physics-based estimate, a simulated nTOF spectrum, and the full modeled solution. The physics-based estimate was chosen based on the objectives

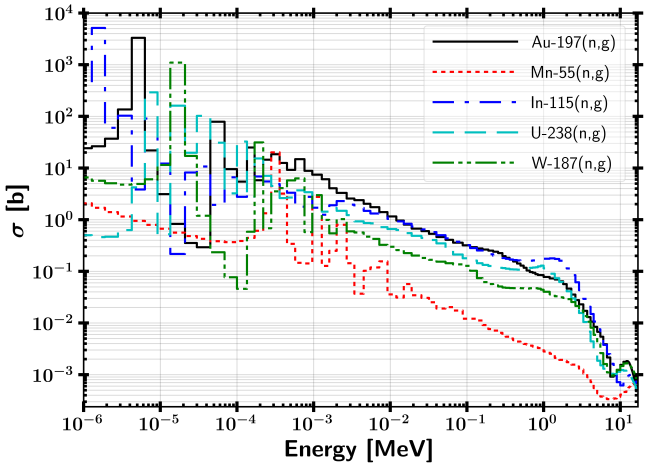

(a) Thermal reaction channels

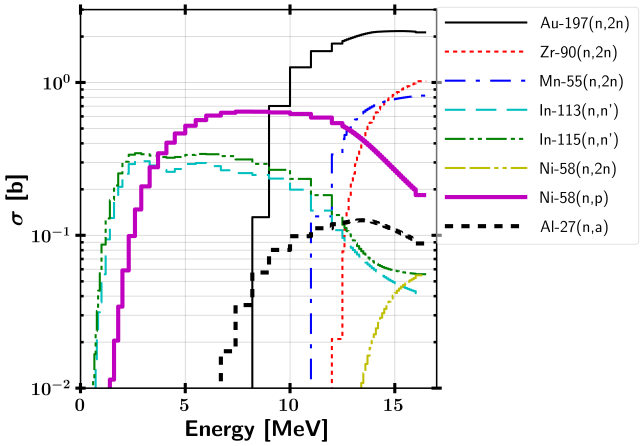

(b) Threshold reaction channels

Figure 7.5. (Color online) Thermal (a) and threshold (b) reaction cross sections utilized in the ETA spectrum unfolding routine.

for the ETA design [37]. Additionally, the simulated nTOF spectrum was based on the modeled solution with a cutoff at 1 MeV. The value of λ_c was chosen to be 0.0362 based on the MCNP5 modeled results, and the short-pulse activation product production approximation integral neutron fluence was constrained at 1.49×10^{12} $\frac{n}{cm^2}$ based on activation foil measurements. The regularized heuristic unfolded results are provided in Figures 7.6, 7.7, 7.8, and 7.9, where the mean and uncertainty were calculated based on a log-normal distribution.

The result with no prior knowledge assumed in Figure 7.6 demonstrates that the

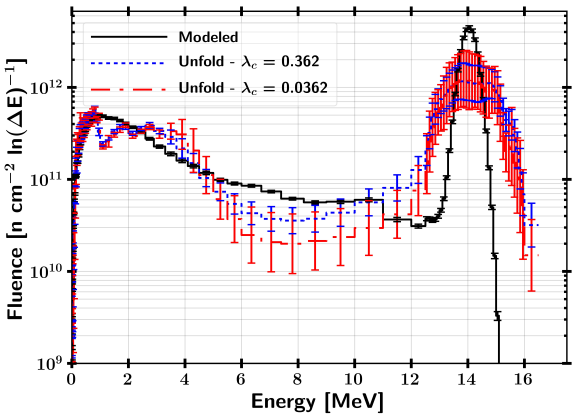

(a) No estimate, linear energy

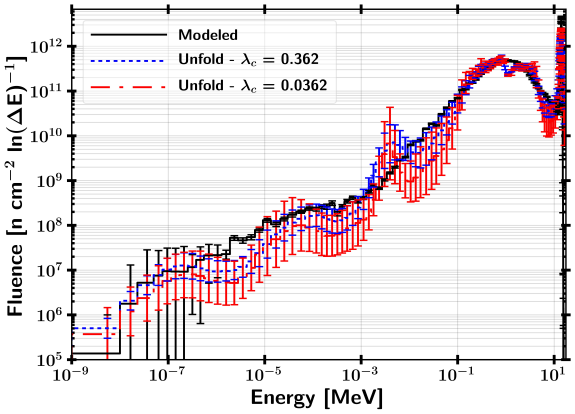

(b) No estimate, logarithmic energy

Figure 7.6. Unfolded neutron spectrum per unit lethargy for the ETA example for no estimate with varied λ_c on a (a) linear and (b) logarithmic energy scale.

general shape of the spectrum could be reconstructed, albeit with large uncertainties due to general limitations to unfolding with activation foil measurements. Threshold reactions are essential for constraining the high energy flux; however, as indicated in Figure 7.5, there is not enough energy dependency to uniquely unfold a neutron spectrum. Near 14 MeV, there is little sensitivity in the reaction products, leading to a relatively large uncertainty in the DT flux contribution and a broader peak. Additionally, the Watt energy region represents a close-to-flat differential neutron fluence, which is advantageous for the continuity constraint. The low-energy threshold reactions' energy sensitivity was not large enough to shape this portion to the modeled

region. At lower energies, the uncertainty bounds are expanded due to the log-normal distribution of the data.

Additionally, Figure 7.6 shows that the choice of λ_c did not drastically change the unfolded result. An increased value of λ_c caused an increased regularization and flatter unfolded spectrum. The choice of λ_c for the ETA neutron flux was derived from the model; however, utilizing the scaled nTOF or the physics-based estimates provided values of 0.087 and 0.375, respectively, in very close proximity to the modeled value of 0.0362 and covered by the range shown in Figure 7.6.

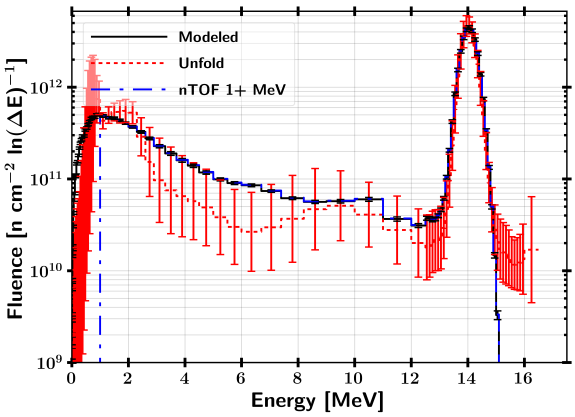

(a) nTOF estimate, linear energy

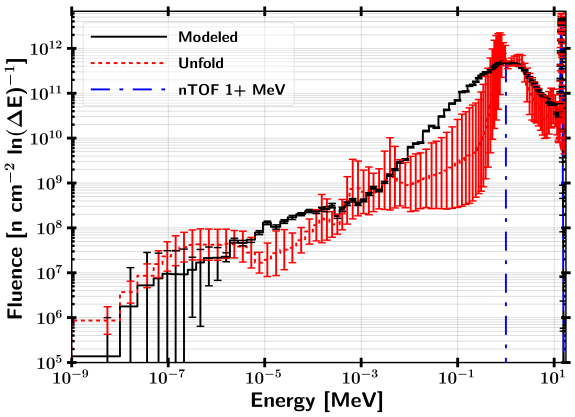

(b) nTOF estimate, logarithmic energy

Figure 7.7. Unfolded neutron spectrum per unit lethargy for the ETA example with the nTOF estimate on a (a) linear and (b) logarithmic energy scale.

Providing more information into the neutron spectrum unfolding routine

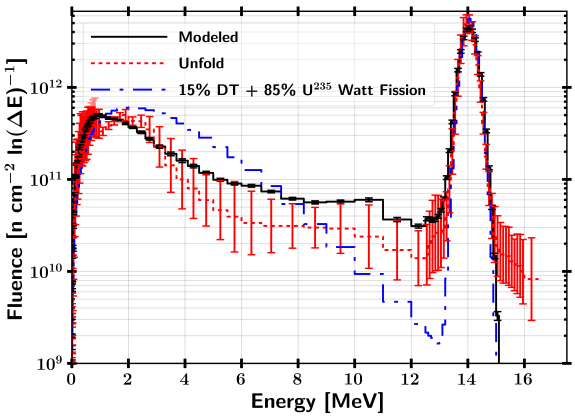

(a) Physics estimate, linear energy

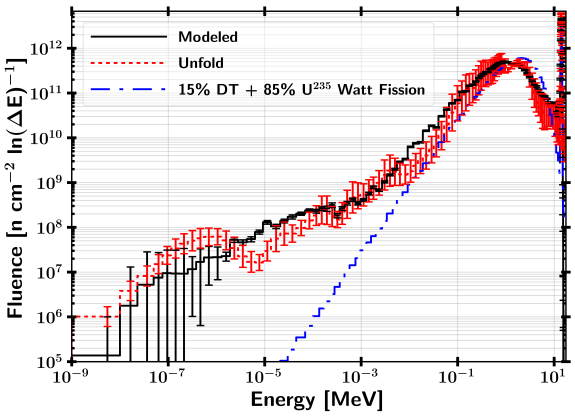

(b) Physics estimate, logarithmic energy

Figure 7.8. Unfolded neutron spectrum per unit lethargy for the ETA example for a physics-based estimate in the optimization population on a (a) linear and (b) logarithmic energy scale.

decreased uncertainty in well-characterized portions of the problem space. The results in Figure 7.7 indicated agreement in regions informed by prior knowledge; however, there were clear issues at the boundary region where the unknown neutron spectrum was built in. In particular, the energy region from 1 keV to several hundred keV represented a particularly difficult area to unfold due to a general lack of nuclear reaction channels with reasonable cross section sensitivity in this energy range. Similarly, Figure 7.8 demonstrate that a physically reasonable, but generally inaccurate, estimate could provide a lower uncertainty over a broad energy range while obtaining an accurate unfold across the 10+ orders of magnitude in energy

considered.

As a final ETA neutron flux unfold, Figure 7.9 demonstrated a result for one of the intended use cases for a heuristic-based neutron spectrum unfolding, where there was a discrepancy between a measured and modeled reaction product. The unfolded neutron energy spectrum overlapped within a 1-σ uncertainty to the modeled result. However, the depression and expanded uncertainty in neutron flux between 4 and 10 MeV was noted as one possibility for the discrepant $^{58}Co^{g+m1}$ activation reaction that was not recovered in the previous STAYSL unfold [177].

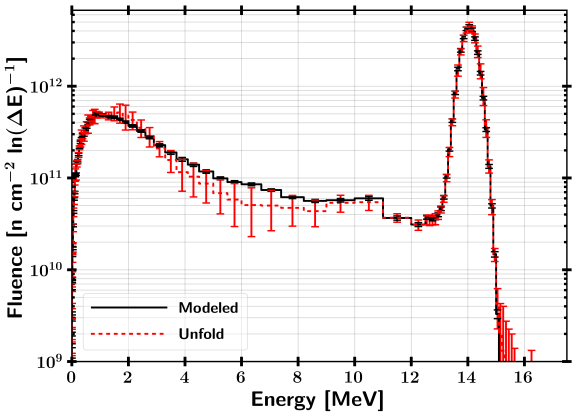

(a) Model estimate, linear energy

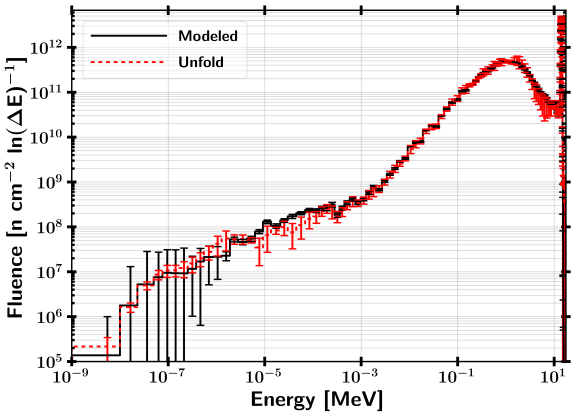

(b) Model estimate, logarithmic energy

Figure 7.9. Unfolded neutron spectrum per unit lethargy for the ETA example for a modeled estimate in the optimization population on a (a) linear and (b) logarithmic energy scale.

Table 7.2 lists the unfolded activation reaction σ-ϕ values along with their

associated χ^2 contribution for the original STAYSL result, physics-based heuristic result, and model heuristic result. Overall, the heuristic method was able to match the measured activation products with a lower reduced χ^2 below 1.0. The σ-ϕ unfolded values are generally in agreement, and the results provided consistent ^{238}U(n,g)^{239}Np and ^{58}Ni(n,p)^{58}Co^{g+m1} reactions.

Similarly, Figure. 7.10 provides a direct comparison between the Monte Carlo model-based unfolded neutron flux results in STAYSL to the model estimated heuristic unfolded results. The ratio of the unfolded neutron flux was generally near unity for each energy bin and statistically consistent with the STAYSL results. The energy regions where the ratio was not near unity, near 10 keV and from approximately 4 to 10 MeV, corresponded to regions which had larger χ^2 contributions in STAYSL from the ^{238}U(n,g)^{239}Np and ^{58}Ni(n,p)^{58}Co^{g+m1} reaction channels, respectively. Finally, the ratio is lower at energies above 15 MeV due to the regularization benefit combined with the general low neutron and activation reaction population above this energy.

7.5.2 Deuteron Breakup.

As a second example, a modified 16 MeV deuterium ^{9}Be breakup neutron source was created to explore the effect of characterization of neutron room return and source. The primary source was based on an experiment performed at the 88-Inch Cyclotron at Lawrence Berkeley National Laboratory where double-nTOF measurements were taken to characterize the neutron flux in the "Cave 0-2" experimental area [240, 241]. Issues present in determining the entire energy range of the neutron energy environment in this application are caused by limitations on timing for the nTOF measurements and room return neutrons. Additionally, source definitions relevant to this area also naturally had these limitations [242].

Table 7.2. Unfolded σ-ϕ and χ^2 results for each measured ETA experiment activation products for the original STAYSL, physics-based heuristic, and model-based heuristic unfolds.

Reaction	STAYSL Model Unfold σ-ϕ (χ^2)	Physics-based Heuristic Unfold σ-ϕ (χ^2)	Model Heuristic Unfold σ-ϕ (χ^2)
^{197}Au(n,2n)^{196}Au^{g+m1}	5.07E-13 (0.0)	5.19E-13 (0.0)	5.11E-13 (0.0)
^{197}Au(n,g)^{198}Au	2.01E-13 (0.2)	2.38E-13 (0.2)	1.99E-13 (0.0)
^{90}Zr(n,2n)^{89}Zr	1.34E-13 (0.0)	1.35E-13 (0.2)	1.35E-13 (0.0)
^{55}Mn(n,2n)^{54}Mn	1.64E-13 (2.0)	1.64E-13 (0.3)	1.66E-13 (2.0)
^{55}Mn(n,g)^{56}Mn	7.64E-15 (1.6)	1.06E-14 (0.0)	7.58E-15 (1.6)
^{113}In(n,n')^{113}In^{m1}	1.30E-13 (1.0)	1.30E-13 (4.0)	1.32E-13 (0.8)
^{115}In(n,n')^{115}In^{m1}	1.63E-13 (0.4)	1.60E-13 (0.0)	1.65E-13 (0.5)
^{115}In(n,g)^{116}In^{m1}	2.30E-13 (2.5)	2.48E-13 (0.8)	2.39E-13 (0.2)
^{238}U(n,g)^{239}Np	1.62E-13 (11.5)	1.52E-13 (0.0)	1.48E-13 (2.6)
^{186}W(n,g)^{187}W	6.89E-14 (0.1)	7.97E-14 (0.0)	6.80E-14 (0.4)
^{58}Ni(n,2n)^{57}Ni	1.50E-13 (22.5)	1.42E-13 (0.0)	1.37E-13 (0.5)
^{58}Ni(n,p)^{58}Co^{g+m1}	4.52E-15 (0.4)	4.68E-15 (0.3)	4.59E-15 (0.4)
^{27}Al(n,a)^{24}Na	2.70E-14 (0.6)	2.78E-14 (5.2)	2.70E-14 (2.1)
^{197}Au(n,2n)^{196}Au^{g+m1}	4.50E-13 (0.4)	4.62E-13 (0.0)	4.53E-13 (0.4)
^{197}Au(n,g)^{198}Au	1.79E-13 (0.1)	2.06E-13 (0.0)	1.77E-13 (0.0)
χ^2 / ν	2.3	0.7	0.8

The neutron environment was modified to include a Watt distribution to add a lower energy room return source term below the nTOF threshold. The Watt spectrum, given by $p(E) = C \times e^{(-E/0.5)} \times \sqrt{sinh(E)}$, was tuned to match the experimentally determined neutron spectrum at 1 MeV. Additionally, thermal room return was simulated by placing the original source in a water scattering medium, and the scaled Monte Carlo model results were used below 4 eV matching with the lower end of the Watt spectrum. The simulated reaction products, shown in Table 7.3, were based on the modeled neutron environment and sampled from a normal distribution with a 3% relative uncertainty.

The heuristic unfold was performed with three cases: a simulated nTOF spectrum, physics-based estimate, and a physics-based estimate with an added resonance in the neutron flux. The nTOF neutron spectrum was used as a estimate

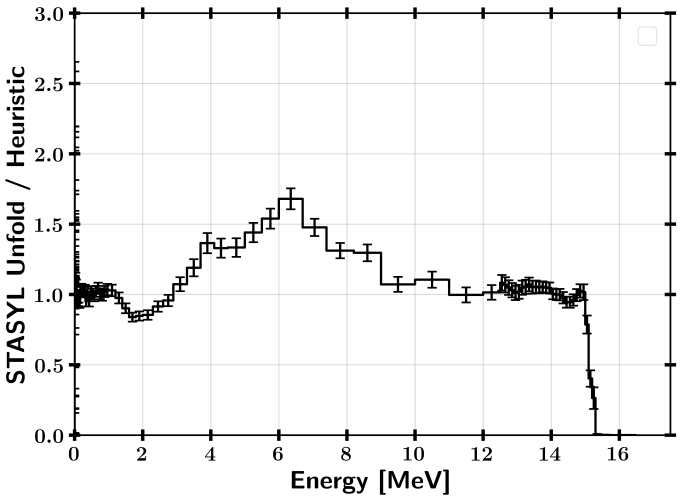

(a) Linear energy

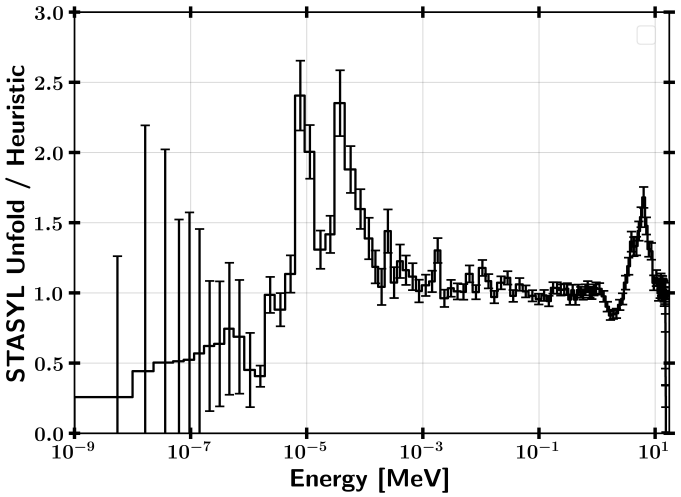

(b) Logarithmic energy

Figure 7.10. Ratio of STAYSL Monte Carlo model-based unfold to the heuristic unfold results with the model estimate in the optimization population on a (a) logarithmic and (b) linear energy scale.

above 1 MeV. Additionally, the physics-based estimate was created through a combination of the nTOF spectrum, $\phi_{nTOF}(E)$, and optimized relative strengths of a thermal Maxwellian, $\phi_{Max}(E)$, and evaporation neutron spectrum, $\phi_{Evap}(E)$. An evaporative spectrum was used instead of a Watt spectrum to not introduce additional bias in the estimate of the neutron environment. The unfold was performed in the 140-group STAYSL structure, using only the first 100 groups

Table 7.3. Simulated σ-ϕ and measurement error used to unfold the modified deuterium ^{9}Be neutron spectrum. (Cd) preceding a reaction indicates that a 1 mm cadmium cover was used for that foil.

Reaction	Measurement [σ-ϕ]	Measurement Error [%]
^{46}Ti(n,p)^{46}Sc	4.412E-15	3.0
^{47}Ti(n,p)^{47}Sc	2.443E-15	3.0
^{48}Ti(n,p)^{48}Sc	3.878E-16	3.0
^{54}Fe(n,p)^{54}Mn	1.159E-14	3.0
^{54}Fe(n,a ^{51}Cr	6.745E-16	3.0
^{56}Fe(n,p)^{56}Mn	9.379E-16	3.0
^{58}Fe(n,g)^{59}Fe	6.323E-16	3.0
(Cd) ^{58}Fe(n,g)^{59}Fe	1.812E-16	3.0
^{64}Zn(n,p)^{64}Cu	5.138E-15	3.0
^{67}Zn(n,p)^{67}Cu	2.605E-16	3.0
^{113}In(n,n')^{113}In^{m1}	7.494E-15	3.0
^{115}In(n,n')^{115}In^{m1}	8.353E-15	3.0
^{115}In(n,g)^{116}In^{m1}	9.343E-14	3.0
(Cd) ^{115}In(n,g)^{116}In^{m1}	7.823E-15	3.0
^{197}Au(n,2n)^{196}Au^{g+m1}	9.788E-15	3.0
^{197}Au(n,g)^{198}Au	6.370E-14	3.0
(Cd) ^{197}Au(n,g)^{198}Au	2.366E-14	3.0
^{59}Co(n,g)^{60}Co	1.595E-14	3.0
(Cd) ^{59}Co(n,g)^{60}Co	5.046E-16	3.0
^{59}Co(n,p)^{59}Fe	6.052E-16	3.0
^{59}Co(n,a)^{56}Mn	1.979E-16	3.0

under 20 MeV. The value of λ_c was chosen to be 0.109 based on the known modeled neutron spectrum, and 0.022 with the added resonance, similar in magnitude used in the ETA modeled results.

The physics-based estimate was determined through a χ^2 minimization of thermal Maxwellian and evaporation spectrum, given by $p(E) = C \times E\ exp(-E/0.25)$ to match the peak of the Watt component. Selecting a physics-based neutron spectrum required estimation of the physical processes which might be contributing to the total neutron spectrum. In this manner, the total neutron spectrum was determined as based on a super-position of the basis spectra as

$$\phi(E) = \phi_{nTOF}(E) + \alpha_{Evap}\phi_{Evap}(E) + \alpha_{Max}\phi_{Max}, \tag{7.7}$$

where α_{Evap} and α_{Max} represent the relative ratio of the component spectrum to the nTOF measurement.

The solution space was shown to be a convex function as depicted in Figure 7.11, and the modeled integral neutron source strength of 5.1×10^{10} $\frac{n}{cm^2-s}$ was reconstructed in this manner based on the simulated nTOF measured source at 3.0×10^{10} $\frac{n}{cm^2-s}$. Introducing more than two additional sources may complicate the estimation of a physics-based estimate. The regularized heuristic unfolded results are provided in Figure 7.12, where the mean and uncertainty were calculated based on a log-normal distribution.

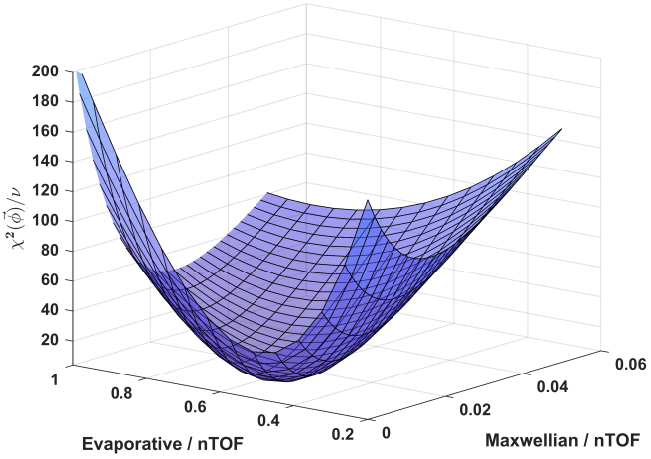

Figure 7.11. (Color online) χ^2 minimization to determine relative strengths of physics-based evaporative and thermal Maxwellian neutron spectra to the measureable nTOF neutron spectrum. The optimized ratios are convex in each direction which enabled locating the global minimum to start the optimization in the vicinity of the convergence criteria.

Figure 7.12 also presented that the general shape of the neutron spectrum can be reproduced without an initial guess, although with larger uncertainties. There was strong agreement and low uncertainty where the neutron spectrum is well characterized at high energies up to 15 MeV. Activation reactions above 15 MeV are saturated and were in a decreasing population of neutrons, leading to larger uncertainties; improvements in the activation foil set could address some of these

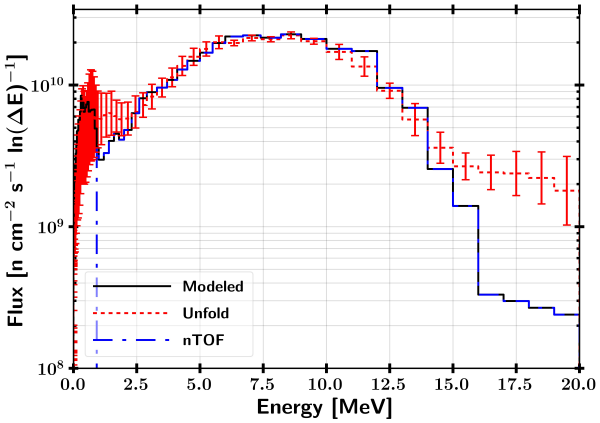

(a) nTOF estimate, linear energy

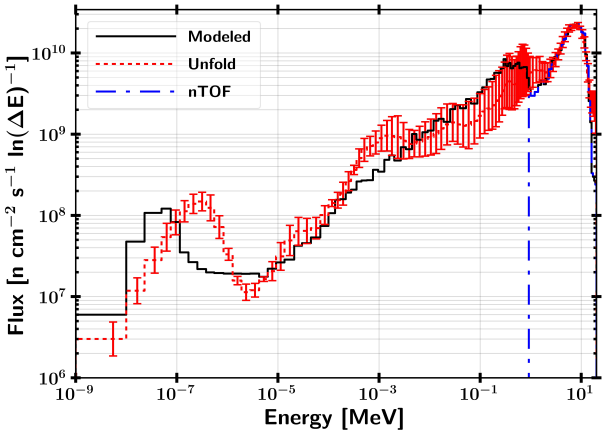

(b) nTOF estimate, logarithmic energy

Figure 7.12. Modified deuterium ^{9}Be breakup unfolded neutron spectrum per unit lethargy for the nTOF estimate on a (a) linear and (b) logarithmic energy scale. The blue horizontal lines were the initial estimate in the seed population, and the black line is the known neutron spectrum.

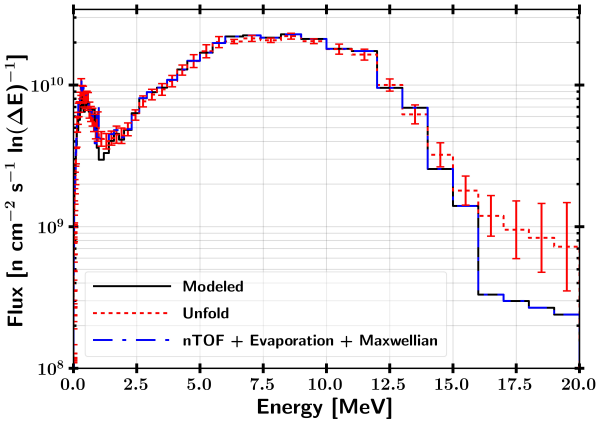

(a) Physics estimate, linear energy

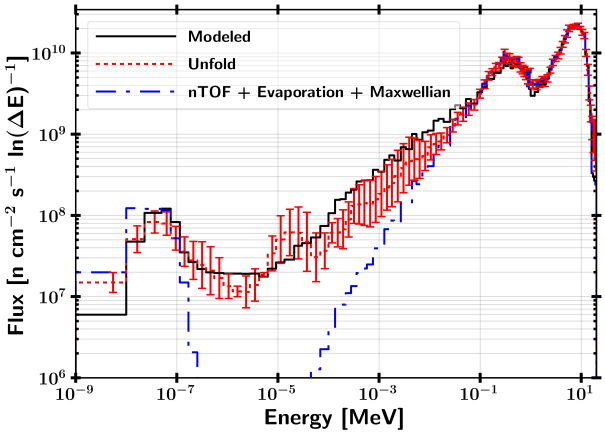

(b) Physics estimate, logarithmic energy

Figure 7.13. Modified deuterium ^{9}Be breakup unfolded neutron spectrum per unit lethargy for the physics-based estimate on a (a) linear and (b) logarithmic energy scale. The blue horizontal lines were the initial estimate in the seed population, and the black line is the known neutron spectrum.

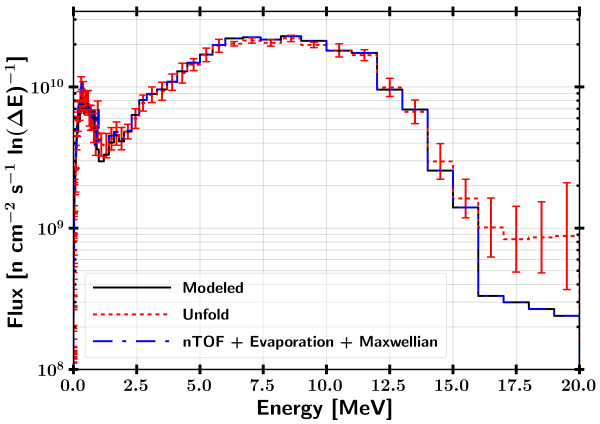

(a) Physics estimate with resonance, linear energy

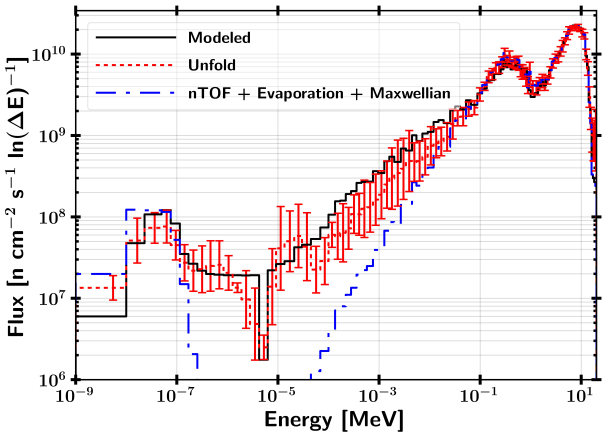

(b) Physics estimate with resonance, logarithmic energy

Figure 7.14. Modified deuterium ^{9}Be breakup unfolded neutron spectrum per unit lethargy for which an added resonance and a physics-based estimate on a (a) linear and (b) logarithmic energy scale. The blue horizontal lines were the initial estimate in the seed population, and the black line is the known neutron spectrum.

discrepancies. The epithermal neutron energy range suffered from low sensitivity due to the lack of strong activation product energy dependency. Additionally, the radiative capture neutron cross sections grow significantly as low-energy neutron energy decreases. The added cadmium cover (n,γ) reaction channels enabled unfolding of the low energy spectrum. Figure 7.13 provide similar results to the nTOF-only based optimization. One important distinction here was that the thermal peak was able to be reproduced based on general physical knowledge of the problem in addition to the cadmium cover reactions. Again, the epithermal energy range had larger uncertainties due to nuclear data reaction limitations. Similarly, Figure 7.14 showcased similar results, and demonstrated the added identification and deconvolution of a resonance was possible as long as the reaction cross sections were sensitive to the resonance.

7.6 Conclusions

Neutron flux unfolding through activation foil reactions is an essential technique to characterize or validate neutron environments. Activation-based diagnostics in particular are important in applications where higher fidelity detection systems may not physically fit, saturate, or survive in the radiation environment. Heuristic based neutron spectrum unfolding methods offer an alternative, complementary technique to robust and validated techniques such as PNNL STAYSL or SAND-II. A heuristic approach has advantages, not uniquely, in scenarios where an initial guess is not available or partly available.

This work demonstrated how regularized heuristic unfolding techniques could help recover or inform on issues with modeling when discrepancies between modeled and experimental activation results are present. Additionally, this work explored the limitations of heuristic unfolding with limited to no prior information for all or part

of the neutron environment. Each unfold considered activation product and nuclear data uncertainty, and the population-based heuristic also added uncertainty in terms of solution degeneracy for well-converged results.

Heuristic methods, like many optimization approaches, benefit greatly from a well-constructed initial guess. The results of the unfolded neutron spectra led to log-normally distributed data in regions less well characterized, due in part to the degenerate nature of the solution absent strong priors. The heuristic unfolded results were statistically consistent with a more robust prior modeling unfold with STAYSL. An unfolded neutron environment distribution was created with regularization, consistent with all activation products, which offers an additional option for performing neutron spectrum unfolding for activation dosimetry. The range of unfolded results are directly applicable to provide critical information on the neutron energy regime where model development or more experimental nuclear data needs would benefit from testing. Future work related to these applications may benefit from varying the regularization penalty term. Finally, the possibility of new reactions at epithermal energy ranges could drastically improve results as more reaction channels become available at shorter measurement times.

Acknowledgment

This work is supported by the Defense Threat Reduction Agency under grant HDTRA-1033292. The views expressed in this article are those of the authors and do not necessarily reflect the official policy or position of the United States Air Force, the Department of Defense, or the United States Government.

VIII. Conclusions and Recommendations

The objective of this work was to demonstrate what capabilities spectral shaping can provide to existing sources such as the National Ignition Facility (NIF), and how ETAs can be utilized to provide a spectrally- and temporally-relevant neutron source term for nuclear environments. Currently, operational radiation sources have limitations on the available radiation environments and timing, with the additional concern of further facility shutdowns, creating a capability gap for the nuclear weapon certification and technical nuclear forensic communities.

To address this issue, an energy tuning assembly (ETA) was developed and fielded at the NIF to target a thermonuclear plus prompt fission neutron spectrum (TN+PFNS). A robust understanding of the neutron environment was required, as observable metrics such as device gain degradation and fission-product production follow directly from the neutron flux environment, which serves as an extremely valuable piece of information for attribution capabilities and nuclear weapons certification testing credibility. Tools were created and modified to measure the environments to aid in the development of an experimentally-validated modeling capability for the analysis of ETA as a TN+PFNS fission product production platform. ATHENA, a next-generation ETA platform, was also developed based on the lessons-learned from the initial ETA experiment with the goal of improving efficiency and adding the capability as a short-pulse neutron source. Finally, a modified technique was developed utilizing a heuristic search strategy with a regularization parameter to unfold a neutron spectrum from measured activation products and nuclear data when there were model needs or discrepancies arise from experimental measurements.

8.1 ETA

Since the novel ETA experiment was high cost, understanding the full affect of uncertainties, including nuclear data, was important to capture. The preliminary ETA experiment nuclear data covariance characterization performed in this research indicated a very strong probability of achieving the surrogate TN+PFNS as designed, but found that the effect of nuclear data uncertainty and covariance on the ETA performance is non-negligible. The neutron transport effect on the fluence uncertainty was assessed with the SCALE Sampler sequence and found to be on the order of a few percent over the broad spectrum; however, the systematic uncertainties increase at lower neutron energies to tens of percent. Additionally, the activation foil pack designed to unfold the neutron energy spectrum in the ETA experiment was found to have broad neutron energy spectrum coverage and multi-reaction coverage at epithermal energies, typically a trouble area for unfolding. The simulated unfolding results provided an 80+% probability of being able to successfully unfold the neutron spectrum with the foil set and the modeled spectrum based on the χ^2 of each unfolded trial.

The NIF ETA experiment on 20 October, 2019 demonstrated the platform capabilities to produce spectrally accurate fission product debris. The 15 activation products produced in an activation foil pack were consistent with the model with the exception of $^{58}Co^{g+m1}$, which was excluded from the analysis due to large inconsistencies, which have been reported elsewhere for this reaction channel at the NIF [175]. The unfolded neutron spectrum passed statistical testing with a reduced χ^2 of 1.6, which validated the modeling and nuclear data covariance framework employed in this research. The experiment resulted in the measurement of 47 cumulative and independent fission yields across 37 mass chains for a highly enriched uranium sample with 5×10^9 fissions. The measured fission product yields

were compared with the General Description of Fission Observables (GEF) code and semi-empirical fits to experimentally measured yields, resulting in general agreement with a reduced χ^2 metric of 1.58 and 2.50, respectively. Larger disagreements between the models and measurements were found in the valley fission product mass chain region between $A = 109 - 113$.

8.2 ATHENA

ATHENA, the next ETA iteration, was developed as an experimental short pulse TN+PFNS platform for neutron effects testing on electronics. The primary improvements from ETA introduced were a better geometric match to the NIF constraints and an expanded irradiation area to enable active measurements of diagnostic components. The improved ATHENA design enabled a peak of 3.6×10^{12} $\frac{n}{cm^2}$ (also 3.6×10^{12} 1-MeV(Si)) at a stand-off of 6 cm for a 10^{16} yield NIF shot, 2.7 times more efficient than ETA with a minimum stand-off of 15 cm. The achievable neutron fluence was on the lower side for radiation effects testing; however, the environment and short 50 ns timescale provide a unique capability to the community. An additional benefit of the ATHENA platform is the inclusion of modular components to allow for an expanded 7 cm diameter, 8 cm high cylindrical irradiation configuration.

The spectrally shaped ATHENA environment was validated during a NIF shot on 29 Nov, 2020, where the modeling and nuclear data covariance framework developed for ETA also was utilized for ATHENA. The 20 fielded activation products were in general consistency with the model, and the unfolded neutron spectrum passed statistical testing with a reduced χ^2 of 1.4. The $^{58}Co^{g+m1}$ reaction product, removed from the ETA analysis, was not removed which provides a clearer picture of the energy range at 2-10 MeV where a potential issue with the nuclear data exists. Additionally,

the total ionizing dose measurements were measured to be 515 ± 7.9% rads(TLD-400), whereas the modeled values indicated a much lower value of 290 ± 4.6% rads(TLD-400). This discrepancy requires additional research to determine the origin as being dominated by either nuclear data/radiation transport models or measurement.

8.3 Unfolding

Neutron flux unfolding was an essential analysis technique throughout this research, as required to understand the neutron environment in ETA and ATHENA. A heuristic-based neutron flux unfolding algorithm was developed to address gaps in available codes that can fail if a relevant starting guess is not available for part of the environment. The method was demonstrated with a regularization parameter in the optimization to remove non-physical oscillations in the neutron spectrum. The optimization was demonstrated to help recover neutron spectrum information or inform issues with modeling when discrepancies between modeled and experimental activation results are present, although with large log-normally distributed uncertainties in the results.

In the context of ETA, the heuristic unfolding work primarily concerned the ^{58}Ni(n,p)^{58}Co^{g+m1} reaction channel, which was systematically lower in the experiment. A clearer understanding can be made of the limitations to predict this reaction during the ETA experiment based on the heuristic unfolding and ATHENA results. Determining the source of the discrepancy proved to be a subjective task, where the initial explanation attributed the reduction to the high energy cross section. The heuristic optimization approach indicated a suppression in the ETA neutron spectrum from approximately 2 to 10 MeV, from the start of the threshold reaction to its peak value. This energy region was also supported by the ATHENA validation work, where the ^{58}Co^{g+m1} was adequately predicted over the softer

ATHENA spectrum. Nonetheless, a determination of the neutron spectrum or cross section as the issue could not be made, as these two quantities are entirely correlated to the observable reaction product.

8.4 Future Work

Several areas presented in this effort would benefit from additional research. The ETA goals focused on generating a spectrally accurate neutron source and the generation of fission products; however, real-world scenario nuclear fallout deposition includes fractionation based on the physical properties and chemistry of the fission product elements. A post-experiment fractionation technique can most readily focus on refractory fission products with low condensation points, as opposed to volatile mass chains as many of these are gases that may be lost in chemical separations. Incorporating the fractionated synthetic fission product debris from fissile samples in the ETA or ATHENA platform into a matrix representative to a nuclear forensic collection would be of great benefit to technical nuclear forensic training and exercises. Additionally, increasing the quantity of produced fission-products through higher neutron yields at the NIF or decreasing the distance from the NIF source would provide improved quantities for technical nuclear forensic use.

There is ample future work related to the ATHENA platform after the preliminary validation shot results. The platform's next planned experiment is scoped to test the device response of 2N2222 bipolar junction transistor, a silicon-based component with a large history of experimental test data. After the follow-on experiment, the ATHENA platform can extend the sample set to more exotic and newer materials such as GaAs. The limits of what components can be tested is generally only restricted in the size of the experimental cavity and hardness of the device, due the the limited

fluence. The ATHENA platform could be used as part of a certification process for radiation hardness requirements of electronic components or to develop improved physics-based models, and the platform would also benefit from increased neutron yields at the NIF.

Finally, although the unfolding method was shown to be successful in two use-cases, more work on the optimization routine would benefit the process. The regularization parameter possibly could be improved by adding energy dependency, where energy regions with a large threshold or resonance reactions could have modified regularization. Finally, the possibility of new reactions at epithermal energy ranges could drastically improve results as more reaction channels become available at shorter measurement times.

The ^{58}Ni(n,p)^{58}Co^{g+m1} reaction channel would benefit from additional experimental measurements over the energy region from 2 to 10 MeV, identified as a possible energy range discrepant with modeled results. The evaluated nuclear data uncertainty in this reaction product may also be underestimated. Newer measurements over this energy region would be beneficial to fully answer the discrepancies reported in the ETA experiment.

Bibliography

1. Office of the Secretary of Defense, "Nuclear Posture Review," 2018.

2. Department of Defense, "Summary of the 2018 National Defense Strategy of the United States of America."

3. Joint Defense Science Board/Threat Reduction Advisory Committee Task Force, "The Nuclear Weapons Effects National Enterprise," Office of the Under Secretary of Defense for Acquisition, Technology, and Logistics, Tech. Rep. June, 2010.

4. J. Bevins, "Targeted Modification of Neutron Energy Spectra for National Security Applications," Ph.D. dissertation, University of California, Berkeley, 2017.

5. D. J. Trump, "State of the Union Address," 2018.

6. Department of Defense, "Operation of the Defense Acquisition System (DOD Instruction 5000.02)."

7. Department of Defense, "DoD Nuclear Weapons Surety Program (DOD Directive 3150.02)."

8. J. C. Martz, "Without Testing: Stockpile Stewardship in the Second Nuclear Age," Los Alamos National Lab.(LANL), Los Alamos, NM (United States), Tech. Rep., 2014.

9. Joint Defense Science Board Task Force, "Nuclear Weapon Effects Test, Evaluation, and Simulation," Office of the Under Secretary of Defense for Acquisition, Technology, and Logistics, Tech. Rep. April, 2005.

10. V. Fedchenko, Ed., *The New Nuclear Forensics: Analysis of Nuclear Materials for Security Purposes*. Solna, Sweeden: Oxford University Press, 2015.

11. Division on Earth and Life Studies and Nuclear and Radiation Studies Board, *Nuclear Forensics: A Capability at Risk (Abbreviated Version)*. Washington, DC: The National Academies Press, 2010. [Online]. Available: https://www.nap.edu/catalog/12966/nuclear-forensics-a-capability-at-risk-abbreviated-version

12. Joint Nuclear Forensics Working Group of the American Physical Society and the American Association for the Advancement of Science, "Nuclear Forensics: Role, State of the Art, and Program Needs." American Physical Society and American Association for the Advancement of Science, Tech. Rep., 2013.

13. US National Security Council, "Review of the doe national security labs' use of archival nuclear test data," Committee on the Evaluation of Quantification of Margins and Uncertainties Methodology for Assessing and Certifying the Reliability of the Nuclear Stockpile, Letter Report, 2005.

14. A. Sood, R. Forster, and D. Kent Parsons, "Analytical benchmark test set for criticality code verification," *Progress in Nuclear Energy*, vol. 42, no. 1, pp. 55–106, 2003. [Online]. Available: https://www.sciencedirect.com/science/article/pii/S0149197002000987

15. R. L. Martz, "Mcnp6 unstructured mesh initial validation and performance results," *Nuclear Technology*, vol. 180, no. 3, pp. 316–335, 2012. [Online]. Available: https://doi.org/10.13182/NT12-A15347

16. D. Heikkinen, "The Rotating Target Neutron Source II Facility: Operational Summary," *Nuclear Instruments and Methods in Physics Research Section B: Beam Interactions with Materials and Atoms*, vol. 40-41, pp. 1162 – 1164, 1989.

17. Sandia National Laboratory, "Sun sets on Sandia Pulsed Reactor," 2007.

18. United States Nuclear Regulatory Commission, "10 CRF Part 75: Safeguards on Nuclear Material," 2018.

19. A. D E772-19, "Standard practice for characterizing neutron fluence spectra in terms of an equivalent monoenergetic neutron fluence for radiation-hardness testing of electronics," ASTM, Tech. Rep., 2019.

20. D. B. King, R. M. Fleming, E. S. Bielejec, J. K. McDonald, and G. Vizkelethy, "Test simulation of neutron damage to electronic components using accelerator facilities," *Nuclear Instruments and Methods in Physics Research, Section B: Beam Interactions with Materials and Atoms*, vol. 365, pp. 294–299, 2015. [Online]. Available: http://dx.doi.org/10.1016/j.nimb.2015.08.026

21. J. G. (Jake) Kelly, P. J. Griffin, and W. C. Fan, "Benchmarking the Sandia Pulsed Reactor III Cavity Neutron Spectrum for Electronic Parts Calibration and Testing," *IEEE Transactions on Nuclear Science*, vol. 40, no. 6, pp. 1418–1425, 1993.

22. C. B. Yeamans and D. L. Bleuel, "The Spatially Distributed Neutron Activation Diagnostic FNADs at the National Ignition Facility," *Fusion Science and Technology*, vol. 72, no. 2, pp. 120–128, 2017. [Online]. Available: https://doi.org/10.1080/15361055.2017.1320499

23. E. J. Parma *et al.*, "Radiation Characterization Summary: ACRR Central Cavity Free-Field Environment with the 32-Inch Pedestal at the Core Centerline (ACRR-FF-CC-32-cl)," *Sand2015-6483*, no. November, 2015.

24. J. Bouchard and R. Heaphy, "QASPR Validation : Moving from Research Codes to Trusted Codes," Sandia National Laboratories, Tech. Rep., 2007.

25. K. P. Carney, M. R. Finck, C. A. McGrath, L. R. Martin, and R. R. Lewis, "The Development of Radioactive Glass Surrogates for Fallout Debris," *Journal of Radioanalytical and Nuclear Chemistry*, vol. 299, no. 1, pp. 363–372, 2014.

26. W. S. K. III, S. Sakamoto, and O. K. Harling, "Neutronic design of a fission converter-based epithermal neutron beam for neutron capture therapy," *Nuclear Science and Engineering*, vol. 131, no. 1, pp. 1–22, 1999.

27. F. Dietrich and J. Escher, "Compound-nuclear Reaction Cross Sections via Surrogate Reactions," *Nuclear Physics A*, vol. 787, no. 1, pp. 237 – 242, 2007, proceedings of the Ninth International Conference on Nucleus-Nucleus Collisions.

28. N. D. Scielzo *et al.*, "Statistical γ Rays in the Analysis of Surrogate Nuclear Reactions," *Physical Review C - Nuclear Physics*, vol. 85, no. 5, 2012.

29. J. E. Escher, J. T. Burke, F. S. Dietrich, N. D. Scielzo, I. J. Thompson, and W. Younes, "Compound-nuclear reaction cross sections from surrogate measurements," *Rev. Mod. Phys.*, vol. 84, pp. 353–397, Mar 2012.

30. N. Gharibyan, "Development af a "fission-proxy" method for the measurement of 14-MeV neutron fission yields at cams," *Radiochemical Acta*, 10 2016.

31. N. Galy *et al.*, "Ion Irradiation Used as Surrogate of Neutron Irradiation in Graphite: Consequences on 14C and 36Cl Behavior and Structural Evolution," *Journal of Nuclear Materials*, vol. 502, pp. 20–29, 2018.

32. I. M. Ardana and Y. Sardjono, "Optimization of a Neutron Beam Shaping Assembly Design for BNCT and Its Dosimetry Simulation Based on MCNPX," *Jurnal Teknologi Reaktor Nuklir Tri Dasa Mega*, vol. 19, no. 3, p. 121, 2017.

33. Y. Kasesaz and M. Karimi, "A Novel Design of Beam Shaping Assembly to use D-T Neutron Henerator for BNCT," *Applied Radiation and Isotopes*, vol. 118, no. September, pp. 317–325, 2016.

34. L. Zaidi, M. Belgaid, S. Taskaev, and R. Khelifi, "Beam Shaping Assembly Design of ^{7}Li(p,n)^{7}Be Neutron Source for Boron Neutron Capture Therapy of Deep-Seated Tumor," *Applied Radiation and Isotopes*, vol. 139, no. May, pp. 316–324, 2018.

35. J. E. Bevins, "Coeus V1.0," 2017. [Online]. Available: https://github.com/SlaybaughLab/Coeus/releases.

36. J. E. Bevins, S. Bogetic, L. A. Bernstein, R. Slaybaugh, and J. Vujic, "Metaheuristic Optimization Method for Neutron Spectra Shaping," *Transactions of the American Nuclear Society*, vol. 118, pp. 455–458, 2018.

37. J. E. Bevins *et al.*, "Performance evaluation of an energy tuning assembly for neutron spectral shaping," *Nuclear Instruments and Methods in Physics Research Section A: Accelerators, Spectrometers, Detectors and Associated Equipment*, 2019.

38. R. Stickney, Jason, "Pulse Height Spectra Analysis of a Neutron Energy Tuning Assembly," Ph.D. dissertation, Air Force Institute of Technology, 2018.

39. N. Quartemont, N. Gharibyan, K. Moody, and J. Bevins, "Uranium integral fission product yields for a spectrally-shaped 14.1 mev neutron source at the national ignition facility," *Applied Radiation and Isotopes*, vol. 173, p. 109711, 2021. [Online]. Available: https://www.sciencedirect.com/science/article/pii/S0969804321001184

40. C. J. Bridgman, *Introduction to the Physics of Nuclear Weapons Effects.* Fort Belvoir, VA: Defense Threat Reduction Agency, 2001.

41. Department of Defense, "Nuclear Weapons Technology," in *Military Critical Technologies List*, 1998.

42. S. Glasstone and P. J. Dolan, *The Effects of Nuclear Weapons*, 3rd ed. Washington D.C.: United States Department Of Defense, 1977.

43. K. J. Moody *et al.*, "Nuclear Spectrometry of 9.6 h $^{196}Au^{m2}$ and the Reaction of ^{197}Au with Fast Neutrons," *J. Phys. G: Nucl. Part. Phys.*, vol. 47, no. 4, pp. 1–48, 2020.

44. X-5 Monte Carlo Team, "MCNP - A General Monte Carlo N-Particle Transport Code, Version 5," *LA-UR-03-1987*, 2008.

45. B. Rearden, M. Jessee, and Eds., *SCALE Code System*, ORNL/TM-2005/39 ,Version 6.2.3, Oak Ridge National Laboratory, Oak Ridge Tennessee, March 2018, available from Radiation Safety Information Computational Center as CCC-834.

46. M. Chadwick and E. Al., "ENDF/B-VII.1 Nuclear Data for Science and Technology: Cross Sections, Covariances , Fission Product Yield," *Nucl.Data Sheets*, vol. 112, no. 12, pp. 2887–2996, 2011.

47. T. Goorley *et al.*, "Initial mcnp6 release overview," *Nuclear Technology*, vol. 180, no. 3, pp. 298–315, 2012.

48. R. Capote, K. Zolotarev, V. Pronyaev, and A. Trkov, "International Reactor Dosimetry and Fusion File IRDFF v.1.05," *J. ASTM International*, vol. 9, no. 4, April 2012.

49. K.-H. Schmidt, B. Jurado, C. Amouroux, and C. Schmitt, "General Description of Fission Observables: GEF Model Code," *Nuclear Data Sheets*, vol. 131, pp. 107–221, Jan. 2016. [Online]. Available: http://hal.in2p3.fr/in2p3-01241907

50. K. H. Schmidt, B. Jurado, C. Amouroux, and C. Schmitt, "General Description of Fission Observables: GEF Model Code," *Nuclear Data Sheets*, vol. 131, no. May, pp. 107–221, 2016.

51. S. Nagy, K. F. Flynn, J. E. Gindler, J. W. Meadows, and L. E. Glendenin, "Mass Distributions in Monoenergetic-Neutron-Induced Fission of U238," *Physical Review C*, vol. 17, no. 1, pp. 163–171, 1978.

52. L. Greenwood and C. Johnson, "Least-Squares Neutron Spectral Adjustment with STAYSL PNNL," *EPJ Web of Conferences*, vol. 106, p. 07001, 2016.

53. J. Turner, *Atoms, Radiation, and Radiation Protection*. Oak Ridge, TN: Wiley, 2008.

54. K. Krane, *Introductory Nuclear Physics*. New York: Jon Wiley & Sons, 1988.

55. H. Salmon, R. Ünal, B. Oruncak, U. Akcaalan, and H. A. Yalim, "(n,2n) and (n,3n) Neutron Induced Reaction Cross Sections above 8 MeV," *Acta Physica Polonica, A*, vol. 128, no. 2B, pp. B–231 – B–235, 2015.

56. A. Tonchev *et al.*, "Energy Evolution of the Fission-Product Yields from Neutron-Induced Fission of 235U, 238U, and 239Pu: An Unexpected Observation," in *The 6th International Conference on "Fission and Properties of Neutron-Rich Nuclei*, 2016.

57. N. Bohr and J. A. Wheeler, "The mechanism of nuclear fission," *Phys. Rev.*, vol. 56, pp. 426–450, Sep 1939. [Online]. Available: https://link.aps.org/doi/10.1103/PhysRev.56.426

58. J. Randrup and R. Vogt, "Nuclear Fission." in *LLNL-BOOK-591732*. Lawrence Livermore National Laboratory, 2012.

59. K.-H. Schmidt and B. Jurado, "General Description of Fission Observables," *JEFF Report 24*, 2014.

60. A. Nichols, D. Aldama, and M. Verpelli, "Handbook of Nuclear Data for Safeguards: Database Extensions," International Atomic Energy Agency, Tech. Rep. August, 2008.

61. M. James, R. Mills, and D. Weaver, "A New Evaluation of Fission Product Yields and the Production of a New Library (UKFY2) of Independent and Cumulative Yields." *Progress in Nuclear Energy*, vol. 26, no. 1, pp. 1 – 29, 1991.

62. E. Privas *et al.*, "Measurements of the Effective Cumulative Fission Yields of ^{143}Nd, ^{145}Nd, ^{146}Nd, ^{148}Nd and ^{150}Nd for ^{235}U in the PHENIX Fast Reactor," *EPJ Nuclear Sciences & Technologies*, vol. 2, no. 32, pp. 1–16, 2016.

63. B. Singh, "Nuclear data sheets for A = 89," *Nuclear Data Sheets*, vol. 114, no. 1, pp. 1 – 208, 2013.

64. D. A. Brown, E. A. Mccutchan, M. W. Herman, S. Hoblit, G. P. A. Nobre, and B. Pritychenko, "Uncertainty Quantification in the Nuclear Data Program," *J. Phys. G: Nucl. Part. Phys.*, vol. 42, no. 034020, 2015.

65. F. Bostelmann and G. Strydom, "Nuclear Data Uncertainty and Sensitivity Analysis of the VHTRC Benchmark Using SCALE," *Annals of Nuclear Energy*, vol. 110, pp. 317–329, 2017.

66. A. Knecht *et al.*, "Precision Measurement of the ^{6}He Half-Life and the Weak Axial Current in Nuclei,," *Phys. Rev. Lett.*, vol. 108, no. 122502, 2012.

67. L. Greenwood, M. Kostal, S. Simakov, and A. Trkov, "Testing and Improving the International Reactor Dosimetry and Fusion File (IRDFF)," International Atomic Energy Agency, Tech. Rep., 2017.

68. A. Trkov *et al.*, "IRDFF-II: A New Neutron Metrology Library." *Nuclear Data Sheets*, vol. 163, pp. 1 – 108, 2020.

69. K. I. Zolotarev and P. K. Zolotarev, "Evaluation of Some (n,n'), (n,γ), (n,p), (n,2n) AND (n,3n) Reaction Excitation Functions for Fission and Fusion Reactor Dosimetry Applications," INDC International Nuclear Data Committee, Tech. Rep. INDC(NDS)-0657, 2013.

70. C. Diez, O. Cabellos, J. Martínez, and C. Ceresio, "Importance of nuclear data uncertainties in criticality calculations." *EPJ Web of Conferences*, vol. 27, p. 4, 2012.

71. D. Rochman, A. J. Koning, S. C. Van Der Marck, A. Hogenbirk, and C. M. Sciolla, "Nuclear data uncertainty propagation: Perturbation vs. Monte Carlo," *Annals of Nuclear Energy*, vol. 38, no. 5, pp. 942–952, 2011.

72. A. Aures, F. Bostelmann, M. Hursin, and O. Leray, "Benchmarking and Application of the State-of-the-art Uncertainty Analysis Methods XSUSA and SHARK-X," *Annals of Nuclear Energy*, vol. 101, pp. 262–269, 2017.

73. C. J. Díez, O. Buss, A. Hoefer, D. Porsch, and O. Cabellos, "Comparison of Nuclear Data Uncertainty Propagation Methodologies for PWR Burn-up Simulations," *Annals of Nuclear Energy*, vol. 77, pp. 101–114, 2015.

74. T. Zhu, A. Vasiliev, H. Ferroukhi, A. Pautz, and S. Tarantola, "NUSS-RF: Stochastic sampling-based tool for nuclear data sensitivity and uncertainty quantification," *Journal of Nuclear Science and Technology*, vol. 52, no. 7-8, pp. 1000–1007, 2015.

75. N. P. Luciano, "A High-Energy Neutron Flux Spectra Measurement Method for the Spallation Neutron Source," Master's thesis, University of Tenessee Knoxville, 2012.

76. E. E. Lewis and W. F. Millar Jr, *Computational Methods of Neutron Transport*. New York: John Wiley & Sons, 1984.

77. M. J. Wang, R. J. Sheu, J. J. Peir, and J. H. Liang, "Criticality Calculations of the HTR-10 Pebble-bed Reactor with SCALE6/CSAS6 and MCNP5," *Annals of Nuclear Energy*, vol. 64, pp. 1–7, 2014.

78. S. R. Johnson and K. T. Clarno, "Comparison of SCALE and MCNP Results for Computational Pebble Bed Benchmarks," *Trans. Am. Nucl. Soc.*, vol. 96, no. April, pp. 420–422, 2007.

79. Y. F. Chen, R. J. Sheu, S. H. Jiang, J. N. Wang, and U. T. Lin, "Surface Dose Rate Calculations of a Spent-Fuel Storage Cask by Using MAVRIC and Its Comparison with SAS4 and MCNP," *Nuclear Technology*, vol. 175, no. 1, pp. 343–350, 2011.

80. G. F. Knoll, *Radiation Detection and Measurement, 4th Edition.* Ann Arbor, MI: Wiley, 2010.

81. L. Kuijpers, R. Herzing, P. Cloth, D. Filges, and R. Hecker, "On the Determination of Fast Neutron Spectra with Activation Techniques; its Application in a Fusion Reactor Blanket Model," *Nuclear Instruments and Methods*, vol. 144, no. 2, pp. 215–224, 1977.

82. E. Vagena, K. Theodorou, and S. Stoulos, "Thick-foils Activation Technique for Neutron Spectrum Unfolding with the MINUIT Routine—Comparison with GEANT4 Simulations," *Nuclear Instruments and Methods in Physics Research, Section A: Accelerators, Spectrometers, Detectors and Associated Equipment*, vol. 887, no. January, pp. 64–69, 2018.

83. M. Reginatto, "Overview of Spectral Unfolding Techniques and Uncertainty Estimation," *Radiation Measurements*, vol. 45, no. 10, pp. 1323–1329, 2010.

84. F. G. Perey, *Least-Squares Dosimetry Unfolding: The Program STAY'SL (ORNL/TM-6062)*, Oak Ridge, Tennessee, 1977.

85. J. Frank and B. Klar, "Methods to test for equality of two normal distributions," *Statistical Methods and Applications*, vol. 25, no. 4, pp. 581–599, 2016.

86. H. R. Vega Carrillo and M. P. I. De La Torre, "Catalogue to Select the Initial Guess Spectrum During Unfolding," *Nuclear Instruments and Methods in Physics Research, Section A: Accelerators, Spectrometers, Detectors and Associated Equipment*, vol. 476, no. 1-2, pp. 270–272, 2002.

87. C. Claeys and E. Simeon, *Radiation Effects in Advanced Semiconductor Materials and Devices*, 1st ed., R. M. Osgood, J. Parisi, and R. Hull, Eds. Berlin Heidelberg: Springer Berlin Heidelberg, 2002.

88. S. M. Myers, "The Science of QASPR (Qualification Alternatives to the Sandia Pulsed Reactor)," in *Sandia' s Physical , Chemical , and Nano Sciences Center (PCNSC)*, 2008.

89. R. K. S. Lawrence R. Greenwood, *SPECTER: Neutron Damage Calculations for Materials Irradiations*. Argonne, Il: Argonne National Laboratory, 1985.

90. K. R. Depriest, "Historical examination of the astm standard e722 1-mev silicon equivalent fluence metric," Sandia National Laboratories, Albuquerque, NM, Tech. Rep. SAND2019 -15194, 12 2019. [Online]. Available: https://www.osti.gov/biblio/1592863

91. P. J. Griffin, "Detailed Description of the Derivation of the Silicon Damage Response Function," Sanida National Laboratories, Albuquerque, NM, Tech. Rep., 2016.

92. M. J. Norgett, M. T. Robinson, and I. M. Torrens, "A proposed method of calculating displacement dose rates," *Nuclear Engineering and Design*, vol. 33, no. 1, pp. 50–54, 1975.

93. P. J. Griffin, "Uncertainty Characterization of Silicon Damage Metrics," *IEEE Transactions on Nuclear Science*, vol. 66, no. 1, pp. 327–336, 2019.

94. J. Bourgoin, P. Ludeau, and B. Massarani, "Threshold energy determination in thick semiconductor samples," *Revue de Physique Appliquée*, vol. 11, no. 2, pp. 279–284, 1976.

95. R. C. REEDY and S. C. FRANKLE, "Prompt gamma rays from radiative capture of thermal neutrons by elements from hydrogen through zinc," *Atomic Data and Nuclear Data Tables*, vol. 80, no. 1, pp. 1–34, 2002. [Online]. Available: https://www.sciencedirect.com/science/article/pii/S0092640X01908708

96. M. Berger, J. Hubbell, S. Seltzer, J. Coursey, and D. Zucker, "Xcom: Photon cross section database (version 1.2)," 1999-01-01 1999.

97. N. J. Quartemont, A. A. Bickley, and J. E. Bevins, "Nuclear Data Covariance Analysis in Radiation Transport Simulations Utilizing SCALE Sampler and the IRDFF Nuclear Data Library," *IEEE Transactions on Nuclear Science*, vol. 67, no. 3, pp. 482–491, 2020.

98. E. Alhassan *et al.*, "Combining Total Monte Carlo and Benchmarks for Nuclear Data Uncertainty Propagation on a Lead Fast Reactor's Safety Parameters," *Nuclear Data Sheets*, vol. 118, no. 1, pp. 542–544, 2014.

99. S. S. Lombardo, F. Cadini, and A. Cammi, "Impact of uncertainties on the safety performances of the lbe-xads concept nuclear reactor." *Nuclear Engineering and Design*, vol. 341, pp. 16 – 24, 2019.

100. D. C. Kammer, K. F. Alvin, and D. S. Malkus, "Combining Metamodels with Rational Function Representations of Discretization Error for Uncertainty Quantification," *Computer Methods in Applied Mechanics and Engineering*, vol. 191, no. 13-14, pp. 1367–1379, 2002.

101. D. Rochman *et al.*, "Nuclear Data Uncertainty for Criticality-Safety: Monte Carlo vs. Linear Perturbation," *Annals of Nuclear Energy*, vol. 92, pp. 150–160, 2016.

102. T. Zhu, A. Vasiliev, H. Ferroukhi, and A. Pautz, "NUSS: A Tool for Propagating Multigroup Nuclear Data Covariances in Pointwise ACE-formatted Nuclear Data Using Stochastic Sampling Method," *Annals of Nuclear Energy*, vol. 75, pp. 713–722, 2015.

103. M. Griseri, L. Fiorito, A. Stankovskiy, and G. Van den Eynde, "Nuclear Data Uncertainty Propagation on a Sodium Fast Reactor," *Nuclear Engineering and Design*, vol. 324, no. February, pp. 122–130, 2017.

104. A. Taavitsainen and R. Vanhanen, "On the Maximum Entropy Distributions of Inherently Positive Nuclear Data," *Nuclear Instruments and Methods in Physics Research, Section A: Accelerators, Spectrometers, Detectors and Associated Equipment*, vol. 854, no. November 2016, pp. 156–162, 2017.

105. G. Zerovnik, R. Capote, and A. Trkov, "On Random Sampling of Correlated Resonance Parameters with Large Uncertainties," *Nuclear Instruments and Methods in Physics Research, Section A: Accelerators, Spectrometers, Detectors and Associated Equipment*, vol. 723, pp. 89–98, 2013.

106. García-Herranz *et al.*, "Propagation of Statistical and Nuclear Data Uncertainties in Monte Carlo Burn-up Calculations," *Annals of Nuclear Energy*, vol. 35, no. 4, pp. 714–730, 2008.

107. M. Herman and A. Trkov, "ENDF-6 Formats Manual," *Brookhaven National Laboratory*, p. 392, 2010.

108. D. Campolina and J. Frybort, "Uncertainty Propagation for Lwr Burnup Benchmark Using Sampling Based Code Scale/Sampler," *Acta Polytechnica CTU Proceedings*, vol. 14, p. 8, 2018.

109. P. Mendius *et al.*, "MCNP: Criticality safety benchmark problems," Los Alamos National Laboratory, Tech. Rep., 1992.

110. B. Rearden, M. Jessee, and Eds., *User Guide for the STAYSL PNNL Suite of Software Tools*, PNNL-22253, Pacific Northwest National Laboratory, Richland, WA, February 2013.

111. J. Rowlands *et al.*, "Intercomparison of Calculations for Godiva and Jezebel," in *JEFF Report 16*. Nuclear Energy Agency, 1999, no. December.

112. C. B. Yeamans and B. E. Blue, "National Ignition Facility Neutron Sources," Lawrance Livermore National Laboraotry, Tech. Rep., 2018.

113. T. Siegl and A. West, "Statistical Bootstrapping Methods in VaR Calculation," *Applied Mathematical Finance*, vol. 8, no. 3, pp. 167–181, 2002.

114. D. A. Brown *et al.*, "ENDF/B-VIII.0: The 8th Major Release of the Nuclear Reaction Data Library with CIELO-project Cross Sections, New Standards and Thermal Scattering Data," *Nuclear Data Sheets*, vol. 148, pp. 1–142, 2018.

115. A. Holcomb *et al.*, "ENDF/B-VIII.0 Testing with AMPX and SCALE," in *SCALE User's Group Workshop*. Oak Ridge, Tennessee: Oak Ridge National Laboratory, 2018.

116. W. J. Marshall, "Validation of Criticality Safety Calculations with SCALE 6.2," in *Proceedings of the American Nuclear Society NCSD 2013: Criticality Saftety in the Modern Era: Raising the Bar*, LaGrange Park, IL, 2013.

117. A. P. J. Hodgson *et al.*, "The impact of neutron cross section group structures on the accuracy of radiological source models," *Nuclear Science and Engineering*, vol. 181, no. 3, pp. 302–309, 2015.

118. E. I. Moses *et al.*, "Overview: Development of the National Ignition Facility and the Transition to a User Facility for the Ignition Campaign and High Energy Density Scientific Research," *Fusion Science and Technology*, vol. 69, no. 1, pp. 1–24, 2016.

119. R. Khan, S. Karimzadeh, T. Stummer, and H. Böck, "Monte Carlo Simulation of the Thermal Column and Beam Tube of the TRIGA Mark II Research Reactor," *Nuclear Engineering and Design*, vol. 241, no. 8, pp. 2859–2864, 2011.

120. W. Wieselquist, T. Zhu, A. Vasiliev, and H. Ferroukhi, "PSI Methodologies for Nuclear Data Uncertainty Propagation with CASMO-5M and MCNPX: Results

for OECD/NEA UAM Benchmark Phase I," *Science and Technology of Nuclear Installations*, vol. 2013, 2013.

121. M. L. Williams *et al.*, "A Statistical Sampling Method for Uncertainty Analysis with SCALE and XSUSA," *Nuclear Technology*, vol. 183, no. 3, pp. 515–526, 2013.

122. D. L. Smith and D. G. Naberejnev, "Confidence Intervals for the Lognormal Probability Distribution," *Nuclear Instruments and Methods in Physics Research, Section A: Accelerators, Spectrometers, Detectors and Associated Equipment*, vol. 518, no. 3, pp. 754–763, 2004.

123. O. Schwerer, M. Winkler-Rohatsch, H. Warhanek, and G. Winkler, "Measurement of cross sections for 14 mev neutron capture," *Nuclear Physics, Section A*, vol. 264, p. 105, 1976.

124. G. Magnusson, P. Andersson, and I. Bergqvist, "14.7 mev neutron capture cross-section measurements with activation technique," *Physica Scripta*, vol. 21, no. 1, p. 21, 1980.

125. J. L. Perkin, L. P. O'Connor, and R. F. Coleman, "Radiative capture cross sections for 14.5 mev neutrons," *Proceedings of the Physical Society (London),*, vol. 72, p. 505, 1958.

126. J. Csikai, G. Peto, M. Buczko, Z. Miligy, and N. A. Eissa, "Radiative capture cross sections for 14.7 mev neutrons," *Nuclear Physics, Section A*, vol. 95, p. 229, 1967.

127. J. Vuletin, P. Kulisic, and N. Cindro, "Activation cross-sections of (n,γ) reactions at 14 mev," *Lettere al Nuovo Cimento*, vol. 10, p. 1, 1974.

128. M. Budnar *et al.*, "Prompt γ-ray spectra and integrated cross sections for the radiative capture of 14 mev neutrons for 28 natural targets in the mass region from 12 to 208," International Atomic Energy Agency, Tech. Rep. 6, 1979, yugoslavian report to the I.N.D.C.

129. N. Otuka *et al.*, "Towards a more complete and accurate experimental nuclear reaction data library (exfor): International collaboration between nuclear reaction data centres (nrdc)," *Nuclear Data Sheets*, vol. 120, pp. 272 – 276, 2014.

130. N. J. Quartemont, J. E. Bevins, R. Slaybaugh, and L. Bernstein, "Analysis of an Energy Tuning Assembly for Simulating Nuclear Weapon Environments at the National Ignition Facility," *Journal of Radiation Effects Research and Engineering*, vol. 38, 2020.

131. J. J. Molgaard, "Production of nuclear debris surrogates for forensic methods development," Master's thesis, The University of Tennessee, Knoxville, 2014.

132. O. Andrew G. and D. Mark R., "Reducing irradiation damage in a long-life fast reactor with spectral softening." *Energies*, no. 6, p. 1507, 2018.

133. U.S. Dept of Energy and U.S. Dept. of Defense, "National Security and Nuclear Weapons in the 21st Century," U.S. Dept of Energy and U.S. Dept. of Defense, Tech. Rep. September, 2008.

134. J. E. Bevins, "Gnowee V1.0," 2017. [Online]. Available: https://github.com/SlaybaughLab/Gnowee

135. E. Bauge *et al.*, "Coherent Investigation of Nuclear Data at Cea Dam: Theoretical Models, Experiments and Evaluated Data," *European Physical Journal A*, vol. 48, no. 8, p. 113, 2012.

136. L. Glendenin, J. Gindler, D. Henderson, and J. W. Meadows, "Mass Distributions for Monoenergetic-Neutron-Induced Fission of 235U," *Physical Review C*, vol. 24, no. 6, pp. 2600–2605, 1981.

137. G. P. Ford and R. B. Leachman, "Fission Mass Yield Dependence on Angular Momentum," *Physical Review*, vol. 137, no. 4 B, 1965.

138. M. E. Gooden *et al.*, "Energy Dependence of Fission Product Yields from 235U, 238U and 239Pu for Incident Neutron Energies Between 0.5 and 14.8 MeV," *Nuclear Data Sheets*, vol. 131, pp. 319–356, 2016.

139. M. E. Gooden, "Energy Dependence of Fission Product Yields from 235U, 238U, and 239Pu for Incident Neutron Energies Between 0.5 and 14.8 MeV," Ph.D. dissertation, North Caroline State University, 2014.

140. D. R. Nethaway and G. Barton, "A Compilation of Fission Product Yields in use at the Lawrence Livermore Labratory," Lawrence Livermore National Laboratory, Tech. Rep., 1973.

141. C. Chapman, T and G. A. Anzelon, "Fission Product Yields from 6-9 MeV Neutron Induced Fission of U-235 and U-238," *Physical Review C*, vol. 17, no. 3, pp. 1089–1097, 1978.

142. T. R. England and B. F. Rider, "Evaluation and Compliation of Fission Product Yields," *La-Ur-94-3106*, pp. 1–173, 1994.

143. J. G. Cuninghame, J. A. B. Goodall, and H. H. Harris, "Absolute Yields in the Fission of 235U By Mono-Energetic Neutrons of Energy 130-1700 keV," *J. Inorg. Nucl. Cham.*, vol. 36, no. 7, pp. 1453–1457, 1974.

144. K. B. Fournier, "NIF and OMEGA X-Ray Environments Summary," in *LLNL-TR-666017*. Livermore, CA: Lawrence Livermore National Laboratory, 2015.

145. B. Appelbe and J. Chittenden, "Relativistically Correct DD and DT Neutron Spectra," *High Energy Density Physics*, vol. 11, no. 1, pp. 30–35, 2014.

146. J. R. Taylor, *An Introduction to Error Analysis: The Study of Uncertainties in Physical Measurements*, 2nd ed. South Orange, NJ: University Science Books, 1997.

147. L. A. Bernstein *et al.*, "Our Future Nuclear Data Needs," *Annual Review of Nuclear and Particle Science*, vol. 69, no. 109, 2019.

148. A. C. Kahler, R. E. MacFarlane, and M. B. Chadwick, "Integral data testing of ENDF/B-VII.1 files - success stories and need to improve stories," *Nuclear Data Sheets*, vol. 118, no. 1, pp. 410–413, 2014.

149. N. Gharibyan, K. J. Moody, J. D. Despotopulos, P. M. Grant, and D. A. Shaughnessy, "First fission yield measurements at the National Ignition Facility: 14-MeV neutron fission of 238U," *Journal of Radioanalytical and Nuclear Chemistry*, vol. 303, no. 2, pp. 1335–1338, 2015.

150. H. Xiaolong, "Nuclear data sheets for A = 196," *Nuclear Data Sheets*, vol. 108, pp. 1093–1286, 2007.

151. X. Huang and M. Kang, "Nuclear Data Sheets for A = 198," *Nuclear Data Sheets*, vol. 133, pp. 221–416, 2016. [Online]. Available: http://dx.doi.org/10.1016/j.nds.2016.02.002

152. B. Singh, "Nuclear Data Sheets for A = 89," *Nuclear Data Sheets*, vol. 114, pp. 1–208, 2013. [Online]. Available: http://dx.doi.org/10.1016/j.nds.2013.01.001

153. Y. Dong and H. Junde, "Nuclear Data Sheets for A = 54," *Nuclear Data Sheets*, vol. 121, pp. 1–142, 2014. [Online]. Available: http://dx.doi.org/10.1016/j.nds.2014.09.001

154. H. Junde, H. Su, and Y. Dong, "Nuclear Data Sheets for A = 56," *Nuclear Data Sheets*, vol. 112, pp. 1513–1645, 2011. [Online]. Available: http://dx.doi.org/10.1016/j.nds.2011.04.004

155. J. Blachot, "Nuclear Data Sheets for A = 113," *Nuclear Data Sheets*, vol. 111, pp. 1471–1618, 2010. [Online]. Available: http://dx.doi.org/10.1016/j.nds.2010.05.001

156. J. Blachot, "Nuclear Data Sheets for A = 115," *Nuclear Data Sheets*, vol. 113, pp. 2391–2535, 2012. [Online]. Available: http://dx.doi.org/10.1016/j.nds.2012.10.002

157. J. Blachot, "Nuclear Data Sheets for A = 116," *Nuclear Data Sheets*, vol. 111, pp. 717–895, 2010. [Online]. Available: http://dx.doi.org/10.1016/j.nds.2010.05.001

158. E. Browne and J. K. Tuli, "Nuclear Data Sheets for A = 238," *Nuclear Data Sheets*, vol. 127, pp. 191–332, 2015. [Online]. Available: http://dx.doi.org/10.1016/j.nds.2015.07.003

159. M. S. Basunia, "Nuclear Data Sheets for A = 187," *Nuclear Data Sheets*, vol. 110, no. 5, pp. 999–1238, 2009. [Online]. Available: http://dx.doi.org/10.1016/j.nds.2009.04.001

160. M. R. Bhat, "Nuclear data sheets for A = 57," *Nuclear Data Sheets*, vol. 85, pp. 415–536, 1998.

161. C. D. Nesaraja, S. D. Geraedts, and B. Singh, "Nuclear Data Sheets for A = 58," *Nuclear Data Sheets*, vol. 111, pp. 897–1092, 2010. [Online]. Available: http://dx.doi.org/10.1016/j.nds.2010.03.003

162. R. B. Firestone, "Nuclear Data Sheets for A = 24," *Nuclear Data Sheets*, vol. 108, pp. 2319–2392, 2007.

163. C. L. Ellison *et al.*, "Development and Modeling of a Polar-direct-drive Exploding Pusher Platform at the National Ignition Facility," *Physics of Plasmas*, vol. 25, no. 7, 2018.

164. C. B. Yeamans and D. L. Bleuel, "The Spatially Distributed Neutron Activation Diagnostic FNADs at the National Ignition Facility," *Fusion Science and Technology*, vol. 72, no. 2, pp. 120–128, 2017. [Online]. Available: https://doi.org/10.1080/15361055.2017.1320499

165. N. J. Quartemont, "NIF ETA Experiment," March 2021. [Online]. Available: http://dx.doi.org/10.17632/92n6k43nt5.2

166. D. Brown *et al.*, "ENDF/B-VIII.0: The 8th Major Release of the Nuclear Reaction Data Library with CIELO-project Cross Sections, New Standards and Thermal Scattering Data"," *Nuclear Data Sheets*, vol. 148, pp. 1 – 142, 2018, special Issue on Nuclear Reaction Data. [Online]. Available: http://www.sciencedirect.com/science/article/pii/S0090375218300206

167. R. Gunnink and J. B. Niday, "Computerized Quantitative Analysis By Gamma-Ray Spectrometry. Vol. 1. Description of the Gamanal Program," Lawrence Livermore Laboratory, Livermore, CA, Tech. Rep., 1972.

168. R. Firestone, *Table of Isotopes*. New York, NY: John Wiley & Sons, 1996.

169. H. Selby *et al.*, "Fission Product Data Measured at Los Alamos for Fission Spectrum and Thermal Neutrons on ^{239}Pu, ^{235}U, ^{238}U," *Nuclear Data Sheets*, vol. 111, no. 12, pp. 2891 – 2922, 2010. [Online]. Available: http://www.sciencedirect.com/science/article/pii/S0090375210001018

170. O. T. Hogdahl, "Radiochemistry of palladium." National Academy of Sciences, Tech. Rep., 1961.

171. D. N. Sunderman and C. W. Townley, "Radiochemistry of silver." National Academy of Sciences, Tech. Rep., 1961.

172. J. R. DeVoe, "The radiochemistry of cadmium," National Academy of Sciences, Washington, D.C., Tech. Rep., 1960.

173. J. P. Faris and J. W. Warton, "Anion exchange resin separation of the rare earths, yttrium, and scandium in nitric acid-methanol mixtures." *Analytical Chemistry*, vol. 34, no. 9, pp. 1077–1080, 1962. [Online]. Available: https://doi.org/10.1021/ac60189a013

174. N. Gharibyan *et al.*, "Development of a "Fission-proxy" Method for the Measurement of 14-MeV Neutron Fission Yields," *Radiochimica Acta*, vol. 106, no. 8, pp. 627–630, 2018.

175. Bogetic, Sandra, "Improvements, Validation, and Applications of a Metaheuristic Optimization Method for Neutron Spectra Tailoring at the National Ignition Facility," Ph.D. dissertation, University of California, Berkeley, 2020.

176. M. A. Koehl, R. S. Rundberg, and J. C. Shafer, "Relative fission product yields in the USGS TRIGA MARK I reactor," *Journal of Radioanalytical and Nuclear Chemistry*, vol. 314, no. 2, pp. 1375–1381, 2017.

177. N. Quartemont, N. Gharibyan, K. Moody, and J. Bevins, "Uranium integral fission product yields for a spectrally-shaped 14.1 mev neutron source at the national ignition facility," *Applied Radiation and Isotopes*, p. 109711, 2021. [Online]. Available: https://www.sciencedirect.com/science/article/pii/S0969804321001184

178. Joint Defense Science Board/Threat Reduction Advisory Comittee Task Force, "The Nuclear Weapons Effects National Enterprise," Office of the Under Secretary of Defense for Acquisition, Technology, and Logistics, Washington, DC, Tech. Rep., 2010.

179. P. Griffin, D. King, and N. Kolb, "Application of spallation neutron sources in support of radiation hardness studies," *Nuclear Instruments and Methods in Physics Research, Section A: Accelerators, Spectrometers, Detectors and Associated Equipment*, vol. 562, no. 2, pp. 684–687, 2006.

180. E. Bielejec, G. Vizkelethy, R. M. Fleming, and D. B. King, "Metrics for comparison between displacement damage due to ion beam and neutron irradiation in silicon bjts," *IEEE Transactions on Nuclear Science*, vol. 54, no. 6, pp. 2282–2287, 2007.

181. N. J. Quartemont, "NIF ATHENA Experiment," May 2021. [Online]. Available: http://dx.doi.org/10.17632/bnvh2btjp3.1

182. J. E. Bevins and R. N. Slaybaugh, "Gnowee: A hybrid metaheuristic optimization algorithm for constrained, black box, combinatorial mixed-integer design," *Nuclear Technology*, vol. 205, no. 4, pp. 542–562, 2019. [Online]. Available: https://doi.org/10.1080/00295450.2018.1496692

183. H. Paxton and N. L. Pruvost, "Critical Dimensions of Systems Containing 235U, 239Pu, and 233U," Los Alamos National Laboratory, Los Alamos, NM, Tech. Rep., 1987.

184. T. Burrows, "Nuclear data sheets for a = 45," *Nuclear Data Sheets*, vol. 109, no. 1, pp. 171–296, 2008. [Online]. Available: https://www.sciencedirect.com/science/article/pii/S0090375207001147

185. S.-C. Wu, "Nuclear data sheets for a = 46," *Nuclear Data Sheets*, vol. 91, no. 1, pp. 1–116, 2000. [Online]. Available: https://www.sciencedirect.com/science/article/pii/S0090375200900140

186. T. Burrows, "Nuclear data sheets for a = 47," *Nuclear Data Sheets*, vol. 108, no. 5, pp. 923–1056, 2007. [Online]. Available: https://www.sciencedirect.com/science/article/pii/S0090375207000403

187. T. Burrows, "Nuclear data sheets for a = 48," *Nuclear Data Sheets*, vol. 107, no. 7, pp. 1747–1922, 2006. [Online]. Available: https://www.sciencedirect.com/science/article/pii/S0090375206000482

188. C. Yeamans and N. Gharibyan, "A neutron activation spectrometer and neutronic experimental platform for the national ignition facility," *Review of Scientific Instruments*, vol. 87, no. 11, p. 11D702, 2016.

189. R. Hatarik *et al.*, "Analysis of the neutron time-of-flight spectra from inertial confinement fusion experiments," *Journal of Applied Physics*, vol. 118, no. 18, 2015.

190. F. Merrill *et al.*, "The neutron imaging diagnostic at nif (invited)," *The Review of scientific instruments*, vol. 83, p. 10D317, 10 2012.

191. C. L. Ellison *et al.*, "Development and modeling of a polar-direct-drive exploding pusher platform at the national ignition facility," *Physics of Plasmas*, vol. 25, no. 7, p. 072710, 2018. [Online]. Available: https://doi.org/10.1063/1.5025724

192. C. Yeamans, G. Kemp, Z. Walters, H. Whitley, P. McKenty, E. Garcia, Y. Yang, R. Craxton, and B. Blue, "High yield polar direct drive fusion neutron sources at the national ignition facility," *Nuclear Fusion*, vol. 61, no. 4, p. 046031, mar 2021. [Online]. Available: https://doi.org/10.1088/1741-4326/abe4e6

193. A. M. McEvoy, H. W. Herrmann, C. J. Horsfield, C. S. Young, E. K. Miller, J. M. Mack, Y. Kim, W. Stoefflˆ, M. Rubery, S. Evans, T. Sedillo, and Z. A. Ali, "Gamma bang time analysis at omega." *Review of Scientific Instruments*, vol. 81, no. 10, p. 10D322, 2010. [Online]. Available: https://afit.idm.oclc.org/login?url=http://search.ebscohost.com/login.aspx?direct=true&db=asn&AN=54858034&site=eds-live

194. H. Brysk, "Fusion Neutron Energies and Spectra," *Plasma Physics*, vol. 15, no. 7, pp. 611–617, 1973.

195. Rooney, B., Garner, S., Felsher, P., Karpius, P., Lombardi, M., *PeakEasy 4.99, Release LA-CC-13-040*, Los Alamos, NM, 2020. [Online]. Available: https://PeakEasy.lanl.gov

196. M. Norgett, M. Robinson, and I. Torrens, "A proposed method of calculating displacement dose rates," *Nuclear Engineering and Design*, vol. 33, no. 1, pp. 50 – 54, 1975. [Online]. Available: http://www.sciencedirect.com/science/article/pii/0029549375900357

197. H. W. Herrmann *et al.*, "Diagnosing inertial confinement fusion gamma ray physics (invited)," *Review of Scientific Instruments*, vol. 81, no. 10, p. 10D333, 2010. [Online]. Available: https://doi.org/10.1063/1.3495770

198. Y. Kim *et al.*, "D-t gamma-to-neutron branching ratio determined from inertial confinement fusion plasmas," *Physics of Plasmas*, vol. 19, no. 5, p. 056313, 2012. [Online]. Available: https://doi.org/10.1063/1.4718291

199. A. Murari *et al.*, "Measuring the radiation field and radiation hard detectors at JET: Recent developments," *Nuclear Instruments and Methods in Physics Research, Section A: Accelerators, Spectrometers, Detectors and Associated Equipment*, vol. 593, no. 3, pp. 492–504, 2008.

200. A. Negret *et al.*, "Cross-section measurements for the Fe 56 (n, xnγ) reactions," *Physical Review C - Nuclear Physics*, vol. 90, no. 3, pp. 1–15, 2014.

201. M. L. Mauborgne *et al.*, "Designing tools for oil exploration using nuclear modeling," *EPJ Web of Conferences*, vol. 146, pp. 4–7, 2017.

202. M. Kerveno *et al.*, "From γ emissions to (n,xn) cross sections of interest: The role of GAINS and GRAPhEME in nuclear reaction modeling," *European Physical Journal A*, vol. 51, no. 12, pp. 1–18, 2015.

203. L. A. Bernstein *et al.*, "Our future nuclear data needs," *Annual Review of Nuclear and Particle Science*, vol. 69, no. 1, pp. 109–136, 2019. [Online]. Available: https://doi.org/10.1146/annurev-nucl-101918-023708

204. C. E. Romano *et al.*, "Discussion session highlights," in *Proceedings of the Workshop for Applied Nuclear Data: WANDA 2020*, 8 2020, pp. 10–12. [Online]. Available: https://www.osti.gov/biblio/1649010

205. S. A. Pozzi, E. Padovani, and M. Marseguerra, "MCNP-PoliMi: A Monte-Carlo code for correlation measurements," *Nuclear Instruments and Methods in Physics Research, Section A: Accelerators, Spectrometers, Detectors and Associated Equipment*, vol. 513, no. 3, pp. 550–558, 2003.

206. T. Wilcox, T. Kawano, G. W. McKinney, and J. S. Hendricks, "Correlated gammas using cgm and mcnpx," *Progress in Nuclear Energy*, vol. 63, pp. 1–6, 2013. [Online]. Available: https://www.sciencedirect.com/science/article/pii/S0149197012001278

207. J. A. Kulesza and R. L. Martz, "Evaluation of pulsed sphere time-of-flight and neutron attenuation experimental benchmarks using mcnp6's unstructured mesh capabilities," *Nuclear Technology*, vol. 195, no. 1, pp. 44–54, 2016. [Online]. Available: https://doi.org/10.13182/NT15-121

208. C. C. Byers, "Cross sections of various materials in the godiva and jezebel critical assemblies," *Nuclear Science and Engineering*, vol. 8, no. 6, pp. 608–614, 1960. [Online]. Available: https://doi.org/10.13182/NSE60-A25848

209. M. Chadwick, S. Frankle *et al.*, "Evaluated iridium, yttrium, and thulium cross sections and integral validation against critical assembly and bethe sphere measurements," *Nuclear Data Sheets*, vol. 108, no. 12, pp. 2716–2741, 2007, special Issue on Evaluations of Neutron Cross Sections. [Online]. Available: https://www.sciencedirect.com/science/article/pii/S0090375207000993

210. R. Stoller, S. Golubov, C. Domain, and C. Becquart, "Mean Field Rate Theory and Object Kinetic Monte Carlo: A Comparison of Kinetic Models," *Journal of Nuclear Materials*, vol. 382, no. 2, pp. 77 – 90, 2008. [Online]. Available: https://doi.org/10.1016/j.jnucmat.2008.08.047

211. R. R. Wixom and A. F. Wright, "Formation energies, binding energies, structure, and electronic transitions of si divacancies studied by density functional calculations," *Phys. Rev. B*, vol. 74, p. 205208, Nov 2006. [Online]. Available: https://link.aps.org/doi/10.1103/PhysRevB.74.205208

212. A. F. Wright and R. R. Wixom, "Density-functional-theory calculations for silicon vacancy migration," *Journal of Applied Physics*, vol. 103, no. 8, p. 083517, 2008. [Online]. Available: https://doi.org/10.1063/1.2906342

213. L. J. Munro and D. J. Wales, "Defect migration in crystalline silicon," *Phys. Rev. B*, vol. 59, pp. 3969–3980, Feb 1999. [Online]. Available: https://link.aps.org/doi/10.1103/PhysRevB.59.3969

214. J. A. Stewart, N. A. Modine, and R. Dingreville, "Re-examining the silicon self-interstitial charge states and defect levels: A density functional theory and bounds analysis study," *AIP Advances*, vol. 10, no. 9, p. 095004, 2020. [Online]. Available: https://doi.org/10.1063/5.0016134

215. M. Posselt, F. Gao, and D. Zwicker, "Migration of di- and tri-interstitials in silicon," *Nuclear Instruments and Methods in Physics Research Section B: Beam Interactions with Materials and Atoms*, vol. 228, no. 1, pp. 212–217, 2005, proceedings of the Seventh International Conference on Computer Simulation of Radiation Effects in Solids. [Online]. Available: https://www.sciencedirect.com/science/article/pii/S0168583X04011073

216. D. A. Richie *et al.*, "Complexity of small silicon self-interstitial defects," *Phys. Rev. Lett.*, vol. 92, p. 045501, Jan 2004. [Online]. Available: https://link.aps.org/doi/10.1103/PhysRevLett.92.045501

217. G. C. Messenger and J. P. Spratt, "The effects of neutron irradiation on germanium and silicon," *Proceedings of the IRE*, vol. 46, no. 6, pp. 1038–1044, 1958.

218. K. Wu *et al.*, "Neutron flux effects in silicon based bipolar junction transistors," *Nuclear Instruments and Methods in Physics Research Section A: Accelerators, Spectrometers, Detectors and Associated Equipment*, vol. 913, pp. 85–90, 2019. [Online]. Available: https://www.sciencedirect.com/science/article/pii/S0168900218313512

219. G. Meneghesso, A. Paccagnella, D. Camin, N. Fedyakin, G. Pessina, and C. Canali, "Study of neutron damage in gaas mesfets," *IEEE Transactions on Nuclear Science*, vol. 44, no. 3, pp. 840–846, 1997.

220. H. J. Barnaby, R. D. Schrimpf, K. F. Galloway, X. Li, J. Yang, and C. Liu, "Displacement damage in bipolar junction transistors: Beyond messenger-spratt," *IEEE Transactions on Nuclear Science*, vol. 64, no. 1, pp. 149–155, 2017.

221. L. Li *et al.*, "Current gain degradation model of displacement damage for drift bjts," *IEEE Transactions on Nuclear Science*, vol. 66, no. 4, pp. 716–723, 2019.

222. D. Chiesa *et al.*, "Measurement of the neutron flux at spallation sources using multi-foil activation," *Nuclear Instruments and Methods in Physics Research, Section A: Accelerators, Spectrometers, Detectors and Associated Equipment*, vol. 902, pp. 14–24, 2018.

223. Z. A. Kulage, C. H. Castano, S. Usman, and G. Mueller, "Characterization of the neutron flux energy spectrum at the Missouri University of Science and Technology Research Reactor (MSTR)," *Nuclear Engineering*

and Design, vol. 261, pp. 174–180, 2013. [Online]. Available: http://dx.doi.org/10.1016/j.nucengdes.2013.03.041

224. B. D. Jeffries *et al.*, "Characterization of the neutron flux during production of 18F at a medical cyclotron and evaluation of the incidental neutron spectrum for neutron damage studies," *Applied Radiation and Isotopes*, vol. 154, no. May, p. 108892, 2019. [Online]. Available: https://doi.org/10.1016/j.apradiso.2019.108892

225. S. M. T. Hoang *et al.*, "Enhancing Neutron Spectral Results Based on the Combination of Genetic algorithm and Activation Method," *Journal of Radioanalytical and Nuclear Chemistry*, vol. 318, no. 1, pp. 631–639, 2018.

226. S. P. Tripathy *et al.*, "Activation foils unfolding for neutron spectrometry: Comparison of different deconvolution methods," *Nuclear Instruments and Methods in Physics Research, Section A: Accelerators, Spectrometers, Detectors and Associated Equipment*, vol. 583, no. 2-3, pp. 421–425, 2007.

227. V. Suman, S. P. Tripathy, C. Sunil, A. A. Shanbhag, S. Paul, G. S. Sahoo, T. Bandyopadhyay, and P. K. Sarkar, "Measurement of neutron energy distributions from p+Be reaction at 20 MeV using threshold activation foils," *IEEE Transactions on Nuclear Science*, vol. 63, no. 4, pp. 2283–2292, 2016.

228. B. Liu, H. Yang, H. Lv, L. Li, F. Jing, J. Liu, and S. Wang, "Neutron spectrum unfolding of the multiple activation foils based on sparse representation," *Annals of Nuclear Energy*, vol. 135, p. 106947, 2020. [Online]. Available: https://www.sciencedirect.com/science/article/pii/S0306454919304347

229. J. Jo, M. Cheon, K.-J. Chung, and Y. Hwang, "Initial result of neutron energy spectrum reconstruction using multi-foil activation method in kstar," *Fusion Engineering and Design*, vol. 136, pp. 793–796, 2018, special Issue: Proceedings of the 13th International Symposium on Fusion Nuclear Technology (ISFNT-13). [Online]. Available: https://www.sciencedirect.com/science/article/pii/S0920379618302990

230. G. Lövestam *et al.*, "Neutron fluence spectrometry using disk activation," *Radiation Measurements*, vol. 44, no. 1, pp. 72–79, 2009. [Online]. Available: https://www.sciencedirect.com/science/article/pii/S135044870800379X

231. H. R. Vega-Carrillo, E. Manzanares-Acuña, M. Pilar Iñiguez, E. Gallego, and A. Lorente, "Study of room-return neutrons," *Radiation Measurements*, vol. 42, no. 3, pp. 413–419, 2007. [Online]. Available: https://www.sciencedirect.com/science/article/pii/S1350448707000443

232. R. Khabaz, "Analysis of neutron scattering components inside a room with concrete walls," *Applied Radiation and Isotopes*, vol. 95, pp. 1–7,

2015. [Online]. Available: https://www.sciencedirect.com/science/article/pii/S0969804314003327

233. Z. Wang, S. F. Kry, R. M. Howell, and M. Salehpour, "Comparison of unfolding methods for determining neutron spectrum and ambient dose equivalent," *Nuclear Technology*, vol. 168, no. 3, pp. 610–614, 2009.

234. R. Prokopowicz and K. Pytel, "On certain heuristic approach to neutron spectrum unfolding," *Nuclear Instruments and Methods in Physics Research Section A: Accelerators, Spectrometers, Detectors and Associated Equipment*, vol. 939, pp. 106–111, 2019. [Online]. Available: https://www.sciencedirect.com/science/article/pii/S0168900219307156

235. M. del Rosario Martinez-Blanco *et al.*, "A neutron spectrum unfolding code based on generalized regression artificial neural networks," *Applied Radiation and Isotopes*, vol. 117, pp. 8–14, 2016, iSSSD2015 Proceedings of the XV International Symposium on Solid State Dosimetry, Leon, Guanajuato, Mexico, September 26-30, 2015. [Online]. Available: https://www.sciencedirect.com/science/article/pii/S0969804316301609

236. W. N. McElroy *et al.*, "A Computer-Automated Iterative Method for Neutron Flux Spectra Determination by Foil Activation Method," Air Force Weapons Laboratory, Canoga Park, CA, Tech. Rep., 1967.

237. M. A. Koehl, R. S. Rundberg, and J. C. Braley, "Measured neutron flux parameters in the usgs triga mark i reactor." *Journal of Radioanalytical and Nuclear Chemistry: An International Journal Dealing with All Aspects and Applications of Nuclear Chemistry*, vol. 306, no. 1, p. 31, 2015.

238. S. Sen *et al.*, "Determination of Neutron Energy Spectrum at KAMINI Shielding Experiment Location," *Applied Radiation and Isotopes*, vol. 115, pp. 165–171, 2016.

239. N. J. Quartemont, "Regularized Heuristic Method for Activation Monitor Neutron Spectrum Unfolding," June 2021. [Online]. Available: http://dx.doi.org/10.17632/shf56c665r.1

240. K. Harrig *et al.*, "Neutron spectroscopy for pulsed beams with frame overlap using a double time-of-flight technique," *Nuclear Instruments and Methods in Physics Research Section A: Accelerators, Spectrometers, Detectors and Associated Equipment*, vol. 877, pp. 359–366, 2018. [Online]. Available: https://www.sciencedirect.com/science/article/pii/S0168900217310215

241. M. Kireeff Covo *et al.*, "The 88-inch cyclotron: A one-stop facility for electronics radiation and detector testing," *Measurement*, vol. 127, pp. 580–587, 2018. [Online]. Available: https://www.sciencedirect.com/science/article/pii/S0263224117306401

242. J. P. Meulders, P. Leleux, P. C. Macq, and C. Pirart, "Fast neutron yields and spectra from targets of varying atomic number bombarded with deuterons from 16 to 50 MeV (for radiobiology and radiotherapy)," *Physics in Medicine and Biology*, vol. 20, no. 2, pp. 235–243, mar 1975. [Online]. Available: https://doi.org/10.1088/0031-9155/20/2/005

REPORT DOCUMENTATION PAGE

Form Approved
OMB No. 0704–0188

1. REPORT DATE *(DD–MM–YYYY)*	2. REPORT TYPE	3. DATES COVERED *(From — To)*
16-09-2021	PhD Dissertation	Mar 2019 — Sep 2021

4. TITLE AND SUBTITLE

Neutron Energy Tuning Assemblies for Nuclear Weapon Environment Applications at the National Ignition Facility

5a. CONTRACT NUMBER

5b. GRANT NUMBER

5c. PROGRAM ELEMENT NUMBER

6. AUTHOR(S)

Quartemont, Nicholas J, Captain, USAF

5d. PROJECT NUMBER

5e. TASK NUMBER

5f. WORK UNIT NUMBER

7. PERFORMING ORGANIZATION NAME(S) AND ADDRESS(ES)

Air Force Institute of Technology
Graduate School of Engineering and Management (AFIT/EN)
2950 Hobson Way
WPAFB OH 45433-7765

8. PERFORMING ORGANIZATION REPORT NUMBER

AFIT-ENP-DS-21-S-033

9. SPONSORING / MONITORING AGENCY NAME(S) AND ADDRESS(ES)

Multiple, primary listed.
ATTN: LTC Nickolas Duncan (nickolas.duncan@westpoint.edu)
Defense Threat Reduction Agency
8725 John J. Kingman Rd. Stop 6201
Fort Belvoir, VA 22060-6201

10. SPONSOR/MONITOR'S ACRONYM(S)

DTRA

11. SPONSOR/MONITOR'S REPORT NUMBER(S)

12. DISTRIBUTION / AVAILABILITY STATEMENT

APPROVED FOR PUBLIC RELEASE; DISTRIBUTION UNLIMITED.

13. SUPPLEMENTARY NOTES

14. ABSTRACT

An energy tuning assembly was developed to spectrally shape the National Ignition Facility deuterium-tritium fusion neutron source to a notional thermonuclear and prompt fission neutron spectrum to fulfill neutron source capability gaps. The experimental neutron environment was characterized with activation dosimetry, neutronics and covariance models, and unfolded to determine the as-fielded neutron spectrum. The first energy tuning assembly was demonstrated to create synthetic spectrally accurate post-detonation fission products, enhancing U.S. technical nuclear forensics capabilities. ATHENA, a second-generation energy tuning assembly, was also optimized to meet similar objectives, but the new platform neutron fluence efficiency was increased by a factor of 2.7. The ATHENA platform was experimentally fielded to benchmark and validate the models, with an unfolded reduced chi-square metric of 1.4, preparing for future active measurement of electronic devices. The novel ATHENA platform provides a capability to perform integral nuclear data measurements and active experimentation on electronics components in a unique radiation environment.

15. SUBJECT TERMS

Short pulse neutron source, fission products, spectroscopy, nuclear data covariance, foil activation, energy tuning assembly, Monte Carlo simulation, neutron spectrum unfolding, attribution

16. SECURITY CLASSIFICATION OF:			17. LIMITATION OF ABSTRACT	18. NUMBER OF PAGES	19a. NAME OF RESPONSIBLE PERSON
a. REPORT	b. ABSTRACT	c. THIS PAGE			Maj James E. Bevins, AFIT/ENP
U	U	U	U	254	19b. TELEPHONE NUMBER *(include area code)* (937) 255-3636, x4767